

High Temperature Behavior of Nano-Structured Ceramic Composites Studied by Mechanical Spectroscopy

THÈSE N° 5523 (2013)

PRÉSENTÉE LE 22 FÉVRIER 2013

À LA FACULTÉ DES SCIENCES DE BASE
LABORATOIRE DE PHYSIQUE DE LA MATIÈRE COMPLEXE
PROGRAMME DOCTORAL EN PHYSIQUE

ÉCOLE POLYTECHNIQUE FÉDÉRALE DE LAUSANNE

POUR L'OBTENTION DU GRADE DE DOCTEUR ÈS SCIENCES

PAR

Mehdi MAZAHERI

acceptée sur proposition du jury:

Prof. C. Hébert, présidente du jury
Prof. R. Schaller, Dr D. Mari, directeurs de thèse
Prof. G. Fantozzi, rapporteur
Prof. Z. J. Shen, rapporteur
Prof. P. Stadelmann, rapporteur



ÉCOLE POLYTECHNIQUE
FÉDÉRALE DE LAUSANNE

Suisse
2013

To my parents

Abstract

Silicon nitride based ceramics (SiAlONs); tetragonal polycrystalline zirconia (3Y-TZP); alumina and their composites reinforced with different amount of multi-walled carbon-nanotubes (CNTs) have been processed by Spark Plasma Sintering (SPS). High temperature mechanical spectroscopy measurements were performed in each material between room temperature and 1600 K. In each of these materials, anelastic and viscoplastic relaxation phenomena were investigated and responsible mechanisms were explained. In particular, grain boundary (GB) sliding, which is responsible for high temperature plasticity in fine grained ceramics, gives rise to a peak or an exponential increase in the high temperature mechanical loss. Peak and exponential background depend on two forces, which control the GB sliding: a friction force due to the GB viscosity and a restoring force due to the elasticity of the surrounding grains. In the present thesis, ceramics and composites have been processed, which allow one to study the role played by these forces on the thermo-mechanical behavior of these refractory materials. SiAlON ceramics were chosen for studying the viscous force due to the inter-granular glassy phase. In zirconia and alumina, it is shown how the CNT reinforcements may improve the restoring force and consequently the creep resistance.

Different grades of SiAlON ceramics, processed with different sintering aids (Ca^{2+} , Y^{3+} , Yb^{3+}), with oxygen rich (CaO , Y_2O_3 and Yb_2O_3) and nitrogen rich (CaH_2 , YN and YbN) compounds, have been studied. Mechanical spectroscopy has been used to analyze the behavior of the residual glassy phase, present after sintering, either as grain-boundary glassy (GB) films or glass pockets located in GB triple junctions. The mechanical loss spectra show a relaxation peak, which is due to a relaxation phenomenon (the so called “ α -relaxation”) associated with the glass transition in the amorphous phase. The peak position depends on the glass viscosity and the peak height is mainly affected by the glassy phase amount and the SiAlON bimodal microstructure, namely equiaxed versus elongated grains. Moreover the peak height depends on the restoring force provided by the neighboring grains, which limit the GB sliding process. As a matter of fact, a good correlation between the mechanical loss peak and plastic deformation in a compression test has been observed. It is concluded that the elongated grains in the bimodal microstructure provide a higher restoring force, which limits the GB sliding of smaller equiaxed grains.

Abstract

In the case of equiaxed fine grained oxide ceramics, such as zirconia and alumina, the restoring force has been increased by CNT additions, which can reinforce the GBs. 3Y-TZP composites with a homogenous distributions of CNTs, ranging within 0.5 – 5 wt%, were processed by SPS. A significant improvement in room temperature fracture toughness and shear modulus as well as creep performance at high temperature were obtained, and interpreted as due to the GB reinforcing role of the CNTs. To support this interpretation, high-resolution electron microscopy and Raman spectroscopy have been carried out. Moreover, a remarkable enhancement of the electrical conductivity up to ten orders of magnitude due to CNT additions has been obtained with respect to the pure ceramics.

The isothermal spectrum of the 3Y-TZP composites (measured at 1600 K) is composed of a mechanical loss peak at a frequency of about 0.1 Hz, which is superimposed on an exponential increase at lower frequency. This is interpreted as primarily due to GB sliding. The absence of a well-marked peak in monolithic 3Y-TZP is justified by considering that the restoring force decreases at low frequencies or high temperatures. Therefore, GB sliding is no more restricted and the mechanical loss increases exponentially, which is correlated to macroscopic creep. With CNT additions the mechanical loss decreases and the relaxation peak is better resolved with respect to the background. This is interpreted by the pinning effect of CNTs on GBs, providing addition source of restoring force, which can hinder GB sliding at high temperature, resulting in a creep resistance improvement.

Similarly to 3Y-TZP based composites, alumina specimens (3 different types of alumina powders) reinforced with different amount of CNTs were sintered by SPS. It is shown how the initial particle size of the powders may affect the dispersion of CNTs. Measurement of different properties, such as hardness, fracture toughness and mechanical loss at high temperature, have evidenced the crucial role of the CNT dispersion in the obtained mechanical properties.

Keywords: mechanical spectroscopy, creep test, Spark Plasma Sintering, electron microscopy, zirconia, alumina, multi-walled carbon nanotubes, silicon nitride.

Résumé

Des céramiques à base de nitrure de silicium (SiAlON), de zircone polycristalline (3Y-TZP) et d'alumine (Al_2O_3) renforcées par différentes quantités de nanotubes de carbone multi-parois (CNTs) ont été produites par Spark Plasma Sintering (SPS). Les matériaux obtenus ont été caractérisés de la température ambiante à 1600 K par des mesures de spectroscopie mécanique. Dans chaque matériau, des phénomènes de relaxation anélastique et viscoplastique ont été observés, étudiés et interprétés. En particulier, le glissement aux joints de grains qui est responsable de la déformation plastique à haute température des céramiques à grains fins, est à l'origine d'un pic ou d'une augmentation exponentielle de l'amortissement. Pic et fond exponentiel dépendent de deux forces qui contrôlent le glissement aux joints de grains, une force de frottement due à la viscosité du joint et une force de rappel due à l'élasticité des grains voisins. Dans la présente thèse, des céramiques et des composites ont été élaborés permettant d'étudier le rôle de ces deux types de forces sur le comportement thermo-mécanique de ces matériaux réfractaires. Les céramiques type SiAlON ont été choisies principalement pour l'étude de la force de frottement visqueux due à la phase amorphe inter-granulaire. Dans le cas de la zircone et de l'alumine, on montre comment les renforts par CNTs augmentent la force de rappel et donc la résistance au fluage.

Ainsi diverses nuances de SiAlON élaborées avec divers ajouts de frittage (Ca^{2+} , Y^{3+} , Yb^{3+}), riches en oxygène (CaO , Y_2O_3 et Yb_2O_3) et riches en azote (CaH_2 , YN et YbN), ont été étudiées. La spectroscopie mécanique est utilisée pour analyser le comportement de la phase amorphe résultant des ajouts de frittage, soit sous forme de films aux joints de grains, soit sous forme de poches amorphes aux nœuds triples. Les spectres de pertes mécaniques présentent un pic d'amortissement qui est dû à un mécanisme de relaxation associé à la transition vitreuse de la phase amorphe (le pic α). La position du pic dépend de la viscosité de la phase vitreuse et sa hauteur dépend de la fraction volumique de celle-ci et de la distribution bimodale en taille de grains du SiAlON (proportion des grains allongés par rapport aux grains équiaxes). D'autre part la hauteur du pic dépend de la force de rappel, qui limite le glissement aux joints de grains. Une bonne corrélation a été observée entre la hauteur du pic d'amortissement et la déformation plastique en compression. On peut en conclure que les grains allongés de la microstructure bimodale offrent une plus grande force de rappel, qui limite le glissement aux joints des plus petits grains.

Résumé

Dans le cas des céramiques à grains fins équiaxes, tels la zircone et l'alumine, la force de rappel a été augmentée grâce à des ajouts de carbones nanotubes (CNTs), susceptibles de renforcer les joints de grains. Les composites à base de zircone 3Y-TZP contenant une distribution homogène de CNTs de 0.5 à 5 % poids ont été élaborés par SPS. Des augmentations significatives de la ténacité et du module élastique à température ambiante, ainsi qu'une meilleure résistance au fluage à haute température ont été obtenues et interprétées comme dues au rôle de renfort des joints de grains par les CNTs. Cette interprétation est soutenue par des observations complémentaires de microscopie électronique à haute résolution et de spectroscopie Raman. De plus, les ajouts de CNTs conduisent à une augmentation remarquable de la conductibilité électrique jusqu'à dix ordres de grandeur par rapport à la céramique de base.

Les spectres isothermes (1600 K) de pertes mécaniques des composites à base de 3Y-TZP présentent un pic de relaxation à une fréquence voisine de 0.1 Hz superposée à un accroissement exponentiel du frottement intérieur à plus basse fréquence. Les pertes mécaniques sont interprétées comme dues aux glissements aux joints de grains. Dans le cas de la zircone non renforcée, le pic se distingue mal du fond exponentiel, ce qui s'explique par une valeur faible de la force de rappel qui encore diminue à basse fréquence ou à haute température. Dans ce cas, le glissement aux joints de grains n'est pas limité et les pertes mécaniques s'accroissent exponentiellement. Cet accroissement exponentiel est corrélé à l'apparition du fluage macroscopique. Avec les additions de CNTs, le fond exponentiel des pertes mécaniques diminue et le pic de relaxation apparaît mieux résolu par rapport au fond. Ceci est interprété par l'effet d'ancrage des joints de grains par les CNTs, qui limitent le glissement aux joints et sont responsables de l'augmentation de la résistance au fluage observée.

D'une manière similaire aux composites à base zircone, des échantillons d'alumine (3 différentes nuances de poudres d'alumine) renforcée par différentes quantités de CNTs ont été produits par SPS. On montre que la taille des particules formant la poudre de départ affecte la distribution des CNTs. Les mesures de divers paramètres, tels que la dureté et la ténacité à température ambiante, et les pertes mécaniques à haute température, mettent en évidence le rôle crucial d'une bonne dispersion des CNTs dans la qualité du composite obtenu.

Mots-clés: spectroscopie mécanique, fluage, Spark Plasma Sintering, microscopie électronique, zircone, alumine, nanotubes de carbone, nitrure de silicium.

Acknowledgments

It was almost four years ago when I started this PhD work. At that period of time, I remember myself having not even a simple idea about mechanical spectroscopy, nor did I know much about solid-state physics. Therefore, following several dreams and going for the aims that I had drawn for my life would have been impossible for me without the absolute support from many people, throughout these years.

First of all, I would like to particularly express my most profound gratitude to my thesis supervisor, Prof. Robert Schaller, who not only proposed the project, but also offered me valuable support through every single step of the thesis. I would like to thank him for his inspiring ideas, patience and company. The unrestricted passion he used to express to his students all these years allows me to say that I found him like a father helping his child to grow, much more than an ordinary boss. Robert! Thanks for giving me this opportunity to work in your lab.

I would like to express my extreme gratefulness to my thesis co-adviser, Dr. Daniele Mari. Working with Daniele was among the greatest opportunities of my life, which not only led me to improve scientifically, but also could teach a lot on a personal level. His amazing intuition and broad knowledge of material science have been an advantage, leading my thesis from the very beginning to the end. His office was next to mine and thanks to his open-door / open-minded policy I was always welcomed for any discussions with him. Thanks Daniele for everything.

It was an honor for me to have, Prof. G. Fantozzi and Prof. Z. Shen, as thesis jury members. I strongly appreciate the time they dedicated to reviewing my thesis, their smart comments and supportive remarks. I would also like to thank Prof. Stadelmann, and Prof. Hebert for their valuable comments.

I would like especially to thank to Dr. I. Tkalcec for helping me a lot regarding experimental troubles. I have profited on many occasions from her very quick reaction to assistance. I would also like to thank other colleagues Ms. E. Ludi, Ms. M. Bettinger, Dr. F. Chowdhury, Dr. A. Sellerio, Dr. R. Martin, Ms. A. Meier, Dr. J. Henning, Prof. W. Benoit, and Prof. G. Gremaud. I would like to thank Dr. Y. Cai for providing Sialon samples and Mr. G. Bonnefont for helping me during SPS sessions. Mr. G. Camarda, Mr. G. Beney, Dr. D. Alexander, Dr. P. Bowen, Dr. M. Cantoni and Ms. F. Bobard are acknowledged for providing their expertise in doing things I can't.

The Last but not the least, I would like to express all my loving thanks to my most dear family for everything. Without having the unconditional supports from my father Hossein, and my mother Azam, I would have never been able to finish this work.

Mehdi Mazaheri, September 2012

List of contents

Introduction	1
Chapter 1: Scientific Background	5
1.1. Superplastic deformation of ceramics	6
1.2. SiAlON ceramics and their properties	8
1.3. Ceramics contained carbon nanotubes	10
1.4. Ceramics reinforced with CNTs: High temperature properties	16
1.5. Objectives of this work	18
Chapter 2: Mechanical spectroscopy and its application in ceramics	23
2.1. Introduction	24
2.2. Anelastic relaxation	24
2.2.1. Phenomenology	24
2.2.2. Standard anelastic solid (Rheological model)	27
2.2.3. Dynamic properties of standard anelastic solid	29
2.3. Mechanical spectroscopy and internal friction	32
2.4. Examples of anelastic relaxations of ceramics	33
2.4.1. Yttria stabilized zirconia	33
2.4.1.1. Low temperature peak (point defect relaxation)	35
2.4.1.2. High temperature damping (grain-boundary relaxation)	36
2.4.1.2.1. GB sliding according to Zener's model	38
2.4.1.2.2. GB sliding: Lakki's model	40
2.4.2. Alumina: Grain boundary dislocation motion	43
2.4.2.1. Dislocation relaxation	43
2.4.2.2. Damping due to GB dislocation	46
2.4.2.3. Master curve method and activation energy calculation	47
2.4.2.4. Creep and exponential background	49
2.4.3. Silicon nitride	50
2.4.3.1. Relaxation peak in Si_3N_4	51
2.4.3.2. Relaxation in Y-Sialon glass	52
Chapter 3: Materials and techniques	57
3.1. Processing of materials	58
3.1.1. Monolithic and composite zirconia ceramics	58
3.1.2. Monolithic and composite alumina ceramics	62
3.1.3. Si_3N_4 based ceramics (SiAlONs)	63
3.2. Microstructural observations	65
3.3. Sample phase characterization	65
3.4. Mechanical and electrical testing	66
3.5. Mechanical spectroscopy	67

Chapter 4: Experimental results and analysis: Silicon nitride based ceramics	71
4.1. Results obtained in nitrogen- and oxygen-rich Y- and Yb-Sialon ceramics	72
4.2. Results obtained in Ca-Sialons	76
4.2.1. Oxygen rich Ca-Sialon	76
4.2.2. Nitrogen rich CaSialon	77
4.3. Analysis of the Ca-Sialon spectrum and theoretical model	86
4.4. Phase characterization of Ca-Sialon sample	94
4.5. Conclusion	96
Chapter 5: Experimental results and analysis: zirconia based composites	99
5.1. Powder composites processing and characterization	100
5.2. Sintered composite characterization	100
5.3. Room temperature mechanical properties	109
5.4. Room temperature electrical conductivity	115
5.5. High temperature mechanical properties	116
5.5.1. Creep results	116
5.5.2. Mechanical spectroscopy results	117
5.5.2.1. Isochronal spectra of 3Y-TZP composites	119
5.5.2.2. Isothermal spectra of 3Y-TZP composites	121
5.5.2.3. Theoretical model	121
5.5.2.4. Activation Energy: New master curve model	128
5.6. Conclusion	134
Chapter 6: Experimental results and analysis: Alumina based composites	139
6.1. Processing and properties obtained in composites produced using submicron α -alumina TM-DAR powder	140
6.2. Processing and properties obtained in composites produced using nano size γ -alumina powder	145
6.3. Processing and properties obtained in composites produced using nano-size α -alumina (MK-40)	150
6.4. Conclusion	153
Chapter 7: General discussion	155
7.1. Effective parameters on grain boundary sliding	156
7.2. Effect of the quantity/ composition of glassy phase	156
7.3. Effect of the pinning agents	159
7.4. Efficiency of the pinning agents: amount and dispersion	160
7.5. Ideas for further research	162
Conclusion	165
Curriculum Vitae	167

Introduction

What is a ceramic? The word of ceramic comes from the Greek word *Keramos*, which translates to mean *burnt earth*. Webster dictionary define ceramics as “of or having to do with pottery”. Both of these two definitions go back to the earliest origin of ceramics, when early people fired to form a hard and brittle pottery. They mixed clay with some water, shaped, dried in the sun and fired, which results in the first human ceramics, probably since the existence of humanity, and has its origin in Jiroft, Persian civilization or Sumer civilization. By the latter half of 20th century, scientists and engineers had synthesized many new ceramics that did not completely fit the initial definition. A more modern definition would be a material that contains metallic and non-metallic element. Depending on the non-metallic element ceramics are defined as oxide ceramics (ZrO_2 , Al_2O_3 , Y_2O_3 , etc) or non-oxide ceramics such as Carbides (SiC, ZrC, etc), Nitrides (Si_3N_4 , BN, etc), SiAlONs, and etc. These materials can be also defined by their inherent properties; they form hard, stiff, and brittle materials due to the nature of their inter-atomic bonding, which is ionic and covalent. These properties are opposite to those of a metal; metals are non-brittle (display elastic behavior), and ductile (show plastic behavior).

Throughout history, ceramics have been the materials of choice for high temperature applications. They have a rich heritage as refractories for smelting and shaping of metals. Nowadays, they play an important role in the emergence of aerospace industry, heat engines, gas turbines and petroleum refining industries. They have, because of many advantages over metals, such as their low density, low sensitivity to corrosion, biocompatibility, and high rigidity and hardness, also several applications at room temperature. Few routine applications of ceramics or in modern technologies can be seen in Fig. I.

It is well-known that poor fracture toughness at room temperature, because of their brittle nature, and plastic deformation at high temperature, because of grain-boundary sliding, limit handling and application of ceramics in many industrial, aerospace and army applications. Accordingly, increasing the fracture toughness at room temperature and improving creep resistance at high temperature is still nowadays a matter of research. Grain refining is a promising route for the simultaneous increase of room temperature mechanical strength and fracture toughness.

Spark Plasma Sintering (SPS) is a promising technique for producing nanostructured ceramics. SPS is a newly developed sintering process that combines

Introduction

the use of mechanical pressure and microscopic electric discharge between the particles. As a result, samples can rapidly reach full density (in few minutes) at relatively low temperature. This technique allows one to process nanostructured ceramics, which exhibit improved fracture toughness at room temperature. On the down side, a nanostructured ceramic does not show promising properties at high temperatures, while the responsible mechanism for plastic deformation of ceramics, the so called grain-boundary (GB) sliding, can be activated at much lower temperature than in the case of conventional ceramics with larger grains.



Fig. 1. Example of ceramic applications in room and high temperatures.

Hence, it can be concluded that nanostructured ceramics exhibit good mechanical properties for room temperature applications (high toughness/ strength), but low creep resistance at high temperature. Therefore, many efforts have been conducted to suppress the grain sliding with pinning GBs in nanostructures.

Owing to their extraordinary mechanical properties, carbon nanotubes (CNTs) have recently attracted some attention as GB pinners in ceramics for high temperature applications as well as toughening agents for room temperature applications. However, because of the difficulties in obtaining a homogenous distribution of CNTs throughout the matrix, CNT damage during high temperature processing and weak

interfacial bonding between the CNTs and the ceramic grains, the CNT benefits in such composites are not clearly recognized.

This study aims at analyzing the high temperature deformation of nano-structured oxide- and non-oxide- structural ceramics to improve their properties. First a model non-oxide nitride ceramics (Si_3N_4 based) is investigated. Their deformation typically occurs by GB sliding. However they may be reinforced by changing the grain shapes. Then, the use of carbon nano-tubes (CNTs) in order to reinforce oxide ceramics such as ZrO_2 and Al_2O_3 will be studied from processing to mechanical testing. Spark Plasma Sintering is used for processing the samples, and the technique will be compared to traditional sintering. The mechanical properties of the processed samples have been studied mainly by mechanical spectroscopy; a technique capable to detect and analyze the GB mobility and viscosity. Therefore thesis guideline would be as following;

The **first chapter**, presents a brief review on the literature about plastic deformation of ceramics, both silicon nitride based and oxide ceramics, and about the processing and properties of ceramic composites reinforced with CNTs.

In the **second chapter**, mechanical spectroscopy, its application in ceramics, and related theoretical models are presented.

Chapter three provides the details of sample processing and their characterization for different monolithic ceramics and CNT reinforced composites: silicon nitride, zirconia, and alumina. Microstructural analysis and the experimental setup used in this research are described in this chapter.

Chapter four, five and six present the results and analysis of the properties of silicon nitride based-, alumina based- and zirconia based- composites, respectively. The models for high temperature deformation of those materials are also proposed in each chapter.

Chapter seven presents a general analysis and discussion on the original results obtained in the different nanostructured ceramics and composites; from Sialon ceramic to Alumina, Zirconia and their composites. It is shown how this research questioned the existing GB sliding model, playing with grain shapes, fraction of GB glassy phase, grain sizes, amount of nano-reinforcements, and the efficiency of the reinforcements (dispersion of CNTs).

Chapter 1

Scientific Background

In this chapter literature around three areas is reviewed: (1) the mechanisms and possible scenarios, being responsible for the high temperature plastic deformation of ceramics, (2) a brief introduction on silicon nitride based ceramics and the effect of microstructure (the glassy phase in the structure and elongated grains) on their properties, and (3) the literature and advances in the processing of carbon nanotube - ceramic composites. The effect of CNTs on room and high temperature mechanical properties of ceramics are also presented. Finally the objectives of the present work are presented.

1.1. Superplastic deformation of ceramics

The ability of ceramics to undergo superplastic deformation was, initially, recognized for the first time in 1979 and 1980 for uranium oxide and magnesium oxide, respectively [1, 2]. In 1986, Wakai et al. [3] reported experiments showing an elongation of 120% for a fine-grained (<300 nm) 3mol%-Y₂O₃ stabilized tetragonal zirconia (3Y-TZP) at 1723 K. Afterwards, a large number of investigations [4-9] have been carried out to identify the underlying mechanism for such a deformation in a wide range of temperatures and applied stresses. In spite of the large number of investigations devoted to the superplastic deformation of 3Y-TZP, several discrepancies still remain, particularly regarding the rate controlling mechanism, which is associated with the slowest process. Nevertheless, we should emphasize that the majority of former investigations have indicated that superplastic deformation mostly occurs by grain boundary (GB) sliding. As Ashby and Raj [10] pointed out, GB sliding creates voids or overlaps between the grains that have to be accommodated. Some of the reported GB sliding accommodation possibilities are grain boundary migration, dislocation slip recovery and diffusional flow of matter. Indeed, GB sliding must accommodate bulk diffusional creep [10]. Moreover, microscopic observations on deformed 3Y-TZP samples generally revealed that the grains always remain equiaxed [4, 8]. It was assumed that in polycrystals the deformation results from a neighboring-switching event. The change in configuration of a four-grain unit by GB sliding with diffusion-accommodation provides a large strain without appreciable deformation of the grains (Fig. 1.1).

Thus, what can be inferred from the literature is that the high temperature ductile behavior of 3Y-TZP should be mainly associated with GB sliding accommodated by diffusional creep mechanisms, such as Coble or Nabarro-Herring creep.

The deformation of polycrystalline materials at high temperature is frequently expressed with the following relation [3]:

$$\dot{\epsilon}(\sigma, T) = A \left(\frac{\sigma}{G}\right)^n \left(\frac{b}{d}\right)^p \exp\left(-\frac{\Delta H_{act}}{RT}\right) \quad (1.1)$$

where G is the shear modulus, b the Burgers vector, n the stress exponent, p the grain size exponent, σ the applied stress, $\dot{\epsilon}$ strain rate, and d is the grain size. ΔH_{act} is the activation enthalpy and R is the universal gas constant, and T is the absolute temperature.

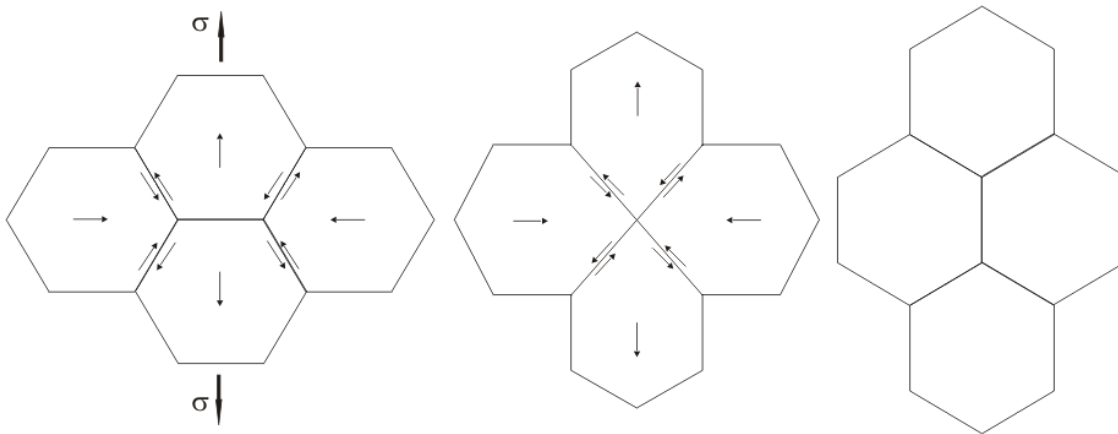


Fig. 1.1. Topological model of superplasticity - a neighboring-switching event, where a group of four grains suffer a 55 % strain without deformation of the grains, except locally in the intermediate state to accommodate GB sliding [10].

Experimental investigations of the deformation of polycrystalline solids at high temperature typically lead to the determination of the n , p , and Q parameters. An attempt to identify the possible rate-controlling mechanism, by comparing the values obtained with theoretical predictions, can then be performed [4, 9, 11-13].

The theoretical models developed for high-temperature deformation are divided into two broad categories: boundary mechanisms, which rely on the presence of grain boundaries and occur only in polycrystalline materials, and lattice mechanisms, which are independent of the presence of grain boundaries and thus occur both in single crystals and polycrystalline materials [14]. Boundary mechanisms are associated with a dependence on the grain size, with the grain-size exponent, p , from relation (1.1) having a value equal to or above 1. Since lattice mechanisms are confined in the bulk of the elemental grains, the value of p is 0. Although most of the theoretical models were originally developed for metallic materials, they can also be applied to ceramics [4, 14].

Among the different possible mechanisms claimed to control the high-temperature superplastic deformation of ultra-pure fine-grained 3Y-TZP, four have been developed to account for the experimental results. Which of these mechanisms is actually involved is still a matter of intense debate [4].

Chapter 1

(1) Two sequential processes: At high stresses, deformation occurs by GB sliding, which is the slower process; whereas at low stresses, the deformation is controlled by an interface-reaction process [9, 15].

(2) Interface-controlled diffusional creep: The flow process is controlled by a Coble-like mechanism. Such a mechanism requires the existence of grain boundary dislocations, with two requirements: the cores of these dislocations are perfect sources and sinks for vacancies, and the dislocations are evenly spaced in the boundary planes so that they can all climb at the same speed [16].

(3) GB sliding with a threshold stress: The superplasticity is due to GB sliding accommodated by the recovery slip processes of grain boundary dislocations along the grain boundaries, the climb of dislocations being controlled by the lattice diffusion of cations. The threshold stress is given by the minimum stress required for dislocation climbing [17].

(4) GB sliding accommodated by intragranular dislocation motion (the recovery of the intragranular dislocations controls the rate of deformation), with a possible threshold stress contribution, at the higher stresses from 15 to 80 MPa and Nabarro–Herring diffusional creep at low stresses [6].

According to the available model on GB sliding of ceramics [11, 18], two parameters can strongly control the high temperature plastic deformation of ceramics, which are (1) amount and viscosity of glassy phase located in the ceramic microstructure, either in the grain boundaries or triple junctions (glass pockets), and (2) strength of triple points. These two terms can be controlled by addition of sintering aids, and pinners, respectively. More details about effect of glassy phase in Sialon ceramics (1.2) and effect of pinners (1.3 and 1.4) are coming as follows.

1.2. Sialon ceramics and their properties

Silicon nitride and its solid solutions, Sialon ceramics, exhibit excellent mechanical properties, good oxidation and thermal shock resistance at both room and high temperature. The high wear resistance and excellent mechanical properties make these ceramics competitive for applications such as cutting tools, balls and rollers for bearings, valves for automotive engines or as turbine components. Because of the highly covalent bonding nature, and the volatility of Si_3N_4 at high temperatures,

Si_3N_4 has to be densified with sintering additives by pressureless sintering (PLS), gas pressure sintering (GPS), hot pressing (HT), hot isostatic pressing (HIP) or spark plasma sintering (SPS). The properties of silicon nitride based ceramics are depended on their microstructures and phase compositions, and on the chemistry of the intergranular grain boundary phase [19].

α -Sialon and β -Sialon, which are the solid solutions based on α - and β - Si_3N_4 respectively, are primarily fabricated by liquid phase sintering (LPS) mixtures of Si_3N_4 , AlN and Al_2O_3 , with metallic oxides as sintering additives. Although the microstructural evolution during the LPS process and post-heat treatment can improve the mechanical properties of Si_3N_4 materials [20], an intergranular aluminosilicate glass phase located in the grain-boundaries and triple grain junctions, which is formed during the LPS process, decreases corrosion resistance and high-temperature strength remarkably [21]. On the other hand, dense Sialons without a glass phase can be predicted theoretically, because Sialons are able to accommodate aluminum and oxygen atoms into their crystal structure. However, in reality the intergranular glass phase and glass pockets, still remains in Sialon when impurities, such as the oxidation of raw powder, exist. Therefore, the elimination of residual glass is an important strategy to improve the high-temperature strength and creep resistance of Sialon ceramics [22].

In the sintering of oxide ceramics, it is important to prevent abnormal grain growth so as to obtain a microstructure with fine and equiaxed grains [23]. In the preparation of Si_3N_4 based ceramics for engineering applications, however, a bimodal microstructure consisting of a small number of large elongated grains and a large number of small equiaxed grains is important to ensure high toughness as well as high strength. Toughening through in-situ formation of elongated grains, rather than addition of whiskers, has advantages over processing [24]. In addition, in whisker toughened Si_3N_4 based materials the matrix is frequently not compatible chemically with the second phase. Reaction between them will not provide the weak interface required for crack deflection or accommodation of vacancies. But a coherent interface is required to maintain other properties like hardness and strength [25].

Self-reinforced Si_3N_4 and Sialon materials have been obtained with toughness as high as $8\text{--}10 \text{ MPa}\cdot\text{m}^{1/2}$. A reasonable explanation for such high toughness is whisker like reinforcement by the development of elongated grain Sialon microstructures. The elongated grains act as fibers in the sintered body. When a crack is propagating, the surface energy to by-pass a grain and the friction to pull out the grain require the applied stress to spend more energy to fracture the material. Thus, the reason

for superior toughness might be the shape of the grain rather than the intrinsic toughness of Si_3N_4 itself. In fact, the fracture toughness of the single crystal Si_3N_4 , is $1.9\text{-}2.8\text{MPa}\cdot\text{m}^{1/2}$ that is much lower than that of sintered Si_3N_4 containing elongated Si_3N_4 grains and grain boundary phase [23-25].

1.3. Ceramics contained carbon nanotubes: Processing and Room temperature properties

Ceramic materials have been an extensively active field of research in the last decades owing to their excellent physical properties as high temperature stability, chemical inertness, strength, wear resistance, which make them suitable for multiple applications in armors and cutting tools among others. Also ceramics present many advantages over metals, because of their low density, low sensitivity to corrosion, and high rigidity and hardness even at high temperature. However, ceramic brittleness restricts them from diverse structural applications and it has been a continuous driving force to encourage researchers to use new approaches with the aim of toughening ceramics. With this goal, second phase reinforcements as particulates, and long/short fibres have been used over last decades [26]. The incorporation of carbon nanotubes (CNTs), in analogy to traditional ceramic composites reinforced with micrometric fibers, is often aimed at enhancing the fracture toughness of ceramic bodies [27].

Since Iijima [28] discovered carbon nanotubes (CNTs). Then, all different forms of CNTs, such as Single Wall Carbon Nanotubes (SWCNTs) and Multi Wall Carbon Nanotubes (MWCNTs), have attracted international scientific interest worldwide. This is due to their unique combination of mechanical (Young's modulus $\sim 1\text{TPa}$ and tensile strength up to 60GPa), electrical (maximum electrical conductivity at 300K $\sim 10^6\text{S/m}$ for SWCNT and $>10^5\text{S/m}$ for MWCNT) and thermal properties (maximum thermal conductivity of 6600W/mK for an individual SWCNT and $>3000\text{W/mK}$ for an individual MWCNT). These properties, add to low density, flexibility, thermal stability (as high as $2000\text{-}2400\text{ }^\circ\text{C}$ in an argon atmosphere or under vacuum) and large aspect ratio (diameter as low as 3.3 \AA and length as high as 6 mm , with an aspect ratio that could range from 10^3 to 10^8) make CNTs as unique materials [29].

Ceramic materials community rapidly considered CNTs as a promising reinforcement element for brittle ceramic matrices to form novel engineered ceramic matrix composites (CMCs) with superior mechanical performance and tailored thermal and electrical properties.

A literature survey reveals that there is a debate about the efficiency of CNTs in the mechanical properties of the ceramic matrix nanocomposites. No tangible improvement or even degradation in the fracture properties and hardness of ceramic-CNT composites was reported by several authors [30-32]. On the other hand numerous investigations demonstrated significant enhancement in hardness, fracture toughness and Young modulus [33-35].

For instance Zhan et al [35] in 2002 reported a notable improvement (from 3.3 to 9.7 MPa.m^{1/2}) of the indentation fracture toughness in single-wall CNTs reinforced alumina ceramics (Fig. 1.2a). This article [35] is considered as the pioneer in this area. However, two years later, Wang et al [36], questioned the reliability of Zhen's fracture toughness measurements, since their own analysis using single edge V-notched beam technique on the same composites showed no improvement in toughness (Fig. 1.2b). This is an argument to be taken into consideration when making fracture toughness assessment. In fact, fracture toughness measured by indentation in ceramics reinforced by CNTs has been matter of dispute [27]. Indentation is an indirect toughness-testing technique in shear mode, whereas the crack tip in fracture toughness measurement should be subjected to mode I tension.

Estili et al [37] reported a 67% increase in fracture toughness of multiwall CNT (MWCNT) - alumina composites (from 3.12 to 5.20 MPa.m^{1/2}) with the addition of 3.5 Vol.% CNTs. They interpreted this result as due to well known toughening mechanisms by fibers, such as crack deflection, fiber pull-out and crack bridging. Another investigation on the fracture behavior of MWCNT-alumino-borosilicate glass ceramic by Mukhopadhyay et al [38] revealed that crack bridging provided the major contribution towards 150% improvement in fracture toughness compared to the monolithic material, where no sign of fiber pull out could be detected. However, the incorporation of nanotubes resulted in a decrease in hardness and elastic modulus, which would be due to easy interfacial debonding of the CNTs. On the contrary, An et al [39] reported dramatical improvements in SiCN elastic modulus (from 74 to 118 GPa) and hardness (from 9.4 to 14.3 GPa) by adding 6.4 Vol.% MWCNTs. They [39] attributed such an improvement in the modulus to the strong bonding between matrix and MWCNTs.

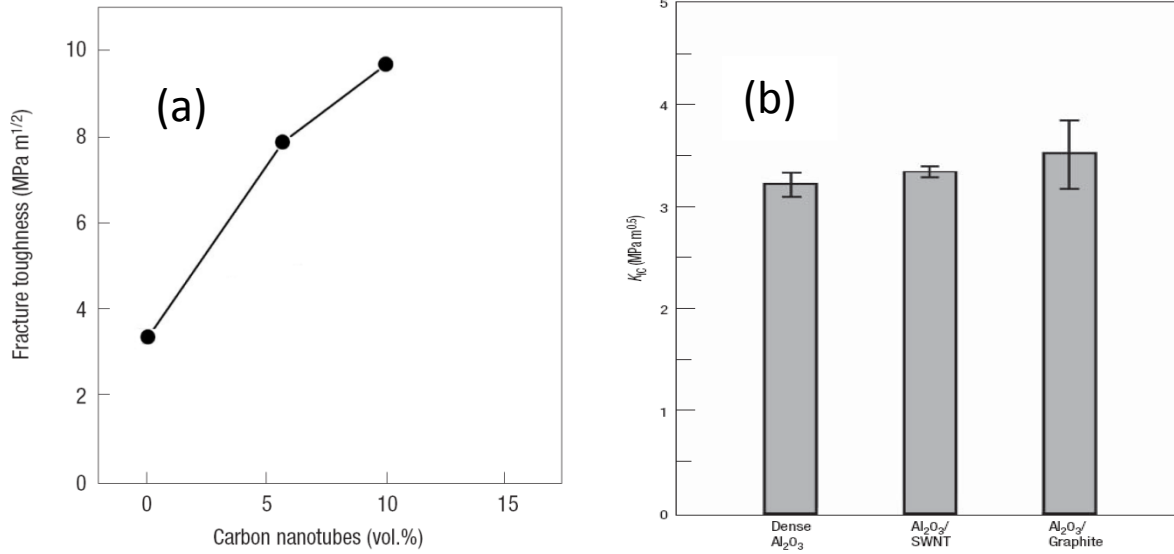


Fig. 1.2. Fracture toughness of the SWCNT-Alumina composites measured by (a) Indentation technique measured by Zhan et al. [35] and (b) SEVNB technique measured by Wang et al. [36].

Tetragonal stabilized zirconia with 3 mol% yttria (3Y-TZP) has been taken into account for many structural applications due to its relatively high strength and fracture toughness (based on - transformation toughening mechanism) [40]. In addition, zirconia based ceramics are interesting for several multifunctional applications such as solid oxide fuel cells, oxygen sensors, and ceramic membranes. Incorporation of CNTs and carbon nano-fibers aiming at enhancing mechanical and electrical properties of ceramics has been documented during the last few years. Early investigations on processing and mechanical/ electrical properties of 3Y-TZP-CNTs (both SWCNT and MWCNT) were carried out by Sun et al [41] and Ukai et al [30], where addition of 1 wt.% (~ 2.5 vol.%) CNTs not only did not show any sign of enhancement in parameters such as fracture toughness, fracture strength and hardness compared to monolithic 3Y-TZP, but also resulted in the degradation of mechanical properties to some extent. They assumed that low fractional density of composites on one hand, together with the weak interfacial bonding between the matrix and the CNTs on the other, are the underlying reasons for lower mechanical properties of the composites.

A similar tendency in the hot-pressed Zirconia/Carbon-nanofiber composites, documented by Duszova et al [32, 42] asserted that the aforementioned disappointing mechanical properties could be attributed to a lower density

compared to the monolithic 3Y-TZP. CNT clustering in the ceramic grain-boundaries, a poor dispersion of fibers into the matrix, and the low volume fractions of CNTs (1.07 wt%) could be other causes for poor toughening. Garmendia et al. [43] used slip casting in order to get a uniform dispersion of CNTs in the zirconia matrix. Although they reported a slight increase in fracture toughness (from 3.8 to 4.0 MPa.m^{1/2}), the Vickers hardness of CNT-zirconia composites was lower by about 12.5%. While their mixing technique showed a fairly good distribution of CNTs, the lower density of the composite with respect to the monolithic specimen, accompanied by a relatively low fraction of CNTs in the composite (only 1 vol%), and sintering in a conventional furnace at a high temperature/ long time (1350 °C/ 1h dwell) may be the critical factors reducing the efficiency of CNT reinforcements.

Dusza et al. [44] compared the properties of 3Y-TZP composites, reinforced with 2 and 3 vol% carbon nano fiber, which were processed by two different sintering techniques: spark plasma sintering and hot-pressing. For all compositions, spark plasma sintered (SPS) samples showed a higher fracture toughness and hardness compared to the hot-pressed (HP) ones. Ultra rapid SPS (5 min dwell) technique can preserve the nanotubes from oxidation and transformation to amorphous carbon. High resolution transmission electron microscopy (HR-TEM) micrographs showed a layer of amorphous carbon in the HP sample [44].

The present review of the literature indicates that there are still several difficulties in processing defect free CNT-zirconia composites with improved mechanical properties. In sum, the critical factors in order to develop CNT-ceramic composites with improved mechanical properties can be regarded as follows [45]:

(1) Homogeneous dispersion of CNTs within the matrix and inhibition of CNTs agglomeration caused by Van der Waals forces[45]. CNTs tend to agglomerate into parallel ropes or bundles due to Van der Waals forces as a consequence of high surface area and high aspect ratio of CNTs, in which is strongly undesirable. Therefore, a uniform and homogeneous CNTs distribution, which individual CNTs are well-separated from each other and uniformly distributed throughout the ceramic matrix, is a major challenge for ceramic community. High CNTs content leads to further agglomeration since the contact between CNTs is more likely as well as ceramic matrix shortage partially impede good wetting with the high surface area of CNTs, limiting potential improvement of physical properties at high content of the reinforcement phase. Different approaches have been carried out to disperse CNTs throughout the ceramic matrix, such as conventional powder processing which involve the use of ultrasounds or ball milling producing shear forces to deagglomerate CNTs, colloidal processing in which dispersants, surfactants or acid

treatment are utilized based on surface modification with the aim of increasing stability suspension and enhancing interaction between CNTs and ceramic matrix, sol-gel processing entrapping dispersed CNT within the gel network. Another novel approach is in-situ growth of CNTs by CCVD, in which CNTs are directly grown on the surface of ceramic-matrix grains by CCVD due to metal impurities doping on the surface that act as catalysts [34].

(2) Optimum bonding in the interface of CNT-ceramic; i.e. interfacial compatibility and wetting between CNTs and ceramic matrix as well as strong entangling of the CNTs within the ceramics grains [45]; The study and characterization of the bonding between CNTs and ceramic matrix is an important issue as well. Bonding has an effect in physical properties of CNT containing CMCs as bonding controls the load transfer between CNTs and ceramic matrix, which could alter the mechanical properties, as well as electrical and thermal resistances between CNT and ceramic matrix interfaces. However, few attempts have been carried out with the aim of understanding and characterizing the bonding of CNT and ceramic matrix. A diffusion layer was identified using high resolution electron microscopy between SWNTs and Al_2O_3 and an interfacial shear strength of 1 GPa was calculated, characterizing SWNTs pull out after fracture [45]. In order to justify the origin of the interfacial shear strength, the interfacial bond strength was attributed to the radial residual thermal stress between SWNTs and Al_2O_3 and a value of 310 MPa was calculated for the interfacial bond strength. Therefore, interfacial bonding is not only due to residual thermal stress but also a chemical reaction could bond CNT to a ceramic matrix forming an intermediate diffusion layer. However, mostly all HRTEM studies qualitatively analyse CNTs area without characterizing possible structures formed at interfaces.

Recently [46], with the goal of characterizing possible phases formed as a consequence of a reaction between CNTs and Al_2O_3 in CNT-reinforced Al_2O_3 , a new approach using differential thermal analysis (DTA), thermal gravimetry (TGA) and X-ray diffraction (XRD) was performed [46]. An exothermic peak related with a new phase formation was detected at 1242 °C, whereas XRD did not show any new crystalline phase different than Al_2O_3 , which is due to small volume of possible new phase formed, as a result of low CNTs content (2 wt.% and 5 wt.%) that makes the new phase invisible to XRD. A 50 wt.% CNT-reinforced Al_2O_3 was fabricated to ensure optimum contact between CNTs and Al_2O_3 , maximizing the volume of the new phase formed. Moreover, Al_2O_3 crystalline phase was formed during sintering as confirmed using XRD on the 50 wt.% composite. As mentioned above, the understanding of how CNTs wet a ceramic matrix is crucial to understand reinforcing and transport phenomena. In addition, bonding could be modified by the functionalization of CNTs, which may alter interaction between CNTs and a ceramic matrix as shown by Gonzalez-Julian et al. [47].

In the latter investigation, the effect of MWCNTs functionalization was analysed by means of oxidation and BN and SiO₂ coatings before sintering MWCNT-reinforced Si₃N₄. As a result of the MWNTs functionalization, room temperature mechanical properties of different composites were modified, whereas SiO₂ functionalization of MWNTs showed best performance compared with the composite fabricated with pristine MWNTs.

(3) Avoiding damage of the CNTs during processing [45]: This point has to be carefully taken into account during mixing and high temperature sintering to prevent from nanotube breaking, oxidation and crystal structure destruction.

A range of techniques has been used with the aim of dispersing CNTs homogeneously throughout the ceramic matrix, such as conventional powder processing, colloidal processing, sol-gel processing and novel in-situ growth of CNTs by catalytic chemical vapour decomposition (CCVD) [45].

Consolidation of CNTs-reinforced CMCs has been carried out using pressureless sintering, hot pressing (HP) spark plasma sintering (SPS) [44]. However, pressureless sintering, HIP and HP might be avoided since degradation of CNTs during densification has been reported in multiple studies, where CNTs damage after sintering is identified through Raman spectroscopy owing to characteristic CNTs phonon scattering. As an example, Daraktchiev et al. [48] observed an amorphous layer of carbon in the grain-boundaries of 3Y-TZP-CNT composite sintered in a conventional furnace.

An increasingly popular technique to fabricate CNT-reinforced CMCs is spark plasma sintering (SPS) due to the fact that SPS allows sintering fully dense composites at lower temperatures and shorter holding times, in which high heating and cooling rates are usually involved. SPS results in preserving nanotube against any damage during processing. Moreover, SPS provides better control of the kinetics related with densification, grain growth and chemical reactions. Opposite to densification techniques described above, SPS ensures CNT integrity after sintering as demonstrated in Raman spectroscopy studies. For example, Balazsi et al. [49] compared SPS with HIP in MWNT-reinforced Si₃N₄ and showed the ability of SPS to preserve CNTs during processing. Moreover, fully dense samples with fine grain size and superior mechanical properties were obtained by SPS at sintering temperature of 1650 °C, whereas HIP at sintering temperature of 1700 °C resulted in samples with high porosity, large grains and subsequently poor mechanical properties. Therefore, porous samples were obtained by HIP regardless of higher sintering temperatures, confirming a densification kinetics enhancement by SPS [45].

(4) *Near fully dense composites are required:* since there is a strong relation between mechanical properties (e.g. hardness) and residual pores after firing. In particular, the presence of nanotubes between the ceramic particles typically delays densification and only in few researches this effect was taken into account so far.

1.4. Ceramics reinforced with CNTs: High temperature properties

While many applications of ceramics and their composites concerns high temperature working condition, very few investigations have been focused on high temperature mechanical properties and creep response of CNT-reinforced ceramics, so far.

Since GB sliding is considered as the most important mechanism for ceramics plastic deformation, the GB nature has a crucial role on the high temperature deformation behavior of polycrystalline ceramics. For instance, presence of a thin layer of glassy phase in the grain boundaries could strongly decrease ceramics creep resistance [7]. Also, it was demonstrated that the addition of particles, whiskers or fibers could strongly decrease the composite creep rate with respect to pure ceramics [50]. Hence, it seems that the presence of well-distributed CNTs in the boundaries can potentially hinder the GB sliding and as a consequence improve the creep resistance of the material. Therefore, there is a clear interest in studying the high temperature mechanical properties of CNT-reinforced CMCs.

Zapata-Solvas et al. [51] studied the creep resistance of 10 vol.% CNT-reinforced Al_2O_3 ceramics and an improvement of two orders of magnitude in the creep resistance compared with pure alumina was reported. The enhancement in the creep resistance was attributed to partial blocking of GB sliding and diffusion inhibition due to CNTs presence at Al_2O_3 grain boundaries. As a consequence, dislocation movement was responsible for stress relaxation during high temperature deformation [51]. Fig. 1.3 illustrates the creep resistance of 10 vol.% SWNT-reinforced Al_2O_3 fabricated using two different processing routes: conventional powder processing and aqueous colloidal processing compared with pure Al_2O_3 [52].

In CNT reinforced 3Y-TZP, the same trend was illustrated by Daraktchiev et al. [53] and Ionascu et al. [54], where they compared mechanical loss of the zirconia-CNT composite with monolithic zirconia. The mechanical loss of the composite at 1600 K showed a remarkable decrease with respect to the monolithic 3Y-TZP, which indicates that the grain boundary sliding in the composite is more difficult than in monolithic zirconia and consequently creep rate is lower.

On the contrary, Peigney et al. [55] reported that superplastic forming of CNT-reinforced Al_2O_3 is made easier by CNT addition, owing to CNTs capacity to withstand extreme shear stresses occurred during high temperature extrusion.

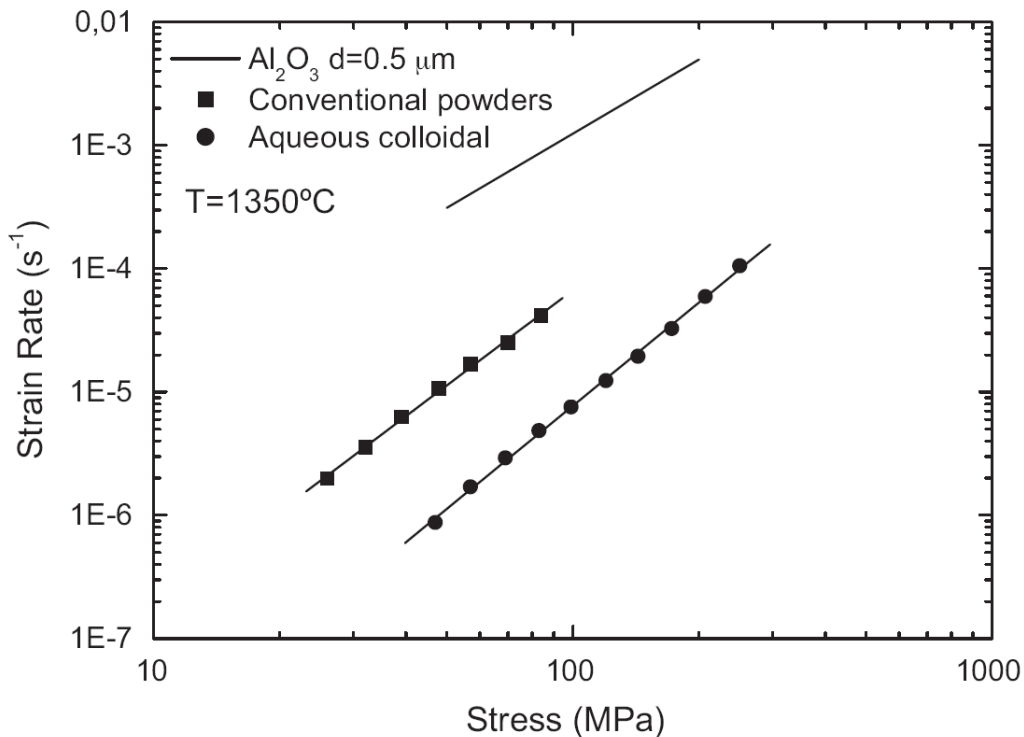


Fig. 1.3. Strain rate versus stress for 10 vol.% CNT-reinforced Al_2O_3 , fabricated using conventional powders processing and aqueous colloidal processing [51].

1.5. Objectives of this work

As shown in the literature review, for many high-tech applications, mostly at high temperatures, ceramics offer a clear advantage with respect to metals and alloys, because of their low density, low sensitivity to corrosion, and high rigidity and hardness even at high temperature. However, the main problem of ceramics is their intrinsic low fracture toughness. Therefore, metals are still preferred to ceramics in many occasions. Accordingly, the increase of fracture toughness is a key feature to broaden the fields of application of technical ceramics.

Grain refining is among the possible mechanisms for the simultaneous strengthening and toughening of ceramics. Large increase in strength and fracture-toughness is frequently documented for ultra-fine ceramic/metallic structures; a phenomenon that is explained in part by small grain sizes using the well-known Hall–Petch relationship. For instance, the author [56] has used two-step sintering approach to obtain nanostructured cubic stabilized zirconia. They have shown up to ~ 96% increase in the fracture toughness (i.e. from 1.61 to 3.16 MPa m^{1/2}) when decreasing the grain size from ~ 2.15 μm to ~ 295 nm.

On the other hand, the high temperature mechanical properties of ceramics depend on grain boundary (GB) properties. GB sliding is an important mechanism in plastic deformation of fine grained ceramics and it is especially important in the deformation of nanostructured ceramics, where GB sliding can be activated at much lower temperature than in the case of ceramics with larger grains. Hence, it appears that nanostructured ceramics exhibit good mechanical properties for room temperature applications (good toughness), but low creep resistance at high temperature due to enhanced GB sliding. GB chemical status also has a direct effect on high temperature deformation of ceramics. For instance presence of impurities or addition of sintering aids could facilitate the sintering step, however, presence of glassy phase, located in the boundaries lubricates the GBs at high temperature and allow them to slide easier.

Therefore, the objectives of this work are:

- (1) The improvement of the high temperature properties of silicon nitride based ceramics. We study the effect of the glassy phase located at the boundaries in this system. The glassy phase amount and chemistry are varied and mechanical spectroscopy is chosen to investigate the viscosity of such glassy phase.
- (2) The production of nano-structured ceramics, using the advantage of Spark Plasma Sintering (SPS). SPS is a newly developed sintering process that combines the use of mechanical pressure and microscopic electric discharge

between the particles. As a result, samples can rapidly reach full density (in few minutes) at relatively low temperature.

- (3) The improvement of high temperature creep resistance of nanostructured ceramics. To reach this purpose, CNTs are added to the monolithic ceramics. The addition of nano particles is believed to pin the grain/ boundaries and consequently reduce the creep of nano-size grain ceramics. Since mechanical spectroscopy is sensitive to GB sliding, it will be used to investigate the pinning efficiency of nanotubes.

References

- [1] T.E. Chung, T.J. Davies, The low-stress creep of fine-grain uranium dioxide, *Acta Metallurgica* 27 (4) (1979) 627-635.
- [2] J. Crampon, B. Escaig, MECHANICAL PROPERTIES OF FINE-GRAINED MAGNESIUM OXIDE AT LARGE COMPRESSIVE STRAINS, *Journal of the American Ceramic Society* 63 (11-12) (1980) 680-686.
- [3] F. Wakai, S. Sakaguchi, Y. Matsuno, Superplasticity of Yttria-Stabilized Tetragonal ZrO₂ Polycrystals, *Advanced Ceramic Materials* 1 (3) (1986) 259-263.
- [4] G. Bernard-Granger, A. Addad, C. Guizard, Superplasticity of a Fine-Grained TZ3Y Material Involving Dynamic Grain Growth and Dislocation Motion, *Journal of the American Ceramic Society* 93 (3) (2010) 848-856.
- [5] M. Jiménez-Melendo, A. Domínguez-Rodríguez, A. Bravo-León, Superplastic flow of fine-grained Y₂O₃-stabilized ZrO₂ polycrystals: constitutive equation and deformation mechanisms, *Journal of the American Ceramic Society* 81 (11) (1998) 2761-2776.
- [6] K. Morita, K. Hiraga, Critical assessment of high-temperature deformation and deformed microstructure in high-purity tetragonal zirconia containing 3 mol.% yttria, *Acta Materialia* 50 (5) (2002) 1075-1085.
- [7] K. Morita, K. Hiraga, B.N. Kim, Effect of minor SiO₂ addition on the creep behavior of superplastic tetragonal ZrO₂, *Acta Materialia* 52 (11) (2004) 3355-3364.
- [8] M. Nauer, C. Carry, Creep parameters of yttria doped zirconia materials and superplastic deformation mechanisms, *Scripta Metallurgica et Materiala* 24 (8) (1990) 1459-1463.
- [9] D.M. Owen, A.H. Chokshi, The high temperature mechanical characteristics of superplastic 3 mol% yttria stabilized zirconia, *Acta Materialia* 46 (2) (1998) 667-679.
- [10] R. Raj, M.F. Ashby, On grain boundary sliding and diffusional creep, *Metallurgical and Materials Transactions B* 2 (4) (1971) 1113-1127.
- [11] A. Lakki, R. Schaller, M. Nauer, C. Carry, High temperature superplastic creep and internal friction of yttria doped zirconia polycrystals, *Acta Metallurgica Et Materialia* 41 (10) (1993) 2845-2853.
- [12] A. Domínguez-Rodríguez, A. Bravo-León, J.D. Ye, M. Jiménez-Melendo, Grain size and temperature dependence of the threshold stress for superplastic deformation in yttria-stabilized zirconia polycrystals, *Materials Science and Engineering: A* 247 (1-2) (1998) 97-101.
- [13] R. Schaller, M. Daraktchiev, S. Testu, Creep behavior of ceramics studied by mechanical loss measurements, *Materials Science and Engineering A* 387-389 (1-2 SPEC. ISS.) (2004) 687-691.

Chapter 1

- [14] A.H. Chokshi, T.G. Langdon, Characteristics of Creep Deformation in Ceramics, *MATERIALS SCIENCE AND TECHNOLOGY* 7 (7) (1991) 577-584.
- [15] M.M.R. Boutz, A.J.A. Winnubst, A.J. Burgraaf, M. Nauer, C. Carry, Low Temperature Superplastic Flow of Yttria Stabilized Tetragonal Zirconia Polycrystals, *Journal of the European Ceramic Society* 13 (2) (1994) 103-111.
- [16] M.Z. Berbon, T.G. Langdon, An examination of the Flow Process in Superplastic Yttria-Stabilized Tetragonal Zirconia, *Acta Materialia* 47 (8) (1999) 2485-2495.
- [17] M. Jimenez-Melendo, A. Dominguez-Rodriguez, High Temperature Mechanical Characteristics of Superplastic Yttria-Stabilized Zirconia. An Examination of the Flow Process, *Acta Materialia* 48 (12) (2000) 3201-3210.
- [18] A. Lakki, Mechanical spectroscopy of fine-grained zirconia, alumina and silicon nitride, in, Vol. Ph.D. Thesis No. 1266, École Polytechnique Fédérale de Lausanne, Lausanne, Switzerland, 1994.
- [19] M.J. Hoffmann, High-temperature properties of Si₃N₄ ceramics, *MRS Bulletin* 20 (2) (1995) 28-32.
- [20] L.A. Pierce, D.M. Mieskowski, W.A. Sanders, Effect of grain-boundary crystallization on the high-temperature strength of silicon nitride, *Journal of Materials Science* 21 (4) (1986) 1345-1348.
- [21] G. Ziegler, J. Heinrich, G. Wolting, Relationship between processing, microstructure and properties of dense and reaction-bonded silicon nitride, *Journal of Materials Science* 22 (9) (1987) 3041-3086.
- [22] G. Bernard-Granger, J. Crampon, R. Duclos, B. Cales, Glassy grain-boundary phase crystallization of silicon nitride: Kinetics and phase development, *Journal of Materials Science Letters* 14 (19) (1995) 1362-1365.
- [23] D. Thompson, Ceramics: Tough cookery, *Nature* 389 (6652) (1997) 675-676.
- [24] F.F. Lange, Relation between strength, fracture energy, and microstructure of hot-pressed Si₃N₄, *Journal of the American Ceramic Society* 56 (10) (1973) 518-522.
- [25] Z. Shen, Z. Zhao, H. Peng, M. Nygren, Formation of tough interlocking microstructures in silicon nitride ceramics by dynamic ripening, *Nature* 417 (6886) (2002) 266-269.
- [26] N.P. Padture, Multifunctional Composites of Ceramics and Single-Walled Carbon Nanotubes, *Advanced Materials* 21 (17) (2009) 1767-1770.
- [27] B.W. Sheldon, W.A. Curtin, Nanoceramic composites: Tough to test, *Nature Materials* 3 (8) (2004) 505-506.
- [28] S. Iijima, Helical microtubules of graphitic carbon, *Nature* 354 (1991) 56-58.
- [29] R.H. Baughman, A.A. Zakhidov, W.A. De Heer, Carbon nanotubes - The route toward applications, *Science* 297 (5582) (2002) 787-792.
- [30] T. Ukai, T. Sekino, A. Hirvonen, N. Tanaka, T. Kusunose, T. Nakayama, K. Niihara, Preparation and electrical properties of carbon nanotubes dispersed zirconia nanocomposites, in: *Key Engineering Materials*, Vol. 317-318, 2006, pp. 661-664.
- [31] J. Duszka, J. Morgiel, P. Tatarko, V. Puchy, Characterization of interfaces in ZrO₂-carbon nanofiber composite, *Scripta Materialia* 61 (3) (2009) 253-256.
- [32] A. Duszova, J. Duszka, K. Tomasek, J. Morgiel, G. Blugan, J. Kuebler, Zirconia/carbon nanofiber composite, *Scripta Materialia* 58 (6) (2008) 520-523.
- [33] A. Peigney, F.L. Garcia, C. Estournès, A. Weibel, C. Laurent, Toughening and hardening in double-walled carbon nanotube/nanostructured magnesia composites, *Carbon* 48 (7) (2010) 1952-1960.
- [34] A. Datye, K.-H. Wu, G. Gomes, V. Monroy, H.-T. Lin, J. Vleugels, K. Vanmeensel, Synthesis, microstructure and mechanical properties of Yttria Stabilized Zirconia (3YTZP) - Multi-Walled Nanotube (MWNTs) nanocomposite by direct in-situ growth of MWNTs on Zirconia particles, *Composites Science and Technology* 70 (14) (2010) 2086-2092.

- [35] G.D. Zhan, J.D. Kuntz, J. Wan, A.K. Mukherjee, Single-wall carbon nanotubes as attractive toughening agents in alumina-based nanocomposites, *Nature Materials* 2 (1) (2003) 38-42.
- [36] X. Wang, N.P. Padture, H. Tanaka, Contact-damage-resistant ceramic/single-wall carbon nanotubes and ceramic/graphite composites, *Nature Materials* 3 (8) (2004) 539-544.
- [37] M. Estili, A. Kawasaki, H. Sakamoto, Y. Mekuchi, M. Kuno, T. Tsukada, The homogeneous dispersion of surfactantless, slightly disordered, crystalline, multiwalled carbon nanotubes in α -alumina ceramics for structural reinforcement, *Acta Materialia* 56 (15) (2008) 4070-4079.
- [38] A. Mukhopadhyay, B.T.T. Chu, M.L.H. Green, R.I. Todd, Understanding the mechanical reinforcement of uniformly dispersed multiwalled carbon nanotubes in alumino-borosilicate glass ceramic, *Acta Materialia* 58 (7) (2010) 2685-2697.
- [39] L. An, W. Xu, S. Rajagopalan, C. Wang, H. Wang, Y. Fan, L. Zhang, D. Jiang, J. Kapat, L. Chow, B. Guo, J. Liang, R. Vaidyanathan, Carbon-nanotube-reinforced polymer-derived ceramic composites, *Advanced Materials* 16 (22) (2004) 2036-2040.
- [40] F.F. Lange, Transformation toughening, *Journal of Materials Science* 17 (1) (1982) 225-234.
- [41] J. Sun, L. Gao, M. Iwasa, T. Nakayama, K. Niihara, Failure investigation of carbon nanotube/3Y-TZP nanocomposites, *Ceramics International* 31 (8) (2005) 1131-1134.
- [42] A. Duszová, J. Dusza, K. Tomášek, G. Blugan, J. Kuebler, Microstructure and properties of carbon nanotube/zirconia composite, *Journal of European Ceramic Society* 28 (5) (2008) 1023-1027.
- [43] N. Garmendia, I. Santacruz, R. Moreno, I. Obieta, Slip casting of nanozirconia/MWCNT composites using a heterocoagulation process, *Journal of the European Ceramic Society* 29 (10) (2009) 1939-1945.
- [44] J. Dusza, G. Blugan, J. Morgiel, J. Kuebler, F. Inam, T. Peijs, M.J. Reece, V. Puchy, Hot pressed and spark plasma sintered zirconia/carbon nanofiber composites, *Journal of the European Ceramic Society* 29 (15) (2009) 3177-3184.
- [45] E. Zapata-Solvas, D. Gómez-García, A. Domínguez-Rodríguez, Towards physical properties tailoring of carbon nanotubes-reinforced ceramic matrix composites, *Journal of the European Ceramic Society* 32 (12) (2012) 3001-3020.
- [46] I. Ahmad, M. Unwin, H. Cao, H. Chen, H. Zhao, A. Kennedy, Multi-walled carbon nanotubes reinforced Al₂O₃ nanocomposites: Mechanical properties and interfacial investigations, *Composites Science and Technology* 70 (8) (2010) 1199-1206.
- [47] J. Gonzalez-Julian, P. Miranzo, M.I. Osendi, M. Belmonte, Carbonnanotubes functionalization process for developing ceramic matrix nanocomposites, *Journal of Materials Chemistry* 21 (16) (2011) 6063-6071.
- [48] M. Daraktchiev, B. Van De Moorto, R. Schaller, E. Couteau, L. Forro, Effects of carbon nanotubes on grain boundary sliding in zirconia polycrystals, *Advanced Materials* 17 (1) (2005) 88-91.
- [49] C. Balazsi, Z. Shen, Z. Konia, Z. Kasztovski, F. Weber, Z.V.e. al., Processing of carbonnanotubereinforced silicon nitride composites by spark plasma sintering, *Composites Science and Technology* 65 (5) (2005) 727-733.
- [50] H.-T. Lin, P.F. Becher, Creep Behavior of a SiC-Whisker-Reinforced Alumina, *Journal of the American Ceramic Society* 73 (5) (2005) 1378 - 1381.
- [51] E. Zapata-Solvas, R. Poyato, D. G³mez-Garc³a, A. Dom³nguez-Rodr³iguez, V. Radmilovic, N.P. Padture, Creep-resistant composites of alumina and single-wall carbon nanotubes, *Applied Physics Letters* 92 (11) (2008).
- [52] E. Zapata-Solvas, D. G³mez-Garc³aa, R. Poyato, Z. Lee, M. Castillo-Rodr³iguez, A. Dom³nguez-Rodr³iguez, V. Radmilovic, N.P. Padture, Microstructural effects on the creep deformation of aluminasingle-wall carbon nanotubes composites, *Journal of the American Ceramic Society* 93 (7) (2010) 2042-2047.

Chapter 1

- [53] M. Daraktchiev, B.V.d. Moortèle, R. Schaller, E. Couteau, L. Forró, Effects of Carbon Nanotubes on Grain Boundary Sliding in Zirconia Polycrystals, *Advanced Materials* 17 (1) (2005) 88-91.
- [54] C. Ionascu, R. Schaller, Influence of carbon nanotubes and silicon carbide whiskers on the mechanical loss due to grain boundary sliding in 3-mol% yttria-stabilized tetragonal zirconia polycrystals, *Materials Science and Engineering A* 442 (1-2 SPEC. ISS.) (2006) 175-178.
- [55] A. Peigney, E. Flahaut, C.H. Laurent, F. Chastel, A. Rousset, Aligned carbonnanotubes in ceramic-matrix nanocomposites prepared by high temperature extrusion, *Chemical Physics Letters* 352 (11) (2002) 20-25.
- [56] M. Mazaheri, M. Valefi, Z.R. Hesabi, S.K. Sadrnezhad, Two-step sintering of nanocrystalline 8Y2O3 stabilized ZrO2 synthesized by glycine nitrate process, *Ceramics International* 35 (1) (2009) 13-20.

Chapter 2

Mechanical spectroscopy and its application in ceramics

The aim of this chapter is to review the theory of mechanical spectroscopy as well as the anelastic relaxation. The rheological formalism is presented for calculation of the standard anelastic solid model. Some examples of relaxation processes that can occur in crystalline solids and especially in ceramic materials are presented and the related models (point defect relaxation, dislocation relaxation, and grain-boundary relaxation) are explained in details. High temperature mechanical spectroscopy of different ceramics such as alumina, zirconia, and silicon nitride is presented and related models (GB sliding models) are described.

2.1. Introduction

Mechanical spectroscopy [1] is a non-destructive method, usefully applicable for investigation of significant features such as local distortion of lattices (point defect relaxation), dislocation motion, grain-boundary (GB) migration as well as the effect of precipitates and structural defects (for example point defects) on the motion of dislocations and GB sliding. Since GB sliding is considered as the main mechanism responsible for high temperature deformation of ceramics, mechanical spectroscopy is a promising method for the study of high-temperature mechanical properties and superplasticity controlling mechanisms of ceramics [2].

In general, the internal friction or mechanical loss represents a quantity, by which the conversion of mechanical energy of a vibrating material into heat can be calculated. The mechanical spectroscopy technique that accounts for such process of energy dissipation consists in applying a periodic stress to the sample ($\sigma(t) = \sigma_0 \sin(i\omega t)$) and then in recording the deformation strain ($\varepsilon(t) = \varepsilon_0 \sin(i[\omega t - \varphi])$) at the same time. The phase lag, φ , normally, taking place between the exertion of stress and strain, arise from the various internal friction mechanisms as mentioned above. It follows that damping can be considered as a first manifestation of non-elastic or plastic behavior of materials. However, in many experiments the vibration mechanical loss can be measured at stress levels much lower than those needed for plastic deformation [1].

2.2. Anelastic relaxation

The concept of anelastic relaxation was first described by Zener in 1948 [3], who studied the energy dissipation due to thermal diffusion macroeddy relaxations in ferromagnetic materials and the internal friction in substitutional solid-solutions (Zener relaxation) [3, 4]. In Europe as well, Snoek studied the relaxations occurring in α -Fe containing small amounts of nitrogen or carbon (Snoek relaxation)[5].

2.2.1. Phenomenology

Anelasticity appears in the simple, but ideal experiment presented in Fig. 2.1. A stress (σ_0) is applied suddenly to the sample at time ($t=0$) and held constant. During

the application of σ_0 , the strain is recorded as a function of time (Fig. 2.1). One can observe the instantaneous increase of elastic strain (ε_{el}), from zero to ε_{el} , which is obviously associated with Hooke's law:

$$\varepsilon_{el} = J_u \sigma_0 \quad (2.1)$$

where J_u is the unrelaxed compliance. The anelastic strain, ε_{an} , increases with time from zero to an equilibrium value ε_{an}^∞ . When this equilibrium is reached:

$$\varepsilon = \varepsilon_{el} + \varepsilon_{an}^\infty = J_r \sigma \quad (2.2)$$

where J_r is the relaxed compliance. This evolution, under an applied stress, from one equilibrium state to a new one is called anelastic relaxation [6].

The main difference between the elastic and non-elastic (involve anelastic and viscoplastic) deformation is the way by which a sample reaches its equilibrium strain after stress application. For instance, in the elastic deformation the equilibrium strain is reached instantaneously after applying the stress. Instead, in the anelastic deformation the strain increases from zero to equilibrium value after a certain time that is called "relaxation time (τ)". Elastic and anelastic processes are entirely reversible. If the stress is removed from the sample, one can observe the instantaneous recovery of the elastic strain and then with the relaxation time (τ), the recovery of anelastic strain. Unlike elastic and anelastic strain which are reversible, the viscoplastic deformation is not reversible. Fig. 2.1 shows elastic, anelastic and viscoplastic strain response to applied stress and then to the release of the stress [6].

In sum, in an ideal elastic material the following conditions are satisfied:

- (1) For a certain applied stress there is a unique equilibrium strain and completely reversible.
- (2) The equilibrium strain depends linearly on the stress.
- (3) The equilibrium strain is reached instantaneously. And when the stress was released, the strain comes to zero abruptly.

Chapter 2

If the third condition is not satisfied, the material behavior is anelastic. If none of these conditions are satisfied, the behavior is viscoplastic; The strain is not recoverable and the strain depends on the material history [1].

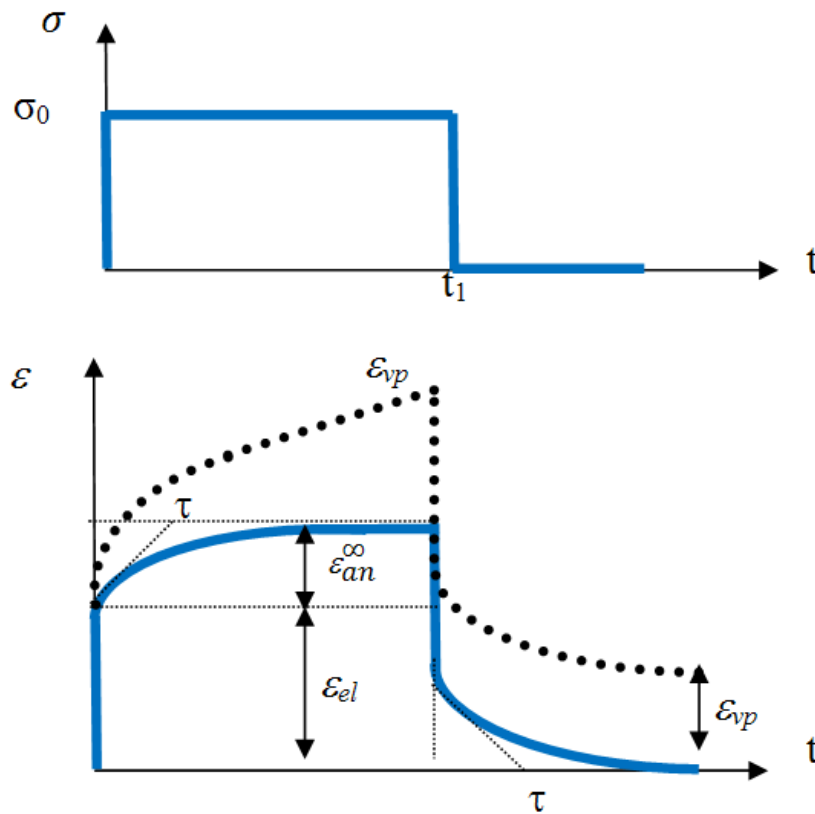


Fig. 2.1. Elastic (ϵ_{el}), anelastic (ϵ_{an}) and viscoplastic (ϵ_{vp}) strain corresponding to an applied stress (σ_0) and to the release of the stress.

Anelastic relaxation may be defined by two main parameters: the relaxation time (τ) and relaxation strength (Δ):

$$\Delta = \frac{\epsilon_{an}^{\infty}}{\epsilon_{el}} = \frac{J_r - J_u}{J_u} \quad (2.3)$$

From a microscopic point of view, the anelastic strain can be presented as the movements of structural defects such as elastic dipoles, dislocation or grain-boundaries from one equilibrium position (at $\sigma = 0$) to another one defined at σ_0 . The relaxation strength (Δ) is proportional to the concentration of the relaxing defects and the relaxation time accounts for their mobility [6].

2.2.2. Standard anelastic solid (Rheological model)

A standard anelastic solid can be represented by the rheological model, in Fig. 2.2. This model is a combination of the Voigt-Kelvin (spring and dashpot in parallel) and Maxwell (a spring and dashpot in series) models. In this model, the spring (having a constant value of $\delta J = J_r - J_u$) in parallel with a dashpot of viscosity $\eta = \frac{\tau}{\delta J}$ is essential for the recoverable nature of the anelastic strain. If this spring does not operate, the anelastic strain does not reach an equilibrium value and thus, it is no longer completely recoverable.

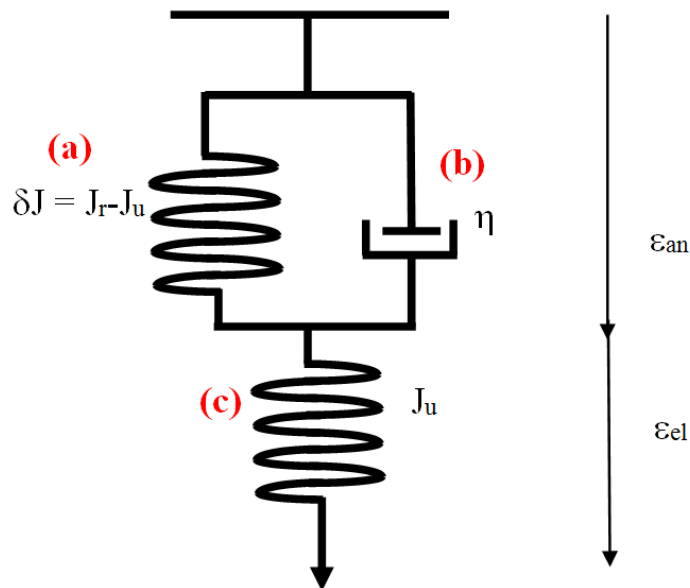


Fig. 2.2. Rheological model corresponding to the three-parameters standard anelastic solid as shown in Fig. 2.1. A dashpot is connected with a spring in parallel (Voigt-Kelvin model) with a constant of δJ , and in series with another spring (Maxwell model) with a constant of J_u .

By using the rheological approach shown in Fig. 2.1 and Fig. 2.2, one can describe successfully the compliance evolution ($J(t) = \epsilon(t)/\sigma_0$) as a function of time (Fig. 2.3). Considering the model of Fig. 2.2 the total stress (σ) is equal to:

$$\sigma = \sigma_a + \sigma_b = \eta \dot{\epsilon}_{an} + \frac{\epsilon_{an}}{\delta J} \quad (2.4)$$

Chapter 2

On the other hand: $\sigma = \sigma_c = \frac{\varepsilon_{el}}{J_u}$

Substitution of $\tau = \eta \cdot \delta J$, and $\delta J = J_r - J_u$ in Eq. 2.4:

which yields; $(J_r - J_u) \sigma = \tau (\dot{\varepsilon} - \dot{\varepsilon}_{el}) + (\varepsilon - \varepsilon_{el})$

$$(J_r \sigma - J_u \sigma = \tau \dot{\varepsilon} - \tau J_u \dot{\sigma} + \varepsilon - J_u \sigma) \quad (2.5)$$

With rearrangement of Eq. 2.5, the standard anelastic solid equation for motion is found to be:

$$J_r \sigma + J_u \tau \dot{\sigma} = \varepsilon + \tau \dot{\varepsilon} \quad (2.6)$$

The static solution of Eq. (2.6), gives the compliance evolution as a form of:

$$J(t) = J_u + (J_r - J_u) \left[1 - \exp\left(-\frac{t}{\tau}\right) \right] \quad (2.7)$$

which is consistent with the graph that observed in Fig. 2.3. Note that the kinetic of the relaxing structural defects in the standard anelastic solid is described by the Debye relaxation function (Eq. 2.7).

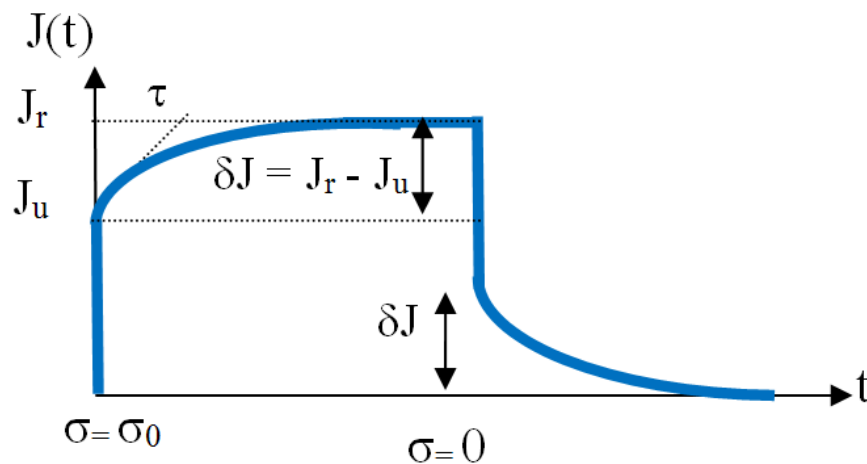


Fig. 2.3. Compliance (J) evolution from an equilibrium position (J_u) to another one (J_r) as a function of time.

2.2.3. Dynamic properties of standard anelastic solid

The measurements performed in the way described in part 2.2.2 are very delicate and it is not practical to measurements. Anelasticity can be better studied dynamically. In this case, an alternating stress with circular frequency ($\omega = 2\pi f$, where f is frequency) is applied to the specimen (anelastic solid):

$$\sigma = \sigma_0 \exp(i\omega t) \quad (2.8)$$

where σ_0 is the stress amplitude. Due to the linearity between stress and strain, the resulting strain is also periodic with the same frequency:

$$\varepsilon = \varepsilon_0 \exp[i(\omega t - \varphi)] \quad (2.9)$$

while ε_0 is the strain amplitude and loss angle, φ , the phase lag between the stress and the strain, loss angle, due to anelasticity of the material. Fig. 2.4a shows a schematic diagram of an applied stress and response strain as a function of time and Fig. 2.4b is vectorial representation of stress and strain.

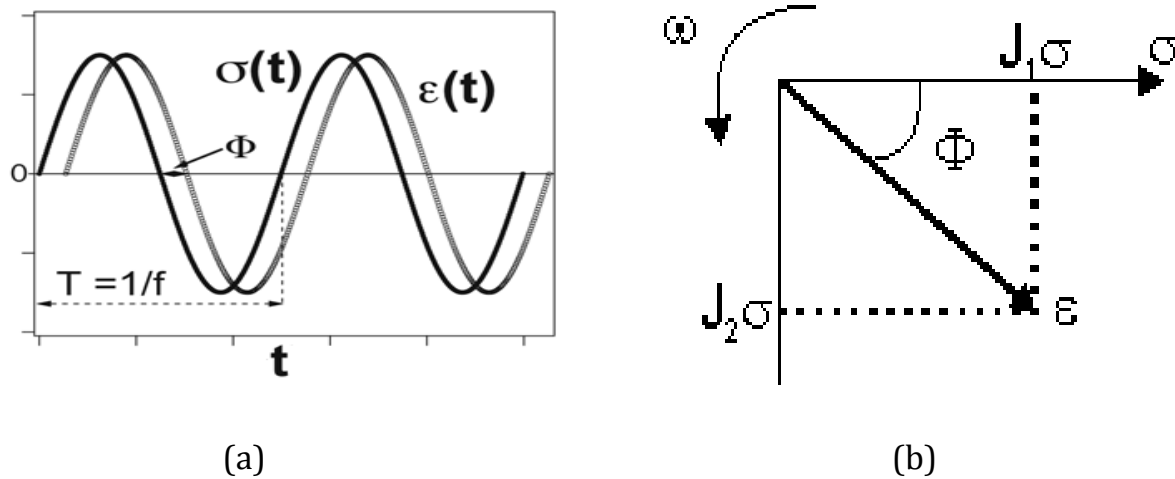


Fig. 2.4. Schematic diagram of an applied stress and response strain as a function of time (a) and vector diagram in the complex showing the phase relationship between the stress and strain (b). φ is phase lag and the diagram rotate around the origin with a circular frequency of ω .

Chapter 2

Substitution of equations (2.8) and (2.9) into the equation of the standard anelastic solid (Eq. 2.6), leads to the following relationship:

$$(J_u + \delta J) \sigma + i\omega J_u \tau \sigma = \varepsilon + i\omega \tau \varepsilon \quad (2.10)$$

and the strain/ stress relation is:

$$\varepsilon = \left(\left[J_u + \frac{\delta J}{1+\omega^2 \tau^2} \right] + i \left[\frac{\delta J \omega \tau}{1+\omega^2 \tau^2} \right] \right) \sigma \quad (2.11)$$

On the other hand, a complex compliance $J^*(\omega)$ can be defined as:

$$\varepsilon = J^*(\omega) \sigma = [J_1(\omega) + i J_2(\omega)] \sigma \quad (2.12)$$

where the real part, and the imaginary part of the complex compliance are J_1 and J_2 , respectively. So that:

$$J_1(\omega) = J_u + \frac{\delta J}{1+\omega^2 \tau^2} \quad (2.13)$$

$$\text{and } J_2(\omega) = \frac{\delta J \omega \tau}{1+\omega^2 \tau^2} \quad (2.14)$$

In metals and ceramics, $\delta J \ll J_u$ and so, the mechanical-loss is given by:

$$\tan(\varphi) = \frac{J_2}{J_1} \cong \frac{J_2}{J_u} = \Delta \left[\frac{\omega \tau}{1+\omega^2 \tau^2} \right] \quad (2.15)$$

and the variation of the dynamic compliance $\delta J/J_u$ due to anelasticity by:

$$\frac{\delta J}{J_u} = \frac{J_1(\omega) - J_u}{J_u} = \Delta \left[\frac{1}{1+\omega^2 \tau^2} \right] \quad (2.16)$$

These two equations (Eqs 2.15 and 2.16) are called Debye's equations (similar to the equations derived for dielectric relaxation phenomena). The mechanical loss ($\tan(\varphi)$) versus $\log(\omega\tau)$ plot, shows a peak (called Debye peak) when $\omega\tau = 1$ (Fig. 2.5). According to Eq. 2.16, the height of the peak would be $\Delta/2$. From the position ($\omega\tau = 1$) and height of the peak ($\Delta/2$), the relaxation time (τ) and the relaxation strength ($\Delta = (J_r - J_u)/J_u$) can be obtained, respectively.

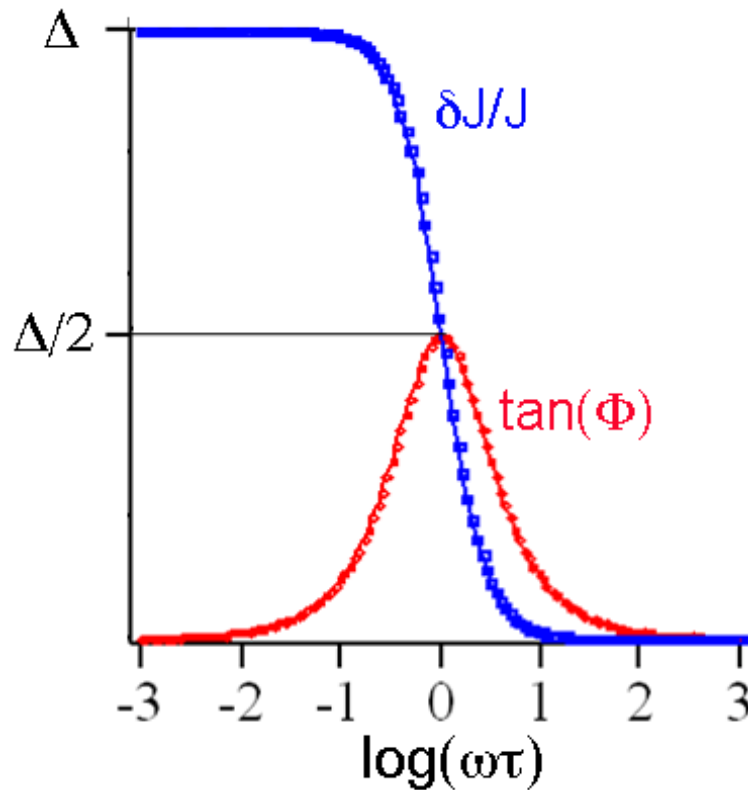


Fig. 2.5. Mechanical loss angle, $\tan(\varphi)$, and dynamic compliance, $\delta J/J_w$, as a function of $\log(\omega\tau)$.

The anelastic relaxation described by the Debye equation corresponds to the relaxation process associated with an unique relaxation time. In many cases, a distribution of the relaxation times has to be considered and so, the mechanical loss is given by Eq. 2.17:

$$\tan(\varphi) = \Delta \left[\frac{(\omega\tau)^\alpha}{1+(\omega\tau)^{2\alpha}} \right] \quad (2.17)$$

where α is broadening factor [6]. If several relaxation mechanisms are activated, the mechanical loss spectrum of the material shows several relaxation peaks. Each of them being characterized by its own relaxation strength (Δ_i) and relaxation time (τ_i). The mechanical loss spectrum that is obtained from experiments is the sum of these components.

Chapter 2

A mechanical loss spectrum, can be obtained either in isothermal condition, while varying frequency (called frequency scan), or in isochronal condition, frequency being kept constant, by varying the temperature (called temperature scan).

Most of the relaxation phenomena are thermally activated; therefore, the relaxation time generally follows an Arrhenius law (Eq. 2.18):

$$\tau = \tau_0 \exp \left(\frac{\Delta H_{act}}{RT} \right) \quad (2.18)$$

where ΔH_{act} is the activation enthalpy (characteristic of energy barrier that the defects have to jump to reach the next equilibrium state), τ_0 the limit relaxation time (inverse of the limit attempt frequency ν_0), R the gas constant and T is the absolute temperature. Where the condition of $\omega\tau = 1$ is satisfied, the mechanical loss as a function of temperature, has a peak at a temperature T_p :

$$T_p = - \frac{R}{\Delta H_{act} \ln(\omega\tau_0)} \quad (2.19)$$

The activation enthalpy and limit relaxation time can be obtained experimentally from the slope of the line obtained in the plot of peak frequency (in log scale) versus inverse of peak temperature, and y-axis intercept, respectively.

2.3. Mechanical spectroscopy and internal friction

By definition, the internal friction (IF) or internal damping is a measure of the energy which is dissipated in the solid and is defined as:

$$IF = \frac{1}{2\pi} \frac{\Delta W_{diss}}{W_{el}} \quad (2.20)$$

where ΔW_{diss} is the energy dissipated in a volume unit during one cycle of vibration and W_{el} is the maximum stored elastic energy per unit of volume.

$$\Delta W_{diss} = \oint \sigma d\varepsilon = \pi J_2 \sigma_0^2 \quad (2.21)$$

$$W_{el} = \int_0^{\sigma_0} \sigma d\varepsilon = \frac{1}{2} J_1 \sigma_0^2 \quad (2.22)$$

and IF follows as, which according to Eq. 2.15 is equal to $\tan(\varphi)$.

$$IF = \frac{1}{2\pi} \frac{\pi J_2 \sigma_0^2}{\frac{1}{2} J_1 \sigma_0^2} = \frac{J_2}{J_1} = \tan(\varphi) \quad (2.23)$$

2.4. Examples of anelastic relaxations of ceramics

Anelastic deformation precedes plastic deformation and consequently it may be the first manifestation of plastic deformation in ceramics. The relative displacement of grains causes damping at high temperature. The mechanical loss spectrum associated with GB sliding exhibits either a peak or an exponential high temperature background. A mechanical loss peak accounts for a dissipative mechanism with a restoring force which limits anelastic strain. On the other hand, when the restoring force becomes zero, the anelastic strain does not reach an equilibrium value and mechanical loss increases with temperature, continuously. This behavior accounts for the onset of creep.

Few examples of mechanical spectroscopy for investigating the relaxation phenomena in different type of ceramics are presented in 2.4.1, 2.4.2 and 2.4.3.

2.4.1. Yttria stabilized zirconia

A typical mechanical loss spectrum of 3mol% yttria stabilized zirconia (3Y-TZP), $\tan(\varphi)$ and dynamic shear modules, as a function of temperature (at fixed frequency) and as a function of frequency (at fixed temperature) is shown in Fig. 2.6 (a) and (b), respectively [7]. In Fig. 2.6 (a), one can clearly distinguish two regions of special interest:

a) Low temperature ($300 < T < 500$ K): a damping peak is observed at around 400 K accompanied by a modulus defect. This damping peak is related to the reorientation

Chapter 2

of elastic dipoles “oxygen vacancy-yttrium cation” under applied stress. The responsible mechanism (point defect relaxation) will be described below (2.4.1.1).

b) High temperature (> 1200 K): In this range of temperature an exponential increase in $\tan(\varphi)$ is observed, and in parallel a steep modulus decrease. A theoretical model was developed by Lakki [7] to account for mechanical loss due to the relative sliding of grains (GB relaxation) under the applied stress (2.4.1.2).

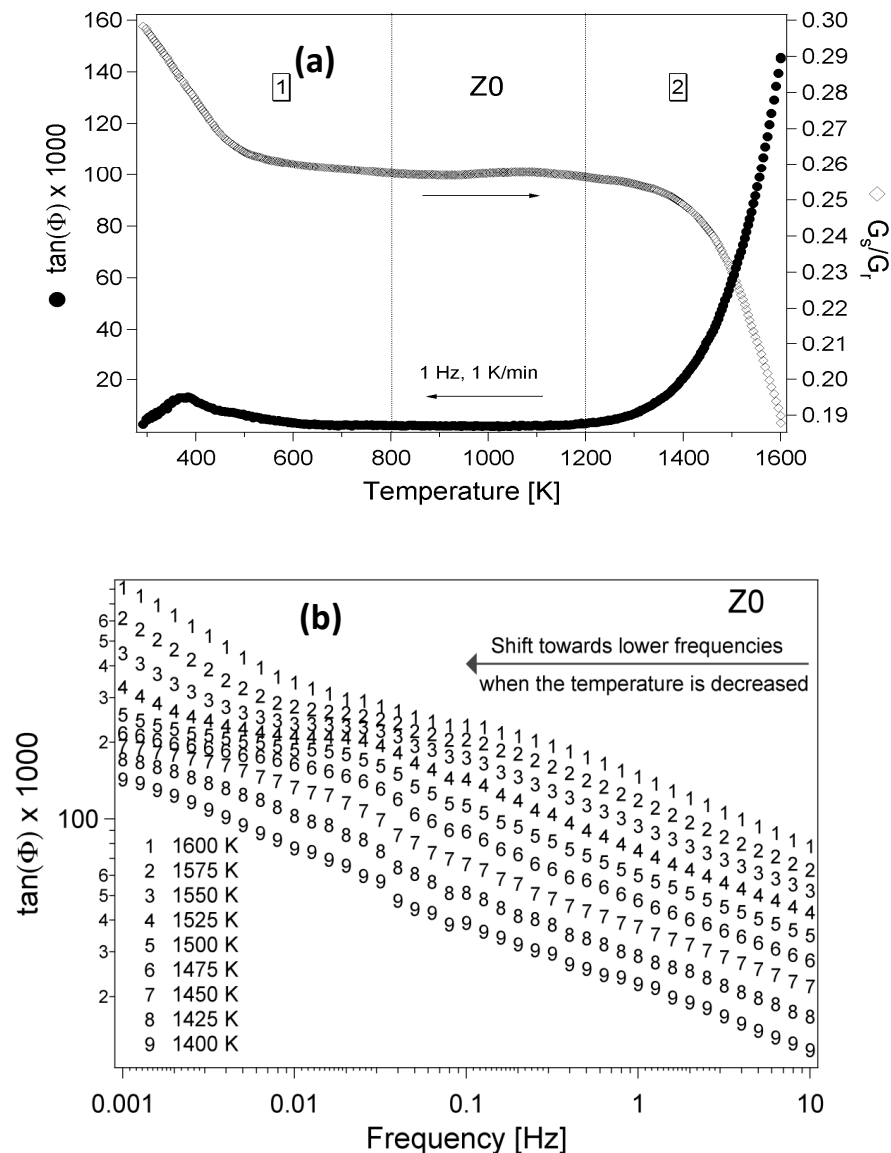
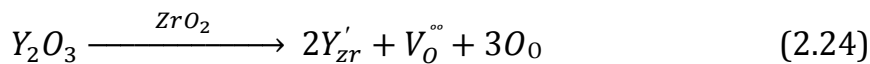


Fig. 2.6. Mechanical loss as a function of temperature (isochronal curve) for frequency of 1 Hz (a) and as a function of frequency in different temperature (isothermal curves).

2.4.1.1. Low temperature peak (point defect relaxation)

An elastic dipole appears, where a point defect produces a local distortion of the lattice. For instance, interstitial atoms, such as O, N, or C in bcc metals can produce elastic dipoles. When an external stress is applied to the specimen, there will be a preferred orientation for elastic dipoles along the most favorable direction. This reorientation causes to anelastic strain [8].

Transport properties (ionic conductivity or diffusion) in oxides type MO_2 (such as Zirconia, Ceria, or Thoria) are closely related to the presence and mobility of point defects such as oxygen vacancies [9, 10]. A considerable amount of oxygen vacancies can be created by doping with lower valence cations. For example doping three valent cations (e.g. Y_2O_3) in ZrO_2 introduce one vacancy for every two Y^{3+} , to preserve charge neutrality [9]. Kroger-Vink notation of this substitution is as below:



These Yttrium cations (Y^{3+}) accompanied by oxygen vacancies ($V_O^{\circ\circ}$) form elastic and electric dipoles. Under the influence of stress/electrical field, these dipoles ($Y'_{Zr} - V_O^{\circ\circ}$) can reorient giving rise to anelastic/dielectric relaxation peak [9, 10]. Fig. 2.7 shows a sketch of an elastic dipole in the unit cell of tetragonal yttria stabilized zirconia. Reorientation of the dipole can occur, when an oxygen vacancy jumps around the immobile-yttrium cation. The relaxation shows in Fig. 2.6 is related to this mechanism [8].

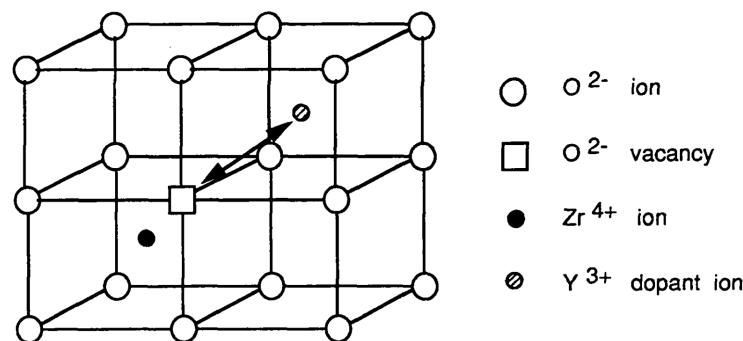


Fig. 2.7. Substitutional yttrium cation in zirconia unit cell forming an elastic and electric dipole with an oxygen-ion vacancy.

2.4.1.2. High temperature damping (grain-boundary relaxation)

The high temperature plastic deformation of ceramics (e.g. zirconia) occurs because of grain-boundary (GB) sliding. Mechanical spectroscopy is sensitive to such a GB sliding process [2].

Effect of impurities on high temperature mechanical loss of 3Y-TZP;

Fig. 2.8a shows typical mechanical loss and shear modulus spectra plotted as a function of temperature for two grades of zirconia: TS2/1 (contains a higher content of impurities) and TS2/2. The TS2/1 spectrum shows a faster increase in the mechanical loss and a steeper decrease in the shear modulus with respect to TS2/2. During creep test at 1623 K, TS2/1 demonstrates in the low stress regime (10 MPa) a higher strain rate then TS2/2 (Fig. 2.8b).

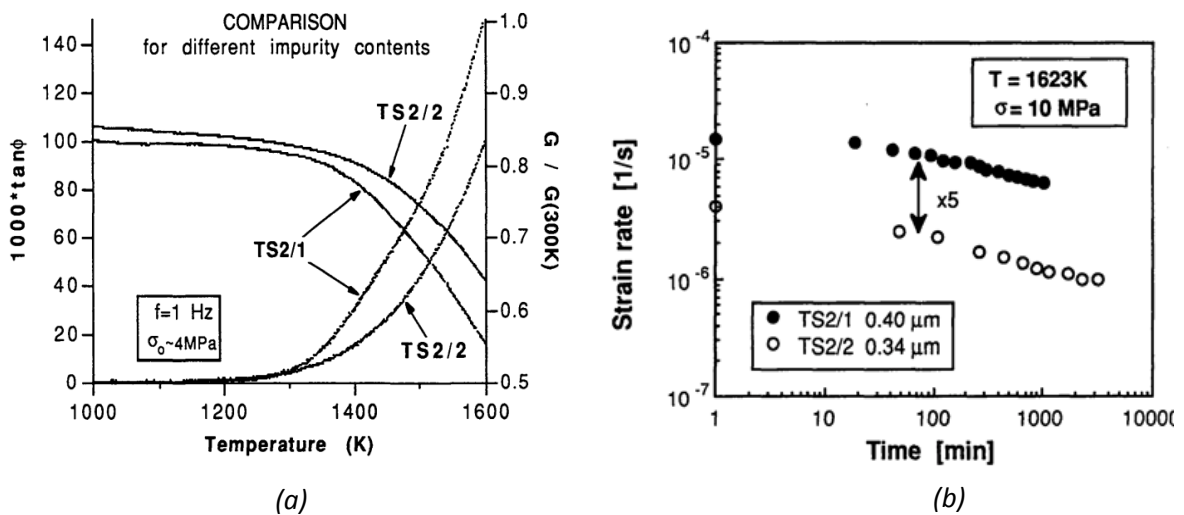


Fig. 2.8. (a) Mechanical loss and shear modulus as a function of temperature for two zirconia samples TS2/1 (high content of impurity) and TS2/2. (b) Creep rate measured at 1623 K as a function of time [2].

Single crystal high temperature mechanical loss of 3Y-TZP;

In Fig. 2.9a the mechanical-loss spectrum of a single crystal is compared with the one of a polycrystalline sample.

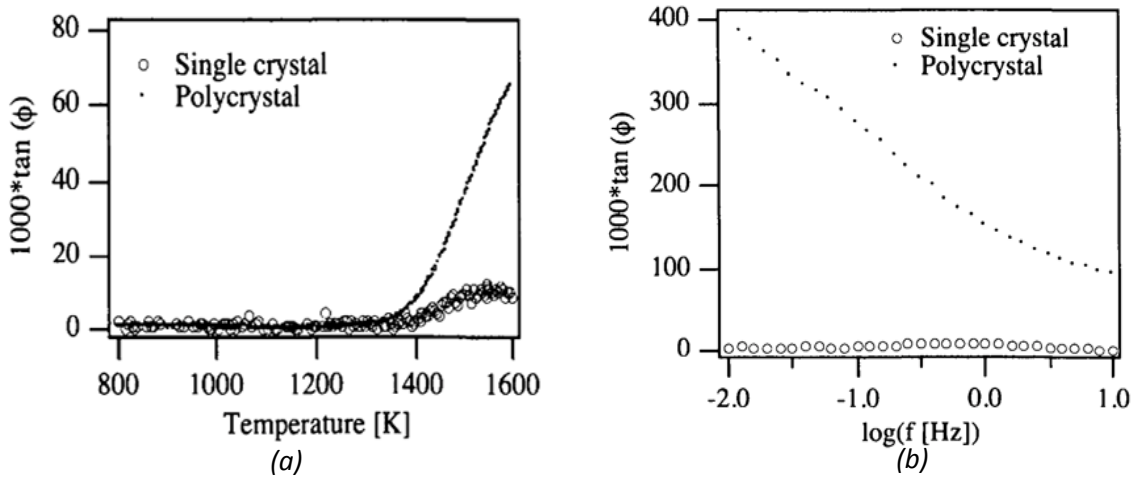


Fig. 2.9. Mechanical losses as a function of a) temperature at 1 Hz and b) frequency at 1600 K are compared for a polycrystalline and single crystal zirconia [11].

The damping in polycrystalline is much higher than in the single crystal. It is even more evident in the isothermal spectra (Fig. 2.9b). As a consequence, the high-temperature damping is due to GBs, and it has been explained by a GB sliding model (2.4.1.2.2), which was proposed by Lakki [7]. The mechanical-loss spectrum of the single crystal exhibits just a peak at 1600 k. Donzel interpreted this peak as being due to the stress-induced reorientation of elastic dipoles (as explained in 2.4.1.1).

Effect of grain size on high temperature mechanical loss of 3Y-TZP;

Fig. 2.10a shows the influence of the grain size d on the mechanical-loss spectrum as a function of temperature. It can be seen that the mechanical loss increases exponentially with temperature and the higher the grain size the smaller the level of damping.

For the samples with a grain size $d < 0.7 \mu\text{m}$ the mechanical-loss spectrum, obtained as a function of frequency, is composed of a not well resolved peak (PS) and an exponential increase at lower frequencies. This peak (PS) has been observed in isothermal measurements made in 2Y-TZP grade [12, 13]. A new peak PL arises in

Chapter 2

the mechanical-loss spectrum at much lower frequencies. The existence of two peaks can be considered as a manifestation of two types of grains: small and large ones. The model described in 2.4.1.2.2 explains well this high-temperature behavior of polycrystalline zirconia (3Y-TZP grade). The peak height depends on $1/d$, while the background depends on $1/\sqrt{d}$ [12].

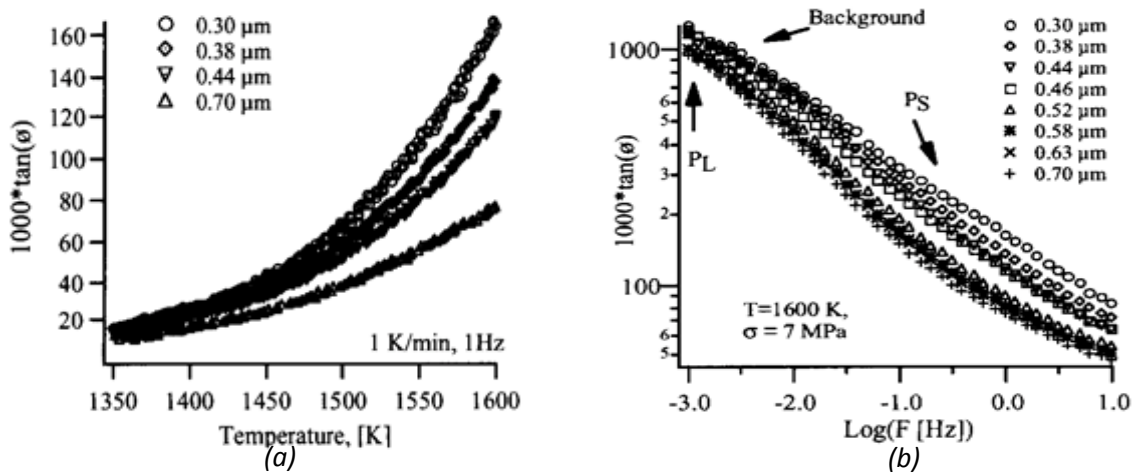


Fig. 2.10. Mechanical loss plotted as a function of (a) temperature and (b) frequency for eight different grain sizes $0.30 \mu\text{m} - 0.70 \mu\text{m}$ [12, 13].

2.4.1.2.1. GB sliding according to Zener's model

In polycrystalline solids, GB sliding can give rise to an anelastic relaxation peak. This phenomenon has been predicted by Zener [4] for the first time and investigated by Ke [14, 15]. Experimental evidence for this suggestion was a higher internal friction level in polycrystalline solids than in single-crystals. Fig. 2.11 shows a GB between two adjacent grains separated by a viscous interface, which cannot sustain the stress. When shear stress (σ) is applied, the grains deform elastically and then they slide one over the other. For example, in Fig. 2.11, to relieve the stress across the GB, grain 1 slides over grain 2, while building up opposite stresses at the triple junctions, due to elastic deformation of neighboring grains. The sliding continues up to the shear stresses relaxed completely.

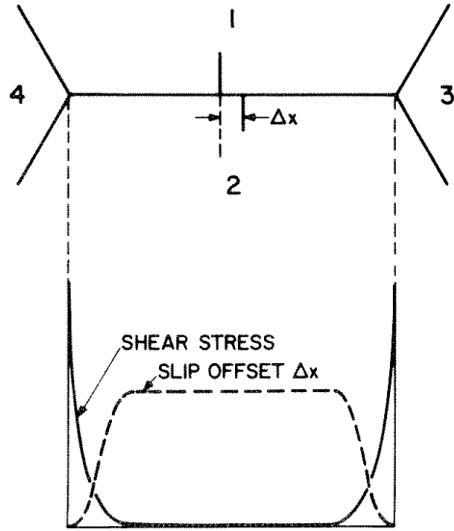


Fig. 2.11. GB sliding relaxation with elastic restoration at the triple points [4].

The equation of motion controlled by the sliding (relaxation) process is:

$$\frac{d[\Delta x(t)]}{dt} = -\frac{\Delta x(t) - \Delta x(\infty)}{\tau} \quad (2.25)$$

where $\Delta x(t)$ and $\Delta x(\infty)$ are the GB slip deformation at time = t and equilibrium condition, respectively. The relaxation time and the relaxed shear modulus (G_R) were calculated:

$$\tau = \frac{\eta d}{\delta G_U} \quad (2.26)$$

$$G_R = \frac{2}{5} \left(\frac{7+5\nu}{7-4\nu} \right) G_U \quad (2.27)$$

where d is the grain size, η the viscosity and δ the thickness of interface, G_R and G_U are the relaxed and unrelaxed shear modulus and ν is the Poisson ratio. For metals $\nu \sim 0.3$, therefore the relaxation strength of mechanical loss peak for GB sliding mechanism would be around 0.64 and $G_R/G_U \approx 0.61$. This model has been verified by different experiments [4].

Although the above equations (Eqs 2.26 and 2.27) show that τ depends on grain size linearly and G_R/G_U is independent on grain size, in some polycrystalline materials

the GB peak is accompanied by an exponential increase in mechanical loss at high temperature and τ does not follow a linear dependence on d while G_R/G_u or Δ is dependent on d .

2.4.1.2.2. GB sliding: Lakki's model

Lakki [7, 16] proposed a theoretical model accounting for the relative sliding of equiaxed grains that are separated by an amorphous viscous layer of viscosity η and thickness δ (Fig. 2.12). The grains are constrained by the triple junctions. In other words, to limit the GB sliding, a restoring force (K) was introduced, originating from the triple junctions. The relative motion (x) of two grains submitted to a shear stress (σ) is described by Newton's law (expressed per unit area):

$$\sigma = \frac{\eta}{\delta} \dot{x} + Kx \quad (2.28)$$

where Kx is the restoring force per unit area due to limiting grains at triple junctions. The solution of Eq. 2.28 for an applied cyclic stress $\sigma = \sigma_0 \cos(\omega t)$ gives the displacement, $x(t)$, occurring during measurement. As already mentioned the internal friction can be measured by the phase lag between the stress ($\sigma = \sigma_0 \cos(\omega t)$), and the total strain ($\varepsilon = \varepsilon_0 \cos(\omega t - \varphi)$), where ε is:

$$\varepsilon = \varepsilon_{elastic} + \varepsilon_{anelastic} = \frac{\sigma}{G} + \frac{x}{d} = \varepsilon_0 \cos(\omega t - \varphi) \quad (2.29)$$

And then the mechanical loss:

$$\tan(\varphi) = \frac{G}{d} \frac{\omega \frac{\eta}{\delta}}{\left(\frac{KG}{d} + K^2\right) + \left(\omega \frac{\eta}{\delta}\right)^2} \quad (2.30)$$

where G is shear modulus and d the grain size. $\tan(\varphi)$ has a form of a peak (dotted line in Fig. 2.13) when the restoring force is constant and strong enough to maintain the grain motion limited in the area of triple junctions.

The peak position, ω_p , and its maximum height, $\tan(\varphi)_{\omega=\omega_p}$, are dependent on d , δ and η and given by:

$$\omega_p = \frac{\delta}{\eta} \sqrt{\frac{KG}{d} + K^2} \quad (2.31)$$

and

$$\tan(\varphi)_{\omega=\omega_p} = \frac{G}{2d\sqrt{\frac{KG}{d} + K^2}} \quad (2.32)$$

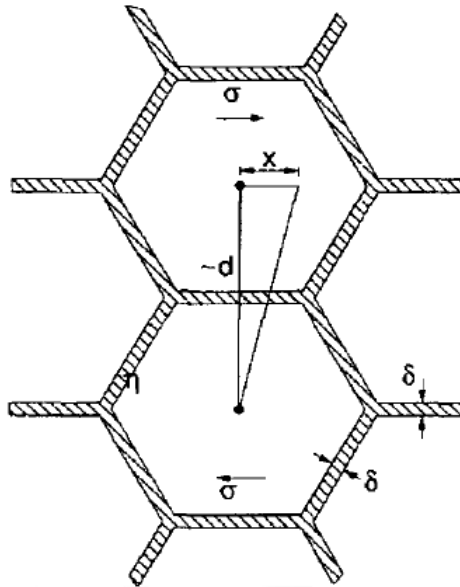


Fig. 2.12. Simple schema representing the model of hexagonal grains separated by a viscous layer of viscosity η and thickness δ , which slide relative to each other with distance x under the effect of applied stress σ_{xy} .

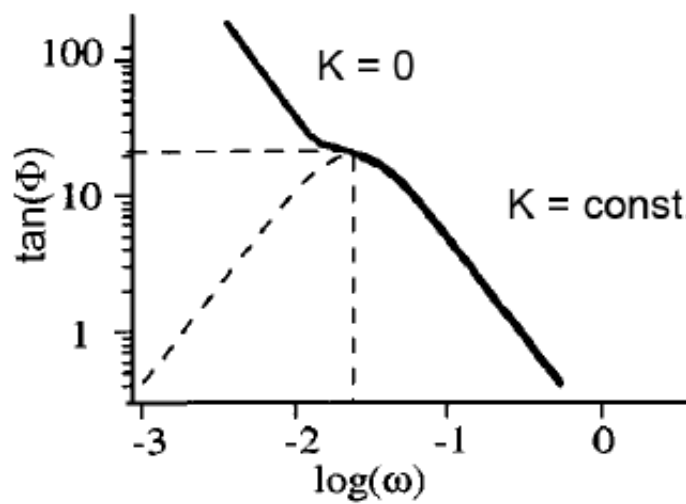


Fig. 2.13. The peak position ω_p and the peak height depend on grain size, viscosity and restoring force, according to Eq. 2.32.

Chapter 2

If $K = 0$ (no restoring force from the triple points), an exponential increase in $\tan(\varphi)$ with temperature is obtained. Then the mechanical loss is given by:

$$\tan(\varphi)_{k=0} \cong \frac{G\delta}{\omega d \eta} = \frac{G\delta}{\omega d \delta_0} \exp\left(-\frac{E_{act}}{kT}\right) \quad (2.33)$$

From the microscopic point of view this means that the relative motion of grains is not limited anymore and the grains start to perform long-range displacements, which means plastic deformation.

In a real material, the restoring force (K) is not zero, but decreases as a function of temperature (weakening of the pinning centers) and inverse of frequency. Assuming that the restoring force is proportional to the shear modulus, $G(t) = \sigma/\varepsilon(t)$, which strongly decreases at high temperature, the anelastic deformation can be negligible compared to plastic deformation and one obtains:

$$K(\omega) = c \cdot \frac{\sigma}{\varepsilon_{el} + \varepsilon_{pl}(t)} = c \cdot \frac{\sigma}{\frac{\sigma}{G} + A \frac{\sigma^2}{d} \exp\left(\frac{E_{act}}{kT}\right) \cdot t} \quad (2.34)$$

Introducing Eq. 2.34 into Eq. 2.30, results in a theoretical spectrum as shown in Fig. 2.13, where a transition from a peak to an exponential background in the mechanical loss spectrum may be interpreted as the onset of creep [7, 16].

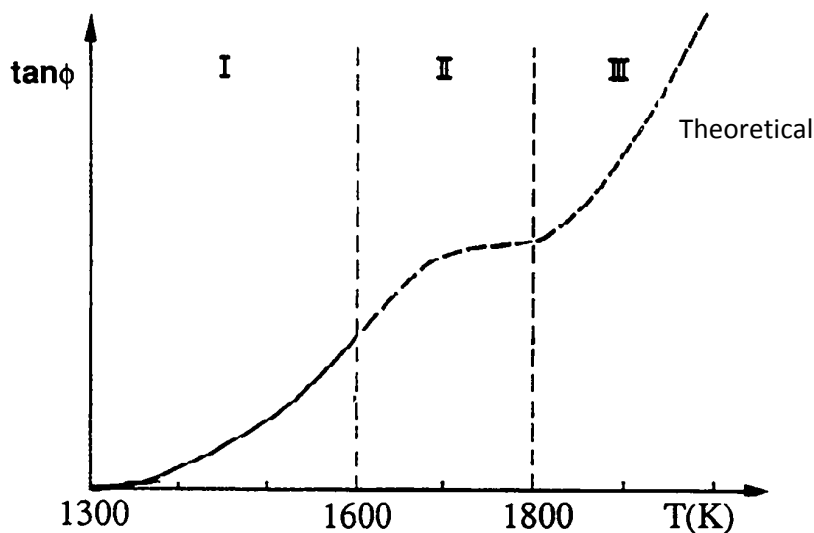


Fig. 2.14. Complete I.F. spectrum of yttria stabilized zirconia polycrystals schematically drawn as a function of temperature [7, 16].

The internal friction (I.F.) measurement at fixed frequency (isochronal spectra at $f = 1$ Hz), for instance Fig. 2.6a, coincide with the high frequency part of the isothermal spectra. A behavior similar to Fig. 2.14 would be qualitatively expected [7, 16].

In Fig. 2.14, part I is the temperature range where the I.F. measurement, presented in Fig. 2.6, were conducted. According to Lakki's model, the first anelastic strain would be due to short range GB sliding of hexagonal grains. The result is shown the exponential increase of $\tan(\varphi)$ in Fig. 2.6. It can be considered as the low temperature part of a peak located at 1700 K (Fig. 2. 14). Transition from region II to region III or from peak to background could be due to a strong decrease of restoring force (weakness of junctions). Consequently, the $\tan(\varphi)$ increases rapidly without reaching an equilibrium value, resulting in micro-creep.

2.4.2. Alumina: Grain boundary dislocation motion

Alumina with a microstructure similar to zirconia (equiaxed grains) shows a similar mechanical loss spectrum at high temperature. In the case of alumina, there is no amorphous layer in the grain boundaries. So, due to the structure of GBs, the level of mechanical loss is lower than in zirconia samples and it may be assumed that in alumina, grain GB sliding can only take place by elementary motion of GB dislocations. Typical high temperature spectra of alumina as a function of temperature (fixed-frequency) and as a function of frequency (fixed-temperature) are shown in Fig. 2.15 (a) and (b) respectively [7, 17]. As in the case of zirconia, the mechanical loss as a function of temperature shows a monotonic increase. However, the relationship between grain size and internal friction is different from one of the zirconia. The spectra are independent of the grain size for small grain sizes, while the mechanical loss decreases as d^{-1} for large grains [2].

2.4.2.1. Dislocation relaxation [2]

The dislocation string model accounts for dislocation relaxation. A dislocation segment of length L , which is fixed between two strong pinning points, bows under an applied stress (Fig. 2.16). Where a viscous friction acts on dislocation segment, the anelastic behavior can be accounted for by a simple vibrating string model. This model was suggested by Koehler and later developed by Granato and Lucke [18].

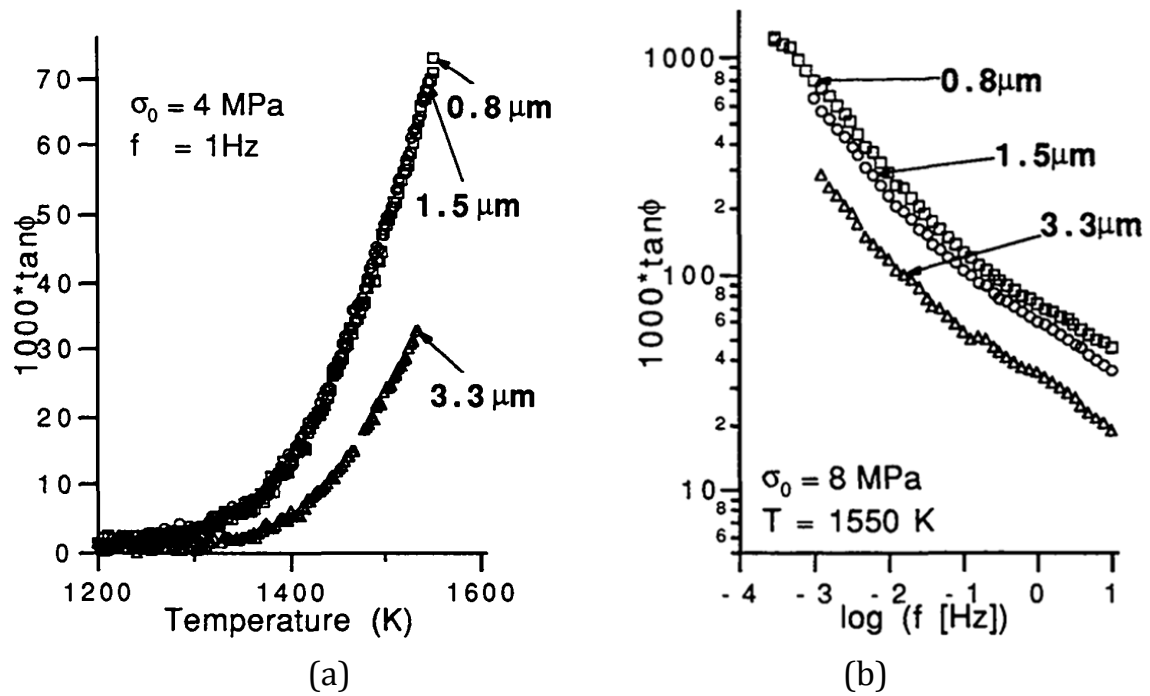


Fig. 2.15. Mechanical loss as a function of temperature (a) for a frequency of 1 Hz and as a function of frequency (b) for MgO doped alumina for three different grain sizes[2].

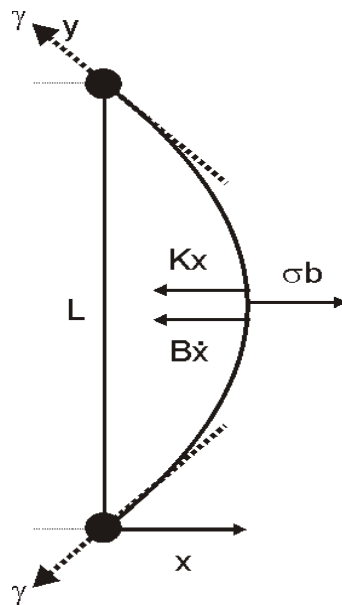


Fig. 2.16. String model: A pinned dislocation segment of length L bowed under the applied stress. Two forces are acting against σ_b , the restoring force Kx due to line tension and dragging force $B\dot{x}$ [2].

When an external stress (σ) is applied to a crystal, a force, $f_{pk} = b\sigma$, called the Peach and Koehler force acts on dislocation, defined per unit length of dislocation, and perpendicular to the dislocation line, where b is Burger's vector. Two main forces act in opposition to this external force (f_{pk}): 1) the restoring force: KxL , this force is due to dislocation line tension ($\gamma = KL^2/12$) where K is the restoring force coefficient, and x is the mean displacement of dislocation. 2) the dragging force, $f_{drag} = B\dot{x}L$, due to interactions of the dislocations with phonons and electrons, point defect dragging, or other impurities. The dragging coefficient, B , depends on the mechanism (such as kink pair formation, dragging) which controls the dislocation motion (there is also a third effective force: inertial force, which is negligible). The equation of motion (presented per unit length of dislocation) is:

$$b\sigma = Kx + B\dot{x} \quad (2.38)$$

On the other hand, the total strain, ε , of a crystal with mobile dislocations is given by:

$$\varepsilon = \varepsilon_{el} + \varepsilon_{an} = \sigma J_u + \Lambda bx \quad (2.39)$$

where Λ is mobile dislocation density.

From Eqs 2.38 and 2.39, the relaxation strength, Δ , and relaxation time, τ , can be calculated as (by taking to account that $K = 12\gamma/L^2$ and $\gamma = b^2/2J_u$):

$$\Delta = \frac{\Lambda b^2}{J_u K} = \frac{\Lambda L^2}{6} \quad (2.40)$$

$$\tau = \frac{B}{K} = \frac{BL^2}{12\gamma} \quad (2.41)$$

And according to Eq. 2.15, the mechanical-loss spectrum shows a relaxation peak, the height of which is proportional to the dislocation density (Λ) and the loop length (L). For example addition of pinning points results in the reduction of the dislocation loop length, and consequently, the peak height decreases [2].

2.4.2.2. Damping due to GB dislocation [17]

In Eq. 2.39, Λ is the dislocation density. In the case of GB dislocations, the total dislocation length per unit GB area (ρ) has to be considered. ρ is an inherent constant of the GB and does not depend on the grain size ($\Lambda = \rho/d$).

Using Eqs 2.15, 2.39, 2.40 and 2.41, the loss angle can be calculated:

$$\tan(\varphi) = \frac{G\rho b^2}{Kd} \left[\frac{\omega \frac{B}{K}}{1 + (\omega \frac{B}{K})^2} \right] \quad (2.42)$$

Imagine that GB dislocations form an array, therefore, the restoring force per unit length of dislocation would come from: 1) the repulsion between vibrating dislocations and from 2) the elasticity of limiting grains at triple junctions. The repulsion between dislocations is independent on grain size and should only depend on the intrinsic geometry of grains. On the other hand, the force associated with triple junctions is inversely proportional to the grain size (d^{-1}). These two forces act in parallel and the restoring force is the sum of two constants:

$$K = c_1 + \frac{c_2}{d} \approx \begin{cases} \frac{c_2}{d} & \text{for small grains} \\ c_1 & \text{for large grains} \end{cases} \quad (2.43)$$

If the grains are small the $1/d$ term is dominating, while for large grains a constant (c_1) value will be obtained. As a consequence, the height of peak ($\Delta/2$) is given by:

$$\max(\tan(\varphi)) \approx \begin{cases} \frac{G\rho b^2}{c_2} & \text{for small grains} \\ \frac{G\rho b^2}{c_1} d^{-1} & \text{for large grains} \end{cases} \quad (2.44)$$

The behavior appearing in Fig 2.15, is in good agreement with the above equation, while, the $\tan(\varphi)$ is constant for small grains and depends inversely on the grain size for large d . Dislocation motion is mainly controlled by climbing process. Therefore, the dragging coefficient, B , estimated by creation and migration of jogs on GB dislocations:

$$B = \frac{kT}{b^2 D c_j} \quad (2.45)$$

where c_j is the linear density of jogs and D the diffusion coefficient. The activation energy (840 kJ mol⁻¹) obtained from the spectrum in alumina samples should be associated with the creation and motion (diffusion) of jogs in the structure.

$$\tau = \frac{B}{K} = \frac{kT}{Kb^2Dc_{j,0}} \exp\left(\frac{E^{jog\ form} + E^{dif}}{kT}\right) \quad (2.46)$$

2.4.2.3. Master curve method and activation energy calculation

The estimation of the activation parameters can be done by a superposition of the mechanical-loss spectra to obtain a master-curve spectrum. This method is valid if the microstructure of the sample does not change during the measurement. Lakki et al. [7] proposed a procedure for determination of ΔH_{act} and τ_0 from the temperature-frequency shift of the mechanical-loss spectra. The isothermal spectra corresponding to two different temperatures T_1 and T_2 are superimposed by a shift along the frequency-axis (x-axis) like in Fig. 2.17.

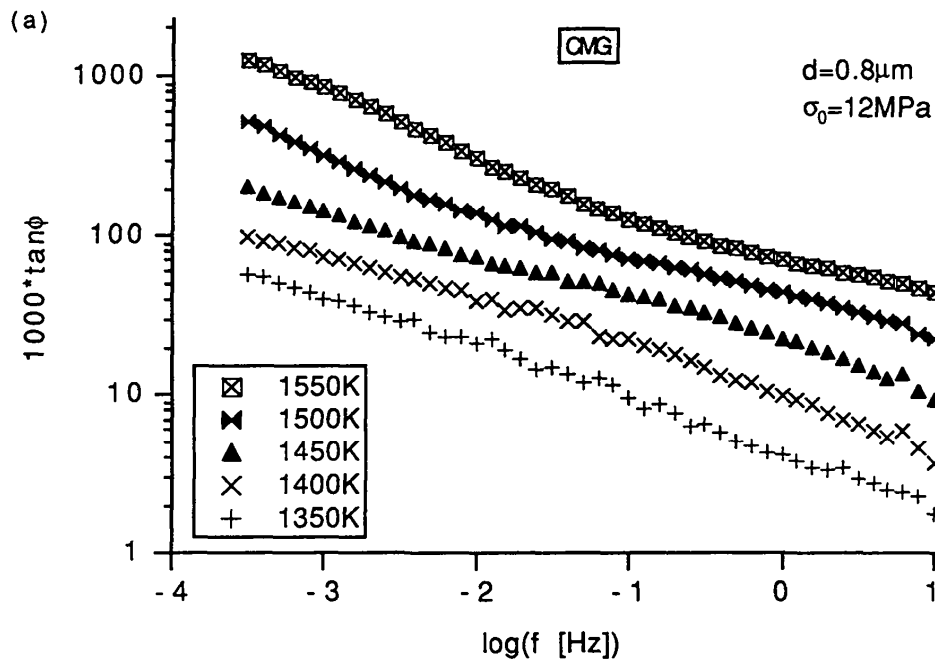


Fig. 2.17. Mechanical loss as a function of frequency for MgO doped alumina taken at different temperatures.

Chapter 2

Reporting the frequency-shift as a function of the inverse of the temperature ($\Delta(1/T) = 1/T_1 - 1/T_2$), we get an Arrhenius plot, the slope of which gives ΔH_{act} (Fig. 2.18a). This procedure is valid if $\tan(\Phi)$ is a function of $\omega\tau$ only, and τ_0 is given by an Arrhenius law with constant activation parameters (Fig. 2.18a).

$$\tan(\Phi) = \tan(\phi[\log(\omega\tau)]) = \tan\left(\Phi\left[\log(\omega) + \frac{\Delta H_{act}}{R \cdot \ln(10)} \frac{1}{T} + \log(\tau_0)\right]\right) \quad (2.47)$$

By bringing into coincidence the isothermal spectra corresponding to two different temperatures by a shift along the frequency-axis, which means a constant $\tan(\Phi)$, the expression in the square brackets does not vary. Therefore, we get:

$$\Delta(\log(\omega)) = -\frac{\Delta H_{act}}{R \cdot \ln(10)} \Delta\left(\frac{1}{T}\right) - \Delta(\log(\tau_0)) \quad (2.48)$$

where the limit attempt frequency ν_0 can be determined by any point on the spectrum. From the superimposition of all spectra together, the so-called "master-curve" spectrum is obtained (Fig. 2.18b). This spectrum together with the activation enthalpy contains the same information as all the spectra together [2].

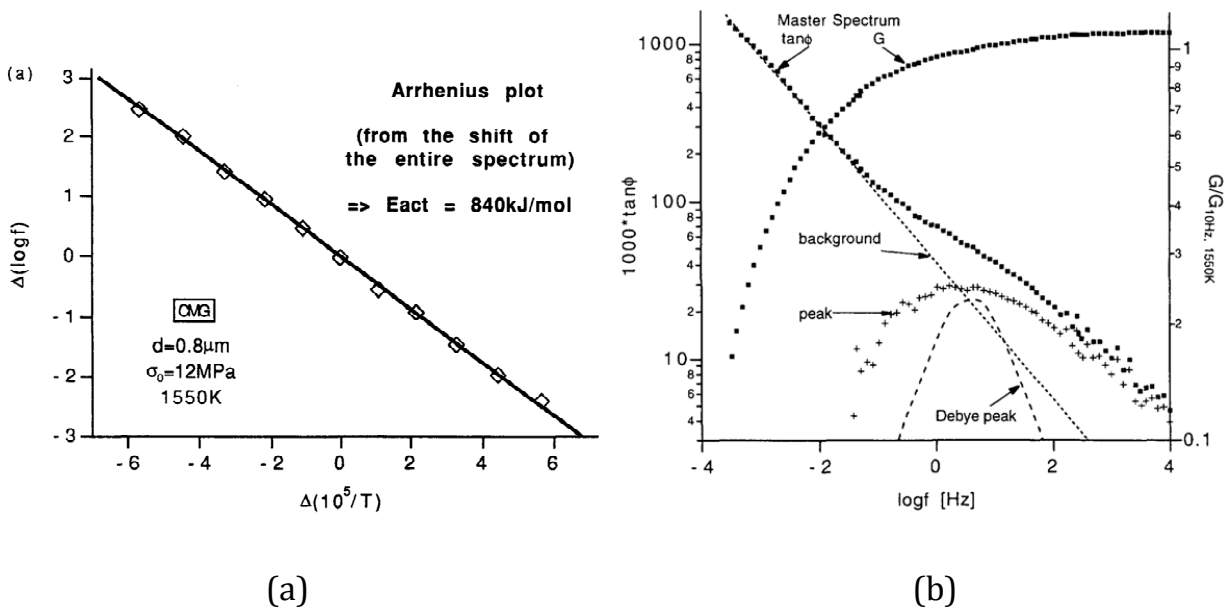


Fig. 2.18. Arrhenius plot (a) derived from the frequency shift of the movement of spectrum in Fig. 2.17 and master curve of MgO-doped alumina (b).

2.4.2.4. Creep and exponential background

The exponential increase in the mechanical loss and the decrease in the shear modulus at high temperature account for the appearance of ductility in ceramics, i.e. a kind of "brittle-to-ductile" transition. In fact, an exponential increase in $\tan(\Phi)$ means an increase in the anelastic strain, which does not reach the equilibrium value: onset of creep. The mechanical loss can be calculated by introducing the phenomenological equation of creep. Creep is described by the ceramic power law equation [2]:

$$\dot{\varepsilon}(\sigma, T) = A \frac{\sigma^n}{d^p} \exp\left(-\frac{\Delta H_{act}}{RT}\right) \quad (2.49)$$

where d , n , p , σ , $\dot{\varepsilon}$, ΔH_{act} , R and T are the average grain size, the stress exponent, the grain size exponent, the applied stress, strain rate, the creep activation enthalpy, universal gas constant and absolute temperature, respectively.

Starting from Eq. 2.49, it is possible to calculate the mechanical loss driven by the creep phenomenon. ΔW_{diss} and W_{el} are:

$$\Delta W_{diss} = \oint \sigma \cdot d\varepsilon = \oint \sigma \cdot \dot{\varepsilon} \cdot dt = A \frac{\sigma_0^{n+1}}{d^p} \exp\left(-\frac{\Delta H_{act}}{RT}\right) \oint dt \quad (2.50)$$

$$W_{el} = \int_0^{\sigma_0} \sigma \cdot d\varepsilon = \frac{1}{2} \frac{\sigma_0^2}{E} \quad (2.51)$$

By using Eq. 2.50, and 2.51 and replacing them into Eq. 2.23, one obtains:

$$\tan(\varphi) = C \frac{\sigma^{n-1}}{\omega d^p} \exp\left(-\frac{\Delta H_{act}}{RT}\right) \quad (2.52)$$

where C is a material constant. Eq. 2.52 has an exponential form, which reflects well the experimental results obtained in the high-temperature domain. This phenomenological equation (Eq. 2.52) could serve as the first approach to study mechanical loss raised from the first stages of creep or micro-creep. In real materials, because of a certain distribution in the activation parameters, Schoeck et al. proposed the following equation for the exponential background:

$$\tan(\Phi) = \frac{C}{\omega^\alpha} \exp\left(-\alpha \frac{\Delta H_{act}}{RT}\right) \quad (2.53)$$

with $1/\alpha$ the broadening factor and C a material constant. The parameter α can be derived from the slope of $\tan(\Phi)$ vs. $\log(\omega)$ spectrum.

2.4.3. Silicon nitride

Among the currently available structural ceramics, silicon nitride based ceramics (Sialons) exhibit excellent mechanical properties at both room and high temperatures [19]. Additionally, good oxidation and thermal shock resistance turn these ceramics into a forceful option for structural applications in combustion engines and gas turbines [19].

Due to the low atomic diffusion of high covalent bonding character silicon nitride (Si_3N_4) ceramics cannot be densified using classical solid state sintering techniques [20]. Full dense bodies can only be obtained through liquid phase sintering instead [21]. The most commonly used liquid forming sintering aids are Al_2O_3 , AlN , MgO , SiO_2 and Y_2O_3 , which yield the formation of an oxynitride liquid during high temperature sintering and later the formation of a certain volume fraction of a residual glassy phase during cooling. The glassy phase is located between neighbouring grains as glassy films or at grain triple junctions as glassy pockets [22, 23]. The composition, volume fraction, and distribution of these residual glassy phases are crucial for determining the thermal, oxidation, and mechanical properties of Si_3N_4 based ceramics, especially at temperatures higher than 1000°C [21, 23]. What can be inferred from the reports of numerous researchers is that the creep resistance strongly decreases above the glass transition temperature (T_g) [24]. In contrast, reaction bonded silicon nitride with no intergranular glassy phase showed no loss of strength at high temperatures [25]. Consequently, much effort has been devoted over the last decades aiming at assessing compositional and structural features of the residual glassy phases, *e.g.* quality, viscosity and glass transition temperature, in order to optimize the material properties.

Different ways can be considered to improve the high temperature mechanical properties of silicon nitride based ceramics namely:

I) the reduction in the amount of glassy phase. For instance, through gas pressure sintering, Testu et al. [26, 27] have decreased the volume percentage of glassy phase and consequently increased the creep resistance;

II) the enhancement of glass mechanical properties by replacing oxygen with nitrogen in the composition of glassy phase [28-30]. Since the substitution of oxygen by nitrogen in the silica tetrahedral network results in a higher bonding density per unit volume of the glass, the nitrogen-rich glassy phase sintered Si_3N_4 based ceramics demonstrated improved high temperature

mechanical properties. Becher et al. [31] have shown that Young's modulus, viscosity, glass transition temperature and chemical durability are strongly depended on the N/O ratio in glassy phase. In another investigation, Hakeem and his coworkers [30] have indicated that hardness and glass transition temperature increase with nitrogen content;

III) processing of self reinforced microstructure consisting of elongated grains. In this way, Ca- α -Sialons have shown [32-34] the advantages of a high solubility of Ca, a lower sintering temperature and the increased possibility for formation of elongated grains yielding tougher and more creep-resistant materials.

2.4.3.1. Relaxation peak in Si_3N_4

In the case of silicon nitride based ceramics (Sialon), many articles [35-40] have reported the occurrence of an anelastic relaxation peak, superimposed on an exponential background due to GB relaxation, which differs from the alumina and zirconia ones [2]. Lakki et al. [36] have shown that the peak can be attributed to the presence of an intergranular glassy phase. Therefore, the sintering aids generate an important volume fraction of glassy phase (Sialon glass), which is not only located as thin film in the GBs, but also at triple points where large glassy pockets were observed (Fig. 2.19a) [36].

The mechanical loss peak and the associated modulus disappear after thermal treatments, which enhance the crystallization of the glassy pockets (Fig. 2.19b). This indicates that the peak is related to relaxation in the glassy phase. This peak is a thermally activated peak because it shifts in temperature when the frequency is changed, a value of 1117 kJ/mol was found for the activation energy of this peak [2]. A general mechanical spectrum of Si_3N_4 during heating and after annealing at 1500 K is shown in Fig. 2.19. A mechanical loss peak occurs around 1300 K, and this peak is superimposed on an exponential increase of damping at higher temperature (Fig. 2.19a) accompanied by a steep modulus decrease (although much smaller than zirconia and alumina) [36, 41, 42].

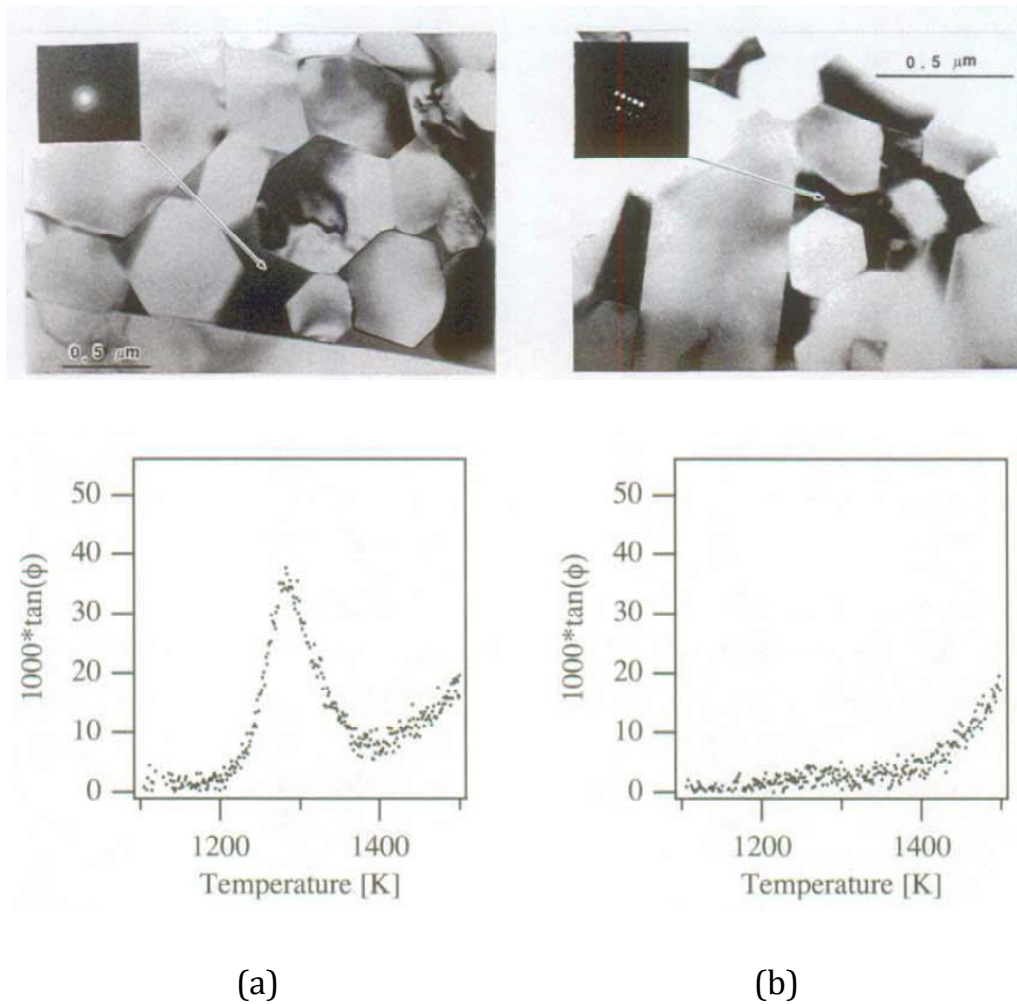


Fig. 2.19. Transmission electron micrographs and isochronal mechanical loss spectra at 1 Hz of silicon nitride sample in as-received (a) and annealed at 1600 k [36].

2.4.3.2. Relaxation in Y-Sialon glass [41, 42]

It is possible to compare the spectrum of Si_3N_4 ceramic and a glass which consisting of Y-Sialon (Fig. 2.20). The damping in Y-Sialon increases exponentially at the same temperature where the peak was observed. This increase in damping is due to α -relaxation in Y-Sialon glass. This type of relaxation can be studied by measuring the real and imaginary part of shear modulus where a relaxation peak is observed in the imaginary part. Donzel [41, 42] obtained an activation energy of 1115 kJ/mol from

the shifts of the peak. This value confirms that the peak in Si_3N_4 is due to α -relaxation in the glassy phase.

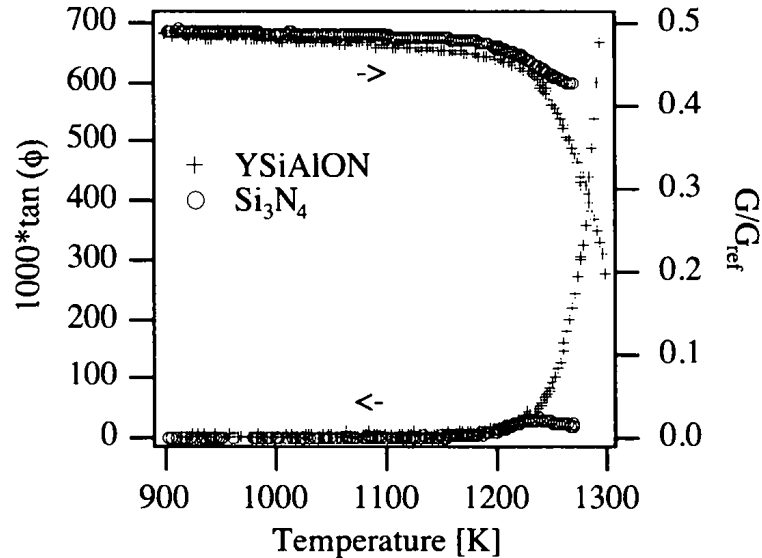


Fig. 2.20. Mechanical loss spectrum of Y-Sialon glass and Si_3N_4 ceramic.

Hence, mechanical spectroscopy can be used as a non-destructive method to analyze the behavior of residual glassy phase either as GB glassy films or glass pockets located in triple junctions. This method can be used as a complementary technique to demonstrate the presence of glassy phases, which cannot be realized by other techniques such as TEM, XRD.

References

- [1] J.S. Juan, Mechanical spectroscopy, Materials Science Forum 366-388 (2001) 32-73.
- [2] R. Schaller, A. Lakki, Grain boundary relaxations in ceramics, Materials Science Forum 366-368 (2001) 315-337.
- [3] C. Zener, Elasticity and anelasticity of metals, University of Chicago Press, Chicago, Illinois, 1948.
- [4] C. Zener, Theory of elasticity of polycrystals with viscous grain boundaries, Physical Review 60 (1941) 906-908.
- [5] I.L. Snoek, Physica (Utrecht) 8 (1941) 711-733.
- [6] A.S. Nowick, B.S. Berry, Anelastic relaxation in crystalline solids Academic Press, New York and London, 1972.

Chapter 2

- [7] A. Lakki, Mechanical spectroscopy of fine-grained zirconia, alumina and silicon nitride, in, Vol. Ph.D. Thesis No. 1266, École Polytechnique Fédérale de Lausanne, Lausanne, Switzerland, 1994.
- [8] M. Weller, Point defect relaxations, *Materials Science Forum* 366-368 (2001) 95-139.
- [9] M. Weller, Mechanical loss measurements on yttria- and calcia-stabilized zirconia, *Journal of Alloys and Compounds* 211-211 (1994) 66-70.
- [10] M. Weller, Defects in oxide ceramics and their characterization - General properties of oxides, *Journal of Materials Education* 17 (1995) 1-32.
- [11] L. Donzel, Intra- and intergranular high-temperature mechanical loss in zirconia and silicon nitride, in, Vol. Ph.D. Thesis No. 1851, École Polytechnique Fédérale de Lausanne, Lausanne, Switzerland, 1998.
- [12] M. Daraktchiev, R. Schaller, High-temperature mechanical loss behaviour of 3 mol% yttria-stabilized tetragonal zirconia polycrystals (3Y-TZP), *Physica Status Solidi (A) Applied Research* 195 (2) (2003) 293-304.
- [13] M. Daraktchiev, R. Schaller, L. Gremillard, T. Epicier, J. Chevalier, G. Fantozzi, How do the grains slide in fine-grained zirconia polycrystals at high temperature?, *Applied Physics Letters* 91 (12) (2007).
- [14] T.S. Ke, Experimental evidence of the viscous behavior of grain boundaries in metals, *Physical Review* 71 (1947) 533-546.
- [15] T.S. Ke, Viscous slip along grain boundary and diffusion of zinc in alpha-brass, *Applied Physics* 19 (285-290) (1948) 285.
- [16] A. Lakki, R. Schaller, M. Nauer, C. Carry, High temperature superplastic creep and internal friction of yttria doped zirconia polycrystals, *Acta Metallurgica Materialia* 41 (10) (1993) 2845-2853.
- [17] A. Lakki, R. Schaller, C. Carry, W. Benoit, High temperature anelastic and viscoplastic deformation of fine-grained MgO-doped Al₂O₃, *Acta Materialia* 46 (2) (1998) 689-700.
- [18] A.V. Granato, K. Lücke, Theory of the mechanical damping due to dislocations, *Journal of Applied Physics* 27 (1956) 583-589.
- [19] K.H. Jack, Sialons and related nitrogen ceramics, *Journal of Materials Science* 11 (6) (1976) 1135-1158.
- [20] K. Kijima, S.I. Shirasaki, Nitrogen self-diffusion in silicon nitride, *The Journal of Chemical Physics* 65 (7) (1976) 2668-2671.
- [21] F.F. Lange, Fabrication and properties of dense polyphase silicon nitride, *American Ceramic Society Bulletin* 62 (12) (1983) 1369-1374.
- [22] J. Crampon, R. Duclos, N. Rakotoharisoa, Creep behaviour of Si₃N₄/Y₂O₃/Al₂O₃/AlN alloys, *Journal of Materials Science* 28 (4) (1993) 909-916.
- [23] C.C. Ahn, G. Thomas, Microstructure and grain-boundary composition of hot-pressed silicon nitride with yttria and alumina, *Journal of the American Ceramic Society* 66 (1) (1983) 14-17.
- [24] M.J. Hoffmann, High-temperature properties of Si₃N₄ ceramics, *MRS Bulletin* 20 (2) (1995) 28-32.
- [25] F.L. Riley, Silicon Nitride and Related Materials, *Journal of the American Ceramic Society* 83 (2) (2000) 245-265.
- [26] S. Testu, R. Schaller, Internal friction peak in silicon nitride sintered without additives, *Diffusion and Defect Data. Pt A Defect and Diffusion Forum* 206-207 (2002) 167-170.
- [27] S. Testu, R. Schaller, J.L. Besson, T. Rouxel, G. Bernard-Granger, Mechanical spectroscopy connected to creep and stress relaxation in a high resistant silicon nitride, *Journal of the European Ceramic Society* 22 (14-15) (2002) 2511-2516.
- [28] S. Sakka, K. Kamiya, T. Yoko, Preparation and properties of CaAlSiON oxynitride glasses, *Journal of Non-Crystalline Solids* 56 (1-3) (1983) 147-152.

- [29] G. Pezzotti, T. Wakasugi, T. Nishida, R. Ota, H.J. Kleebe, K. Ota, Chemistry and inherent viscosity of glasses segregated at grain boundaries of silicon nitride and silicon carbide ceramics, *Journal of Non-Crystalline Solids* 271 (1) (2000) 79-87.
- [30] A.S. Hakeem, R. Dauceì , E. Leonova, M. Edè n, Z. Shen, J. Grins, S. Esmaeilzadeh, Silicate glasses with unprecedented high nitrogen and electropositive metal contents obtained by using metals as precursors, *Advanced Materials* 17 (18) (2005) 2214-2216.
- [31] P.F. Becher, S.B. Waters, C.G. Westmoreland, L. Riester, Compositional effects on the properties of Si-Al-RE-based oxynitride glasses (RE = La, Nd, Gd, Y, or Lu), *Journal of the American Ceramic Society* 85 (4) (2002) 897-902.
- [32] Y. Cai, Z. Shen, J. Grins, S. Esmaeilzadeh, Sialon Ceramics Prepared by Using CaH₂ as a Sintering Additive, *Journal of the American Ceramic Society* 91 (9) (2008) 2997-3004.
- [33] Y. Cai, Z. Shen, J. Grins, S. Esmaeilzadeh, T. Höche, Self-Reinforced Nitrogen-Rich Calcium–SiAlON Ceramics, *Journal of the American Ceramic Society* 90 (2) (2007) 608-613.
- [34] Y. Cai, Z. Shen, T. Höche, J. Grins, S. Esmaeilzadeh, Superplastic deformation of nitrogen-rich Ca-sialon ceramics, *Materials Science and Engineering A* 475 (1-2) (2008) 81-86.
- [35] T. Akatsu, Y. Kawakami, Y. Tanabe, E. Yasuda, K. Yamada, N. Kamiya, An irreversible disappearance of the mechanical loss peak of an yttria-doped silicon nitride, *Journal of Materials Research* 19 (9) (2004) 2532-2535.
- [36] A. Lakki, R. Schaller, G. Bernard-Granger, R. Duclos, High temperature anelastic behaviour of silicon nitride studied by mechanical spectroscopy, *Acta Metallurgica Et Materialia* 43 (2) (1995) 419-426.
- [37] D.R. Mosher, R. Raj, R. Kossowsky, Measurement of viscosity of the grain-boundary phase in hot-pressed silicon nitride, *Journal of Materials Science* 11 (1) (1976) 49-53.
- [38] G. Pezzotti, K. Okamoto, K. Ota, Rheological Behavior of Dilute SiAlON with or without Intergranular X-Phase, *Journal of the American Ceramic Society* 84 (3) (2001) 598-602.
- [39] G. Pezzotti, K. Ota, H.J. Kleebe, Grain-boundary relaxation in high-purity silicon nitride, *Journal of the American Ceramic Society* 79 (9) (1996) 2237-2246.
- [40] G. Roebben, L. Donzel, M. Steen, R. Schaller, O. Van Der Biest, Internal friction decrease in silicon nitride due to crystallization of intergranular phases, *Key Engineering Materials* 132-136 (1997) 655-658.
- [41] L. Donzel, A. Lakki, R. Schaller, Glass transition and relaxation in Y-Si-Al-O-N glasses and in Si₃N₄ ceramics studied by mechanical spectroscopy, *Philosophical Magazine A: Physics of Condensed Matter, Structure, Defects and Mechanical Properties* 76 (5) (1997) 933-944.
- [42] L. Donzel, R. Schaller, Mechanical spectroscopy of a YSiAlON glass, *Journal De Physique. IV : JP* 6 (8) (1997) C8-663-C668-666.

Chapter 3

Materials and techniques

In this chapter, the material processing and microstructure characterizations are presented for different monolithic ceramics and ceramic matrix composites (CMCs), involving Zirconia, Alumina, and Silicon Nitride. Also, the experimental setups used to characterize the materials, are presented.

3.1. Processing of materials

3.1.1. Monolithic and composite zirconia ceramics

The raw materials that were used to process monolithic 3 mol% Ytria tetragonal stabilized zirconia (3Y-TZP) ceramics, and their composites reinforced with multiwalled carbon nanotubes (CNTs), are listed as below:

(1) A commercially available 3Y-TZP raw powder (supplied by Tosoh Corporation, Japan) has been selected as the starting zirconia material. Apart from Y_2O_3 (5.35 wt.%) which is present as an intentional zirconia tetragonal phase stabilizer, the main impurities (in wt.%) are: Al_2O_3 (0.005), SiO_2 (0.006), Fe_2O_3 (0.002), HfO_2 (1.93), and Na_2O (0.021). Scanning electron microscope (SEM, XLF-30, Philips, Netherlands) examinations show that the raw powder is constituted by more or less spherical spray dried granules having an average diameter between 10 and 80 μm (Fig. 3.1a). Each granule is composed of elemental more or less spherical crystallites having an average diameter around 70 nm (Fig. 3.1b), which is in good agreement with the specific surface area (SSA) 16.4 m^2/g reported by the producer.

The X-ray diffraction (XRD) pattern of the powder taken by $Cu K\alpha$ radiation (Rigaku X-ray diffractometer, 40 kV, 30 mA) is shown in Fig. 3.2. The XRD pattern could show that the raw 3Y-TZP powder is composed of tetragonal and monoclinic zirconia phases. Using the XRD results, the weight fraction of the monoclinic phase was $\sim 23\%$, and the rest was tetragonal phase. The average crystallite size was determined by Scherrer equation (base in the main peak of the tetragonal phase) and found to be 27 nm.

(2) Commercially available multiwall carbon nanotubes (CNTs, C-100, Arkema, France) have been selected. According to the product technical data sheet, nanotubes were synthesized by catalytic chemical vapor deposition at elevated temperature of ethylene on metal/ceramic catalyst. Carbon purity of the nanotubes is higher than 90 wt.% and the main impurities are Al_2O_3 and Fe_2O_3 with quantity of less than 7 and 3 wt.%, respectively. Detailed information on the nanotube synthesis is available in [1].

The CNTs were synthesized by purpose to contain compact agglomerates in order to enable a safe handling during transport and decanting. The agglomerates are more or less spherical shaped with diameter of between 0.2 and 0.5 mm (Fig. 3.3a).

According to high resolution SEM (HR-SEM, FEI-SFEG, Philips, Netherlands) and transmission electron microscopy (TEM, CM-20, Philips, Netherlands) images, the agglomerates are constituted by free amorphous nanotubes with the length of around 5-20 μm and diameter of about 10-20 nm (Fig. 3.3b and c). Imaging of a nanotube cross section by high resolution electron microscopy (HR-TEM, CM-300, Philips, Netherlands) shows the number of walls is between 5 and 15 (Fig. 3.3d).

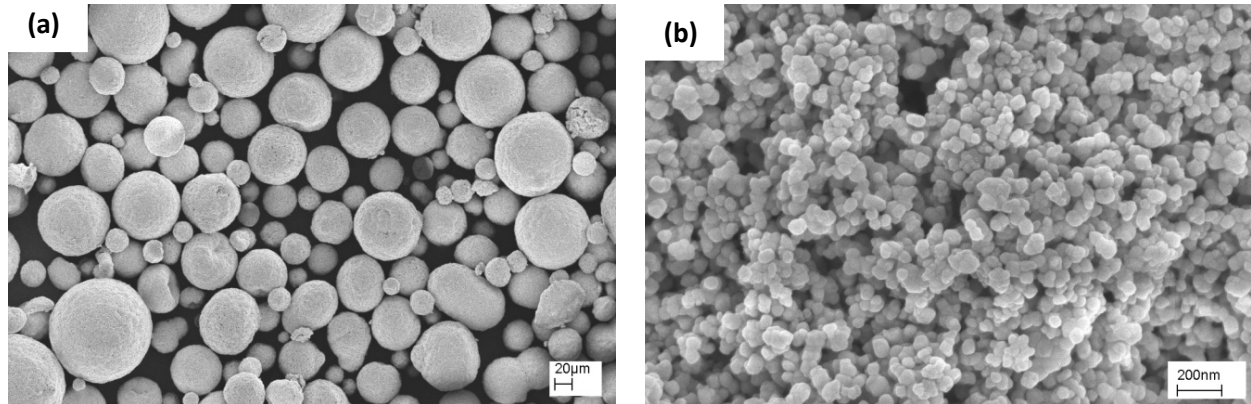


Fig. 3.1. SEM micrographs show the particle morphology of raw 3Y-TZP: (a) spray-dried granules; (b) primary particles

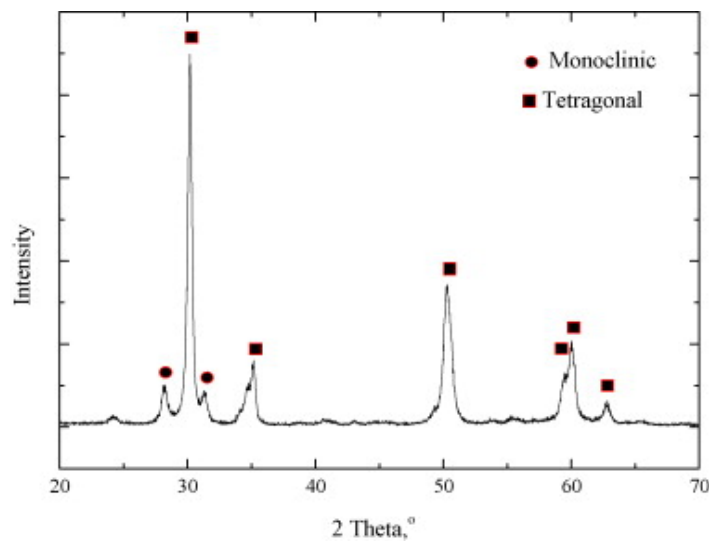


Fig. 3.2. X-ray diffraction pattern of nanocrystalline 3Y-TZP powder.

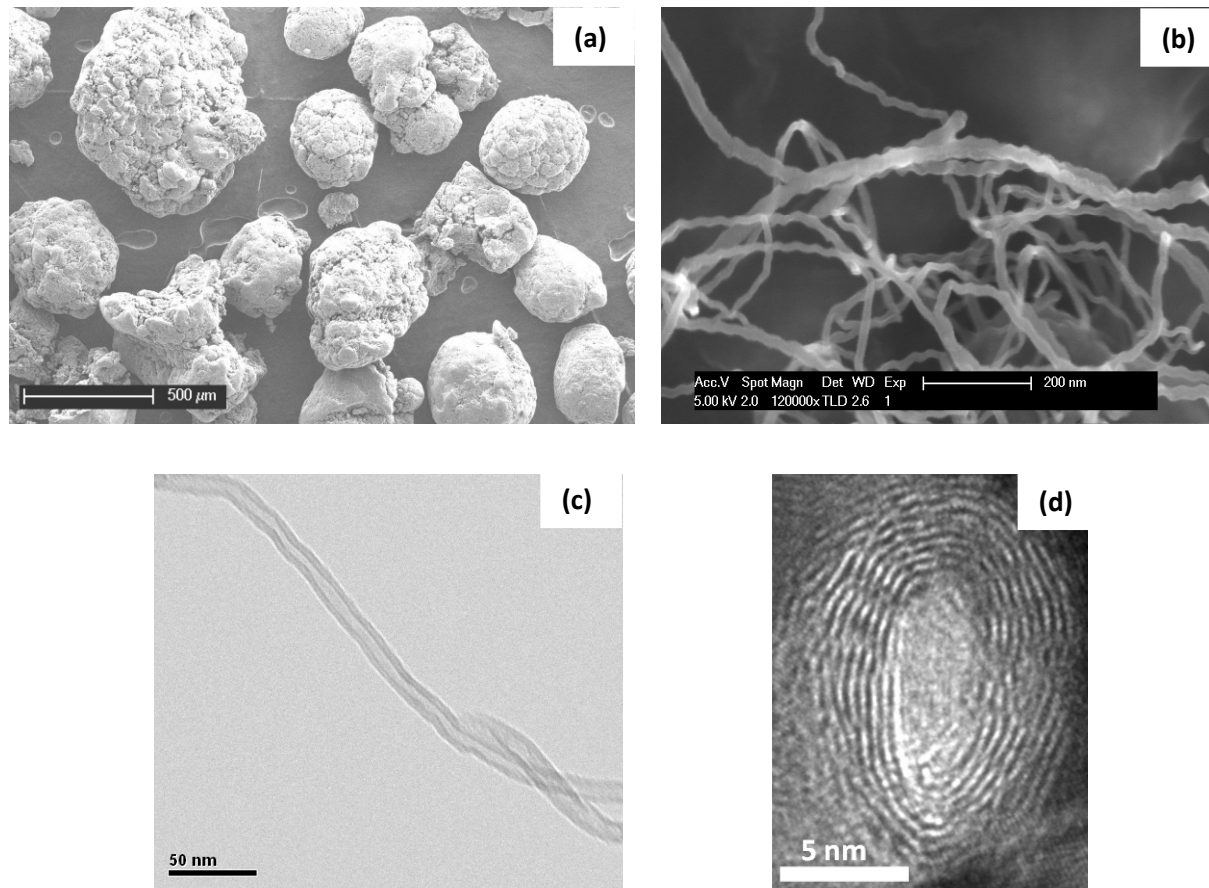


Fig. 3.3. Electron microscopy micrographs of the as-received CNTs: SEM (a), HR-SEM (b), TEM (c) and HR-TEM (d).

Dense samples were obtained by powder metallurgy technique. 3Y-TZP powder with 0, 0.5, 1.5, 3 and 5 wt% CNTs, were mixed by a turbula mixer (Fig. 3.4a) with zirconia balls for 24 hours. The morphology and distribution of the mixtures with variable amount of nanotubes has been analyzed by SEM, and transmission electron microscopy (TEM, CM-20, Philips, Netherlands).

The samples were processed by Spark Plasma Sintering at INSA-Lyon (SPS, FCT GmbH, Germany), Fig. 3.4b, under vacuum (10^{-2} mbar). The temperature was measured by means of an optical pyrometer focused on the upper graphite punch, at about 4 mm from the sample. The SPS was carried out with a fixed heating rate of $50\text{ }^{\circ}\text{C}\cdot\text{min}^{-1}$ under a constant applied pressure of 50 MPa with a soaking time of 2 minutes. The sintering soak temperature depends on the powder composition and varies between 1250 and 1350 $^{\circ}\text{C}$. For monolithic zirconia and composites with a low percentage of CNTs (0, 0.5, 1.5 wt%), 1250 $^{\circ}\text{C}$ was enough to obtain rather

dense (relative density > 98%) specimens. Instead, for composites with 3 and 5 wt% this temperature had to be increased to 1300 and 1350 °C respectively.

The densities of sintered samples were determined by the Archimedes method in deionized water, using an accurate balance (10^{-5} g). The theoretical densities of the composites were calculated according to the rule of mixtures. The density of graphite (2.25 g.cm^{-3}) has been used for MWCNT.

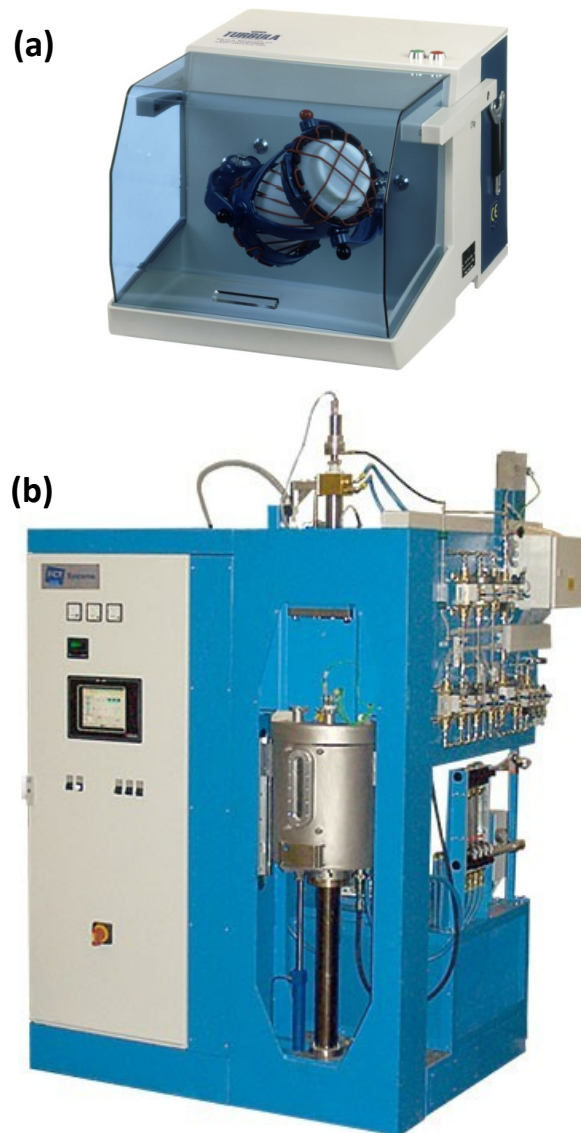


Fig. 3.4. Photo of the (a) turbula mixer and (b) FCT spark plasma sintering furnace at INSA-Lyon.

3.1.2. Monolithic and composite alumina ceramics

Three different types of alumina powders have been used in order to process well-dispersed CNTs-alumina composites; which are:

1) Pure ultra fine commercial α -alumina (TM-DAR); This alumina powder produced by Taimei Chemicals Co. Ltd., Tokyo, Japan, with average particle size around 150 nm was used as raw powder. TM-DAR is considered as the commercially available finest pure α -alumina powder. According to the technical data sheet the purity is higher than 99.99%. The theoretical density, surface area and primary particle size of powder as reported by supplier was 3.98 g cm^{-3} , $14.5 \text{ m}^2 \text{ g}^{-1}$, 150 nm, respectively. Fig. 3.5a. shows the HR-SEM micrograph of the as-received powder.

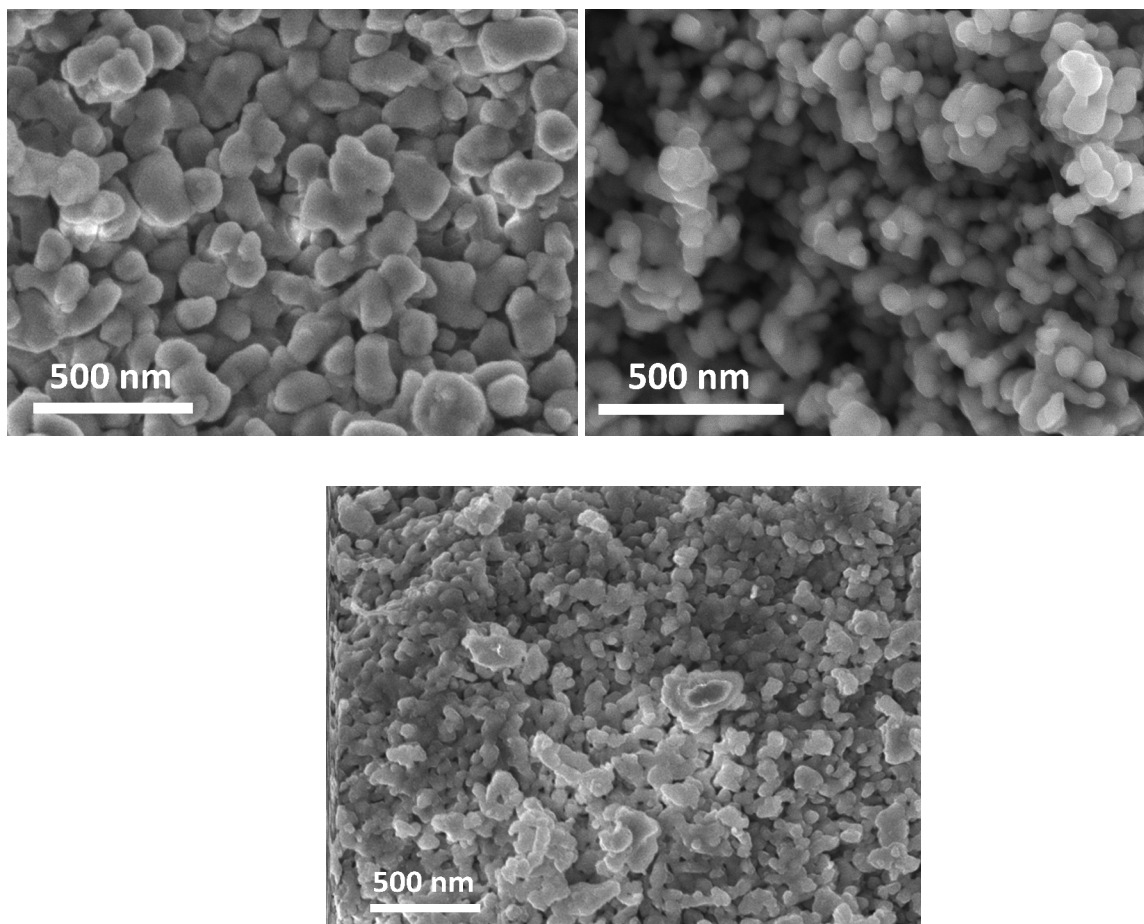


Fig. 3.5. HR-SEM of (a) ultra pure TM-DAR alumina powder, (b) nano size gamma alumina, (c) nano alpha alumina (MK-40).

2) Pure nano size gamma alumina ($\gamma\text{-Al}_2\text{O}_3$); The powder used was a high purity (99.995) $\gamma\text{-Al}_2\text{O}_3$ powder (type CR 125 Baikowski, France) with a specific surface areas of around $100\text{ m}^2/\text{g}$, reported by the producer. The particle size of the powder is around 30 nm and the micrograph of which was shown in Fig. 3.5b.

3) Nano alpha alumina (MK-40); This powder (MKN- $\text{Al}_2\text{O}_3\text{-A040}$, M K Impex Corp., Canada) is less pure ($> 95\%$) than TM-DAR powder. However with average particle size of 40 nm (Fig. 3.5c), which is much finer than TM-DAR. The surface area of the powder has been reported by the producer $\sim 90\text{ m}^2.\text{g}^{-1}$.

Alumina sample processing procedure is very similar to the Zirconia samples (3.2.1). The powders are initially mixed with different amount of CNTs (0.5, 1.5, 3 and 5 wt%) in the turbular mixer for 24 hours. In order to obtain full dense nanostructured composites ($> 98\%$ of theoretical density TD), to retain the alumina grains in submicron-scale and avoid damage of nanotubes, the samples were processed by SPS under vacuum at different sintering temperatures ranging between 1200 to 1400 °C. Density measurements were carried out very similar to what explained for zirconia based composites.

3.1.3. Si_3N_4 based ceramics (SiAlONs)

In this work, SiAlON ceramics were processed with six different sintering aids. The samples were processed in collaboration with Prof. Shen (Arrhenius Laboratory, Stockholm University). Ca- Sialons were produced by addition of CaH_2 or CaO (CaCO_3), which result in Nitrogen- and Oxygen-rich Ca-Sialon respectively. Similarly, YN, Y_3O_2 have been used to produce Nitrogen- and Oxygen- rich Y-Sialons. And addition of YbN, Yb_2O_3 results in Nitrogen- and Oxygen-rich Yb-Sialons, respectively. Details about the phase diagrams and the tie lines used to choose the proper composition of the Sialons can be found in [2-5]. However, Table 3.1, 3.2 and 3.3 shows the composition of starting mixtures and phase assemblages of the samples after of the hot pressing.

Powders of Si_3N_4 (O contamination $< 2.0\%$, UBE, SN-E10, UBE Industries, Tokyo, Japan), AlN (O contamination $< 1.0\%$, H. C. Starck, grade A, ABCR GmbH, Karlsruhe, Germany) and CaH_2 (99.8%, Johnson Matthey Chemicals Ltd., Karlsruhe, Germany), CaCO_3 (99.9%, Merck, Darmstadt, Germany), Y_2O_3 (99.9%, HC Starck-Berlin,

Chapter 3

Germany), Yb_2O_3 (99.9%, Johnson Matthey Chemicals Ltd., Germany), were used as precursors. The oxygen contents in Si_3N_4 and AlN powders corresponded to 2.74 wt% SiO_2 and 1.9 wt% Al_2O_3 , respectively. The powders were mixed in a planetary mill using Si_3N_4 balls in a sealed tank within hexane for 1 h.

Pellets of the mixtures, compacted using a steel die were hot pressed in BN-coated graphite dies in nitrogen atmosphere in a graphite resistance furnace at 2073 K for 4 h under 35 MPa uniaxial pressure. More details about the sintering process, phase assemblages after sintering, characterization, and thermal stability of the phases are presented in [2-4].

Table. 3.1. Composition of the precursor mixtures, the density and phase assemblages of hot pressed nitrogen riched Ca-SiAlON ceramics.

Sample label (Ca[10x]N)	Composition of starting mixtures (wt%)			Density (g.cm ⁻³)	Overall compositions* $\text{Ca}_x\text{Si}_{12-2x}\text{Al}_{2x}\text{N}_{16}$	Phase assemblages (mol%)	
	Si_3N_4	CaH_2	AlN			α -SiAlON	β -SiAlON
Ca2N	95.64	1.47	2.88	3.16	$\text{Ca}_{0.2}\text{Si}_{11.6}\text{Al}_{0.4}\text{N}_{15.53}\text{O}_{0.70}$	62	38
Ca4N	91.38	2.91	5.71	3.16	$\text{Ca}_{0.4}\text{Si}_{11.2}\text{Al}_{0.8}\text{N}_{15.54}\text{O}_{0.69}$	97	3
Ca8N	83.11	5.71	11.18	3.18	$\text{Ca}_{0.8}\text{Si}_{10.4}\text{Al}_{1.6}\text{N}_{15.55}\text{O}_{0.67}$	100	0
Ca16N	67.55	10.96	21.48	3.25	$\text{Ca}_{1.6}\text{Si}_{8.8}\text{Al}_{3.2}\text{N}_{15.57}\text{O}_{0.64}$	100	0

*Starting compositions, taking into account the oxide content in the powders i.e. SiO_2 , Al_2O_3 and CaO on the surface of Si_3N_4 , AlN and CaH_2 , respectively.

Table. 3.2. Composition of the precursor mixtures, the density and phase assemblages of hot pressed nitrogen riched Ca-SiAlON ceramics.

Sample label	Composition of starting mixture (wt%)			Density (g.cm ⁻³)	overall compositions*	Phase assemblages (mol%)	
	Si_3N_4	CaCO_3	AlN			α -SiAlON	β -SiAlON
Ca40	95.64	1.47	2.88	3.16	$\text{Ca}_{0.4}\text{Si}_{11.8}\text{Al}_{1.2}\text{N}_{15.6}\text{O}_{0.4}$	100	0
Ca140	91.38	2.91	5.71	3.16	$\text{Ca}_{1.4}\text{Si}_{7.8}\text{Al}_{4.2}\text{N}_{14.6}\text{O}_{1.4}$	100	0

Table. 3.3. Composition of the precursor mixtures, and phase assemblages of hot pressed nitrogen- and oxygen-riched Y- and Yb-SiAlON ceramics.

N-rich RE-sialon, $RE_xSi_{12-3x}Al_{3x}N_{16}$, RE=Y, Yb; x=0.4		
Sample	Starting powders	Phases
YN04	Si ₃ N ₄ , AlN, YN	α-SiAlON and β-SiAlON (trace)
YbN04	Si ₃ N ₄ , AlN, YbN	α-SiAlON

O-rich RE-sialon, $RE_xSi_{12-3x-1.5x}Al_{3x+1.5x}O_{1.5x}N_{16-1.5x}$, RE=Y, Yb; x=0.4		
Sample	Starting powders	Phases
Y004	Si ₃ N ₄ , AlN, Y ₂ O ₃	α-SiAlON
Yb004	Si ₃ N ₄ , AlN, Yb ₂ O ₃	α-SiAlON

3.2. Microstructural observations

The microstructure studies were performed by high resolution scanning electron microscopy, HR-SEM (FEI-SFEG, Philips, Netherlands), transmission electron microscopy (TEM, CM-20, Philips, Netherlands), and high resolution transmission electron microscopy (HR-TEM, CM-300, Philips, Netherlands).

SEM and HR-SEM were carried out on the fracture surface and polished surface of carbon-coated specimens. The average grain size of the sintered compacts was determined by the linear intercept method on polished surfaces, multiplying by Mendelson factor (1.56) [6]. To observe the grains on the HR-SEM, samples were mechanically polished (with diamond pastes from 1 and up to 0.05 μm), thermally etched at 50 K less than the firing temperature for 30 min in Ar atmosphere and coated with a thin layer of carbon. TEM specimens were tripod polished down to 80 μm and then thinned by ion-milling (Ar+, 4 kV). HR-TEM was made with a field emission gun operating at 200 kV on electron transparent area.

3.3. Sample phase characterization

The amount of stress-induced monoclinic phase on fracture surface of zirconia samples was determined by XRD analysis (Rigaku diffractometer operating with

Chapter 3

mono-chromatized CuK α radiation). The weight fraction of the monoclinic phase, X_m , was calculated using the following equation (Eq. 3.1).

$$X_m = \frac{I(111)_{\bar{m}} + I(111)_m}{I(111)_{\bar{m}} + I(111)_m + I(111)_t} \quad (3.1)$$

Where $I(111)_{\bar{m}}$, $I(111)_m$ and $I(111)_t$ are the integrated intensity from the monoclinic ($\bar{111}$), monoclinic (111), and the tetragonal (111) peaks, respectively.

Raman spectroscopy was used for characterization of the as-received CNTs and spark plasma sintered composite reinforced with 5wt% CNTs. The radiation source was a laser of 514.5 nm wavelength.

3.4. Mechanical and electrical testing

Hardness and fracture toughness measurements were carried out using the indentation method. The tests were carried out with a diamond Vickers indenter under 20 Kg load with a dwell of 20 s on carefully polished surfaces. The hardness (H_v) was calculated from the diagonal length of the indentation determined by SEM observations using the following equation, according to ASTM C1327.

$$H_v = \frac{1.854P}{d^2} \quad (3.2)$$

Where P is the applied load and d is the mean value of the diagonal length.

The fracture toughness was calculated by Antis equation [7]. The crack lengths were measured immediately after indentation using a calibrated optical microscope or SEM. At least ten valid measurements were carried out for each sample and averaged.

Bar ($4 \times 3 \times 30 \text{ mm}^3$) specimens were used for Single Edge V-Notch Beam (SEVNB) fracture toughness measurements using the standard method. The notch preparation was made using a standard procedure [8]. The V-notch width was between 20 and 30 μm . The specimens were bended using 4 point bending fixture with inner and outer span of 10 and 20 mm, respectively.

Shear dynamic modulus of composites with size $1 \times 4 \times 35 \text{ mm}^3$ was measured at room temperature in a free torsion pendulum.

Conventional compressive creep tests (deformation versus time) were performed on specimens with size $3 \times 3 \times 8 \text{ mm}^3$ under vacuum and at constant stress of 6 MPa (comparable with mechanical spectroscopy results) at 1600 K.

Compressive plastic deformation tests of Sialon specimens, under a constant load and as a function of temperature, were performed in Stockholm University, in a spark plasma sintering apparatus, Dr. Sinter 2050, Tokyo, Japan. The initial applied load corresponds to a compressive stress of 40 MPa. The temperature was increased in a ramp of $1 \text{ K}\cdot\text{min}^{-1}$.

The electrical conductivity of composite with size of $2 \times 2 \times 10 \text{ mm}^3$ was measured at room temperature by a four point probe setup using a digital multimeter and DC source.

3.5. Mechanical spectroscopy

A common experimental apparatus, which is used for measuring the mechanical loss in a wide range of temperatures (300-1800 K) and frequencies (10^{-3} to 10 Hz) is the inverted forced pendulum. This installation works in sub-resonant mode. The internal friction measurements can be done in either isochronal (fixed frequency as a function of temperature) or isothermal (as a function of frequency) condition. A schematic of the experimental setup is shown in Fig. 3.6, and an image of the apparatus is shown in Fig. 3.7.

In this apparatus, a sample, which has a rectangular shape ($4 \times 1 \text{ mm}^2$ and a variable length), is clamped on the pendulum rod. The lower rod is fixed to the bottom of pendulum, and the top part is suspended with a thin tungsten wire. The wire is connected to a double balance system for thermal expansion accommodation. The rod and sample weight are equilibrated by a counterweights. Two Helmholtz coils and a permanent magnet, which are fixed on the upper part of rod, applied torsional vibration. The oscillations are detected by a laser, mirror and photo-detector device. The mirror is fixed on the rod above the sample and the photo-detector is fixed on a translation stage that corrects the static drift of the laser spot due to plastic deformation of the sample. A tubular furnace surrounds the sample. The whole

Chapter 3

parts of system (laser and photo-detector) are set under vacuum of 10^{-5} using a rotary pump and a secondary oil diffusion pump. The external induced vibrations are prevented via a pneumatic damping frame which the pendulum mounted on it. The excitation signal is obtained via a frequency response analyzer (Schlumberger-Solatron 1250) which is used as a signal generator and two channel analyzer for measuring the phase lag and the ration between the excitation signal and the strain signal. The generated sinusoidal signal is applied to the Helmholtz coils and the response is detected by the photo-detector. The heating system consists of a Eurotherm 903 P (PID), which controls a power supply Hewllet Packard 6030 A and a thermocouple Pt/RhPt (type S) placed on the furnace inner wall to read the temperature close to the specimen. The length of the tubular furnace insures a low thermal gradient along the specimen. All components are connected to a Dell Dimension DV051 Intel(R) personal computer (PC) with a Labview software, which controls the measurements and experimental data acquisition.

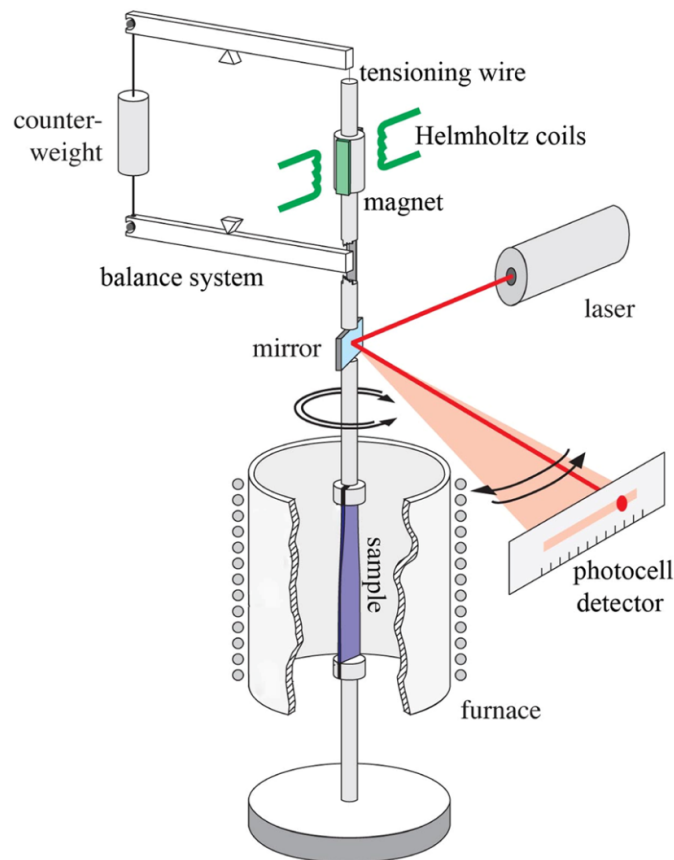


Fig. 3.6. Sketch of the simple inverted torsion-pendulum.

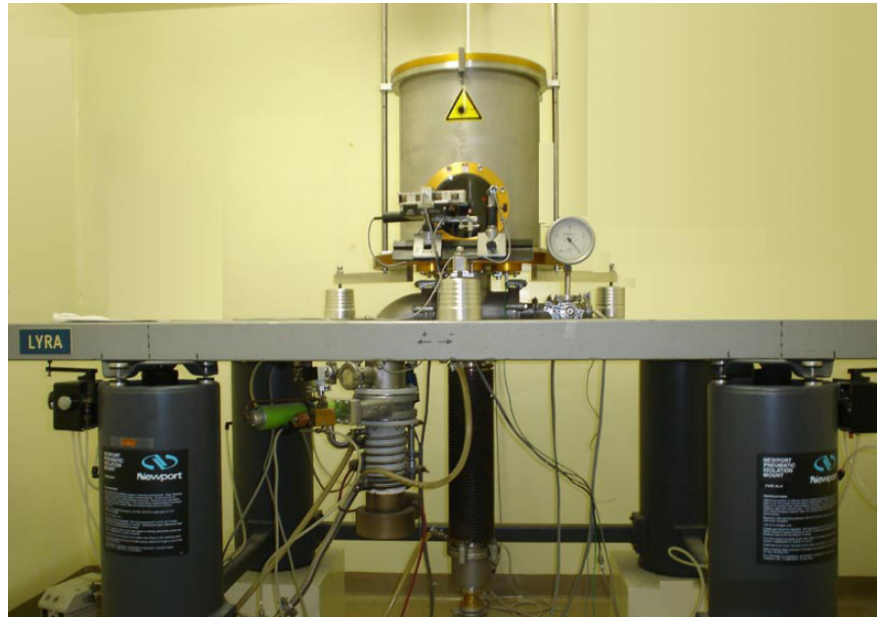


Fig. 3.7. Photo of the mechanical spectroscopy experimental installation.

References

- [1] <http://www.graphistrength.com>.
- [2] Y. Cai, M. Nygren, Z. Shen, J. Grins, S. Esmailzadeh, Thermal properties of the nitrogen-rich Ca-Sialons, *Journal of the European Ceramic Society* 29 (16) (2009) 3409-3417.
- [3] Y. Cai, Z. Shen, J. Grins, S. Esmailzadeh, Sialon Ceramics Prepared by Using CaH₂ as a Sintering Additive, *Journal of the American Ceramic Society* 91 (9) (2008) 2997-3004.
- [4] Y. Cai, Z. Shen, J. Grins, S. Esmailzadeh, T. Höche, Self-Reinforced Nitrogen-Rich Calcium-SIALON Ceramics, *Journal of the American Ceramic Society* 90 (2) (2007) 608-613.
- [5] Y. Cai, Z. Shen, T. Höche, J. Grins, S. Esmailzadeh, Superplastic deformation of nitrogen-rich Ca-sialon ceramics, *Materials Science and Engineering A* 475 (1-2) (2008) 81-86.
- [6] M.I. Mendelson, Average grain size in polycrystalline ceramics, *Journal of the American Ceramic Society* 52 (8) (1969) 443-446.
- [7] G. Anstis, P. Chantikul, B. Lawn, D.B. Marshall, A Critical-Evaluation of Indentation Techniques for Measuring Fracture-Toughness .1. Direct Crack Measurements *Materials*, *Journal of the American Ceramic Society* 64 (9) (1981) 533-538.
- [8] J. Kubler, Fracture Toughness of Ceramics using the SEVNB Method: From a Preliminary Study to a Standard Test Method, in: J.A. Salem, G.D. Quinn, M.G. Jenkins (Eds.) *Fracture resistance testing of monolithic and composite brittle*, American Society for Testing and Materials, West Conshohocken, Pennsylvania, 2002, pp. 93-106.

Chapter 4

Experimental results and analysis:

Silicon nitride based ceramics (Sialons)

The composition, volume fraction, and distribution of the residual glassy phases are crucial for determining the thermal, and mechanical properties of Si_3N_4 based ceramics. Mechanical spectroscopy can be used as a non-destructive method to analyze the behavior of the residual glassy phase either as GB glassy films or glass pockets located in the triple GB junctions. This method can be used as a complementary technique to demonstrate the presence of glassy phases, which cannot be realized by other techniques such as TEM, XRD. In this chapter, mechanical spectroscopy is used in order to characterize the residual glassy phase, present after sintering in different grades of nitrogen- and oxygen-rich Sialon ceramics. The effect of the microstructure on the height of the relaxation peak, namely the effect of equiaxed versus elongated grains, and the effect of the quantity of the glassy phase have been studied. A rheological model of the material including an anelastic relaxation in the glassy phase and high temperature GB sliding is presented. In order to obtain a relation between the anelastic deformation determined by mechanical spectroscopy measurements and plastic deformation, compressive deformation tests were conducted in a SPS apparatus.

4.1. Results obtained in nitrogen- and oxygen-rich Y- and Yb-Sialon ceramics

The mechanical-loss spectrum of the nitrogen- and oxygen-rich Y-Sialon specimens, called YN04, YO04, and nitrogen- and oxygen-rich Yb-Sialon, called YbNO4, YbO04, are represented in this part. The specimen overall compositions and phase assemblages were presented in Table 3.3.

Fig. 4.1 demonstrates the typical spectrum (mechanical loss and shear modulus as a function of temperature) through heating and cooling of YO04 sample at a frequency of 1 Hz. During the heating stage, the mechanical loss spectrum is mainly composed of a mechanical loss peak that occurs around 1280 K, and this peak is superimposed on an exponential increase in damping at higher temperature, while the modulus decreases. After heating up to 1450 K, upon cooling the peak has disappeared and the level of internal friction background at high temperature is low.

Fig. 4.2 shows the microstructure of YO04 sample in the as-received condition after sintering, which displays a large amount of glassy phase at triple junctions. Annealing at high temperatures probably resulted in the crystallization of the glassy phase and consequently in the peak disappearance (Fig. 4.1). A relaxation peak is due to an anelastic strain, in which a restoring force limits this strain. In the case of Si_3N_4 based ceramics, this restoring force comes from the adjacent grains, which limit molecular mobility in the glassy phase at temperature higher than the glass transition temperature [1, 2].

It was found that pure Sialon glass spectrum does not exhibit a relaxation peak, because there is no restoring force and anelastic strain increase without any limitation. It means that, three parameters are effective in the occurrence of the peak: the composition of the glassy phase (in position of the peak), the restoring force, and the content of glassy phase (in amplitude of the peak). For instance, Fig. 4.3 compares the mechanical spectra of YO04 and YN04 as a function of temperature. The YN04 peak is located at a temperature around 100 K lower than the YO04 peak. The different composition of glassy phases in YN04 and YO04 due to the change of the N/O ratio may affect the peak behavior [3]. The lower height of the peak in the case of YN04 can be attributed to the lower quantity of glassy phase in the microstructure.

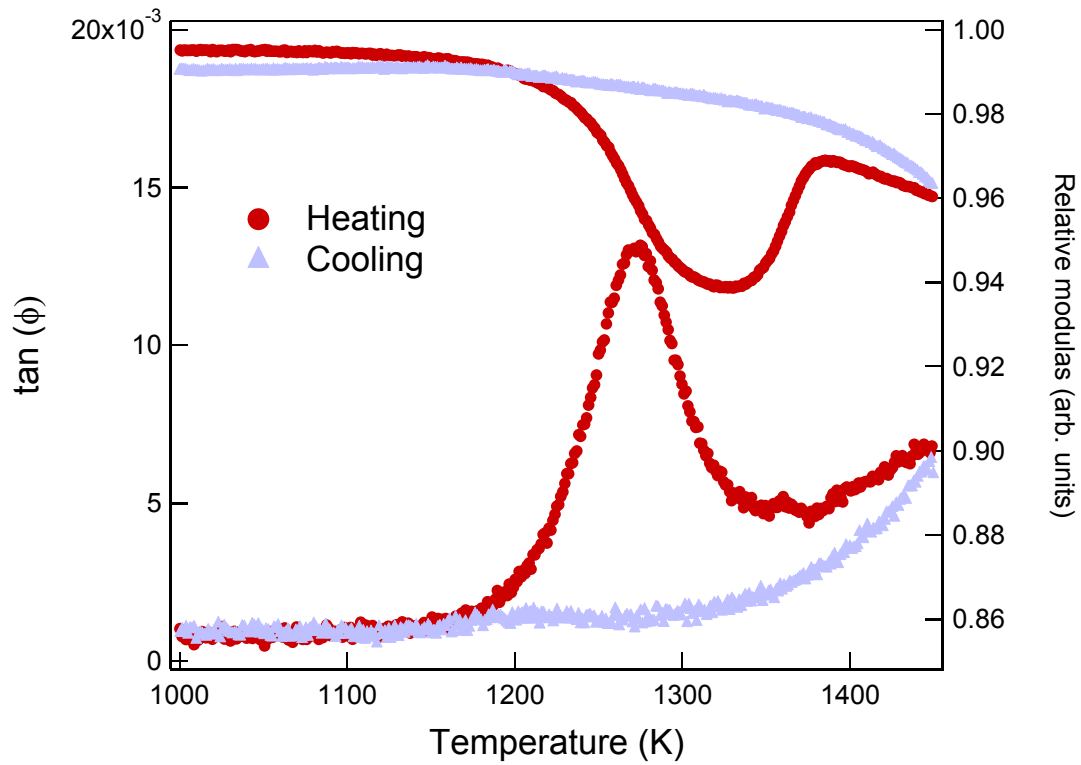


Fig. 4.1. Mechanical loss spectrum of Y004 during heating and cooling (after annealing at 1450 K).

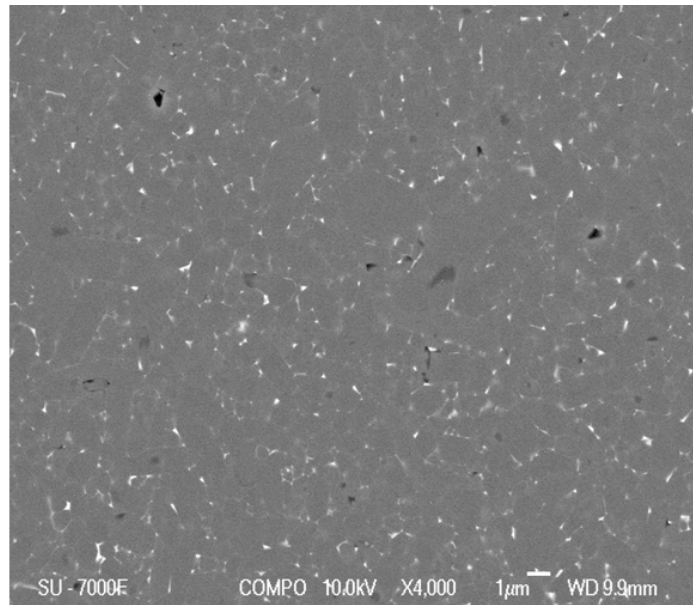


Fig. 4.2. SEM of Y004. One observes the equiaxed grains and lot amount of glassy phase pockets which located between the grains (white phase in image).

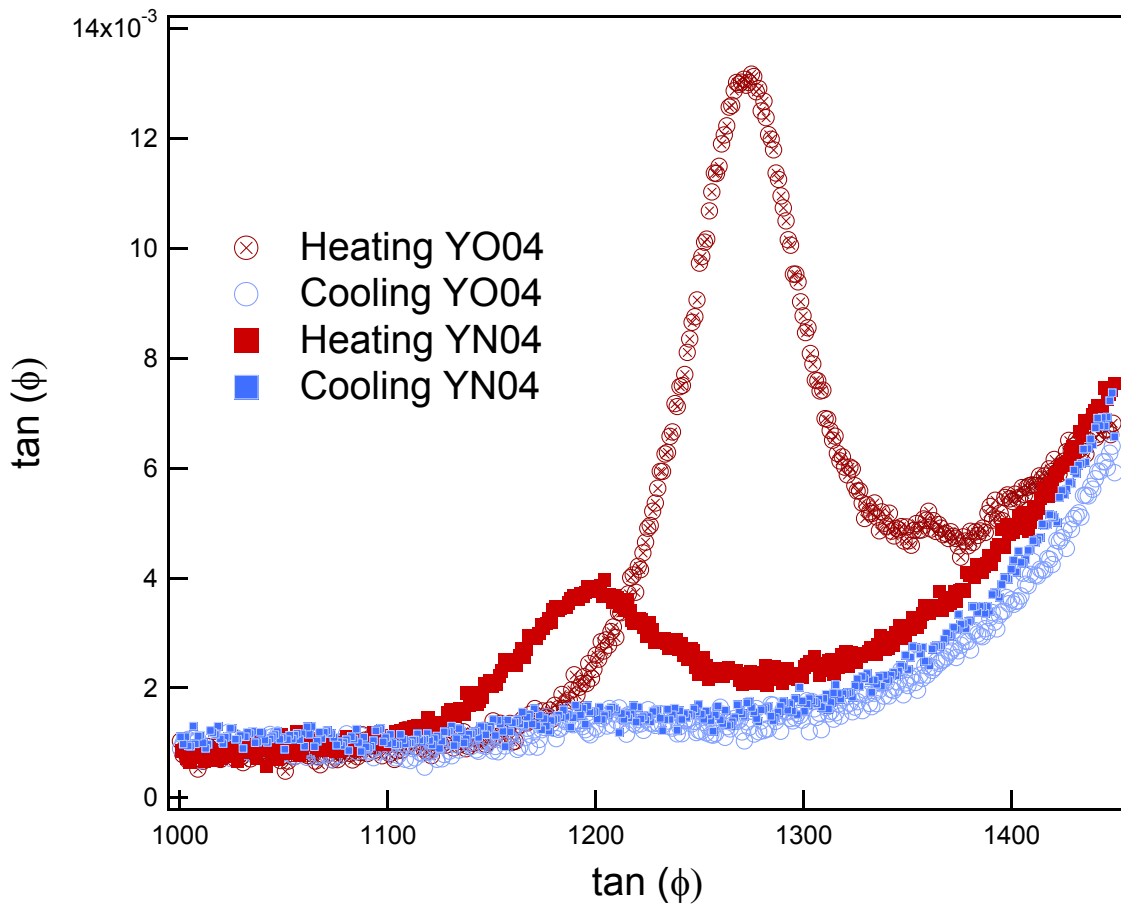


Fig. 4.3. Mechanical loss spectrum of YO04 and YN04 during cooling and after annealing at 1450 K. The position and height of the peak are related to chemistry of glassy phase and quantity of glassy phase.

Fig 4.4 and 4.5 represent the mechanical loss spectrum of Yb_2O_3 and YbN , compared to Y_2O_3 and YN , respectively. As observed in this figure, the spectrum of samples with Yb additive, for both oxygen and nitrogen rich states, suppresses the peak.

The level of high temperature background in $\text{Yb}_2\text{O}_3/\text{YbN}$ samples is lower than $\text{Y}_2\text{O}_3/\text{YN}$ ones. Such a behavior is related to the very low content of glassy phase, together with the presence of elongated grains. Also, according to the literature, a powerful strategy to improve the high temperature performance of silicon nitride based ceramics is replacing glass-forming refractory oxides, with oxides such as Yb_2O_3 as sintering aids. The results of high temperature compressive deformation (in SPS apparatus) of $\text{Yb}_2\text{O}_3/\text{YbN}$ and $\text{Y}_2\text{O}_3/\text{YN}$ samples show a similar trend. The onset of deformation for $\text{Yb}_2\text{O}_3/\text{YbN}$ is reported to be at 1580/1594 °C, while this value for $\text{Y}_2\text{O}_3/\text{YN}$ is 1543/1576 °C [4].

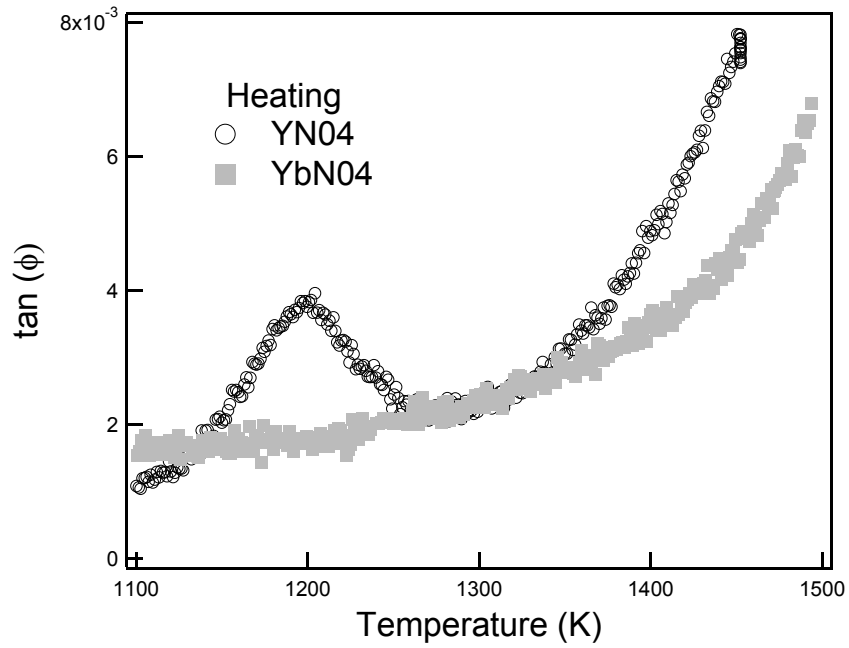


Fig. 4.4. The mechanical loss spectrum YN04 and YbN04.

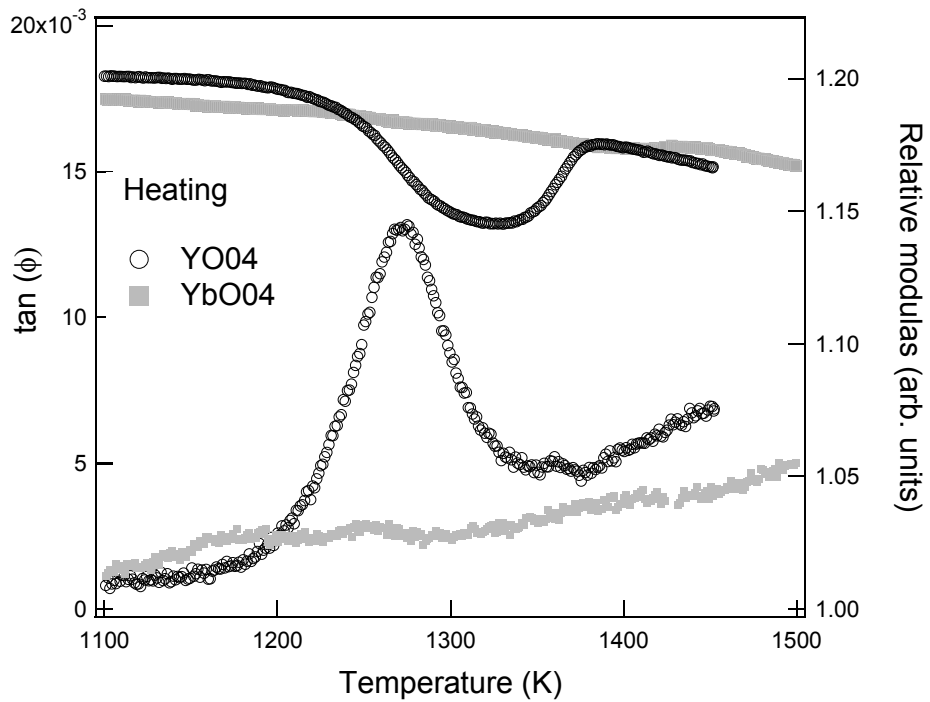


Fig. 4.5. The mechanical loss spectrum YO04 YbO04.

4. 2. Results obtained in Ca-Sialons

The mechanical-loss spectrum of the oxygen-rich Ca-Sialon samples, called Ca4O and Ca14O (Table 3.2), and nitrogen rich Ca-Sialon specimens, named Ca2N, Ca4N, Ca8N and Ca16N in Table 3.1 are represented in this part. The specimen overall compositions and phase assemblages were presented in Table 3.1 and Table 3.2.

4.2.1. Oxygen rich Ca-Sialon

Mechanical spectroscopy results of as-sintered oxygen rich Ca- Sialon samples with different raw mixture of powders (Table 3.2) are compared in Fig. 4.6. The mechanical loss spectrum of Ca4O and Ca14O are very similar to the general behavior of other Sialons. At temperatures lower than 1100 K, however, the mechanical loss is very low. Above 1100 K, the mechanical loss increases and shows a peak at 1160 (for Ca4O) and 1200 K (for Ca14O).

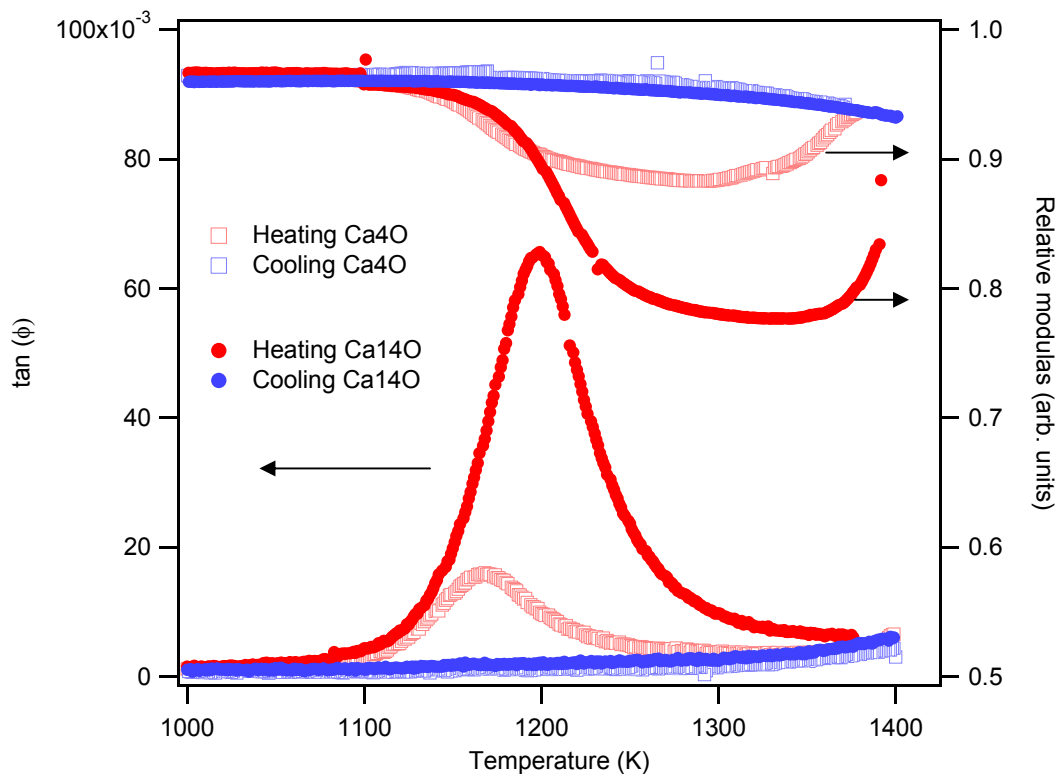


Fig. 4.6. The mechanical loss spectrum Ca4O and Ca14O (a) as a function of temperature ($f=1$).

This comparison shows a clear effect of various Ca content (x-value, see table 3.1) on the peak height and position. The lower height of the peak in the case of Ca40 in comparison with Ca140 can be attributed to the lower quantity of glassy phase in the microstructure.

4.2.2. Nitrogen rich CaSialon

Fig. 4.7 shows the typical spectrum, i.e. mechanical loss and shear modulus as a function of temperature, upon heating and cooling of the Ca2N sample at a frequency of 1 Hz between room temperature and 1600 K. Upon heating, the mechanical loss spectrum is primarily composed of a mechanical loss peak, which is superimposed on an exponential increase (background) in damping. A step modulus decrease is observed in correspondence with the high temperature exponential background. The peak appears at a temperature of 1110 K for the frequency of 1 Hz and is accompanied by a relative modulus change of about 6%. Above the peak (in the range 1210-1290 K), a modulus recovery is observed, probably due to recrystallization of glassy pockets. It practically compensates the entire drop observed at the peak.

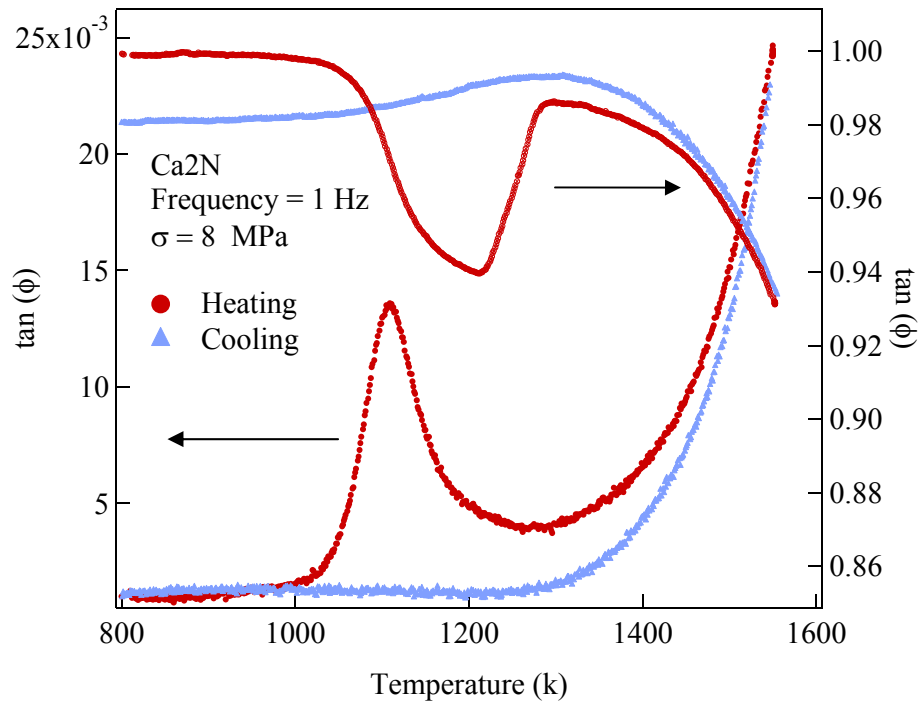


Fig. 4.7. Mechanical loss spectrum and shear modulus of Ca2N during heating (as sintered) and cooling (after annealing at 1600K for 1h) as a function of temperature.

Chapter 4

As shown in Fig. 4.8, the peak and the associated modulus drop also appear in frequency scan measurements (isothermal measurements between 1025 K and 1125 K). The peak shifts in frequency when the temperature of isothermal measurements is changed, which means that it is due to a thermally activated relaxation.

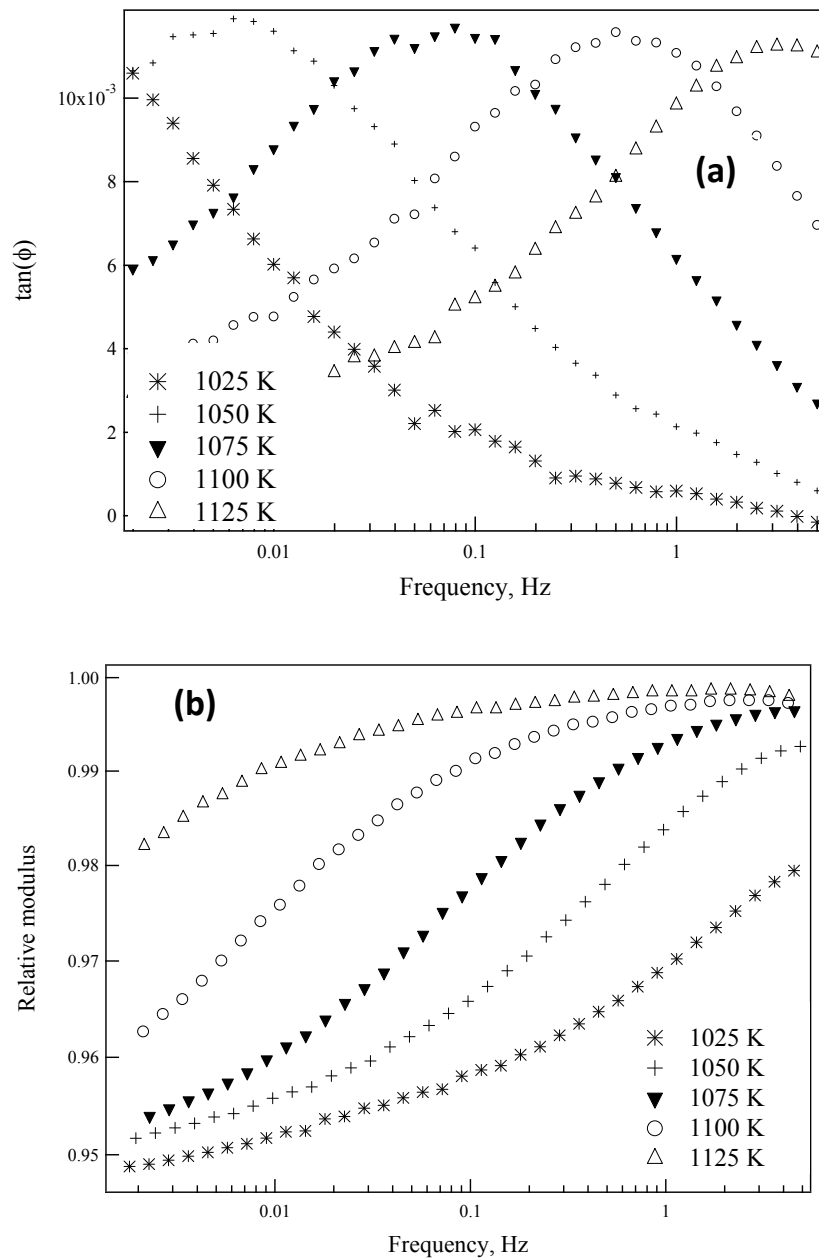


Fig. 4.8. Shift of the mechanical loss peak (a) and of the elastic shear modulus (b) by changing the temperature in frequency scan measurements.

An Arrhenius plot of \log (peak frequency) versus T^{-1} (where T is the absolute temperature of isothermal measurement) can be obtained. For the sample Ca₂N, this linear behaviour is shown in Fig. 4.9 and the relaxation parameters are obtained from the slope of the fit line and from the Y-axis intercept. The activation energy was $E_{act} = 810 \text{ kJ mol}^{-1}$ and the relaxation limit time was $\tau_0 = 2 \times 10^{-40} \text{ s}$. These values are rather unusual and they have to be considered as apparent values [5, 6].

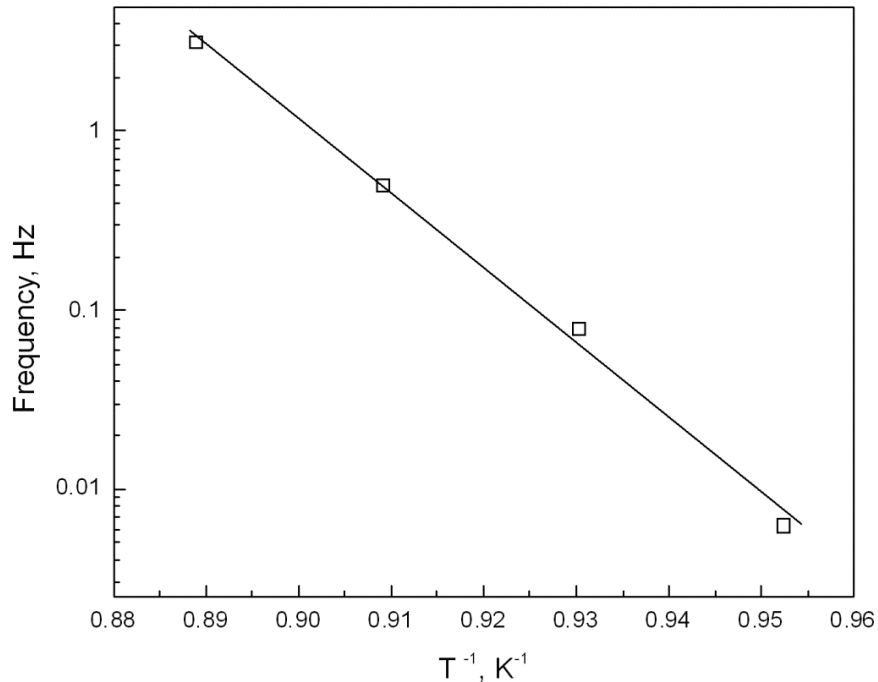


Fig. 4.9. Arrhenius plot of temperature peak shift in as a function of frequency (Fig. 4.8a). From this plot the activation energy and the relaxation time limit τ_0 were calculated as $E_{act} = 810 \text{ kJ mol}^{-1}$ and $\tau_0 = 2.10^{-40} \text{ s}$, respectively.

The relaxation peak found in the past in different YSialon system exhibited characteristics (apparent activation energy and high attempt frequency) similar to the relaxation that characterizes Y-Sialon glass [5, 6], so proving that the peak around the glass transition temperature is due to the α -relaxation in the glassy phase. The present mechanical loss peak (e.g. shown in Fig. 4.7) owns all the characteristics found in the past in YSialon ceramics. The activation energy is apparent with a limit relaxation time of $2 \times 10^{-40} \text{ s}$. The modulus drop corresponding to the peak recovers almost completely and in an irreversible manner. The temperature of the peak at 1 Hz is lower (1100 K with respect to 1270 K) which justifies a lower activation energy (810 kJ.mol^{-1} against 1170 kJ.mol^{-1}) with the same attempt frequency.

Chapter 4

Upon cooling (Fig. 4.7), after dwelling for 1h at 1600 K, the mechanical loss peak and the modulus anomaly disappear and the high temperature mechanical loss background is lower than in the as-sintered sample. The features observed in the first heating are irreversibly lost in the next heating.

A stable and reversible exponential background and the corresponding decrease in shear modulus are then observed above 1300 K (Fig. 4.7). They may be attributed to extensive GB sliding. When the temperature raises enough, the thin films between grains also undergo a glass transition and the grains can slide for longer distances. This phenomenon would finally result in a high temperature plastic deformation (onset of creep). The appearance of an exponential background at low stresses, for instance 8 MPa in this work, and at temperatures below the onset of creep, can be interpreted as a micro-creep mechanism. According to Pezzotti et al. [7, 8], the exponential background could be also the low temperature shoulder of a peak due to GB relaxation for which the maximum is located at higher temperatures. For instance, in high purity silicon nitride specimens, these authors observed a peak at about 1900 K and they interpreted this peak as a GB relaxation peak [7, 8].

Mechanical spectroscopy results of as-sintered nitrogen rich Ca- Sialon samples with different raw mixture of powders (Table 3.1) are compared in Fig. 4.10. In general, the mechanical loss spectrum of Ca4N, Ca8N and Ca 16N are very similar to that of Ca2N in Fig. 4.7. At temperatures lower than 1000 K, however, the mechanical loss is very low. Above 1000 K, the mechanical loss increases and shows a peak at temperatures between 1110 (for Ca2N) and 1142 K (for Ca8N), depending on the sample. This comparison shows a clear effect of various Ca content (x-value).

Table 4.1 summarizes the characteristics of the mechanical loss peak (peak height and temperature) for different samples measured at 1 Hz. Excluding sample Ca16N, the peak height depends on the Ca content.

Fig. 4.11 shows secondary electron SEM micrograph of fractured surface of the samples Ca2N, Ca4N, Ca8N and Ca16N. In general, coarser grain microstructures are formed with increasing x-value. Based on the phase composition of samples represented in Table 4.1, Ca2N sample is dual-phase, i.e. consisting of 62 mol% α -Sialon and 38 mol% β -Sialon, and the remaining samples are single phase or almost single phase consisting of more than 97 mol% α -Sialon [9]. The dual-phase sample Ca2N shows a bimodal microstructure (Fig. 4. 11a) consisting of elongated β -Sialon grains embedded in a matrix of small equiaxed grains of α -Sialon. As shown in Fig. 4.11, the single α -Sialon phase sample with low calcium contents, e.g. Ca4N, shows a

fine equiaxed grain microstructure. On the other hand, in the samples with x-value higher than 0.4, the quantity and aspect ratio of elongated α -Sialon grains increases with increasing x-value.

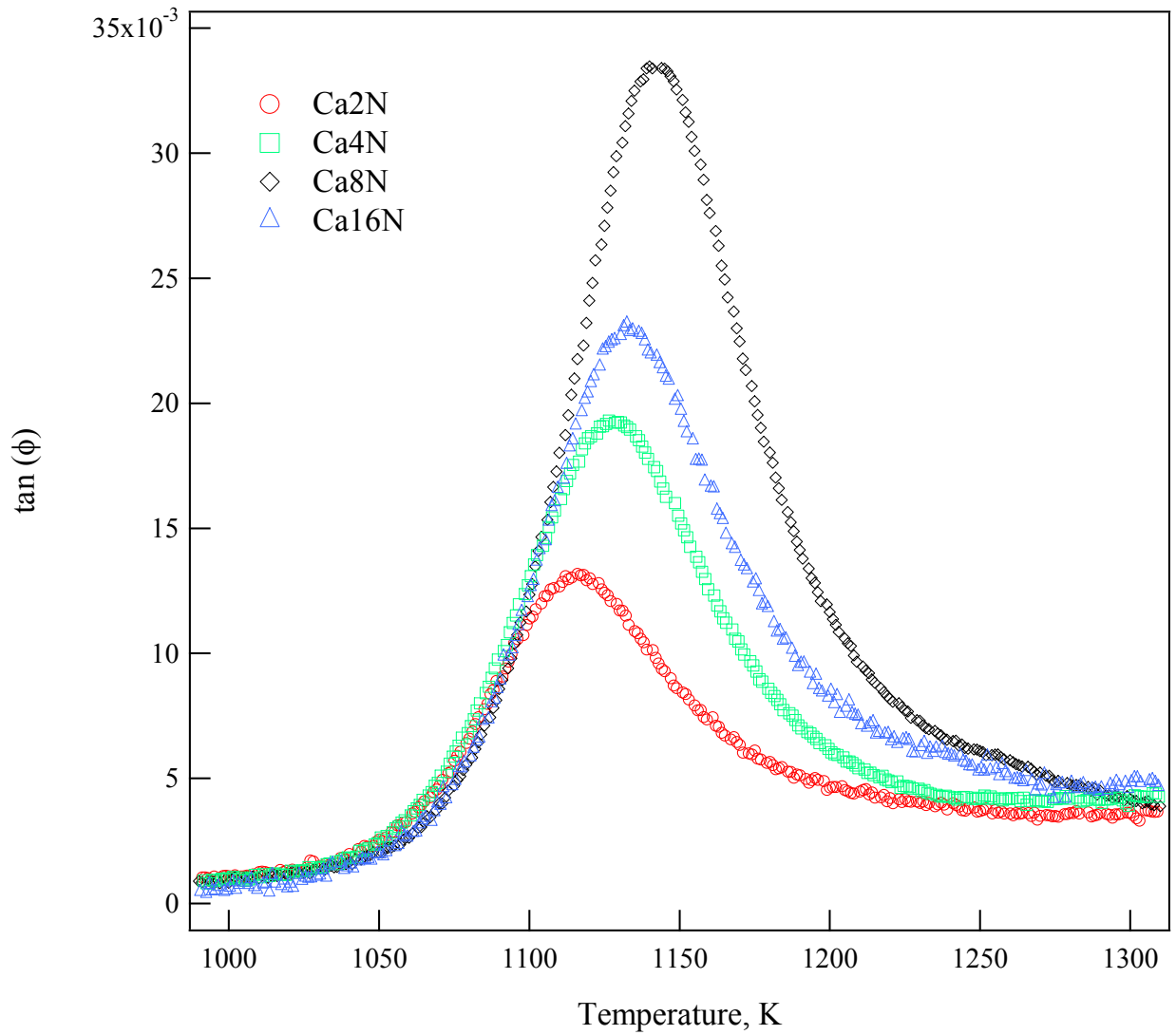


Fig. 4.10. Mechanical loss spectrum of as sintered samples, Ca₂N, Ca₄N, Ca₈N and Ca₁₆N, upon heating in temperature range 1000-1300 K and f=1 Hz.

Chapter 4

Table 4.1. Characterization of internal friction peak measured at 1 Hz for different Ca-Sialon samples.

Sample label	Peak position, K	Peak height/ 10^{-3}
Ca2N	1110	13.5
Ca4N	1133	23.8
Ca8N	1142	34.3
Ca16N	1125	19.6

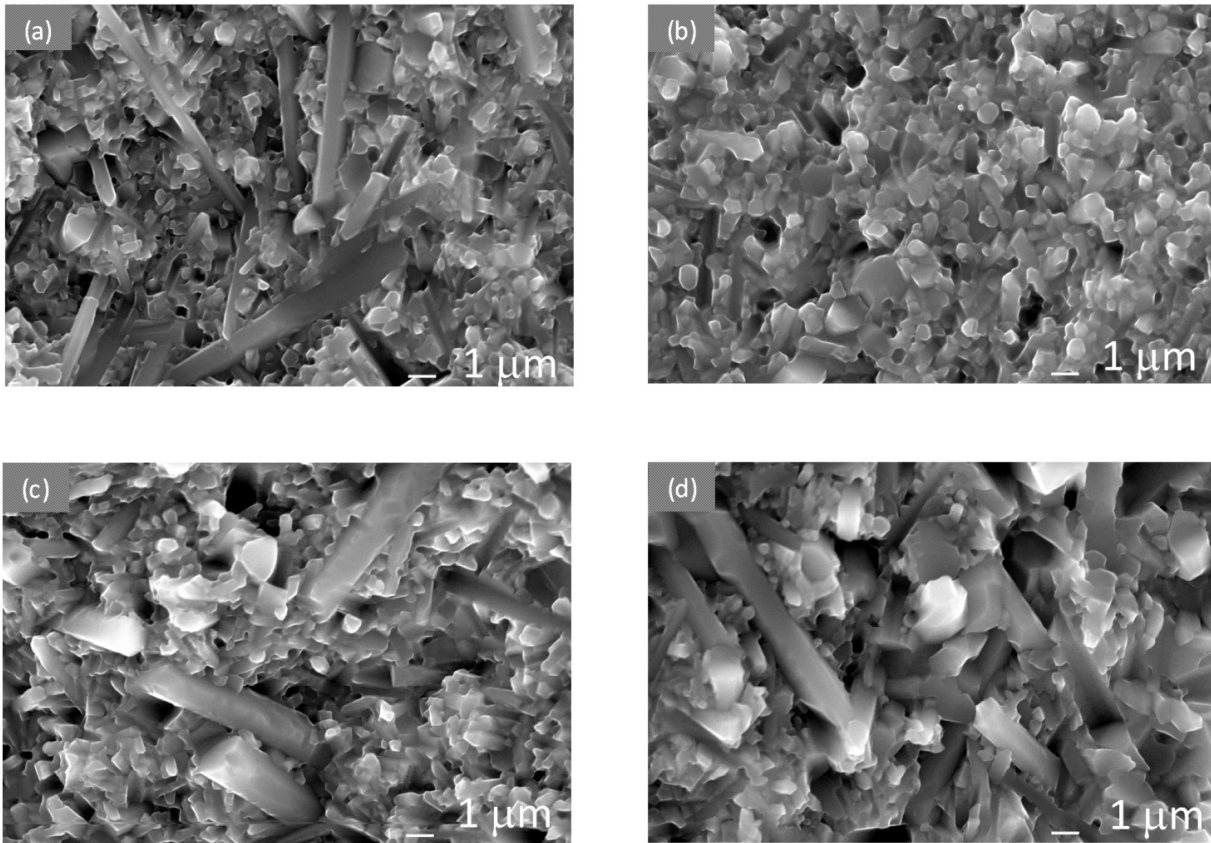


Fig. 4. 11. Scanning electron micrographs showing the fractured surfaces of Ca2N (a), Ca4N (b), Ca8N (c) and Ca16N (d) samples.

Coarse microstructures and the presence of elongated grains in the samples of Ca₄N, Ca₈N and Ca₁₆N appear more evident in the micrographs taken on polished and etched surface as shown in Fig. 4.12 (a-d). To determine the aspect ratio of grains, a statistical analysis of SEM images is presented in Fig. 4.13. The average of grain aspect ratios and the amount of elongated grains (grains with aspect ratio of higher than 5 was considered as elongated) are displayed in this graph. This analysis proves that the aspect ratio and the amount of elongated grains (for each sample 500 grains are counted) increase with Ca content or x-value.

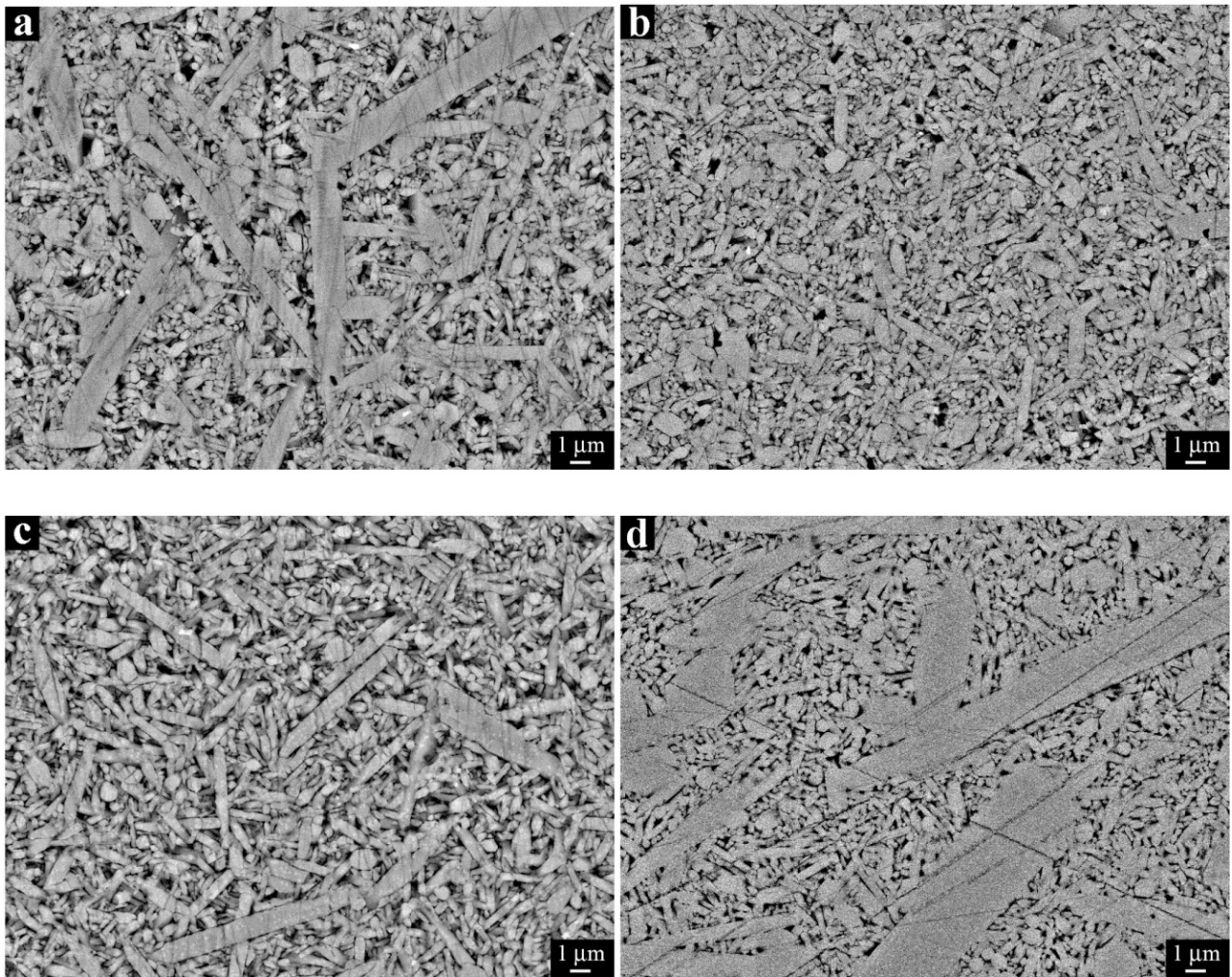


Fig. 4.12. Polished and chemically etched surface of samples Ca₂N(a), Ca₄N (b), Ca₈N (c) and Ca₁₆N (d). The quantity and aspect ratio of elongated α -Sialon grains increases with increasing of x-value (Fig. 4.13).

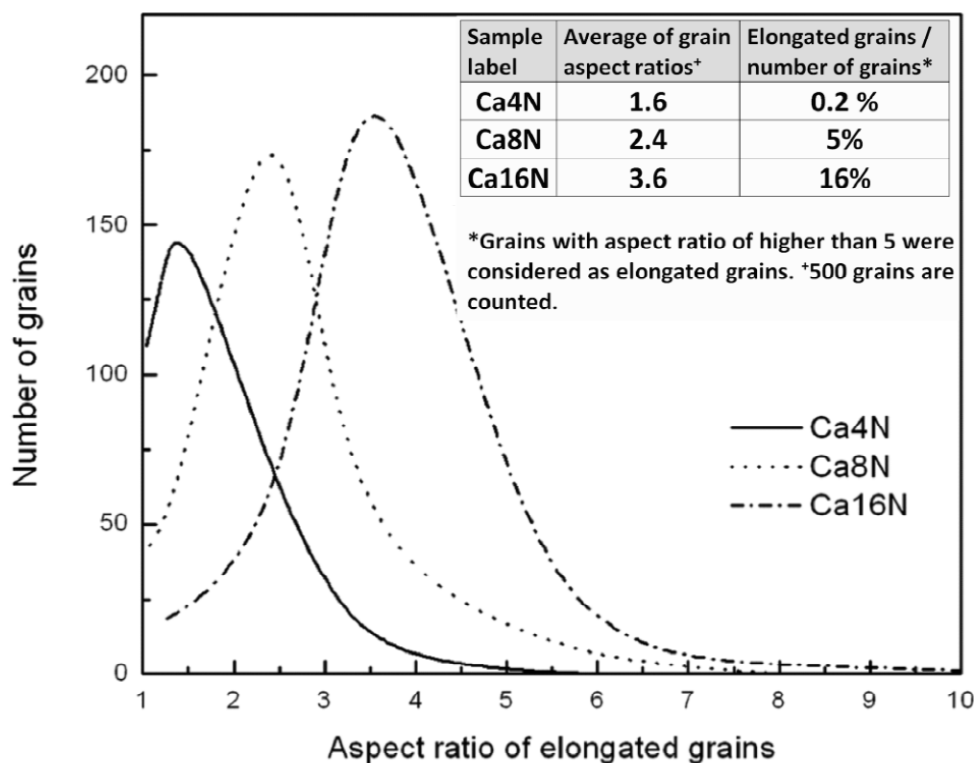


Fig. 4.13. Distribution of grain aspect ratios for Ca- α -Sialon samples obtained from statistical analysis of SEM images.

Fig. 4.14 represents the compressive plastic deformation curves of the samples Ca4N, Ca8N and Ca16N recorded up to 2030 K. As shown, the onset deformation temperature for these three samples are very close to each other, i.e. it appears at \sim 1800 K. However, it is obvious that sample Ca4N starts to deform at higher temperatures in comparison with the other samples. At 1973 K, the deformation strain of the samples Ca4N, Ca8N and Ca16N have been found to be 18, 27 and 23%, respectively.

Although the formation of dense Sialons without a glassy phase can be predicted theoretically, since Sialons are able to accommodate aluminum and oxygen atoms into their crystal structure, an intergranular glassy phase or glass pockets in triple junctions are always found in Sialon ceramics [10]. However, the quantification of such a glassy phase is a point of controversy. Our samples show the presence of a glassy phase (Fig. 4. 15). TEM observations in the present system (nitrogen rich Ca- α -Sialons) for low x-values (low Ca content) show a very low amount of glassy phase in the triple junctions, whereas for high x-values more glassy phase in the boundaries and pockets in triple junctions are found. EELS analysis of the glassy

phase indicates high oxygen and calcium contents at triple junctions [11]. The first conclusion we can draw is that the present mechanical loss peak should be attributed to the presence of a glass phase in the form of pockets or films at grain boundaries. Moreover, it looks clear that for samples Ca₂N, Ca₄N and Ca₈N the amplitude of the peak is proportional to the Ca content (x-value).

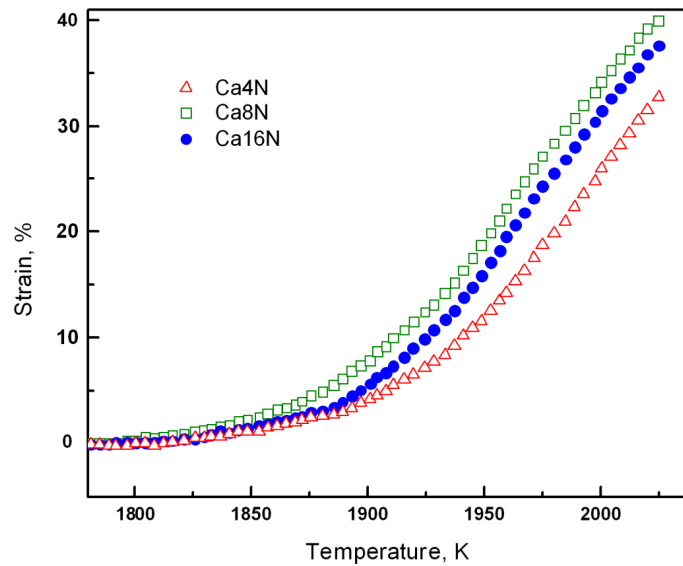


Fig. 4.14. Compressive deformation of nitrogen rich Ca- α -Sialon measured in a spark plasma sintering apparatus by continuously heating the samples.

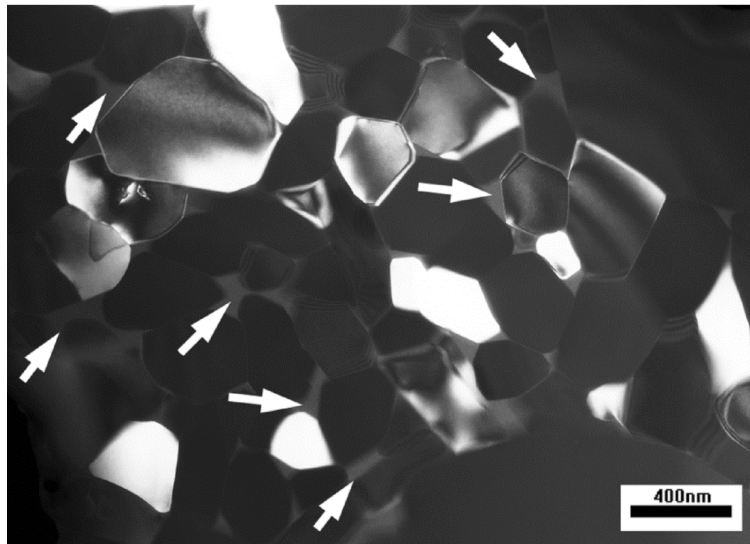


Fig. 4. 15. TEM image of the Ca- α -Sialon ($x = 2.0$), shows the presence of residual glassy phase at triple junctions. The arrows indicate the glassy phase pockets.

4.3. Analysis of the Ca-Sialons spectrum and theoretical model

One can consider the Sialon ceramics as a two phase material:

Phase1 is a polycrystalline Sialon separated by an intergranular viscous layer (glassy phase located in grain boundaries) with volume fraction V_1 . Phase2 is a Sialon pure glass (glassy phase located in triple point of grains) with volume percentage V_2 . Imagine that any mixture (V_1 and V_2) of the abovementioned phases is possible. This hypothesis allows us to study the damping behavior in pure glass ($V_1=0$ and $V_2=1$), in polycrystalline Sialon with glassy phase located between the grains, without glassy pockets ($V_1=1$ and $V_2=0$) and finally in a real Sialon ceramic (mixture of both phases, $V_1+V_2=1$).

1. Analysis of pure glass ($V_1=0$): A glass (or any amorphous material) which is submitted to a cyclic stress in the temperature range of the glass transition (T_g), undergoes the so called α -relaxation. The α -relaxation can be attributed to the onset of a thermally activated long range molecular movement. It is characterized by a mechanical loss peak [2]. On the other hand, suppose that, as the temperature increases, the viscosity of bulk glass drops enough ($<10^{12}$ Pa.s) to allow for unlimited movement of glass molecules (flow). The Newtonian viscosity, η of a glass or fluid is then defined as:

$$\eta = \frac{\sigma}{\dot{\epsilon}} \quad (4.1)$$

where σ is the applied stress and $\dot{\epsilon}$ the strain rate.

Considering the liquid state, i.e. the glass in the iso-configurational state, the viscosity can be described by an Arrhenius law:

$$\eta = \eta_0 \cdot \exp\left(\frac{\Delta H_{act}}{RT}\right) \quad (4.2)$$

The evolution of the viscosity of a glass with temperature (T) at temperatures higher than T_g and below the melting point can be defined by the Vogel-Fulcher-Tamman law (Eq. 4.3):

$$\eta = \eta_0 \cdot \exp\left(\frac{\Delta H_{act}}{R(T-T_0)}\right) \quad (4.3)$$

where R is the gas constant, ΔH_{act} the activation energy, T_0 is an adjustable parameter specific to a glass, η_0 is the viscosity constant. When a cyclic stress ($\sigma = \sigma_0 \sin [\omega t]$) is applied to the material, by definition, the mechanical loss, $\tan (\phi)$, can be found using:

$$\tan(\phi) = \frac{1}{2\pi} \cdot \frac{\Delta W}{W_{\text{max}}^{\text{el}}} \quad (2.20)$$

The mechanical loss related to the α -relaxation in glassy phase is due to non-reversible movement of glass molecules. Hence, taking to account the Eq. 4.2, 4.3 and 4.4, the dissipated energy is obtained by a straightforward calculation.

$$\Delta W = \oint \sigma \, d\varepsilon = \int_0^{2\pi/\omega} \sigma \dot{\varepsilon} \, dt = \int_0^{2\pi/\omega} \frac{\sigma_0^2}{\eta_0} \exp\left(-\frac{\Delta H_{\text{act}}}{R(T-T_0)}\right) \sin^2(\omega t) \, dt \quad (4.4)$$

$$\text{where } \dot{\varepsilon} = \frac{\sigma}{\eta}, \text{ and } \sigma = \sigma_0 \sin(\omega t) \quad (4.5)$$

$$W_{\text{max}}^{\text{el}} = \int_0^{\sigma_0} \sigma \, d\varepsilon = \frac{1}{2} \sigma_0^2 J_u \quad (4.6)$$

where J_u is unrelaxed compliance.

And the mechanical loss can be calculated as:

$$\tan(\phi) = \frac{1}{\eta_0 \omega J_u} \cdot \exp\left(-\frac{\Delta H_{\text{act}}}{R(T-T_0)}\right) \quad (4.7)$$

The above equation shows that the mechanical loss at temperatures high enough (when the viscosity is $< 10^{12}$ Pa.s) increases exponentially with temperature without any limitation. Such a result was observed by Donzel et al. for Y-Sialon pure glass [5, 6]. The calculated mechanical loss spectrum using the proposed model (Eq. 4.7) is presented in Fig.4.16a. It shows an exponential increase in the mechanical loss at temperatures higher than 1050 K, when the viscosity of the glass decreases very quickly. The rheological model (Fig. 4.16b) composed of a dashpot of viscosity (η) in series with a spring ($E_u = 1/J_u$, where E_u represents the unrelax modulus) can describe the deformation of a glass phase at high temperatures.

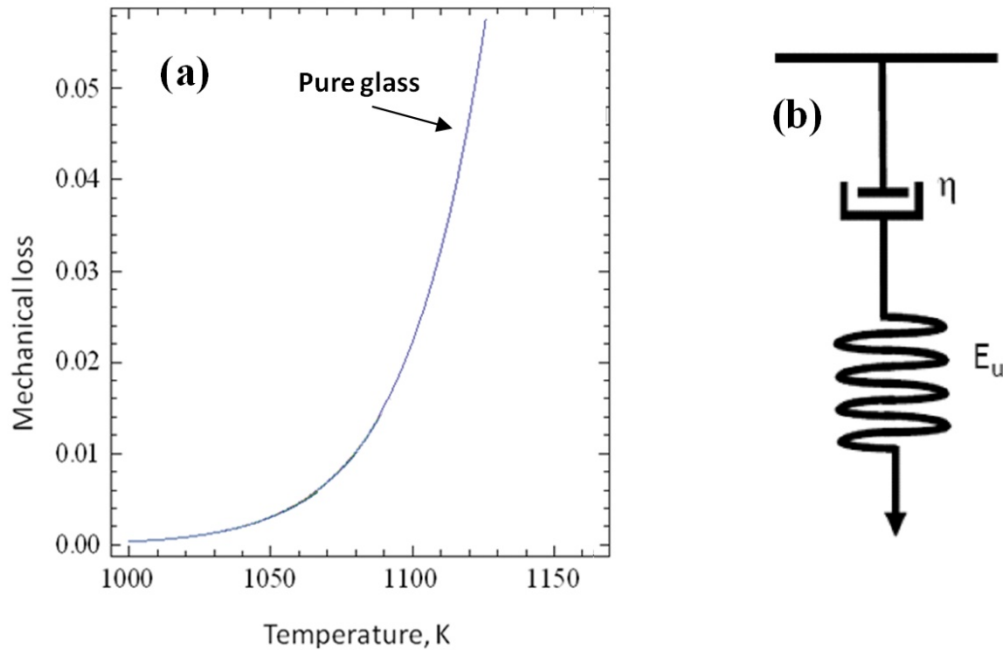


Fig. 4.16. (a) Mechanical loss as calculated from the proposed model presented for a pure glass. (b) Rheological model describing the elastic and anelastic deformation of pure Sialon glass.

2. Analysis of polycrystalline Sialon with glassy phase located between the grains and without glass pockets ($V_2=0$ and $V_1=1$); High temperature plastic deformation of polycrystalline ceramics is generally associated with grain boundary (GB) as a basic process. GB sliding may be lubricated by an intergranular glassy phase or GB dislocations. Lakki and her coworkers [12, 13] proposed a theoretical model accounting for the relative sliding of equiaxed grains, separated by an amorphous viscous layer of viscosity η and thickness δ , while the grains are constrained by the triple junctions. To keep grains together from separation, a restoring force with a spring constant, k was introduced. Bearing in mind that the restoring force is proportional to the shear modulus, which strongly decreases at high temperatures, an exponential increase in $\tan(\varphi)$ with temperature is obtained (no restoring force from the triple points). Therefore, the mechanical loss is given by:

$$\tan(\varphi)_{k=0} \cong \frac{G\delta}{\omega d \eta} = \frac{G\delta}{\omega d \eta_0} \exp\left(-\frac{E_{act}}{RT}\right) \quad (4.8)$$

From the microscopic point of view, this means that the relative motion of grains is not limited anymore and the grains start to perform long-range displacements. Therefore, the mechanical loss undergoes an exponential increase with temperature

(Eq. 4.8). The calculated spectrum using the model is presented in Fig. 4.17. An exponential increase in the mechanical loss is observed at temperature higher than 1400 K, when the restoring force decreases strongly (Fig. 4.18).

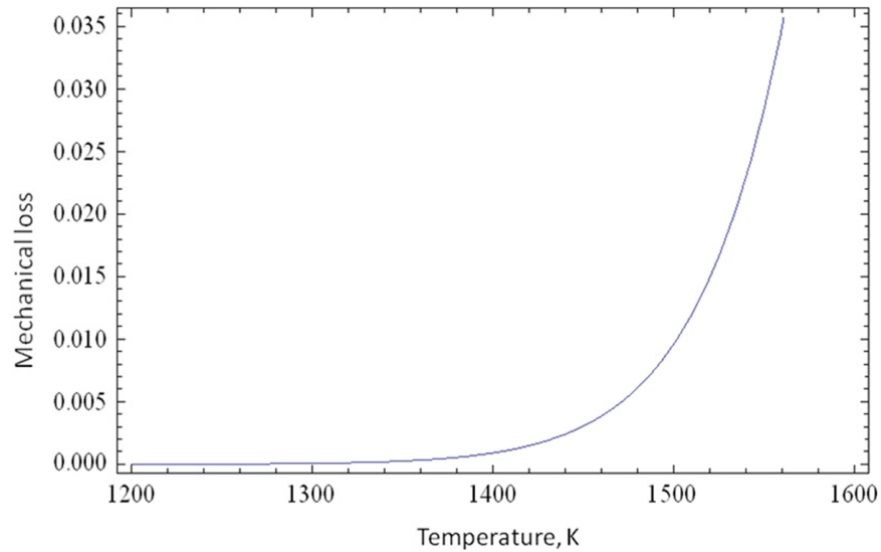


Fig. 4.17. Mechanical loss as calculated from the proposed model presented for a pure recrystallized Sialon.

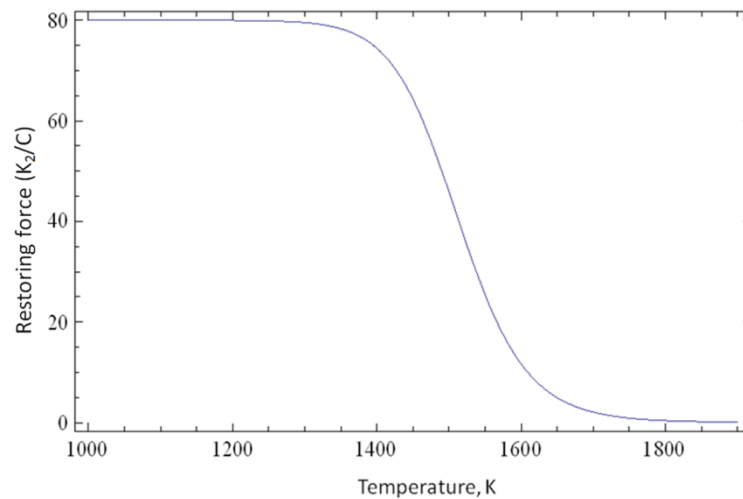


Fig. 4.18. Variation of the restoring force as a function of temperature according to Lakki's model [12, 13].

3. Analysis of two phase Sialon (polycrystalline Sialon and glassy pockets): This system is actually generated by the combination of both above-described mechanisms. The high temperature exponential background ($T > 1400$), is due to the long-range displacements of the grains giving rise to plastic deformation (onset of creep). The mechanical loss peak refers the relaxation phenomenon associated with the glass transition of bulk regions, which constitute a non-negligible amount of the material. Opposite to the pure glass (as explained in Eq. 4.7 and Fig. 4.16), the relaxation in the pockets does not lead to an exponential background, but to a peak (Fig. 4.1, 4.3, 4.4, 4.5, 4.7, 4.10). In the case of Sialon ceramics (as-sintered condition), the restoring force is provided by the skeleton of the grains surrounding the glass pockets. In the rheological model shown in Fig. 4.19, the restoring force is represented by a spring of constant k_1 in parallel with a dashpot of viscosity ($\eta_{g,p}$). Another dashpot-spring pair represents the amorphous layer between the grains with viscosity $\eta_{g,b}$. A spring (k_2) represents the restoring force due to the shear limitation at triple junctions. Hence, the total strain (ϵ_{tot}) can be calculated as:

$$\epsilon^{tot} = \epsilon^{el} + \epsilon_{g,p}^{an} + \epsilon_{g,b}^{an} \quad (4.9)$$

where ϵ^{el} is elastic strain, $\epsilon_{g,p}^{an}$ and $\epsilon_{g,b}^{an}$ are anelastic deformation of glass pockets and grain boundaries, respectively.

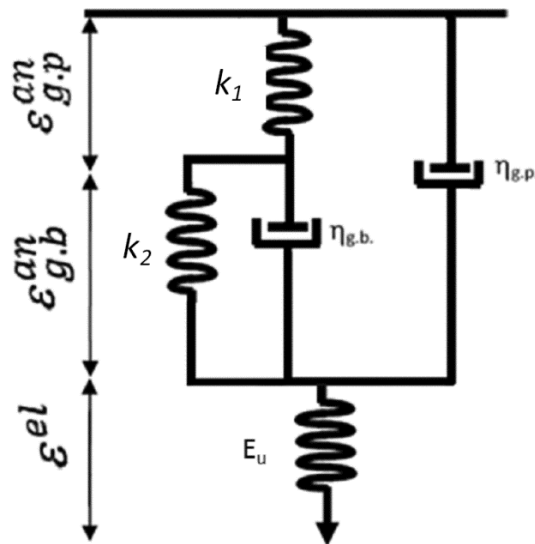


Fig. 4. 19. Rheological model describing the elastic and anelastic deformation of two phase Sialon(model 3).

The proposed model (Fig. 4.19) should exhibit two relaxation phenomena in the mechanical loss spectrum. In an intermediate range of temperatures ($1000 < T < 1300$ K), the shear modulus is still close to that measured at room temperature. This means that the grains are constrained and the restoring force (k_2) is quite high (a representation of the restoring force as a function of temperature is presented in Fig. 4.18). On the other hand, it must be taken into account that the viscosity of the thin films with a thickness of some interatomic distance is higher than the viscosity of the bulk pocket glass [1].

Due to the high stiffness of the dashpot with viscosity $\eta_{g,b}$, the $\epsilon_{g,b}^{an}$ is negligible between 1000 and 1300 K and there is no movement due to GB sliding. If we apply a cyclic stress ($\sigma = \sigma_0 \sin [\omega t]$), the mechanical loss ($\tan (\varphi)$) will be obtained accordingly:

$$\tan (\varphi) = \frac{1}{J_u k_1} \cdot \frac{\omega \cdot \eta / k_1}{1 + (\omega \cdot \frac{\eta}{k_1})^2} \quad (4.10)$$

Where the $J_u = 1/E_u$ is the unrelaxed compliance. Eq. 4.10 shows a peak under the condition: $\omega \cdot \frac{\eta}{k_1} = 1$. According to Lakki's model [12, 13], the restoring force is stable at such a temperature (Fig. 4.17) and when the frequency is constant, the peak position is only a function of viscosity. From the microscopic point of view, the chemical composition of the glass can change the position of the peak due to different viscosity. Results of Roebben and his coworkers [14, 15], Testu et al. [16, 17] and Lakki et al. [13] are in agreement with this hypothesis. For the Ca- Sialon samples measured in the present work (Table 4.1), the peak temperatures for all samples are very close, which means that the chemical composition of the glass is similar. We assume that the small differences between the peak positions (Fig. 4.6 and Fig. 4.10) are probably related to different microstructures of the sintered bodies that resulted in different restoring forces. In fact, according to Eq. 4.10, an increase in the restoring force would result in a peak shift to lower temperatures.

The height of the peak is equal to $\frac{1}{J_u k_1}$, which implies that, when the restoring force (k_1) increases, the height of the peak should decrease. The restoring force mainly depends on the microstructure, temperature and frequency [12, 13]. As observed in the SEM micrographs (Fig. 4.12) and represented in Fig 4.13, increasing the Ca content or x-value (for $x > 0.2$) led to a coarser microstructure and to higher aspect ratio of the elongated Sialon grains. For instance, grains with aspect ratios of six to ten are observed in the sample with a high x-value of 1.6 (Fig. 4.12d), where the elongated grains act as reinforcing fibers in the sintered bodies [11]. It is well

known that toughening through in-situ formation of elongated grains, rather than addition of whiskers, has potential advantages [18, 19]. The formation of a coherent interface or chemical bonds between elongated grains and equiaxed matrix grains are recognized to produce a superior microstructure called “interlocking microstructure” [20]. A higher aspect ratio of the elongated grains or a higher fraction of them increases the interlocking effect, and therefore should increase the restoring force. Thus, according to Eq. 4.10, the height of the peak should decrease with x -value. However, as seen in Table 4.1 and Fig. 4.10 the general trend is opposite. In effect, Eq. 4.10 should be modified when the amount of glassy phase is varying. The deformation of the sample that involves a volume fraction “ f ” of glassy phase in glass pockets and the complement in the grain boundaries is:

$$\varepsilon^{\text{tot}} = \varepsilon^{\text{el}} + (1 - f) \varepsilon_{\text{g,b}}^{\text{an}} + f \varepsilon_{\text{g,p}}^{\text{an}} \quad (4.11)$$

As a consequence, the mechanical loss is:

$$\tan(\varphi) = \frac{f}{1-f} \cdot \frac{1}{J_u k_1} \cdot \frac{\omega \eta / k_1}{1 + (\omega \frac{\eta}{k_1})^2} \quad (4.12)$$

Thus, the height of the peak is equal to $\frac{f}{1-f} \cdot \frac{1}{J_u k_1}$. Therefore, a very small amount of glassy phase, as in the case of $x = 0.2$, and a relatively high restoring force (in relation to elongated β -Sialon grains) in Ca2N should result in the lowest peak height. Ca4N shows a minimum restoring force (very small equiaxed grains). Therefore, the peak height of Ca4N is higher than Ca2N. Ca8N has a higher restoring force in comparison to Ca4N, due to a coarser microstructure (elongated grains), but it seems that the effect of a large quantity of glassy phase would be predominant. Testu et al. [16, 17] have reported a similar effect for pressure gas sintered silicon nitride based ceramics. According to their report, the intensity of the mechanical loss peak for non-annealed, 2h and 4h annealed (followed by rapid cooling) samples at 1873 K were found to be 0.76×10^{-3} , 6.02×10^{-3} and 22.1×10^{-3} , respectively. Their observations have shown that the material may contain a liquid phase at 1873 K, which would be then fixed into the microstructure as an amorphous phase (glass) during rapid cooling (quenching). Longer annealing time at 1873 K would result in a higher amount of liquid phase (dissolution of Y-Sialon crystallites), and consequently in more glassy phase, which causes the increase of the peak.

A surprising result is observed in Ca16N. This sample owns a high content of glassy phase and a relatively low mechanical loss peak. Again, there is a competition between an increase in the restoring force (a large amount of elongated grains) and

the glass phase content (maximum x-value). The lower intensity of the peak in this sample (Ca16N) should be due to the higher restoring force (k_1) due to the high amount of elongated grains with high aspect ratio as it can be seen in Fig. 4.13 and 4.12d.

Interestingly, the compressive deformation measurements, in the SPS apparatus, show the same trend, as well (Fig. 4.14). Therefore, it could be concluded that the presence of elongated grains can sensibly reduce the creep rate even if the onset temperature for deformation is much higher than the temperature of mechanical loss peak. This temperature difference may be justified by the higher heating rate in the SPS apparatus (40 K min^{-1}) which can shift the thermally activated process to higher temperature. On the other hand, two elements of spectrum (peak and background) are often associated with micro-creep mechanisms, as it has been reported in alumina and zirconia ceramics [12, 21]. Therefore, they can appear at temperatures and stresses below those needed for macroscopic plastic deformation.

At temperature higher than 1400 K, the shear modulus strongly decreases with temperature (Fig. 4.7). We can consider that the restoring force (k_2) due to elastic interaction at the triple points decreases when temperature raises or when frequency decreases. The calculation of the restoring force as a function of temperature can be done according to Lakki's model (Fig. 4.18). In the rheological model, at such temperatures ($T > 1400$) both parallel springs (k_1 and k_2) lose their strength and a creep is observed according to the model in Fig. 4.19. As Schaller [22-24] and Daraktchiev [25] have shown, if the spring constant goes to zero, there is no limitation to strain and as a consequence mechanical loss increases continuously with temperature or when frequency decreases.

The rheological model presented in Fig. 4.19 is also applicable for both pure glass and recrystallized Sialon samples. For pure glass there is no restoring force (k_1 and k_2 close to zero) and the model reduces to that shown in Fig. 4.19. For the recrystallized samples, there are no glass pockets, and "f" is equal to zero in Eq. 4.12. In this case, the dashpot of pocket viscosity ($\eta_{g,p}$) and the related parallel spring (k_1) should be removed.

Using Eq. 4.12 and proper constant values, we have calculated the mechanical loss versus temperature for the present four different Sialon samples (represented as Ca2N, Ca4N, Ca8N and Ca16N) (Fig. 4.20). The activation energy is taken constant as calculated in Fig. 4.9. To evaluate the effect of the glassy phase content on the peak height, the restoring force, k_1 , was taken constant equal to 40×10^{-4} for samples Ca2N, Ca4N and Ca8N, while the amount of the glassy phase, f, is varying (for sample

Ca₂N, Ca₄N and Ca₈N f is taken as 2%, 4% and 8%, respectively). There is a good agreement between the theoretical model calculations, and the experimental measurements (Fig. 4.10). In the case of sample Ca₁₆N, if we take $f = 16%$, k_1 should be four times more than in Ca₈N and the height of the peak decreases, observed in the experimental results. However, these results have to be taken with precaution, since the content of the glassy phase is hardly determined in these materials. The model, however, explains well the origin of the damping peak and its trend.

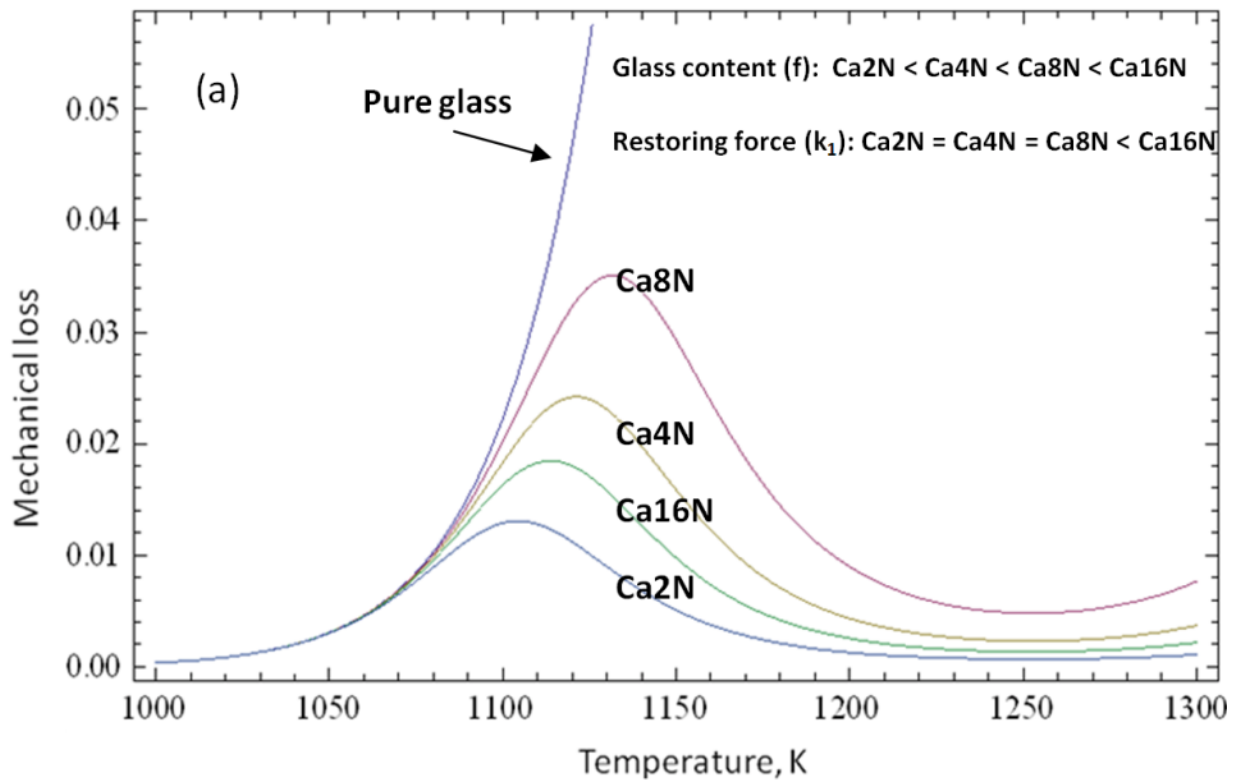


Fig. 4.20. Mechanical loss as calculated from the proposed model presented for a pure glass and Sialons. The peak amplitude variation is obtained by increasing the glassy phase fraction in Ca₂N, Ca₄N, Ca₈N and by increasing the restoring force in Ca₁₆N.

4.4. Phase characterization of Ca-Sialon sample

As it was shown in the general spectrum of Sialon ceramics (e.g. Fig. 4.1, Fig. 4.3, and Fig. 4.7), upon cooling after annealing at high temperatures (for 1h at 1600 K), the mechanical loss peak and the modulus anomaly disappear and the high temperature mechanical loss background is lower than in the as-sintered sample. It means that

the feature observed in first heating is irreversible. As explained in 2.4.3.1, this occurs because the peak is related to relaxation in glassy phase and after thermal treatments, these pockets re-crystallize, leading to the disappearance of the glassy phase and consequently to the mechanical loss peak. Using TEM observation and selected area diffraction pattern of the phase located at triple junctions, it has been shown [12] that such phase is completely amorphous in the as sintered condition, but it converts into a crystalline one after high temperature thermal cycling.

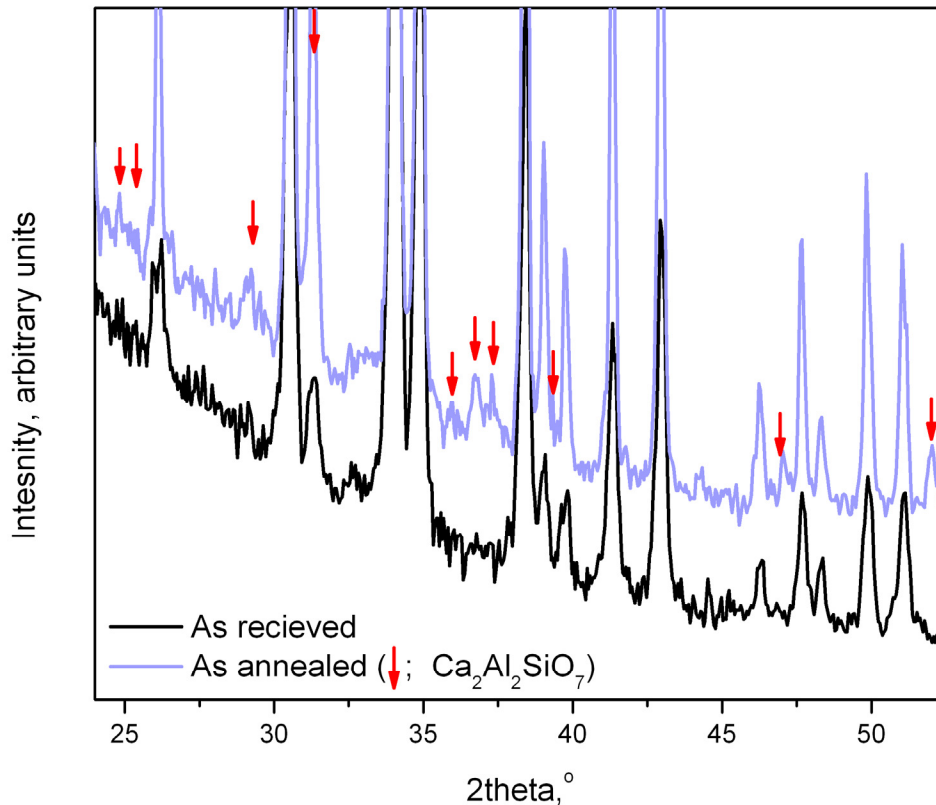


Fig. 4.21. XRD of the Ca16N after and before mechanical loss measurements. The red arrows show the new phase generated during annealing at 1600 K for 1 h.

This hypothesis could also be investigated using X-ray diffraction (XRD) analysis of the Sialon samples, before (as-sintered condition) and after mechanical loss measurements. Since the samples contain small amounts of glassy pockets, the sample with the highest glass content was chosen (Ca16N) for this analysis. Fig. 4.21 shows the XRD pattern of the Ca16N sample before and after mechanical loss measurements. It is clearly visible that a new phase (Ca₂Al₂SiO₇), indicated by red arrows has been generated during the annealing at 1600 k for 1 h. This may be a further confirmation of crystallization of the pockets.

4.5. Conclusion

Sialon ceramics were considered as a two-phase material involving (1) polycrystalline grains separated by an intergranular phase, and (2) pure glass pockets located in the GB triple points. From the mechanical loss spectra of these materials and their comparison it can be concluded that: (1) upon heating the amorphous pockets undergo a the glass transition, which results in a mechanical loss peak, related to the α -relaxation in the glassy phase. The results have shown that the peak position is a function of glass viscosity, which strongly depends on the composition of the glassy phase. The peak amplitude is affected by two-parameters: (1) the glassy phase quantity and (2) the restoring force due to the grain elasticity, which depends on the grain shapes. A rheological model was developed accounting for both above-mentioned relaxation mechanisms. The model shows a good agreement with experimental results.

References

- [1] A. Lakki, R. Schaller, G. Bernard-Granger, R. Duclos, High temperature anelastic behaviour of silicon nitride studied by mechanical spectroscopy, *Acta Metallurgica Et Materialia* 43 (2) (1995) 419-426.
- [2] R. Schaller, A. Lakki, Grain boundary relaxations in ceramics, *Materials Science Forum* 366-368 (2001) 315-337.
- [3] S. Sakka, K. Kamiya, T. Yoko, Preparation and properties of CaAlSiON oxynitride glasses, *Journal of Non-Crystalline Solids* 56 (1-3) (1983) 147-152.
- [4] Y. Cai, Synthesis and Characterization of Nitrogen-rich Calcium -Sialon Ceramics in, Vol. PhD, Stockholm University, Stockholm, 2009.
- [5] L. Donzel, A. Lakki, R. Schaller, Glass transition and relaxation in Y-Si-Al-O-N glasses and in Si₃N₄ ceramics studied by mechanical spectroscopy, *Philosophical Magazine A: Physics of Condensed Matter, Structure, Defects and Mechanical Properties* 76 (5) (1997) 933-944.
- [6] L. Donzel, R. Schaller, Mechanical spectroscopy of a YSiAlON glass, *Journal De Physique. IV : JP 6* (8) (1997) C8-663-C668-666.
- [7] G. Pezzotti, K. Okamoto, K. Ota, Rheological Behavior of Dilute SiAlON with or without Intergranular X-Phase, *Journal of the American Ceramic Society* 84 (3) (2001) 598-602.
- [8] G. Pezzotti, K. Ota, H.J. Kleebe, Grain-boundary relaxation in high-purity silicon nitride, *Journal of the American Ceramic Society* 79 (9) (1996) 2237-2246.
- [9] Y. Cai, Z. Shen, J. Grins, S. Esmaeilzadeh, T. Höche, Self-Reinforced Nitrogen-Rich Calcium-SiAlON Ceramics, *Journal of the American Ceramic Society* 90 (2) (2007) 608-613.
- [10] K. Chihara, D. Hiratsuka, J. Tatami, F. Wakai, K. Komeya, High-temperature deformation of α -SiAlON nanoceramics without additives, *Scripta Materialia* 56 (10) (2007) 871-874.

- [11] Y. Cai, Z. Shen, T. Höche, J. Grins, S. Esmailzadeh, Superplastic deformation of nitrogen-rich Ca-sialon ceramics, *Materials Science and Engineering A* 475 (1-2) (2008) 81-86.
- [12] A. Lakki, Mechanical spectroscopy of fine-grained zirconia, alumina and silicon nitride, in, Vol. Ph.D. Thesis No. 1266, École Polytechnique Fédérale de Lausanne, Lausanne, Switzerland, 1994.
- [13] A. Lakki, R. Schaller, M. Nauer, C. Carry, High temperature superplastic creep and internal friction of yttria doped zirconia polycrystals, *Acta Metallurgica Materialia* 41 (10) (1993) 2845-2853.
- [14] G. Roebben, L. Donzel, M. Steen, R. Schaller, O. Van Der Biest, Internal friction decrease in silicon nitride due to crystallization of intergranular phases, *Key Engineering Materials* 132-136 (1997) 655-658.
- [15] G. Roebben, L. Donzel, S. Stemmer, M. Steen, R. Schaller, O. Van Der Biest, Viscous energy dissipation at high temperatures in silicon nitride, *Acta Materialia* 46 (13) (1998) 4711-4723.
- [16] S. Testu, R. Schaller, Internal friction peak in silicon nitride sintered without additives, *Diffusion and Defect Data. Pt A Defect and Diffusion Forum* 206-207 (2002) 167-170.
- [17] S. Testu, R. Schaller, J.L. Besson, T. Rouxel, G. Bernard-Granger, Mechanical spectroscopy connected to creep and stress relaxation in a high resistant silicon nitride, *Journal of the European Ceramic Society* 22 (14-15) (2002) 2511-2516.
- [18] D. Thompson, Ceramics: Tough cookery, *Nature* 389 (6652) (1997) 675-676.
- [19] F.F. Lange, Relation between strength, fracture energy, and microstructure of hot-pressed Si₃N₄, *Journal of the American Ceramic Society* 56 (10) (1973) 518-522.
- [20] Z. Shen, Z. Zhao, H. Peng, M. Nygren, Formation of tough interlocking microstructures in silicon nitride ceramics by dynamic ripening, *Nature* 417 (6886) (2002) 266-269.
- [21] A. Lakki, R. Schaller, C. Carry, W. Benoit, High temperature anelastic and viscoplastic deformation of fine-grained MgO-doped Al₂O₃, *Acta Materialia* 46 (2) (1998) 689-700.
- [22] R. Schaller, Mechanical spectroscopy of the high-temperature brittle-to-ductile transition in ceramics and cermets, *Journal of Alloys and Compounds* 310 (1-2) (2000) 7-15.
- [23] R. Schaller, M. Daraktchiev, S. Testu, Creep behavior of ceramics studied by mechanical loss measurements, *Materials Science and Engineering A* 387-389 (1-2 SPEC. ISS.) (2004) 687-691.
- [24] R. Schaller, C. Ionascu, High-temperature mechanical loss and creep behavior of fine-grained zirconia-containing nano-sized reinforcements, *Materials Science and Engineering A* 521-522 (2009) 217-220.
- [25] M. Daraktchiev, R. Schaller, High-temperature mechanical loss behaviour of 3 mol% yttria-stabilized tetragonal zirconia polycrystals (3Y-TZP), *Physica Status Solidi (A) Applied Research* 195 (2) (2003) 293-304.

Chapter 5

Experimental results and analysis: zirconia based composites

In this chapter the properties of the zirconia (3Y-TZP) composites reinforced with different amount of CNTs are presented. In the first part, details concerning the processing and the dispersion of CNTs within nano sized 3Y-TZP particles are presented. Also, it is shown that spark plasma technique preserves the nanotubes during sintering. The results of systematic analyses of the mechanical properties and the electrical conductivity of the zirconia based composites, containing different amount of CNTs (ranging between 0.5 and 5 wt.%), are given. Also, measurements of mechanical loss as a function of temperature, and frequency allow the investigation of the effect of CNTs on the general spectrum. A new model has been developed to explain the effect of CNTs on the grain boundary (GB) sliding at high temperature.

5.1. Powder composites processing and characterization

According to the literature review presented in chapter 1, it can be concluded that there are still several difficulties in processing defect free CNT-zirconia composites with improved mechanical properties. In sum, the critical factors for developing CNT-ceramic composites with improved mechanical properties can be regarded as follows: (1) homogeneous dispersion of CNTs within the matrix and inhibition of CNT agglomeration (caused by Van der Waals forces); (2) optimum bonding of the CNT-ceramic interface; i.e. interfacial compatibility and wetting between CNTs and ceramic matrix as well as strong entangling of the CNTs within the ceramics grains; (3) avoiding damage of the CNTs during processing. The last point has to be carefully taken into account during mixing and high temperature sintering to prevent from nanotube breaking, oxidation and crystal structure destruction. Finally (4) near fully dense composites are required since there is a strong relation between mechanical properties (e.g. hardness) and residual pores after firing. In particular, the presence of nanotubes between the ceramic particles typically delays densification and only in few researches this effect was taken into account so far.

Fig. 5.1 a-d, show the HR-SEM micrographs relative to the mixture of 3Y-TZP with various amounts (0.5, 1.5, 3 and 5 wt%) of CNTs after mechanical blending. HR-SEM micrograph indicates the highly dispersed CNT inclusions without traces of CNTs agglomeration within 3Y-TZP powder.

TEM images of the 5 wt% CNTs-3Y-TZP powder mixture (Fig. 5.2) indicates well-mixed and non-damaged CNTs as well. What can be seen in TEM images clearly, the uniquely flexible nature of CNTs makes them bend and pass through space between nanopowders or wrap around them. The same features were observed in composite powders with various amounts of CNTs.

5.2. Sintered composite characterization

Table 5. 1 summarizes the sintering temperatures and characteristics (density and grain size) of nanostructured composites and monolithic zirconia. Nearly full-dense structures ($\rho > 98\%$ theoretical density) were obtained by SPS processing. As CNTs suppress densification to some extent, with an increase of CNTs content, higher sintering temperature has been employed. Nevertheless, the short SPS soaking/lower sintering temperature (Table 5.1) in comparison with conventional sintering [1] and hot-pressing [2, 3] is the key to preserve the CNT structure in the sintered composites [4, 5]. Interestingly, though the highest sintering temperature

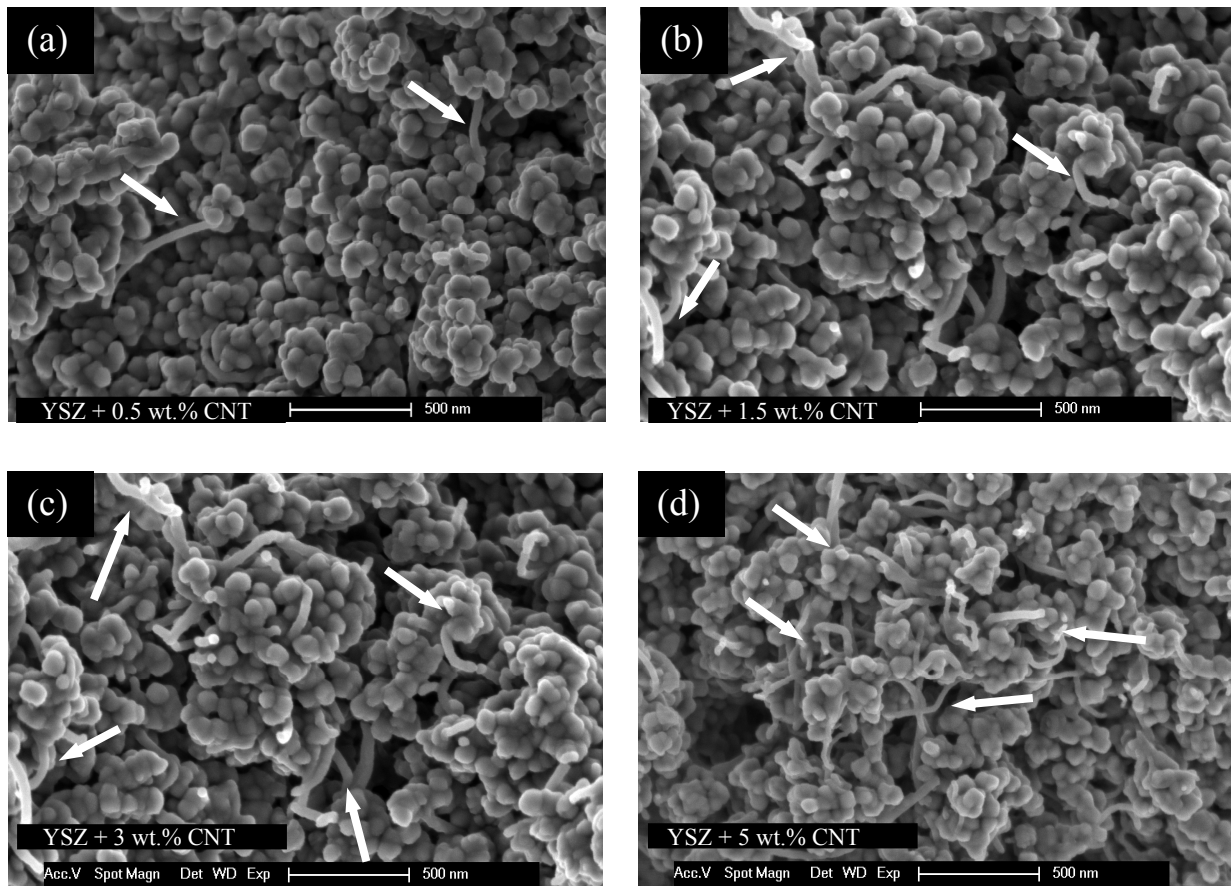


Fig. 5.1. High resolution scanning electron microscopy of blended yttria stabilized zirconia powder with (a) 0.5 wt%, (b) 1.5 wt%, (c) 3 wt% and (d) 5 wt% carbon nanotubes (arrows indicate nanotubes).

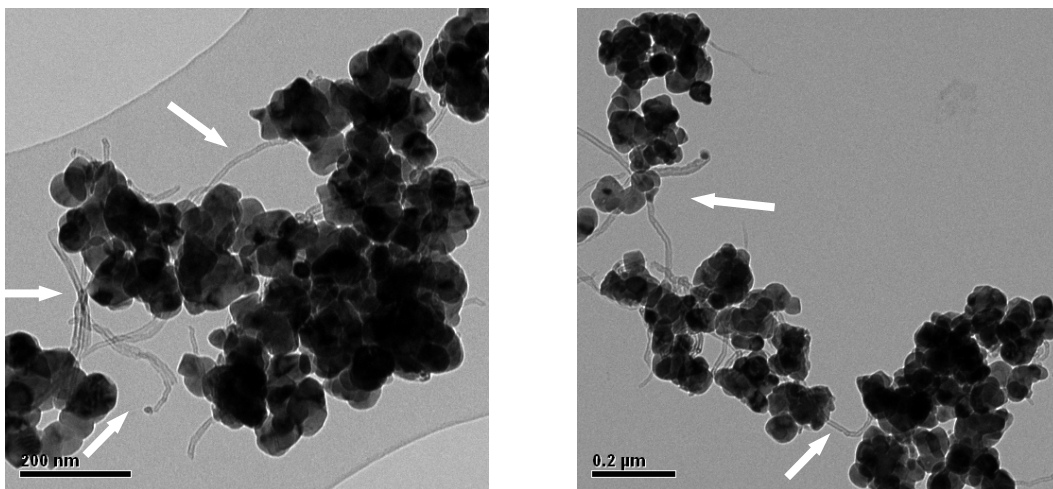


Fig. 5.2. TEM micrograph of yttria stabilized zirconia-5wt% CNTs raw composite.

Chapter 5

was employed for zirconia reinforced with 5 wt.% CNTs, the final microstructure exhibits the smallest grain size. Therefore, CNTs substantially reduce grain growth and should also be able to pin GBs.

Table 5.1. Sintering temperature and characteristics of sintered 3Y-TZP/CNTs nanocomposites in comparison with monolithic zirconia.

Material composition	Sintering temperature (°C)	Fractional density (%)	Grain size (nm)
3Y-TZP	1250	99.3	145
3Y-TZP/ 0.5wt% CNT	1250	98.9	131
3Y-TZP/ 1.5wt% CNT	1250	98.5	121
3Y-TZP/ 3wt% CNT	1300	98.7	109
3Y-TZP/ 5wt% CNT	1350	98.4	96

Throughout all the SPS cycle it was possible to measure the height variation of the powder body (L) precisely and instantaneously. Knowing the instantaneous variation of the sample height, one can calculate the instantaneous relative density (D) based on the following equation (Eq. 5.1).

$$D = \left(\frac{L_f}{L} \right) D_f \quad (5.1)$$

where L_f and D_f are the final sample height and final relative density (which was determined by Archimedes method), respectively. Using this procedure the composite relative densities vary as a function of temperature with heating (non isothermal sintering) and dwelling at the maximum sintering temperature (isothermal sintering) is shown in Fig. 5.3.

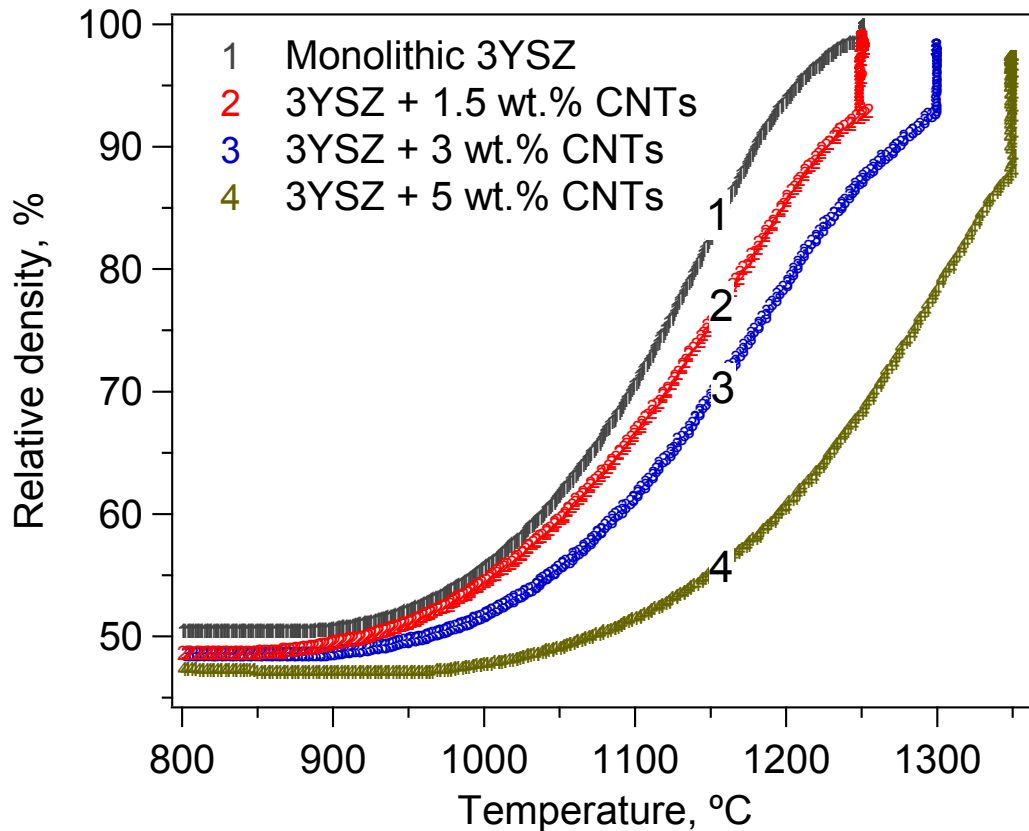


Fig. 5.3. Densification (relative density vs. temperature) obtained in the monolithic 3Y-TZP and composites reinforced with different amount of CNTs during spark plasma sintering. (Dwell time was 2 min)

A typical density-temperature curve pertaining to the majority of materials exhibits a classical sintering sigmoidal shape [6]. However, the graphs shift to higher temperatures with increasing the CNT amount. Three different stages of sintering can be clearly observed in Fig. 5.3. In spite of the absence of a significant densification at low temperatures (e.g. less than 900 °C in pure 3Y-TZP), the second stage of sintering gave rise to an enhanced densification rate in the second sintering stage (1000-1200 °C). In monolithic 3Y-TZP, for instance, one can monitor a dramatic improvement in the values of fractional density from 57% to 95% theoretical density, generated by a temperature increase from 1000 to 1200 °C. In the final stage of sintering, the compaction rate decreases and a further increase in temperature (e.g. from 1200° to 1250°C) results in a slight density enhancement up to 2%. This sintering trend is a common behavior regardless the processed material as also observed by [6, 7] for 3Y-TZP during spark plasma and conventional sintering.

The relative density at low temperatures, before the densification starts, can be considered as the specimen green density, as shown in Fig. 5.3. It can be seen that the addition of CNTs causes a systematic decrease in the composite green densities under a compressive pressure of 50 MPa. The green relative density of monolithic 3Y-TZP was 50.8%, while this value dropped to about 47.4% for the 5wt% CNT reinforced composite. According to previous investigations [8] the consolidation of ceramic-powders in a rigid die include: (1) sliding and rearrangement of the particles; (2) fragmentation of brittle grains and (3) elastic deformation of bulk compacted powders. At low stress (e.g. lower than 370 MPa for zirconia [8]), sliding and rearrangement of the particles dominate the mechanisms of nanopowders consolidation. Hence, to explain the lower compaction of zirconia powders in presence of CNTs it can be argued that the ceramic powder sliding and rearrangement have been reduced. This is in line with TEM observation of raw composite powder (Fig. 5.2), which shows entangled and kinked nanotubes around the 3Y-TZP nanopowder hindering the powders from rearranging freely during compaction.

Based on the densification results (Fig. 5.3), the addition of CNTs gave rise to a significant increase in the temperature at which sintering starts (the temperature at which 1% densification occurs) and proceeds. For instance, 1% densification occurs at 936 °C in monolithic 3Y-TZP, while the addition of 3 and 5 wt% CNTs hoisted the starting temperature of sintering up to 955 and 1042 °C, respectively. The addition of CNTs requires higher temperatures and longer times to complete the densification. For example, non-isothermal sintering at 1250 °C resulted in a fully dense (98% relative density) monolithic 3Y-TZP, while 3 and 5 wt% CNTs reinforced composites have not shown densities higher than 87% and 67% respectively. The reports of several authors [3, 9-12] confirm that the addition of CNTs slackens the densification process of 3Y-TZP/CNT composites, compared to monolithic zirconia. They all sintered the monolithic 3Y-TZP and 3Y-TZP/CNT composite at identical sintering conditions (i.e. sintering temperature and dwelling time) and they all obtained a lower density in composites. Duszova et al. [3, 10, 13] also showed that the final grain size of the sintered composites was smaller than in monolithic zirconia, which evidences that the nanotubes could inhibit the grain growth of zirconia.

Often, the sintering of traditional whiskers and fiber reinforced composites is limited by differential densification rates. Similar problem may be expected for carbon nanotubes, as well. Recently, Bernard-Granger and Guizard [7] have identified the controlling mechanism through the spark plasma sintering of Tosoh-3Y-TZP powder in a wide range of applied pressure and temperature. At

intermediate compaction or medium temperature (which is close to the present experiment conditions) they have proposed that densification proceeds with GB sliding accommodated by the series interface-reaction/ lattice diffusion of Zr^{4+} and/or Y^{3+} cations. In a former paper, this has been also shown that GB sliding in 3Y-TZP 1.5 wt% CNTs in the temperature range of about 1100-1300 °C could be controlled by the cation lattice diffusion [7]. Therefore, the lower densification rate of CNT reinforced composites with respect to the pure 3Y-TZP could be attributed to a slower GB sliding during sintering. In other words, CNTs located in the GBs could pin them and hinder their movement (sliding or migration) and consequently hinder the densification rate. This hypothesis is supported by results that we have obtained by mechanical spectroscopy. Details of the GB sliding of the composites are presented in part 5.5.2.

The relatively low density of the CNT-zirconia compacts (compared to the pure zirconia) may be the underlying reason for which recent investigations do not show an improvement of the mechanical properties in CNT reinforced zirconia composites. What should be primarily considered is the strong relationship between microstructural defects such as retained porosities after sintering and mechanical properties, while this issue has been neglected in many papers [11, 14].

HR-SEM (fracture surface) images of 3Y-TZP reinforced with variable amounts of CNTs are represented in Fig. 5.4 a-d. The interesting features can be highlighted as follows: (1) CNT have surrounded a great fraction of zirconia grains. (2) Most of zirconia grains have maintained a size lower than 100 nm, confirming that CNTs lead to grain refinement. (3) CNTs are homogeneously dispersed in the matrix even at high volume percentages of nanotubes (5 wt% is equal to 12.5 vol.%). (4) The nanotubes have not been damaged both during the powders blending, and upon spark plasma sintering. (5) The fracture mode is mainly intergranular and debonded CNTs from the matrix can be observed on the fracture surfaces.

A homogenous distribution of CNTs is observed on the ceramic GBs, which is essential to improve mechanical properties [15]. As can be inferred from in TEM micrograph (Fig. 5.2), the flexibility of CNTs allow them to bend and pass through the space between nano-powders and wrap them around. This is not possible in 3Y-TZP ceramics reinforced with carbon nano-fibers, since they are not enough flexible, which would not allow them to wrap around the zirconia particles. Probably, the flexibility of CNTs can be regarded as one of the major benefits of nanotubes with respect to carbon nanofibers. Moreover, the absence of agglomeration in pre-dispersed / surface-modified CNTs (Fig. 3.3) leads to a good distribution within the ceramic powder using a conventional mixing technique. Surface modifications, made

Chapter 5

during synthesis of the CNTs, create electrical charges on the CNTs surface, acting against agglomeration of the nanotubes. Same features can be seen in a TEM image of as-sintered 3Y-TZP/5wt.% CNTs (Fig. 5.5) that shows a homogenous grain size distribution and a random distribution of CNTs mostly located at GBs and surrounding the zirconia grains.

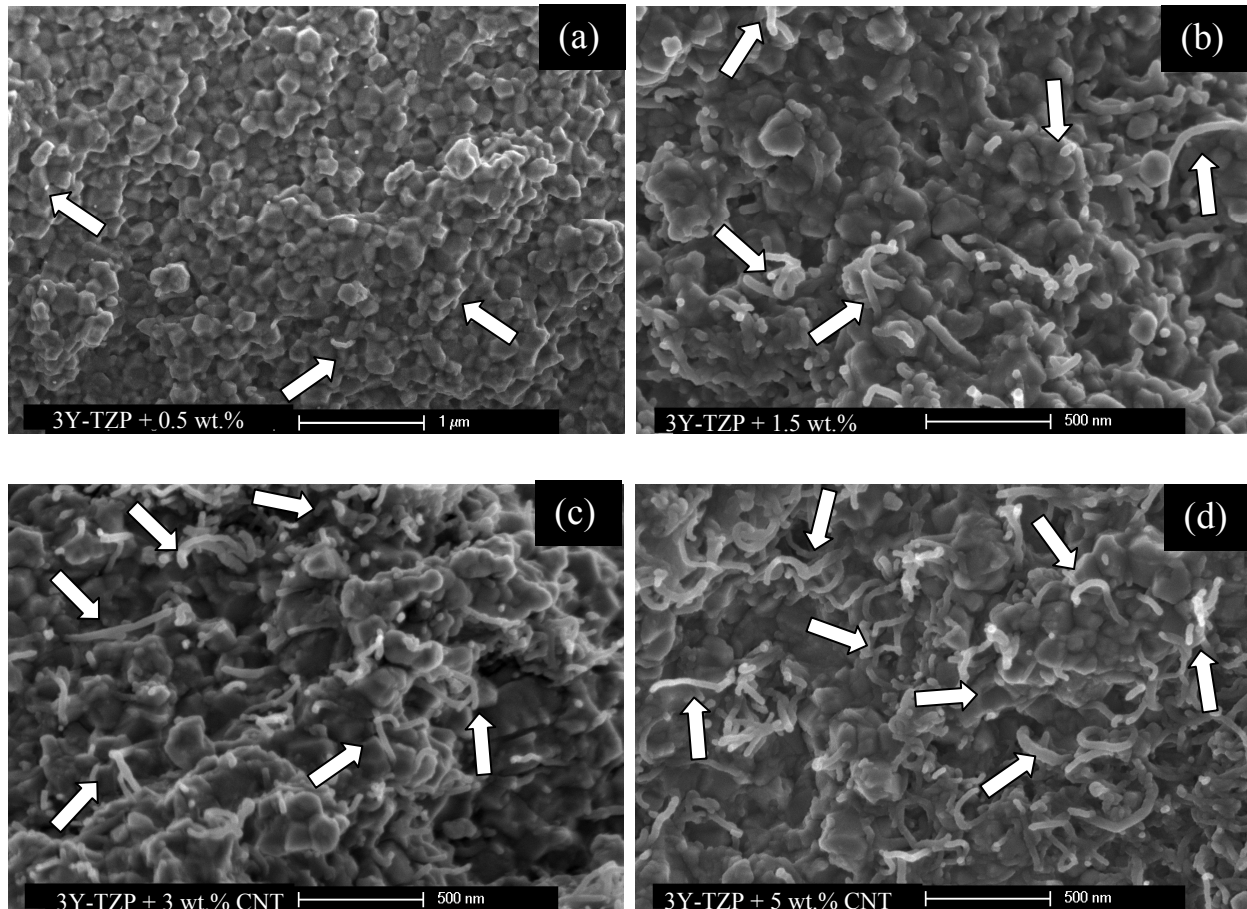


Fig. 5.4. High resolution SEM of fracture surface of 3Y-TZP composites reinforced with (a) 0.5 wt%, (b) 1.5 wt%, (c) 3 wt% and (d) 5wt% CNTs.

Fig. 5.6 shows the Raman spectra of the as-received CNTs and spark plasma sintered composite reinforced with 5wt.% CNTs. Specific Raman peaks of CNTs [16], i.e. G and D bands measured in the sintered bodies are nearly identical to those of the raw CNT specimen, providing a definitive evidence for the presence of nanotubes in the 3Y-TZP-CNT composites sintered at 1350 °C for 2 min that was the highest sintering temperature compared to other specimens. The slight deviation of both bands to a

higher wave number in the sintered composites may be attributed to residual stresses due to the difference between thermal expansion coefficients of CNT and 3Y-TZP ceramics. A simple comparison between these two spectra confirms that CNTs were not damaged during processing.

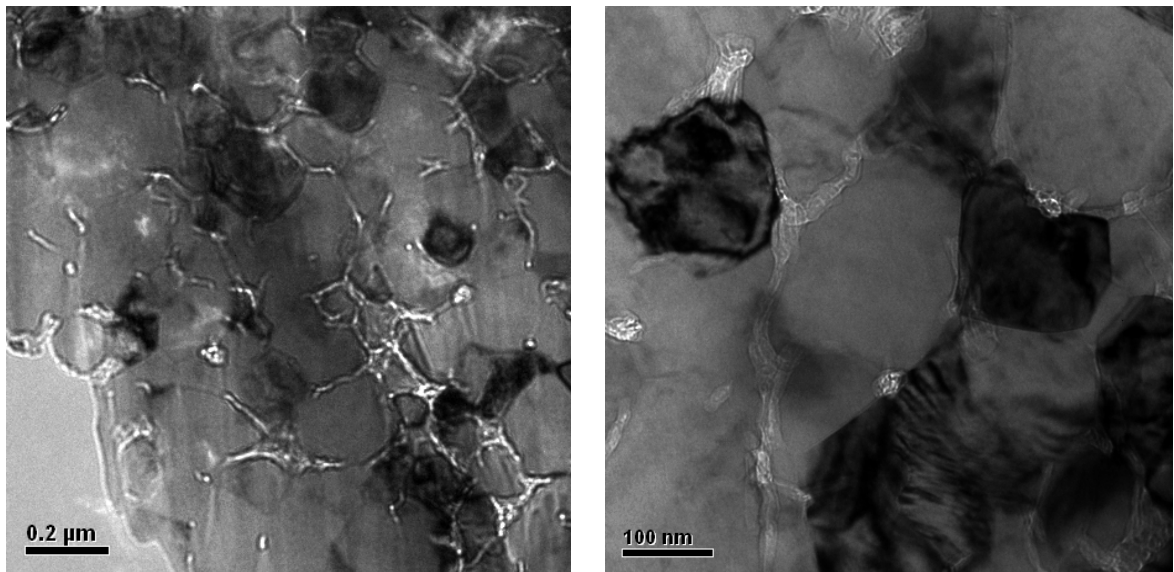


Fig. 5.5. TEM micrograph of the as-sintered 3Y-TZP / 5wt% CNTs composite.

HR-TEM micrograph of the composites reinforced with 5wt% CNTs is presented in Fig. 5.7. Several noticeable features can be pointed out. (1) No trace of amorphous carbon could be detected in the GBs as well as in triple junctions. Similar observations have also been reported for the Alumina-CNT system by Vasiliev et al [5]. However, conventionally sintered 3Y-TZP/ CNT at 1753 K for 3 h [1], show the presence of an amorphous layer of carbon. (2) Owing to the very fast firing (2 min soaking) and relatively low sintering temperatures in SPS technique, CNTs maintained their structure unchanged during sintering as they were before the process. The fringe spacing in Fig. 5.7 is 0.34 nm, which is typical of graphite. (3) CNTs in the GBs are randomly oriented. A cross section of CNT bundles seen from the top as well as a CNT located along the GB can be seen. (4) The interface between CNTs and 3Y-TZP grains is flawless and entrapped porosities or defects at the interface could not be detected.

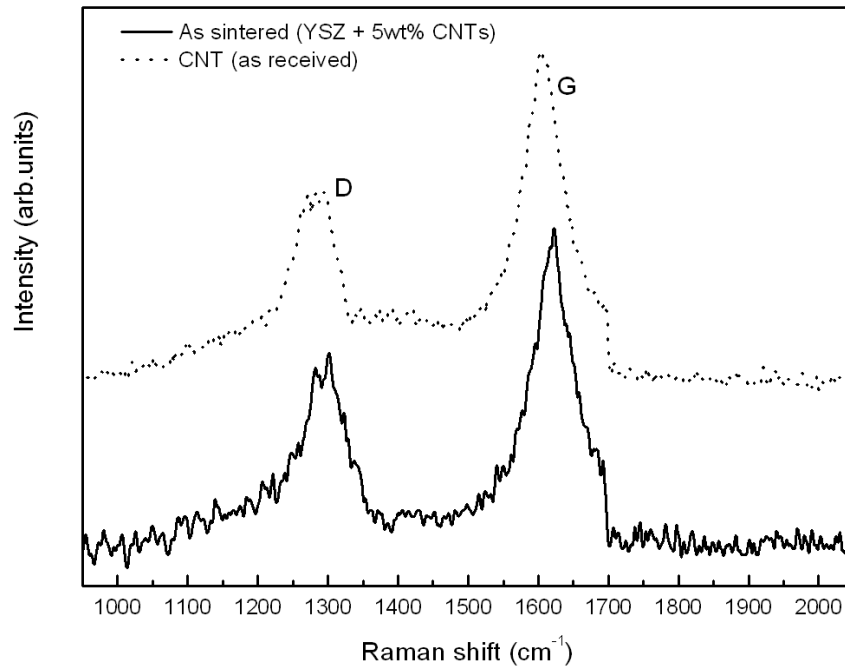


Fig. 5.6. Raman spectra in the D-band and G-band of as-received CNTs and sintered 3Y-TZP composites reinforced with 5 wt% CNTs.

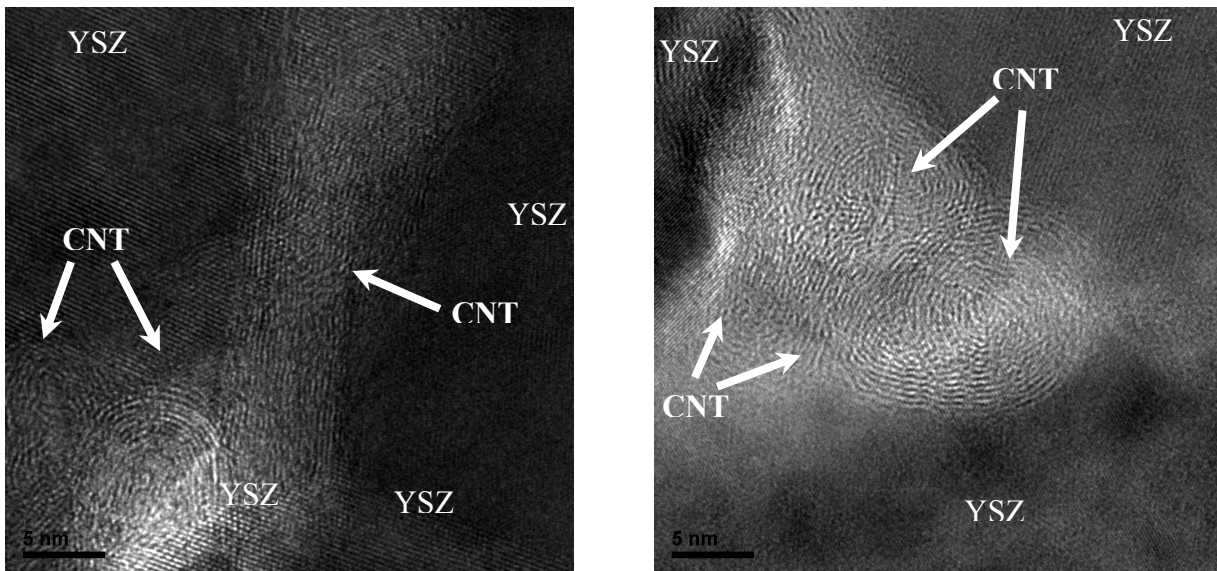


Fig. 5.7. HR-TEM of sintered 3Y-TZP reinforced with 5 wt% CNTs. Randomly oriented non-damaged CNTs in the grain-boundaries are observed.

Contrary to several investigations in which nanotubes have been damaged by high temperature sintering in a conventional furnace or hot pressing, the present study shows that spark plasma sintering is a promising method to produce full dense materials where the nanotube structure is not altered. The advantages of this sintering method are lower sintering temperatures, higher heating rates and shorter firing time compared to conventional techniques. Raman spectroscopy results (Fig. 5.6) in addition to HR-TEM images (Fig. 5.7) confirm that the processing route chosen here produces a good dispersion of the CNTs in the 3Y-TZP matrix without modification of their crystal structure (Fig. 5.7).

5.3. Room temperature mechanical properties

Fig. 5.8a and 5.8b, represent some interesting mechanical properties of CNTs reinforced zirconia nanostructured composites at room temperature. First, a significant increase in indentation fracture toughness (Fig. 5.8a) is found with increasing CNT content accompanied with a slight but steady increase in the hardness (Fig. 5. 8b). The indentation fracture toughness of 3Y-TZP reinforced by 5 wt.% CNTs reached $\sim 11 \text{ MPa}\cdot\text{m}^{1/2}$, which doubles that of monolithic 3Y-TZP. The fracture toughness was also measured by the single edge V-notch beam (SEVNB) method and is superimposed on data obtained by indentation showing that SEVNB fracture toughness also increases with CNTs amounts.

This improvement can be attributed to the extent of interfacial bonding between CNTs and zirconia grains formed during SPS and to the survival of CNTs after consolidation. A variation of the composite shear modulus versus monolithic specimen is related to the interfacial bonding of CNTs with matrix, since a good bonding can allow the load transfer to the strong CNTs to carry the applied stress. The shear dynamic modulus - measured in a free torsion pendulum- at room temperature for different composites is represented in Table 5.2. The excellent interfacial bonding between CNTs and zirconia is proven by the increase in the modulus of reinforced ceramics in comparison with the monolithic one (see Table 5.2). The shear modulus reaches 107 GPa for zirconia reinforced with 5 wt.% ($\sim 12.5 \text{ vol}\%$) of CNTs showing a 38% increase in comparison with monolithic zirconia.

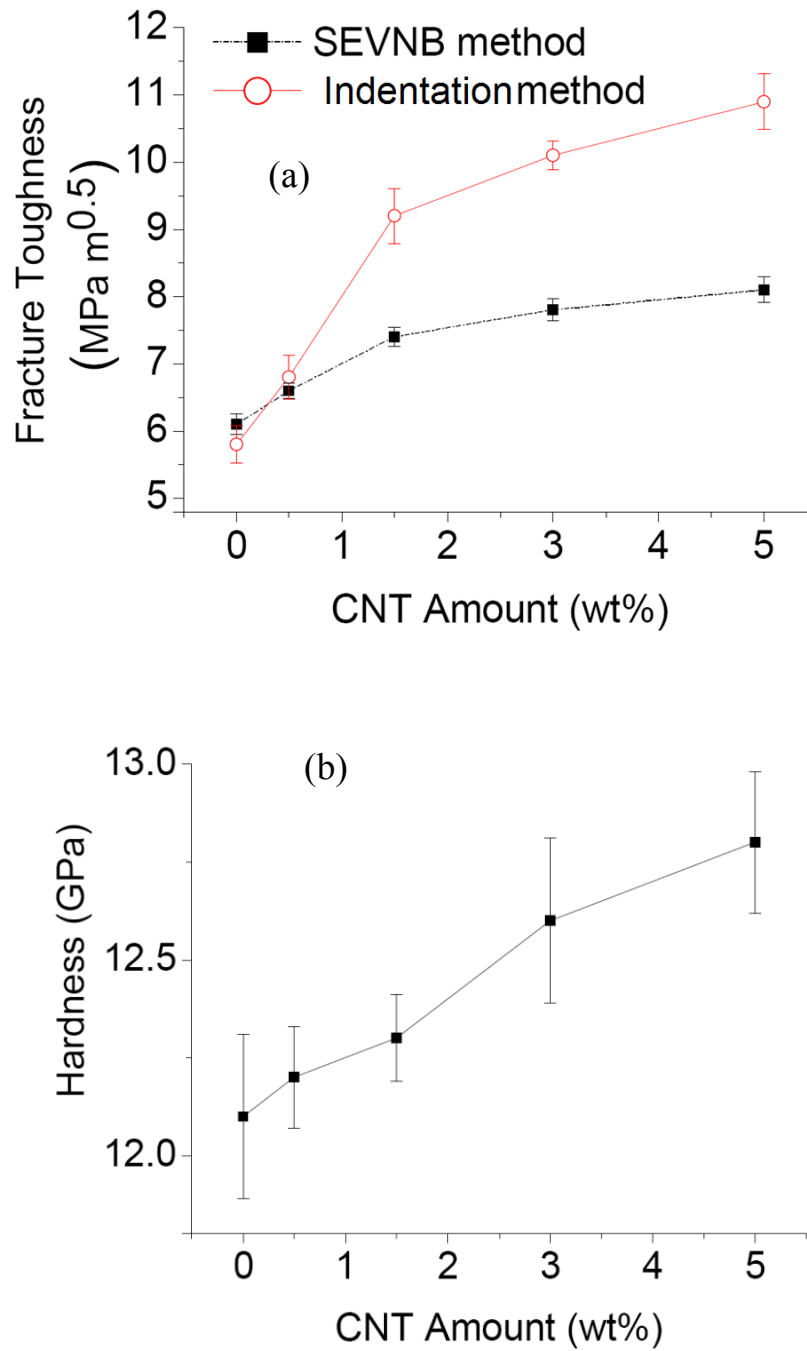


Fig. 5.8. Fracture toughness (a), Vickers hardness (b), as a function of CNTs wt%. Fracture toughness was measured by indentation as well as single-edge V-notch beam method.

Table 5.2. Shear modulus of sintered 3Y-TZP/CNTs nanocomposites with various amounts of CNTs in comparison with monolithic zirconia.

Material composition	Shear modulus (GPa)
3YSZ	78 ± 6.5
3YSZ/ 0.5wt% CNT	82 ± 5.4
3YSZ/ 1.5wt% CNT	92 ± 4.3
3YSZ/ 3wt% CNT	99 ± 3.8
3YSZ/ 5wt% CNT	107 ± 3.8

As mentioned in chapter 2, fracture toughness measured by indentation has been a matter of dispute [4, 17, 18]. Indentation is an indirect toughness-testing technique in shear mode, whereas the crack tip in fracture toughness measurement should be subjected to mode I tension. Wang et al. [4] showed that even if the indentation fracture toughness of alumina reinforced by CNTs is higher than that of monolithic alumina, their single edge V-notched beam (SEVNB) fracture toughness results did not demonstrate a significant difference. This is an argument to be taken into consideration when making fracture toughness assessment. Therefore, we also measured fracture toughness of 3Y-TZP/CNTs nanocomposite in bending tests. Although the increase in fracture toughness is not as high as in tests obtained by the indentation method, it is significant (Fig. 5.8a). To the best of our knowledge, the present result is the first that shows an improvement in fracture toughness of zirconia/CNTs under bending stress. The homogeneous distribution of high amounts (~12.5 vol.%) of CNTs (Fig. 5.4 and Fig. 5.5), the survival of CNTs after SPS consolidation (Fig. 5.7 and Fig. 5.6), the extended bonding between CNTs and zirconia grains and the high density of SPS samples (Table 5.1) result in high fracture toughness of nanocomposites. Cha et al. [19] have employed molecular level mixing (MLM) to fabricate Al₂O₃/CNTs nanocomposite to produce homogeneously dispersed CNTs in Al₂O₃ powder. However, the hardness decreased with an increase in the CNT volume fraction beyond 2 vol% because of CNT agglomeration. On the contrary, the present study shows a continuous increase in fracture toughness and hardness with CNT content up to 12.5 vol%.

It is well-known that in 3Y-TZP based ceramics, transformation toughening could result in a significant improvement in the toughness of the material. To distinguish the effect of phase transformation toughening [20] from the effect of CNTs on fracture toughness, the amount of stress-induced monoclinic phase on fracture surface was determined by XRD analysis. Fig. 5.9 shows the variation of the monoclinic phase on the fracture surface of the composites as a function of CNTs percentage.

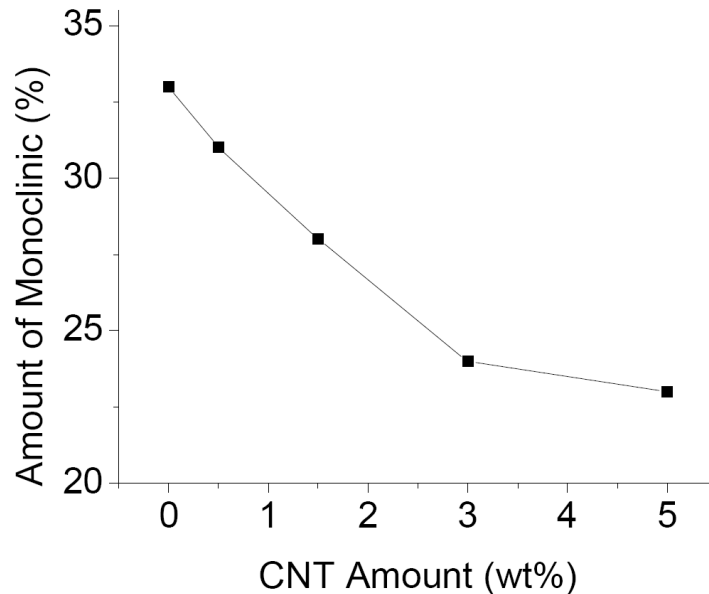


Fig. 5.9. Amount of stress-induced monoclinic phase in fracture surface of the nanocomposites as a function of CNTs wt.%.

Interestingly, a continuous decrease of stress-induced monoclinic phase with the increase of CNTs content is obtained. Thus, a higher fracture toughness of nanocomposite cannot result from transformation toughening and can only be attributed to nanotubes. The decreasing content of monoclinic phase in the composites with higher amount of CNTs is probably due to their smaller grain size. It is recognized that the propensity to undergo the transformation decreases with decreasing zirconia grain size [21].

It was frequently reported that in fiber-reinforced composite, fiber pull-out, crack deflection and crack bridging are the most effective toughening mechanisms. Fig. 5.10 shows a SEM picture of indentation-induced crack on the surface of 3Y-TZP/5 wt.%CNTs. The CNTs are stretched between crack faces, which shows crack bridging (Fig. 5.10b and c). Crack deflection (Fig. 5.10a) and CNTs pull-out (Fig. 5.10b) can also be seen.

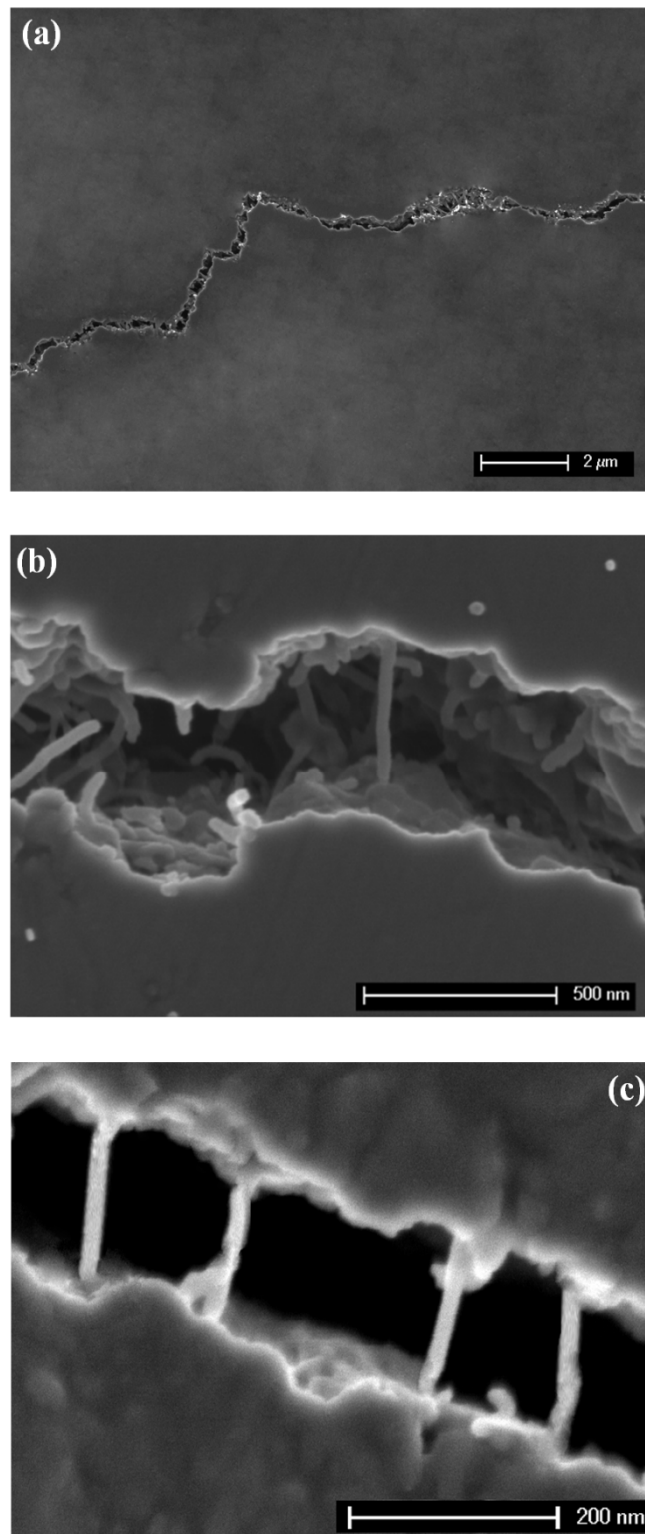


Fig. 5.10. SEM picture of indentation-induced crack on the surface of 3Y-TZP/5 wt.% CNTs shows different toughening mechanism.

The above-mentioned mechanisms are among possible classical toughening mechanisms of conventional ceramic composites reinforced by fibers and whiskers [22]. Although these mechanisms were mentioned several times as forceful ones to explain toughening in CNT-ceramic composites [23-28], there is a clear difference between fiber-reinforced and CNT-reinforced ceramics. It has been demonstrated that conventional fiber-ceramic composites show a compromise between toughness and strength [22, 29]. The fibers can bridge the crack in its wake and are pulled out as the crack advances, which dissipates energy and increases the toughness [30]. However, large fibers also produce large flaws, which in turn result in lower hardness and strength. In the present system, instead, we observe a simultaneous improvement in fracture toughness and hardness. Moreover, the classical fiber pull-out toughening mechanisms of traditional fibers/whiskers composites should be absent in the present CNT-composites for two reasons. (1) The conventional composites usually contain straight fibers, with a diameter larger than or equal to ceramic grain size (several micrometers) and with a length of several hundreds of micrometers. Instead, nanotubes that are flexible because of the high aspect ratio are not embedded within the ceramic grains like fibers and lie essentially at GBs. Therefore, they are not expected to give raise to a fiber pull-out toughening mechanism. The short length of emerging CNTs (< 200 nm) at fracture surface supports this hypothesis, as evidenced by Todd and his coworkers [26] energy dissipation produced by few nanometers (~ 100 nm) debonding of randomly oriented CNTs is negligible. (2) The interface between fiber and matrix has to be optimally designed [30]. A rather weak interface is needed in order to allow for fiber pull-out, which produces energy dissipation by friction, and consequently toughening [29]. However, in the present CNT-ceramic composite, the shear modulus measurements (Table 5.2) and HR-TEM observation (Fig. 5.11) indicate that we have a strong interface, which does not allow pull-out.

Another possible mechanism in CNT-ceramic composite, which could explain both toughening and strengthening is uncoiling and stretching of nanotubes. When the crack propagates intergranularly, the entangled nanotubes bundles are uncoiled in the first step. With further propagation of crack, the uncoiled nanotubes would stretch, while their end is anchored within the grains. Fig. 5.10c shows these stretched nanotubes, which produce crack bridging. With further propagation of crack, the nanotubes will separate from the ceramic interface or fail (Fig. 5.4 and Fig. 5.10b). The uncoiling/stretching produces friction work and dissipates energy at the crack tip, which results in higher toughness. Moreover, nano-scale CNTs would produce smaller or no flaws relative to conventional fiber and whiskers.

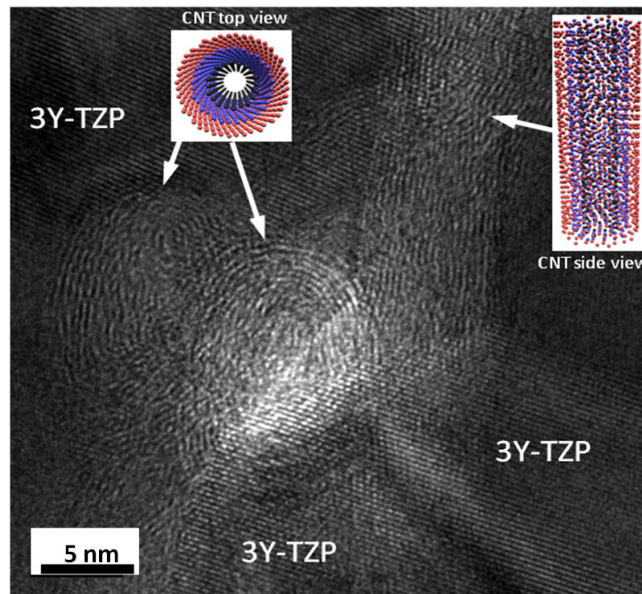


Fig. 5.11. HR-TEM of interface between CNTs and zirconia grains.

5.4. Room temperature electrical conductivity

The electrical conductivity as a function of CNT concentration is presented in Fig. 5.12. A significant enhancement in the conductivity, varying in orders of magnitude, is observed with CNT addition. This is not surprising and was already observed in different ceramics[31-34]. Long, thin and electrical conductive nanotubes create an interconnected percolation network through an insulating matrix.

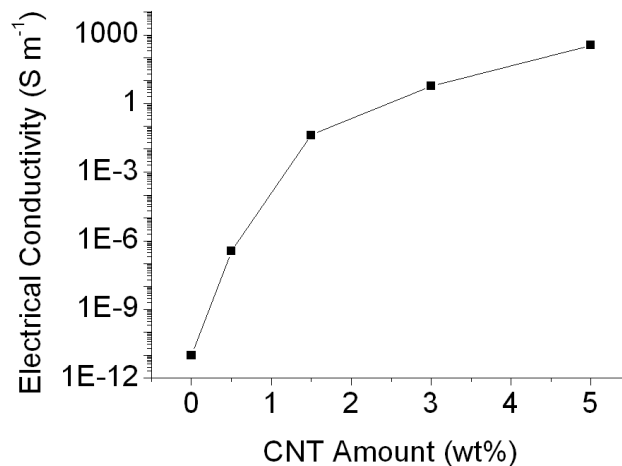


Fig. 5.12. Electrical conductivity of the nanocomposites as a function of CNTs wt.%.

5.5. High temperature mechanical properties

High temperature deformation of the composites was analyzed by two techniques in parallel;

- 1- Compressive creep test at 1600 K and low stress regime (8 MPa).
- 2- Mechanical loss measurements as a function of temperature (between 300 and 1600 K) / and as a function of frequency (at constant temperature equal to 1600 K).

It will be shown that there is a close correlation between the results obtained by these techniques, both indicating how the materials structure influence the creep rate.

As it was explained in chapter 2, mechanical spectroscopy is a very sensitive technique to measure the mobility of structural defects such as point defects, dislocations and GBs and phase transformations [35]. What can be inferred from the literature is that the high temperature ductile behavior of 3Y-TZP should be mainly associated with GB sliding [36]. Therefore, mechanical spectroscopy technique can be applied as a complementary method by which GB motion and nature during creep can be explained in order to clarify the effect of CNTs on high temperature plastic deformation of ceramics.

5.5.1. Creep results

Fig. 5.13 shows the strain recorded as a function of time during compressive creep tests in low stress regime (6 MPa). In general, the creep response of the materials is influenced by the addition of CNTs, i.e. the creep strain tends to smaller values with the increase of CNTs addition. In the case of specimens reinforced by the highest amounts of CNTs (3 and 5 wt%), the strain reaches a constant value, soon after a transient creep in the first few minutes of the test. On the other hand, for monolithic 3Y-TZP, strain continuously increases with time, in spite strain hardening.

The variation of zirconia grain sizes with different amounts of nanotubes (Table 5.1) evidences that such creep reduction is effectively due to CNTs. Opposite to common behavior of ceramics at high temperature, the specimen with smallest grain size

(highest CNT content) shows the lowest creep. The reason for the higher creep resistance in finer structures is the presence of CNTs pinning GBs at high temperature.

To analyze the creep results more into depth, the creep strain rate is represented in Fig. 5.14 as a function of creep strain for monolithic 3Y-TZP and for the composites. It is obvious that, whatever the creep strain is, the creep rate decreases with increasing the nanotube percentage. This result is consistent with those reported by Zapata-Solvas [37, 38] for alumina-CNT composite. For monolithic zirconia, steady state creep is reached, where the constant creep rate is about 1.5×10^{-4} . This behavior is attributed to the well known superplastic deformation of 3Y-TZP at high temperatures. 3Y-TZP reinforced with very low amount of CNTs i.e. 0.5 wt%, demonstrates steady state creep, however, the deformation rate was less than in monolithic zirconia. A slow linear decrease in the creep rate (in log scale) as a function of strain was observed in monolithic zirconia and 3Y-TZP/ 0.5 wt% CNTs. Bernard-granger et al. [39], recently have proven that this tendency in nanostructured zirconia is owed to dynamic grain growth, which acts as accommodation process. For other composites with higher amount of reinforcements i.e. 1.5, 3 and 5 wt%, the steady state area was not observed. However, after a transitory of small strain, creep rate drops significantly (several decades). In contrast, monolithic 3Y-TZP shows steady state superplastic deformation. For instance in 3Y-TZP reinforced with 5 wt% CNTs, the creep rate decreases three orders of magnitudes after only strain of 0.07.

As TEM (Fig. 5.5) observation has shown, CNTs seem to form an interwoven network around zirconia grains. In the beginning stage of creep, the grains may slightly rearrange to reach a relaxed status, which results in a higher creep rate at the beginning (Fig. 5.14). As strain increases, the CNTs entangle and the creep rate decreases strongly to almost zero.

5.5.2. Mechanical spectroscopy results

Isothermal (at fixed temperature) and isochronal (at fixed frequency) mechanical loss measurements of high purity 3Y-TZP monolithic ceramics and composites reinforced with CNTs were conducted. All samples were produced by spark plasma sintering and their initial properties (density and grain size) are presented in Table 5.1.

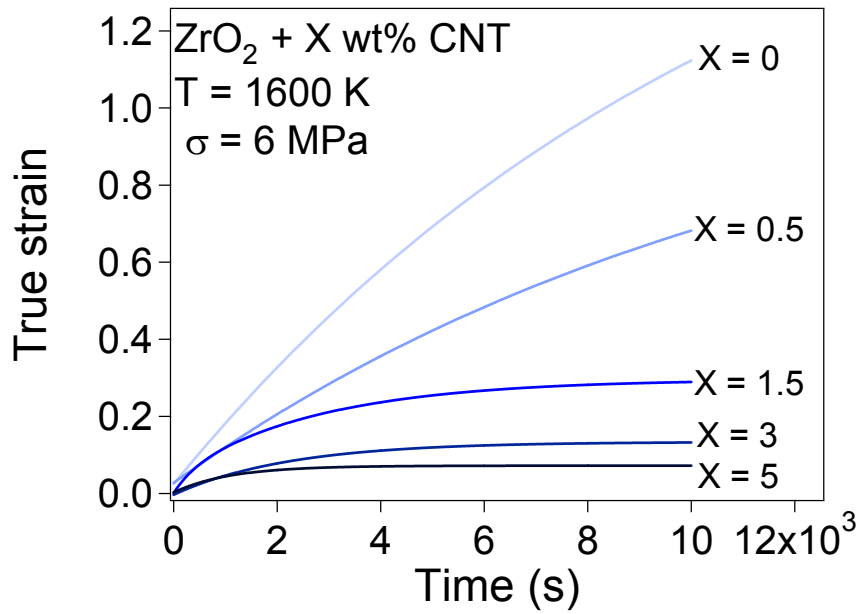


Fig. 5.13. Strain recorded as a function of time during compression creep tests at 1600K for the composites with different amount of CNTs.

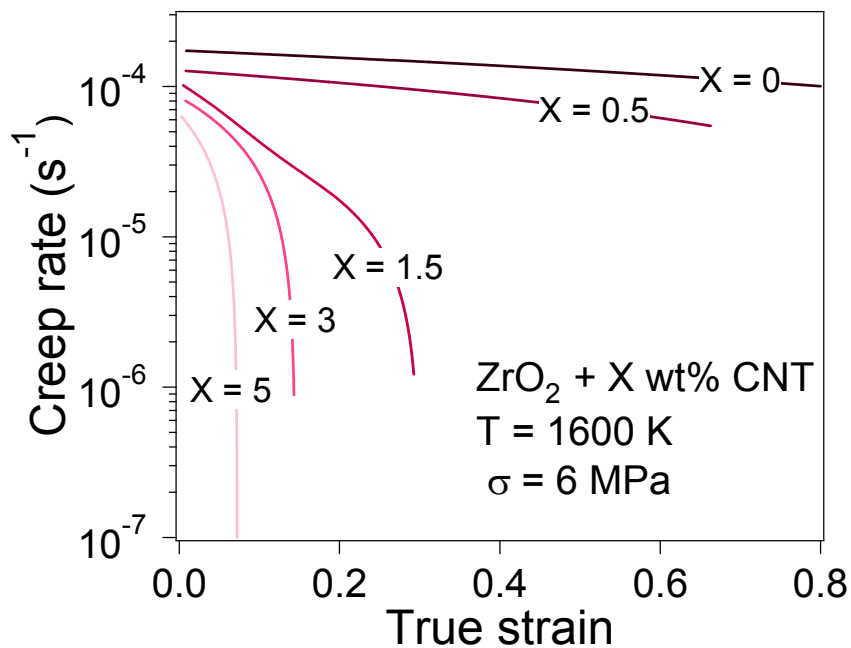


Fig. 5.14. Creep rate as a function of creep strain measured at 1600 K for composites with different amount of CNTs.

5.5.2.1. Isochronal spectra of 3Y-TZP composites

Fig. 5.15a and b show the variation of mechanical loss $\tan(\phi)$ and relative shear modulus as a function of temperature for composites with different amounts of CNT in comparison with monolithic zirconia. As previously observed in zirconia [40-43], and explained in chapter 2, the spectra are characterized by an exponential increase in mechanical loss at temperatures above 1250 K in the monolithic sample, accompanied by a steep decrease in the shear modulus. The exponential increase in $\tan(\phi)$ has been associated with the right shoulder of a GB sliding peak, located at temperature higher than 1600 K at 1 Hz [44].

Clearly, the presence of CNTs shifts the exponential increase at higher temperature, e.g. for 3Y-TZP/5wt.%CNT it starts at about 1400 K. Another interesting point to notice in Fig. 5.15b is the higher shear modulus of 3Y-TZP/CNTs nano-composite in comparison with monolithic zirconia in the whole range of testing temperature, which is in agreement with the results of the modulus measured at room temperature (Table 5.2). Daraktchiev et al. [1] showed higher mechanical loss of monolithic zirconia in comparison with zirconia-CNTs composite, but their HR-TEM analysis have revealed that conventional sintering at 1723 K for 3 h could not preserve the nanotube structure (probably due to long time of/ higher temperature of sintering), leading to formation of amorphous carbon at the GBs. Therefore, the CNT pinning efficiency in their composites was lower than that of the present work [1].

Diffusional creep and GB sliding are the dominant deformation mechanisms in zirconia at high temperatures. The higher creep resistance of the present nanocomposite may result from a pinning effect of GBs by the CNTs. A theoretical model was developed by Lakki et al. [44, 45] (see chapter 2) to investigate the role of material stiffness on the presence of microcreep in ceramics. Based on the model, the presence of the CNTs at GBs can provide an additional restoring force that is not temperature dependent. Therefore, creep decreases or is suppressed and anelastic strain that is measured by mechanical spectroscopy is strongly reduced or delayed to higher temperature. The details of possible mechanisms will be explained in 5.5.2.3.

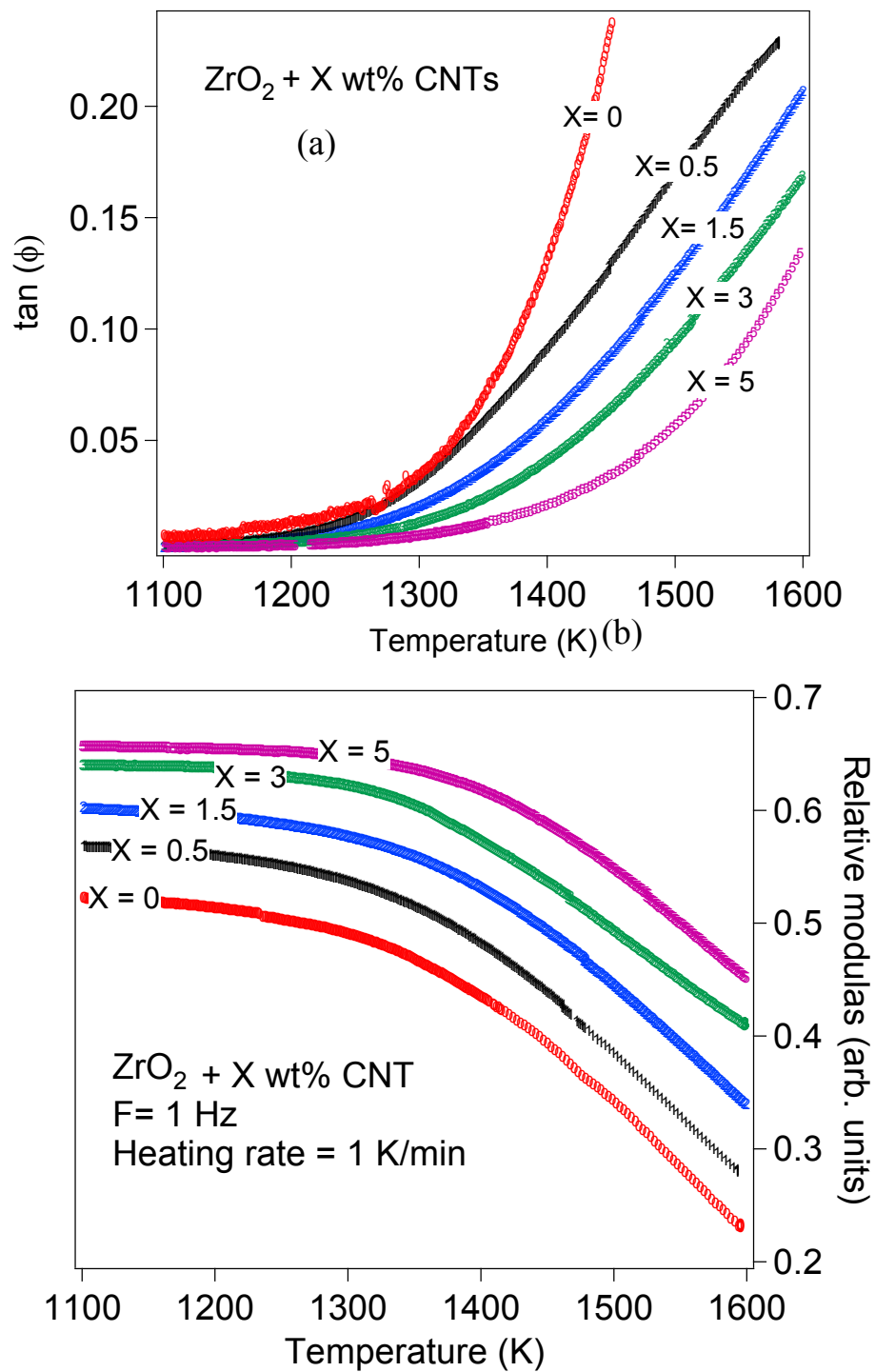


Fig. 5.15. Mechanical loss ($\tan(\phi)$) and relative shear modulus as a function of temperature for zirconia/CNTs nanocomposites in comparison with monolithic zirconia. The measurement frequency was 1 Hz.

5.5.2.2. Isothermal spectra of 3Y-TZP composites

Fig. 5.16a and b show the effect of CNTs on mechanical loss $\tan(\phi)$ and shear modulus as a function of frequency, measured at 1600 K. The typical spectrum of 3Y-TZP was observed in all spectra, which consists of a mechanical loss peak at a frequency of approximately 0.1 Hz, superimposed on an exponential increase at lower frequency. Two main differences between the monolithic zirconia spectrum and the composites spectra can be observed in Fig. 5.16a. First, the addition of CNTs leads to a better resolved peak. Second, the mechanical loss in CNT containing specimens is lower.

A general modulus drop at low frequencies is observed in 3Y-TZP and composites (Fig. 5.16b); however two differences should be noted. Firstly, regardless to the value of frequency, the relative shear modulus of the reinforced composites increases with increasing CNT contents. Secondly, the composite stiffness in the specimens with high amounts of CNTs (3 and 5wt%), although it decreases at low frequencies, it remains at relatively high values in comparison to monolithic specimen. For instance, the 3Y-TZP/ 5 wt% CNTs modulus at $f = 1$ mHz is equal to that of monolithic zirconia at $f = 1$ Hz.

5.5.2.3. Theoretical model

A general isothermal spectrum of monolithic 3Y-TZP, consisting of a mechanical loss peak at a frequency of about 0.1 Hz superimposed on the exponential increase at lower frequencies, can be explained by a theoretical GB sliding model of ceramics, as presented by Lakki et al [44, 45] and reviewed in Chapter 2. The model accounts for relative sliding of equiaxed grains separated by a viscous layer with viscosity and thickness of η and δ , which constrained at the triple junctions. When a periodic stress (σ) is applied on hexagonal grains, two distinguished forces are influential on the anelastic relaxation of the system. (1) a dissipative force resulting from the viscosity η of the intergranular layer and (2) a restoring force k_{jun} , corresponded to the elasticity of the adjacent grains in the triple junctions, by which the sliding is suppressed. The mechanical loss, calculated by Lakki et al [44, 45](Eq. 2.30).

$$\tan(\Phi) = \frac{G}{d} \frac{\omega \frac{\eta}{\delta}}{\left(\frac{k_{jun} G}{d} + k_{jun}^2 \right) + \left(\omega \frac{\eta}{\delta} \right)^2} \quad (2.30)$$

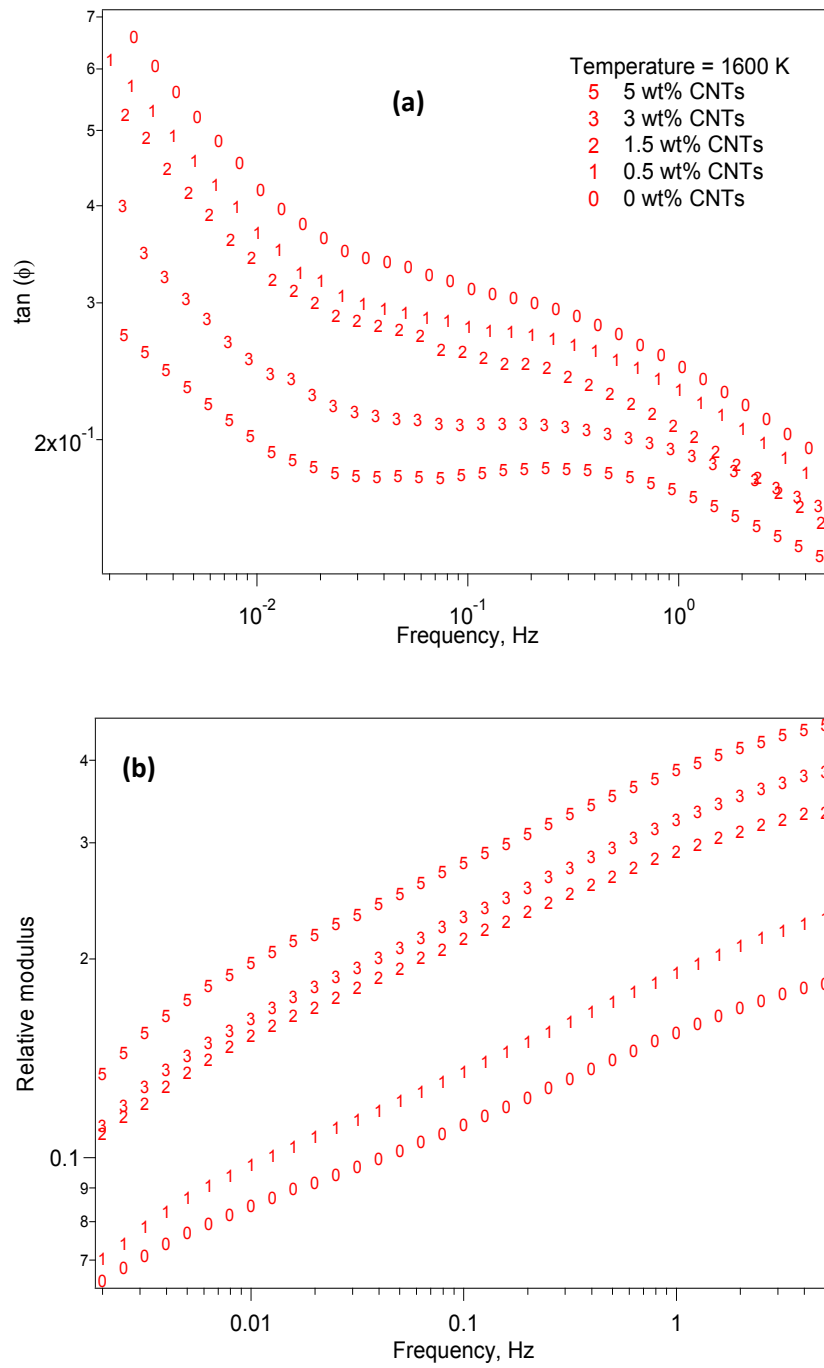


Fig. 5.16. Mechanical loss (a) and relative shear modulus (b) measured at 1600 K as a function of frequency for composites with different amount of CNTs.

If the restoring force (k_{jun}) is constant, the mechanical loss has to form a Debye peak. However, the experimental results (Fig. 5.16a) and calculations do not show a well-marked peak (Fig. 5.17), but an exponential increase in $\tan(\Phi)$ at low frequencies or high temperatures. The absence of a well-marked peak was justified considering that the restoring force due to the elasticity of adjacent grains decreases strongly at low frequencies or high temperatures [45]. The restoring force is due to neighbor grain elasticity against sliding at triple junctions. Therefore, it seems reasonable to assume that k_{jun} would be proportional to the material time dependent shear modulus $G(t)$, which decreases strongly at high temperature and low frequencies.

$$k_{\text{jun}} \approx G(t) \approx \frac{\sigma}{\varepsilon_{\text{el}} + \varepsilon_{\text{pl}}(t)} \quad (2.34)$$

In order to express k_{jun} in the condition of mechanical spectroscopy, we shall consider further assumptions. Given that creep conditions (temperature and stress), as presented in Fig. 5.13 and 5.14, are close to the temperature and stress amplitude used in mechanical spectroscopy measurements, it is plausible to admit that during the mechanical spectroscopy experiments micro-creep can occur to some extent. However, stress is acting during each half period with a mean value of half of maximum stress amplitude ($\sigma_0 / 2$). Then, k_{jun} becomes as :

$$k_{\text{jun}}(f) = C \frac{\sigma}{\frac{\sigma}{G} + A \frac{\sigma/2}{2d} \exp\left(-\frac{\Delta H_{\text{act}}}{kT}\right) \frac{1}{f}} \quad (2.34)$$

where ΔH_{act} is the deformation activation enthalpy, A is a constant which is obtained from the creep curves. ΔH_{act} can be obtained by the method of the so called master curve (details of calculation of the activation energy is explained in 5.5.2.4). G has been measured for different compositions by free torsion pendulum (Table 5.2).

In Fig. 5.17b the theoretical evolution of K_{jun} as a function of frequency is shown at 1600 K for monolithic 3Y-TZP. A predicted sharp decrease of the sample rigidity in the low frequency range (~ 0.1 Hz) is observed. For frequencies below 0.01 Hz (periods longer than 100 s) the restoring force almost disappears, which is in good agreement with micro-creep, taking place at low frequency.

The equation (Eq. 2.34) is now introduced into Eq. 2.30 and the resulting calculated spectra are plotted in Fig. 5.17c. Indeed, the absolute value of $\tan(\phi)$ in Fig. 5.17c,

Chapter 5

has not meaning, while no assumption was taken into account for the number of boundaries which participate in micro plastic deformation. Nevertheless, the similarities between the calculated spectrum (Fig. 5.17c) and the measured one (Fig. 5.16a) allows us to interpret the peak as GB sliding peak and the transition from peak to mechanical loss background as due to the disappearance of the restoring force. In this case, strain is not anymore limited and macroscopic creep occurs.

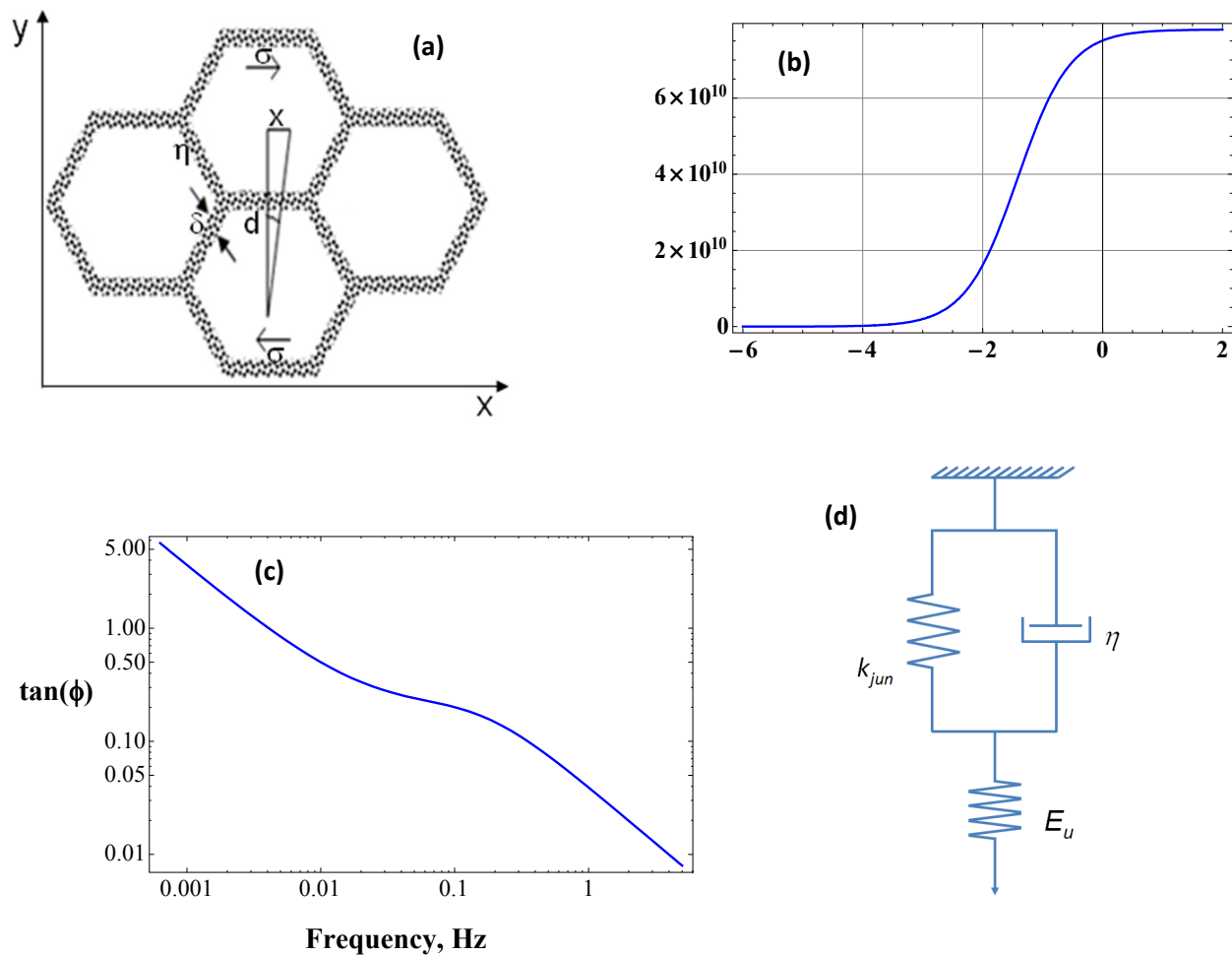


Fig. 5.17. (a) Model of two hexagonal grains separated by an intergranular layer of viscosity (η) and sliding relatively to each other under the effect of applied shear stress (σ). (b) Calculation of the modeled restoring force as a function of frequency for pure zirconia. (c) Isothermal mechanical spectra at 1600 K as calculated by the proposed model. (d) The rheological model representing the anelastic/plastic deformation of pure 3Y-TZP.

From a rheological point of view, Fig. 5.17d shows a model which can represent the relative sliding of grains as explained in Fig. 5.17a. A dashpot of viscosity (η) in parallel with a spring of constant (K_{jun}) and both in series with a spring of constant (E_u). In the model, K_{jun} represents the restoring force corresponding to the elasticity of the adjacent grains, and dashpot of viscosity η represents the amorphous layer between the grains. The unrelaxed young modulus E_u spring accounts for the elastic deformation of material. The spring K_{jun} represents the recoverable nature of the anelastic deformation. If this spring does not operate, theoretically there is no limitation for anelastic strain and consequently creep occurs, which may happen in the case of very low frequencies or high temperatures (as shown in Fig. 5.17b).

Derived from the relative sliding of grains (Fig. 5.17a) and the rheological model (Fig. 5.17d) two parameters can influence micro-creep: either (1) the intergranular viscosity (η), or (2) the restoring force (K_{jun}).

The variation of the viscosity of intergranular phase has been described by several authors [45]. For instance, Daraktchiev et al. [46] have shown that 2 wt% SiO₂ doped 3Y-TZP can form a significant amount of intergranular amorphous phase with respect to the monolithic 3Y-TZP, which results in a significant increase in GB sliding. A good correlation to creep test was observed by Morita et al.[47, 48], who showed that by an addition of a small amount of SiO₂ the creep rate increases 100 times compared to monolithic 3Y-TZP [48]. Since high resolution TEM observations (Fig. 5.7) have not revealed any amorphous carbon in the boundaries, we assume that the addition of CNTs does not affect the viscosity of intergranular amorphous layer. In contrast, one can observe the nanotube fringe spacing that suggests the CNT structure unchanged during sintering.

The second influencing parameter is the restoring force. According to Eq. 2.34, the restoring force may be associated with $G(t)$. Experimental results (Fig. 5.13 and 5.15a, 5.16a), show that CNTs can suppress the GB sliding as well as creep strain. Hence, it seems that the nanotubes may improve the restoring force at high temperatures. Even if our measurements have shown that the addition of CNTs increases the shear modulus at room temperature (Table 5.2), this could not insure higher stiffness at high temperature. Nevertheless, the relative shear modulus measured by mechanical spectroscopy as a function of frequency at 1600 K (Fig. 5.15b and 5.16b) shows that the addition of CNTs increases the high temperature stiffness. As a consequence, CNTs represent a new way to produce a restoring force at high temperature. This new restoring force may be represented by a new spring K_{CNT} in the rheological model (Fig. 5.18d). In view of the fact that these two springs are in parallel, they can be presented as one spring with a resultant spring constant

of $K_{\text{tot}} = K_{\text{CNT}} + K_{\text{jun}}$ (compare Fig. 5.17d and 5.18d). Thus, in the theoretical model (Fig. 5.18a), a new term has to be considered for CNTs located in GBs, which can hinder the relative sliding of two grains. The same calculations have been carried out in order to demonstrate the effect of CNTs on the restoring force (K_{tot}) as well as on $\tan(\phi)$ (Fig 5.18b and 5.18c). Interestingly, a good agreement is observed between the measured $\tan(\phi)$ in Fig. 5.16a, and the calculated one (Fig. 5.18c). $\tan(\phi)$ decreases with increasing the CNT amounts. At high temperature for all specimens three anelastic/ micro-plastic deformation regions can be distinguished:

(1) High frequency region ($f > 10^{-1}$ Hz): K_{tot} has a constant value (Fig. 5.18b), although has different values for different composites. According to the calculations, higher K_{tot} is obtained with a higher amount of CNTs. A higher K_{tot} for composites involving more CNTs, which gives rise to a higher shear modulus, may be caused by a strong bonding between CNTs and matrix. In this region, the anelastic deformation would be only due to short range relative sliding of grains. Hence, this part can be considered as the high frequency shoulder of peak, located at lower frequencies. Thus, no permanent deformation (creep) could be expected, where, K_{tot} is strong enough strong. In this region, $\tan(\phi)$ for the specimens is almost zero.

(2) At low frequencies ($f < 10^{-3}$ Hz) or very high temperatures, whatever the composition is, the restoring force fully disappears (Fig. 5.18b). In other words, the diffusional creep occurs readily and there is no limitation for long range GB sliding, and $\tan(\phi)$ increases exponentially. Meanwhile, it can be seen that for specimens with higher amounts of CNTs, even at very low frequencies (see Fig. 5.16a and 5.18c), $\tan(\phi)$ shows smaller values. From the phenomenological point of view, GB sliding is the controlling mechanism while the accommodation process (diffusion) is fast. The presence of nanotubes cannot affect diffusional process significantly, since it is controlled by Nabarro-Herring type diffusion (volume diffusion). While, CNTs can suppress grain sliding by providing obstacles on the boundaries, as nanoparticles or conventional whiskers act against grain sliding. Therefore a less uniform dispersion of CNTs at the GBs results in less effective obstruction of GB sliding [37].

(3) Intermediate frequencies $10^{-3} < f < 10^{-1}$ Hz: transition between anelastic and plastic (creep) deformation or transition from the peak to the background. Yet, this transition could stem from a strong decrease in the restoring force (K_{tot}). As calculated (Fig. 5.18b), addition of CNTs could shift the K_{tot} reduction to lower frequencies. Consequently, the transition from the peak to the background is observed at lower frequencies (Fig. 5.18c and 5.16a). The better resolved peak in composites with a higher amount of CNTs should be attributed to the fact that CNTs provide a higher restoring force, which is maintained at lower frequencies or higher

temperatures. This is in a good agreement with the theoretical model initially developed by Lakki, which says that if the restoring force remains constant at low frequency or high temperature, $\tan(\phi)$ spectrum exhibits a peak [44].

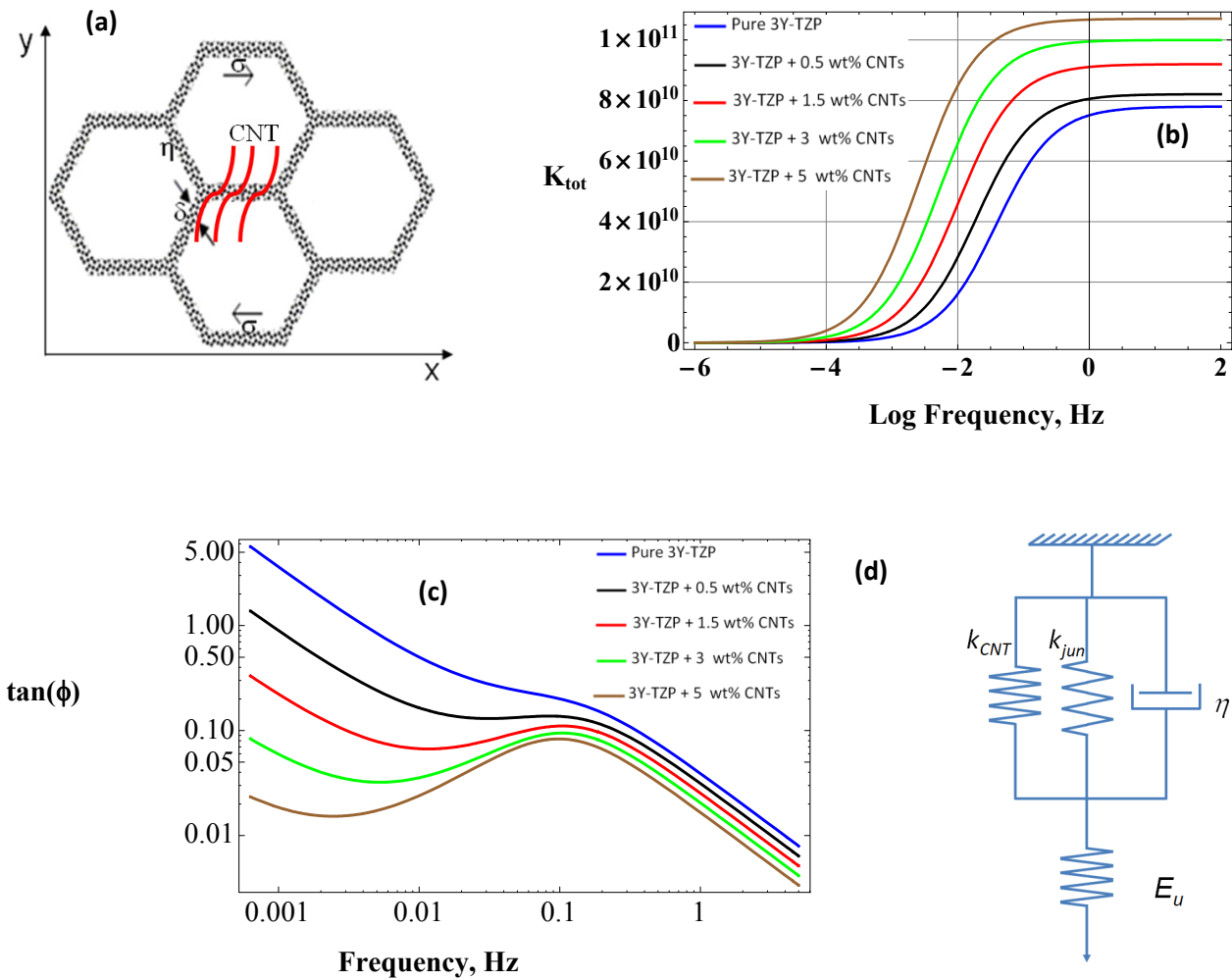


Fig. 5.18. (a) Modified model of two hexagonal grains reinforced with nanotubes separated by an intergranular layer of viscosity (η) and sliding relatively to each other under the effect of applied shear stress (σ). (b) Calculation of the modeled restoring force ($K_{tot} = K_{jun} + K_{CNT}$) as a function of frequency for zirconia reinforced with different amount of CNTs. (c) Isothermal mechanical spectra at 1600 K as calculated by the proposed model for composites. (d) The rheological model representing the anelastic/plastic deformation of 3Y-TZP reinforced with CNTs. K_{jun} and K_{CNT} represent the restoring force due to elasticity of adjutant grains and carbon nanotubes, respectively.

It is worth to mention the fact that sliding between CNTs within the bundles is likely to occur easily, as the bonding between individual CNTs or between layers of CNT is relatively weak. Perhaps, the CNTs may even act as lubricant for GB sliding. But, due to the 3 dimensional random distributions of CNTs in the boundaries (Fig. 5.11), some CNTs would be subjected to tension. Therefore, the GBs are partially blocked, and higher stresses are needed to maintain a given steady-state creep rate.

5.5.2.4. Activation Energy: New master curve model

One way to estimate the activation enthalpy ΔH_{act} and the limit relaxation time τ_0 is through an Arrhenius diagram. Reporting the logarithm of the peak frequency (without background) as a function of the inverse of peak temperature produces a straight line, the slope of which yields ΔH_{act} . τ_0 is obtained from the intersection of the line with the y-axis. In fact, background subtraction is not allowed when the same mechanisms are responsible for the entire mechanical spectrum (peak superposing on an exponential increase) as is the case of zirconia and alumina ceramics. In such cases, the estimation of the activation parameters can be done by a superposition of the mechanical-loss spectra to obtain a master-curve spectrum. This method is valid if the microstructure of the sample does not change during the measurement. The details of this technique have been explained in Chapter 2 (2.4.2.3).

Therefore, several isothermal measurements in the range from 1400 to 1600 K of the reinforced specimens have been carried out in the present study. Fig. 5.19 shows isothermal mechanical loss spectra data collected upon heating (black markers) and cooling (gray markers) for 3wt% CNTs+ 3Y-TZP sample. One can observe that the peak position and the peak to background transition strongly depend on the temperature.

Based on the calculation presented in chapter 2 (2.4.2.3), by shifting the isothermal spectra in Fig. 5.19 along the frequency axis, a master curve can be obtained (as shown in Fig. 5.20) with superimposition over the spectrum at 1600K. The master curve confirms that the high temperature spectrum is composed of a peak located at middle frequency ($\sim 0.5\text{Hz}$) and a background in the low frequency range ($<0.01\text{Hz}$). It is important to note that the master curve can cover a range of 8 decades in frequency, while one spectrum only covers 4 decades. However, the result of the superimposition in the master curve is rather disappointing (Fig. 5.20).

In order to determine ΔH_{act} and τ_0 , a procedure has been developed (see details in 2.4.2.3). According to Eq. 2. 48 and reporting the $\Delta(\log(f))$ versus $\Delta\left(\frac{1}{T}\right)$ results in an Arrhenius plot (the plot is embedded in Fig. 5.20), the slope of which gives the ΔH_{act} , which was found to be 805 kJ.mol^{-1} .

This value is higher than the activation enthalpy values of all possible deformation mechanisms as deduced by numerous authors [39, 42, 43, 45, 47, 49-51] over a wide range of creep stresses, grain sizes and temperatures. For instance in the same stress regime ($<10 \text{ MPa}$), Owen and Chokshi [51] proposed a GB sliding mechanism controlled by interface-reaction with an activation enthalpy of 550 kJ.mol^{-1} . A similar value of enthalpy was reported by Morita and Hiraga [47] for deformation of fine grain 3Y-TZP ($0.35\mu\text{m}$). These authors proposed Nabarro-Herring creep as probable mechanism for low-stress deformation of 3Y-TZP, where no intragranular dislocation activity was observed. Based on mechanical-loss analysis, Ionascu and Schaller reported 636 kJ.mol^{-1} as the activation enthalpy for GB sliding in CNT-reinforced 3Y-TZP [12, 43, 52]. It appears that the activation enthalpy obtained from the master curve in Fig. 5.20 is overestimated.

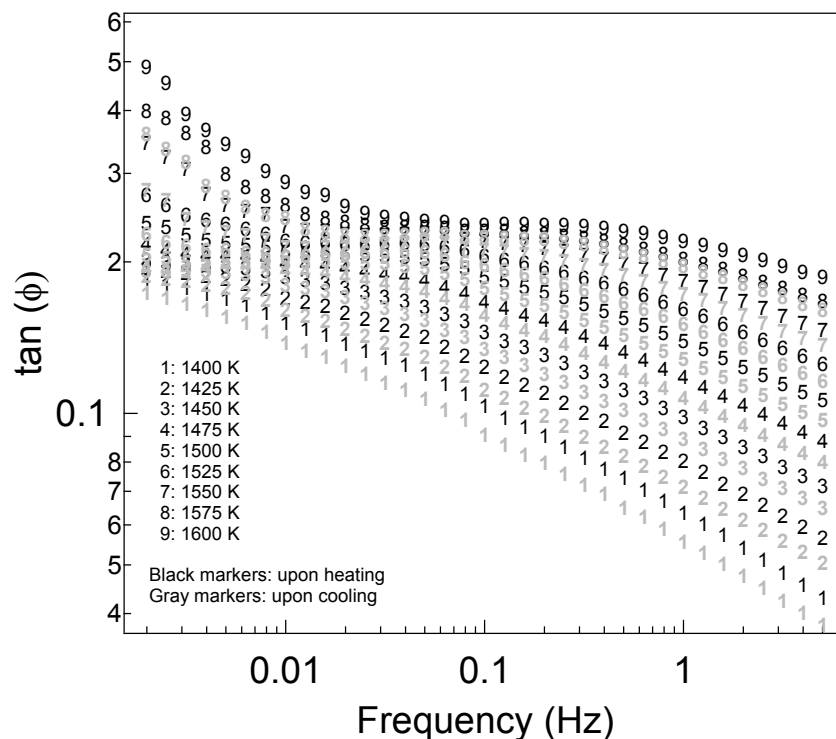


Fig. 5.19. Isothermal mechanical loss spectra of 3Y-TZP with 3wt% CNTs in temperature range 1400-1600K.

On the other hand we know that the master curve construction and the relevant ΔH_{act} are valid if the microstructure of the sample does not change during measurements. Indeed, if the microstructure changes, e.g. if grain growth occurs during measurements, $\tan(\phi)$ will not be only a function of the product $\omega\tau$. In particular, this is possibly the case for nanoscale grains, because they have higher potential for grain growth. Also, it has been reported that the GB migration (dynamic grain growth) can be accelerated during deformation [39, 53]. An interesting feature that can be observed in Fig. 5.19, is that upon cooling the level of mechanical loss in all of the spectra obtained between 1400 and 1600 K is lower than upon heating, while the peak moves to a lower frequency. This is a hint that during annealing at high temperature, the microstructure has changed.

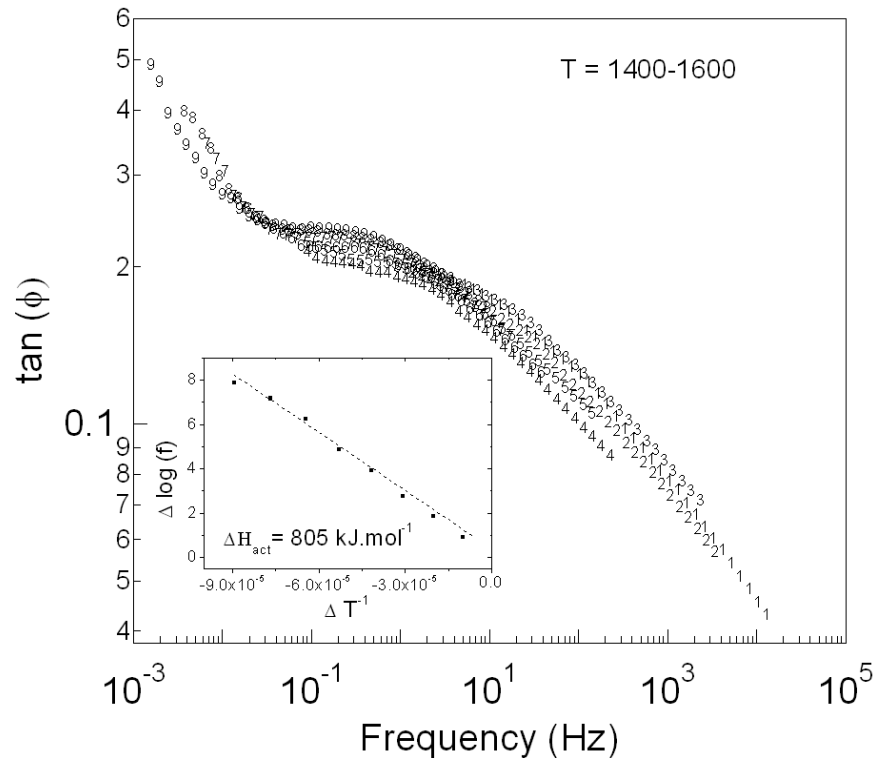


Fig. 5.20. Master curve construction using former method and (c) master curve construction using new developed model of 3Y-TZP with 3wt% CNTs in temperature range 1400-1600K. The $\Delta(\log(f))$ versus $\Delta\left(\frac{1}{T}\right)$ results in an Arrhenius plot embedded in the figure.

A literature review also confirms this hypothesis. Bernard-Granger [39] and Morita [47] have shown that at temperature higher than ~ 1500 K a significant grain growth occurs during creep measurements. It is also known that for ultrafine 3Y-TZP, the static grain growth can start at a temperature of about 1500 K [6]. Fig. 5.21a and b show SEM micrographs of polished surface of as sintered sample before and after mechanical spectroscopy measurements. The images prove that the size of the grains increases by a factor ~ 2 (from ~ 120 nm in as sintered to ~ 230 nm after measurements).

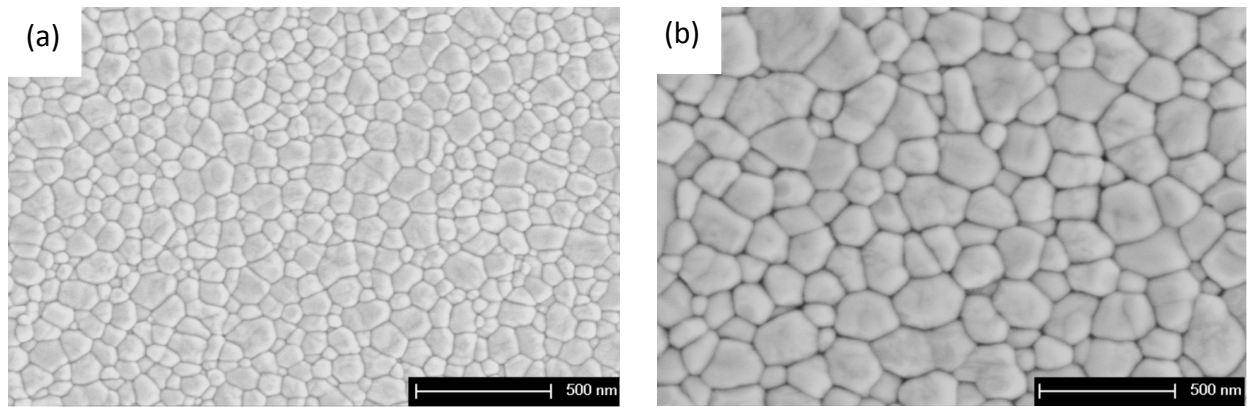


Fig. 5.21. SEM micrographs of the sample in (a) as sintered condition (before measurements) and (b) after mechanical spectroscopy measurements.

The mechanical loss can be calculated by introducing the phenomenological equation of creep (see chapter 2.4.2.4). Which define as:

$$\tan(\phi) = C \frac{\sigma^{n-1}}{\omega d^p} \exp\left(-\frac{\Delta H_{\text{act}}}{RT}\right) \quad (2.52)$$

Rearrangement of Eq. 2.52 in logarithmic form yields:

$$\log(\tan(\phi)) + p \log(d) + (1 - n) \log(\sigma) = -\frac{\Delta H_{\text{act}}}{RT \ln(10)} + \log(\omega) + C \quad (5.2)$$

The present equation (Eq. 5.2) introduces the effect of grain size on $\tan(\phi)$. Similarly to Eq. 2.47, Eq. 5.2 can be used to obtain a corrected master curve and consequently the activation enthalpy. In the present measurements, the stress amplitude was constant. As a consequence, the stress variation between two spectra ($\Delta[(1 - n) \log(\sigma)]$) is equal to zero. Therefore, from Eq. 5.2 one obtains:

$$\Delta [\log(\tan(\phi)) + p \log(d)] = -\frac{\Delta H_{\text{act}}}{R \ln(10)} \Delta \left(\frac{1}{T}\right) - \Delta \log(f) \quad (5.3)$$

This equation shows that if the microstructure changes during the measurements, the master curve can be obtained by two shifts of the initial spectra: along Y-axis ($\tan(\phi)$ axis) in order to take into account the grain growth and in the X-direction (frequency axis) to account for thermal activation.

The general decrease in $\tan(\phi)$ that occurred in Fig. 5.19 during cooling (gray markers) with respect to heating (black markers) can be explained by Eq. 5.2. At constant temperature and frequency, the right hand side of Eq. 5.2 is constant. In order to get equilibrium, the left hand side must be constant, as well. Since the grains grow during annealing at high temperature, $p \log(d)$ increases, and consequently, the other $\log(\tan(\phi))$ should decrease. As Owen and Chokshi [51] have shown, concurrent grain growth and changes in deformation mechanisms can lead to an erroneous evaluation of the activation enthalpy even with small differences in the grain size. The advantage of Eq. 5.3 with respect to Eq. 2.48 is that it integrates the effect of grain size. Eq. 5.3 has been used to make a new construction of the master curve as presented in Fig. 5.22.

Using this new model, the resulting master curve has been improved in quality (compare Fig. 5.20 with Fig. 5.22) and the peak is now, in the new master curve, well-defined. The activation enthalpy deduced using this new equation (the plot is embedded in Fig. 5.22) is 517 kJ.mol^{-1} . The value of the grain growth exponent that has been obtained from the vertical shift for superimposing the spectra is $p=2$, which is in the range of those obtained for creep in 3Y-TZP [39, 54]. Using this procedure, very similar values (in the range of $500 - 550 \text{ kJ.mol}^{-1}$) were obtained for other composites with different amount of CNTS.

Swaroop et al. [55] have obtained 515 and 500 kJ.mol^{-1} for the energy of lattice diffusion of Zr^{4+} and Y^{3+} cations respectively in ultra-fine 3Y-TZP materials while the values obtained for GB diffusion of the same elements are 370 and 390 kJ.mol^{-1} . Therefore, our value is closer to that of lattice diffusion. On the other hand, the characteristics of the mechanical loss peak found in zirconia have been already discussed by other authors [43, 50, 56, 57] showing that it cannot be attributed to point defect relaxations but instead to some extended defect such as dislocations or GBs. Moreover, the effect of CNT that decrease the overall background and the peak cannot be a bulk effect since they are located at GBs. Therefore, it can be inferred that even if GB sliding is the mechanism that produces creep, the limiting mechanism or the slowest one that controls creep is determined by lattice diffusion.

Such controlling mechanism should be therefore of Nabarro-Herring type. High temperature plastic deformation would be achieved by GB sliding accommodated by a diffusional mechanism of Nabarro-Herring type to overcome the GB pinning centers. However Nabarro-Herring creep is not a widely accepted mechanism for deformation process of fine structure materials, which instead is Coble creep. In 3Y-TZP, TEM analysis has indicated that Y^{3+} segregates along the GBs [58]. Such significant yttrium segregation may decrease the diffusivity of the cations along GBs with respect to lattice diffusion, making lattice diffusion a preferential way for mass transport.

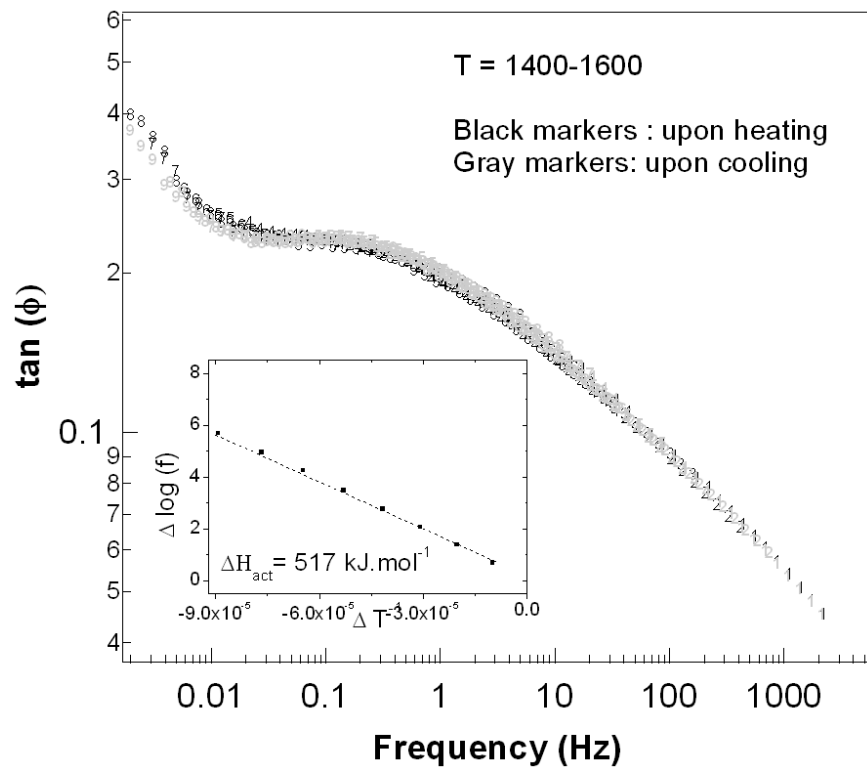


Fig. 5.22. Master curve construction using new developed model (Eq. 5.3) of 3Y-TZP with 3wt% CNTs in temperature range 1400-1600K.

5.6. Conclusion

In this chapter, the mechanical properties of nano-structured zirconia based composites, have been studied in a wide range of temperature. The mechanical loss spectra are mainly composed of a relaxation peak, which is not well-resolved, turning to an exponential background at lower frequency or higher temperature. This background is interpreted as extensive relative sliding of grains without obstacles, while the grain junctions loose their strength and macroscopic creep occurs. The experimental results as well as a theoretical model, show that the addition of nano-particles (e.g. CNTs), could hinder grain boundary sliding with providing additional obstacles against GB sliding, therefore, the mechanical loss decreases and a better resolved peak is observed. Consequently, the creep rate drastically decreases with CNT additions. The results have shown that addition of CNTs could also improve room temperature mechanical properties such as toughness, hardness and shear modulus. The related mechanisms responsible for such improvements have been presented in this chapter.

References

- [1] M. Daraktchiev, B.V.d. Moortèle, R. Schaller, E. Couteau, L. Forró, Effects of Carbon Nanotubes on Grain Boundary Sliding in Zirconia Polycrystals, *Advanced Materials* 17 (1) (2005) 88-91.
- [2] J.P. Zhou, Q.M. Gong, K.Y. Yuan, J.J. Wu, Y.f. Chen, C.S. Li, J. Liang, The effects of multiwalled carbon nanotubes on the hot-pressed 3 mol% yttria stabilized zirconia ceramics, *Materials Science and Engineering A* 520 (1-2) (2009) 153-157.
- [3] A. Duszová, J. Dusza, K. Tomášek, G. Blugan, J. Kuebler, Microstructure and properties of carbon nanotube/zirconia composite, *Journal of European Ceramic Society* 28 (5) (2008) 1023-1027.
- [4] X. Wang, N.P. Padture, H. Tanaka, Contact-damage-resistant ceramic/single-wall carbon nanotubes and ceramic/graphite composites, *Nature Materials* 3 (8) (2004) 539-544.
- [5] A.L. Vasiliev, R. Poyato, N.P. Padture, Single-wall carbon nanotubes at ceramic grain boundaries, *Scripta Materialia* 56 (6) (2007) 461-463.
- [6] M. Mazaheri, A. Simchi, M. Dourandish, F. Golestani-Fard, Master sintering curves of a nanoscale 3Y-TZP powder compacts, *Ceramics International* 35 (2) (2009) 547-554.
- [7] G. Bernard-Granger, C. Guizard, Spark plasma sintering of a commercially available granulated zirconia powder: I. Sintering path and hypotheses about the mechanism(s) controlling densification, *Acta Materialia* 55 (10) (2007) 3493-3504.
- [8] M. Mazaheri, Z.R. Hesabi, F. Golestani-Fard, S. Mollazadeh, S. Jafari, S.K. Sadrnezhad, The Effect of Conformation Method and Sintering Technique on the Densification and Grain Growth of Nanocrystalline 8 mol% Yttria-Stabilized Zirconia, *Journal of the American Ceramic Society* 92 (5) (2009) 990-995.

- [9] J. Dusza, G. Blugan, J. Morgiel, J. Kuebler, F. Inam, T. Peijs, M.J. Reece, V. Puchy, Hot pressed and spark plasma sintered zirconia/carbon nanofiber composites, *Journal of the European Ceramic Society* 29 (15) (2009) 3177-3184.
- [10] A. Duszova, J. Dusza, K. Tomasek, J. Morgiel, G. Blugan, J. Kuebler, Zirconia/carbon nanofiber composite, *Scripta Materialia* 58 (6) (2008) 520-523.
- [11] N. Garmendia, I. Santacruz, R. Moreno, I. Obieta, Slip casting of nanozirconia/MWCNT composites using a heterocoagulation process, *Journal of the European Ceramic Society* 29 (10) (2009) 1939-1945.
- [12] C. Ionascu, High temperature mechanical spectroscopy of fine-grained zirconia and alumina containing nano-sized reinforcements, in, Vol. Ph.D. Thesis No. 3994, École Polytechnique Fédérale de Lausanne, Lausanne, Switzerland, 2008.
- [13] P. Hvizdos, V. Puchy, A. Duszova, J. Dusza, Tribological behavior of carbon nanofiber-zirconia composite, *Scripta Materialia* 63 (2) (2010) 254-257.
- [14] J. Sun, L. Gao, M. Iwasa, T. Nakayama, K. Niihara, Failure investigation of carbon nanotube/3Y-TZP nanocomposites, *Ceramics International* 31 (8) (2005) 1131-1134.
- [15] E. Zapata-Solvas, D. Gómez-García, A. Domínguez-Rodríguez, Towards physical properties tailoring of carbon nanotubes-reinforced ceramic matrix composites, *Journal of the European Ceramic Society* 32 (12) (2012) 3001-3020.
- [16] P. Delhaes, M. Couzi, M. Trinquescoste, J. Dentzer, H. Hamidou, C. Vix-Guterl, A comparison between Raman spectroscopy and surface characterizations of multiwall carbon nanotubes, *Carbon* 44 (14) (2006) 3005-3013.
- [17] B.W. Sheldon, W.A. Curtin, Nanoceramic composites: Tough to test, *Nature Materials* 3 (8) (2004) 505-506.
- [18] G.D. Zhan, J.D. Kuntz, J. Wan, A.K. Mukherjee, Single-wall carbon nanotubes as attractive toughening agents in alumina-based nanocomposites, *Nature Materials* 2 (1) (2003) 38-42.
- [19] S.I. Cha, K.T. Kim, K.H. Lee, C.B. Mo, S.H. Hong, Strengthening and toughening of carbon nanotube reinforced alumina nanocomposite fabricated by molecular level mixing process, *Scripta Materialia* 53 (7) (2005) 793-797.
- [20] F.F. Lange, Transformation toughening, *Journal of Materials Science* 17 (1) (1982) 225-234.
- [21] M. Trunec, Z. Chlup, Higher fracture toughness of tetragonal zirconia ceramics through nanocrystalline structure, *Scripta Materialia* 61 (1) (2009) 56-59.
- [22] D.G. Green, An introduction to the mechanical properties of ceramics, Cambridge university press, Cambridge, UK, 1998.
- [23] I. Ahmad, H. Cao, H. Chen, H. Zhao, A. Kennedy, Y.Q. Zhu, Carbon nanotube toughened aluminium oxide nanocomposite, *Journal of the European Ceramic Society* 30 (4) (2010) 865-873.
- [24] I. Ahmad, M. Unwin, H. Cao, H. Chen, H. Zhao, A. Kennedy, Multi-walled carbon nanotubes reinforced Al₂O₃ nanocomposites: Mechanical properties and interfacial investigations, *Composites Science and Technology* 70 (8) (2010) 1199-1206.
- [25] E.L. Corral, J. Cesarano Iii, A. Shyam, E. Lara-Curzio, N. Bell, J. Stuecker, N. Perry, M. Di Prima, Z. Munir, J. Garay, E.V. Barrera, Engineered nanostructures for multifunctional single-walled carbon nanotube reinforced silicon nitride nanocomposites, *Journal of the American Ceramic Society* 91 (10) (2008) 3129-3137.
- [26] A. Mukhopadhyay, B.T.T. Chu, M.L.H. Green, R.I. Todd, Understanding the mechanical reinforcement of uniformly dispersed multiwalled carbon nanotubes in alumino-borosilicate glass ceramic, *Acta Materialia* 58 (7) (2010) 2685-2697.

Chapter 5

- [27] Z. Xia, L. Riester, W.A. Curtin, H. Li, B.W. Sheldon, J. Liang, B. Chang, J.M. Xu, Direct observation of toughening mechanisms in carbon nanotube ceramic matrix composites, *Acta Materialia* 52 (4) (2004) 931-944.
- [28] J.P. Fan, D.M. Zhuang, D.Q. Zhao, G. Zhang, M.S. Wu, F. Wei, Z.J. Fan, Toughening and reinforcing alumina matrix composite with single-wall carbon nanotubes, *Applied Physics Letters* 89 (12) (2006).
- [29] B. Harris, K. Anthony, Z. Carl, Long-fiber-reinforced Dense Glass-and Ceramic-Matrix Composites, in: *Comprehensive Composite Materials*, Pergamon, Oxford, 2000, pp. 489-531.
- [30] N.P. Padture, Multifunctional Composites of Ceramics and Single-Walled Carbon Nanotubes, *Advanced Materials* 21 (17) (2009) 1767-1770.
- [31] R.L. Menchavez, M. Fuji, M. Takahashi, Electrically Conductive Dense and Porous Alumina with In-Situ-Synthesized Nanoscale Carbon Networks, *Journal of the American Ceramic Society* 20 (12) (2008) 2345-2351.
- [32] S.L. Shi, J. Liang, Effect of multiwall carbon nanotubes on electrical and dielectric properties of yttria-stabilized zirconia ceramic, *Journal of the American Ceramic Society* 89 (11) (2006) 3533-3535.
- [33] J. Tatami, T. Katashima, K. Komeya, T. Meguro, T. Wakihara, Electrically conductive CNT-dispersed silicon nitride ceramics, *Journal of the American Ceramic Society* 88 (10) (2005) 2889-2893.
- [34] T. Ukai, T. Sekino, A. Hirvonen, N. Tanaka, T. Kusunose, T. Nakayama, K. Niihara, Preparation and electrical properties of carbon nanotubes dispersed zirconia nanocomposites, in: *Key Engineering Materials*, Vol. 317-318, 2006, pp. 661-664.
- [35] J.S. Juan, Mechanical spectroscopy, *Materials Science Forum* 366-388 (2001) 32-73.
- [36] R. Schaller, A. Lakki, Grain boundary relaxations in ceramics, *Materials Science Forum* 366-368 (2001) 315-337.
- [37] E. Zapata-Solvas, D. Gamez-Garcia, R. Poyato, Z. Lee, M. Castillo-Rodriguez, A. Domanguez-Rodriguez, V. Radmilovic, N.P. Padture, Microstructural effects on the creep deformation of alumina single-wall carbon nanotubes composites, *Journal of the American Ceramic Society* 93 (7) (2010) 2042-2047.
- [38] E. Zapata-Solvas, R. Poyato, D. Gamez-Garcia, A. Domanguez-Rodriguez, V. Radmilovic, N.P. Padture, Creep-resistant composites of alumina and single-wall carbon nanotubes, *Applied Physics Letters* 92 (11) (2008).
- [39] G. Bernard-Granger, A. Addad, C. Guizard, Superplasticity of a Fine-Grained TZ3Y Material Involving Dynamic Grain Growth and Dislocation Motion, *Journal of the American Ceramic Society* 93 (3) (2010) 848-856.
- [40] C. Ionascu, R. Schaller, High temperature mechanical loss spectrum of 3Y-TZP zirconia reinforced with carbon nanotubes or silicon carbide whiskers, in: *Diffusion and Defect Data Pt.B: Solid State Phenomena*, Vol. 137, 2008, pp. 29-34.
- [41] M. Daraktchiev, R. Schaller, High-temperature mechanical loss behaviour of 3 mol% yttria-stabilized tetragonal zirconia polycrystals (3Y-TZP), *Physica Status Solidi (A) Applied Research* 195 (2) (2003) 293-304.
- [42] R. Schaller, M. Daraktchiev, S. Testu, Creep behavior of ceramics studied by mechanical loss measurements, *Materials Science and Engineering A* 387-389 (1-2 SPEC. ISS.) (2004) 687-691.
- [43] R. Schaller, C. Ionascu, High-temperature mechanical loss and creep behavior of fine-grained zirconia-containing nano-sized reinforcements, *Materials Science and Engineering A* 521-522 (2009) 217-220.
- [44] A. Lakki, Mechanical spectroscopy of fine-grained zirconia, alumina and silicon nitride, in, Vol. Ph.D. Thesis No. 1266, École Polytechnique Fédérale de Lausanne, Lausanne, Switzerland, 1994.

- [45] A. Lakki, R. Schaller, M. Nauer, C. Carry, High temperature superplastic creep and internal friction of yttria doped zirconia polycrystals, *Acta Metallurgica Et Materialia* 41 (10) (1993) 2845-2853.
- [46] M. Daraktchiev, R. Schaller, L. Gremillard, T. Epicier, J. Chevalier, G. Fantozzi, How do the grains slide in fine-grained zirconia polycrystals at high temperature?, *Applied Physics Letters* 91 (12) (2007).
- [47] K. Morita, K. Hiraga, Critical assessment of high-temperature deformation and deformed microstructure in high-purity tetragonal zirconia containing 3 mol.% yttria, *Acta Materialia* 50 (5) (2002) 1075-1085.
- [48] K. Morita, K. Hiraga, B.N. Kim, Effect of minor SiO₂ addition on the creep behavior of superplastic tetragonal ZrO₂, *Acta Materialia* 52 (11) (2004) 3355-3364.
- [49] M.M.R. Boutz, A.J.A. Winnubst, A.J. Burgraaf, M. Nauer, C. Carry, Low Temperature Superplastic Flow of Yttria Stabilized Tetragonal Zirconia Polycrystals, *Journal of the European Ceramic Society* 13 (2) (1994) 103-111.
- [50] M. Nauer, C. Carry, Creep parameters of yttria doped zirconia materials and superplastic deformation mechanisms, *Scripta Metallurgica et Materialia* 24 (8) (1990) 1459-1463.
- [51] D.M. Owen, A.H. Chokshi, The high temperature mechanical characteristics of superplastic 3 mol% yttria stabilized zirconia, *Acta Materialia* 46 (2) (1998) 667-679.
- [52] C. Ionascu, R. Schaller, Influence of carbon nanotubes and silicon carbide whiskers on the mechanical loss due to grain boundary sliding in 3-mol% yttria-stabilized tetragonal zirconia polycrystals, *Materials Science and Engineering A* 442 (1-2 SPEC. ISS.) (2006) 175-178.
- [53] T.E. Chung, T.J. Davies, The low-stress creep of fine-grain uranium dioxide, *Acta Metallurgica* 27 (4) (1979) 627-635.
- [54] M. Daraktchiev, High-temperature mechanical loss in yttria-stabilized tetragonal zirconia and in calcium hexaluminate, in, Vol. Ph.D. Thesis No. 2802, École Polytechnique Fédérale de Lausanne, Lausanne, Switzerland, 2003.
- [55] S. Swaroop, M. Kilo, C. Argirusis, G. Borchardt, A.H. Chokshi, Lattice and grain boundary diffusion of cations in 3YTZ analyzed using SIMS, *Acta Materialia* 53 (19) (2005) 4975-4985.
- [56] F. Wakai, S. Sakaguchi, Y. Matsuno, Superplasticity of Yttria-Stabilized Tetragonal ZrO₂ Polycrystals, *Advanced Ceramic Materials* 1 (3) (1986) 259-263.
- [57] M. Nygren, Z. Shen, On the preparation of bio-, nano- and structural ceramics and composites by spark plasma sintering, *Solid State Sciences* 5 (1) (2003) 125-131.
- [58] T.G. Nieh, D.L. Yaney, J. Wadsworth, Analysis of grain boundaries in a fine-grained, superplastic, Yttria-containing, tetragonal zirconia, *scripta Metallurgica* 23 (2) (1989) 2007-2011.

Chapter 6

Experimental results and analysis:

Alumina based composites

In this chapter, the properties of the alumina (three different raw alumina powders) composites reinforced with different amount of CNTs are presented. The processing and the dispersion of CNTs within nano / submicron sized alumina particles are first described. It is shown that the initial particle size of the powders affects the dispersion of CNTs. Systematic analyses of the mechanical properties of the composites reinforced with different amount of CNTs (ranging between 0 and 5 wt.%) have been performed both at room and at high temperature. It is concluded that the dispersion of the nanotubes has a vital role to achieve interesting properties.

6.1. Processing and properties obtained in composites produced using submicron α -alumina TM-DAR powder

As it was mentioned in 3.2, the powder, named “TM-DAR” is constituted of ultrafine particles having an average diameter of about 150 nm. This commercial alumina powder has very interesting sintering ability, since it can be easily fully densified at relatively low temperature in comparison to other alumina powders. This is because of (1) a very good packing in the raw state (green state), (b) small pores (smaller than 100 nm) in the green bodies, and (c) the absence of hard agglomerates in the initial state of the powders.

Table 6.1 summarizes the sintering temperatures and characteristics (density and grain size) of sintered nanostructured composites and monolithic alumina. Nearly full-dense structures ($\rho > 98\%$ theoretical density) were obtained by SPS processing. Since CNTs hinder densification to some extent, similarly to zirconia composites, with an increase of CNTs content, higher sintering temperature has been employed. Nevertheless, the short SPS soaking/lower sintering temperature (Table 6.1) in comparison with conventional sintering and hot-pressing is the key to preserve the CNT integrity in the sintered composites. Interestingly, though the highest sintering temperature was employed for alumina reinforced with 5 wt.% CNTs, the final microstructure exhibits the smallest grain size, which evidences that the nanotubes could inhibit the grain growth.

Table 6.1 Sintering temperature and characteristics of sintered alumina/CNTs nano-composites in comparison with monolithic alumina.

Alumina + X wt% CNT	Sintering temperature (°C)	Pressure(MPa)/ Heating Rate(°Cmin ⁻¹)/ Soak time(min)	Relative density	Grain size (μm)
X= 0	1200	80 / 100/ 2	98.3	1.8
X= 0.5	1250	80 / 100/ 2	98.4	0.45
X= 1.5	1250	80 / 100/ 2	97.9	0.32
X= 3	1300	80 / 100/ 2	98.2	0.21
X=5	1350	80 / 100/ 2	98.0	0.15

Fig. 6.1 represents the room temperature mechanical properties; i.e. indentation hardness and fracture toughness obtained from CNTs reinforced alumina nanostructured composites. A significant increase in indentation fracture toughness

is found with increasing MWCNT content up to 1.5 wt% accompanied with a slight but steady increase in the hardness. The indentation fracture toughness of alumina reinforced by 1.5 wt.% CNTs reached 5.5 MPa m^{1/2}, which doubles that for monolithic specimen. Instead, the addition of more nanotubes (i.e. 3 and 5 wt%) results in a degradation of the properties. Fracture toughness of the 3 and 5 wt% CNT reinforced specimens do not show any improvement with respect to the 1.5 wt% CNT-alumina specimen. The addition of more than 1.5 wt% CNTs, results in a strong decrease in the hardness.

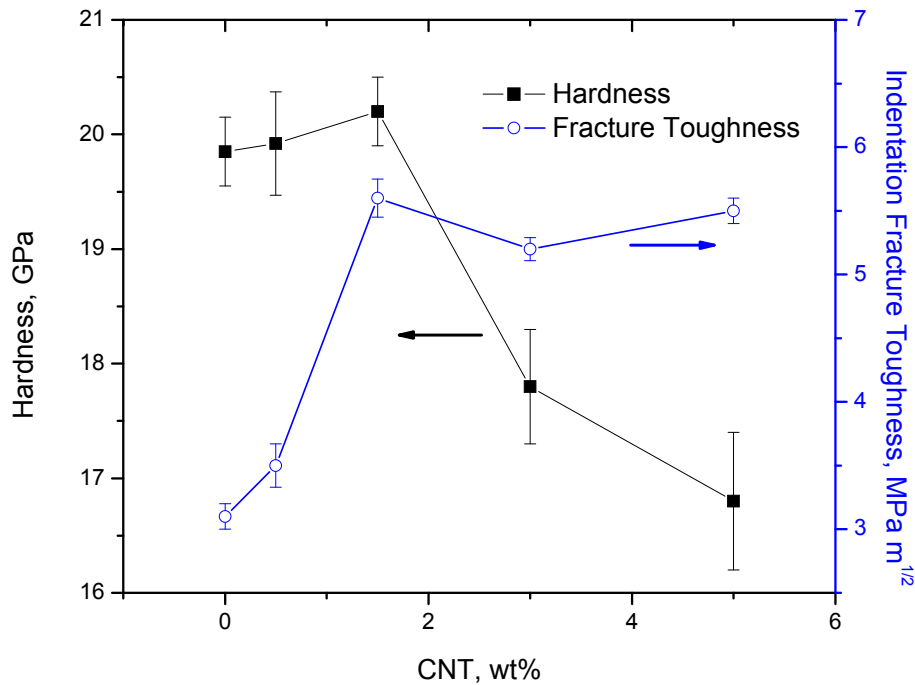


Fig. 6.1. Indentation fracture toughness and Vickers hardness of TM-DAR composites as a function of CNTs wt.%.

Fig. 6.2 shows the variation of the mechanical loss $\tan(\phi)$ as a function of temperature for composites with different amounts of CNT in comparison with monolithic alumina in the range of 900 – 1500 K. Very similar to the case of zirconia, and as previously observed in alumina by Lakki et al. [1, 2], the spectra are characterized by an exponential increase in mechanical loss at temperature above 1000 K in the monolithic sample. As explained by Lakki in the case of alumina, there is no amorphous layer in the grain boundaries. So, due to the structure of GBs, the level of mechanical loss is lower than in zirconia samples. It might be due to this fact

that in alumina, grain boundary (GB) sliding can only take place by elementary motion of GB dislocations. The exponential increase in $\tan(\phi)$ can also be considered as the right shoulder of a GB sliding peak, located at temperature higher than 1500 K.

It is apparent that the addition of 0.5 and 1.5 wt% CNTs shifts the exponential increase at higher temperature, which leads to a lower level of $\tan(\phi)$ at 1500 K for the specimen containing 1.5 wt% CNTs. An opposite behavior was observed in specimen containing more than 1.5 wt% CNT, i.e. samples reinforced with 3 and 5 wt% CNTs show higher mechanical loss at high temperature.

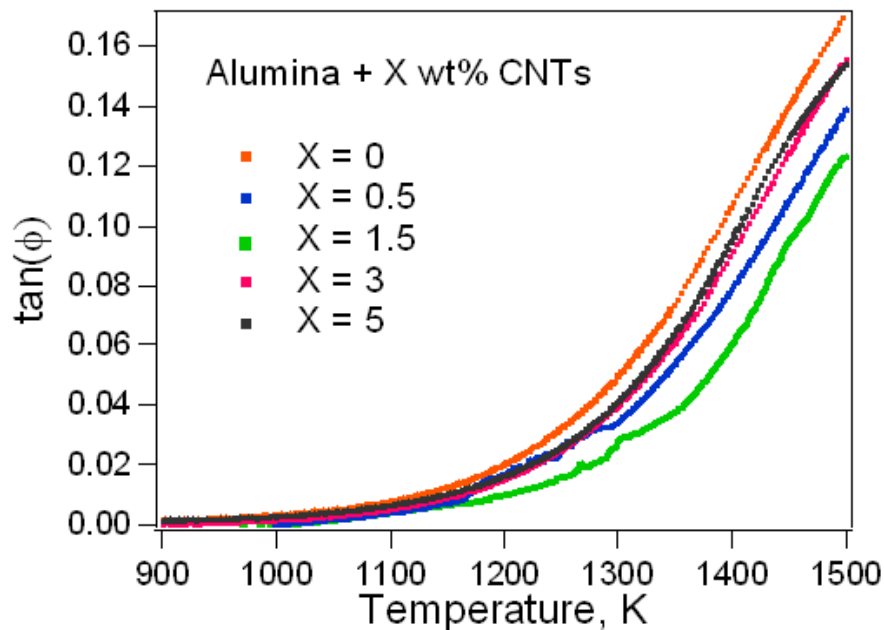


Fig. 6.2. Mechanical loss ($\tan(\phi)$) versus temperature for alumina/CNTs composites in comparison with monolithic alumina. The measurement frequency: 1 Hz.

Therefore, it seems that there is a coherency between both the room and high temperature properties.

High resolution SEM (fracture surface) images of alumina reinforced with different amounts of CNTs are represented in Fig. 6.3a–d. Two regions can be distinguished: 1) at low amounts of CNTs (i.e. 0.5 and 1.5 wt% CNTs) a good dispersion of CNTs can be observed. 2) for higher amount of CNTs, the nanotubes tend to cluster and large bundles of CNTs located between the alumina grains can be easily found (Fig. 6.3c and d).

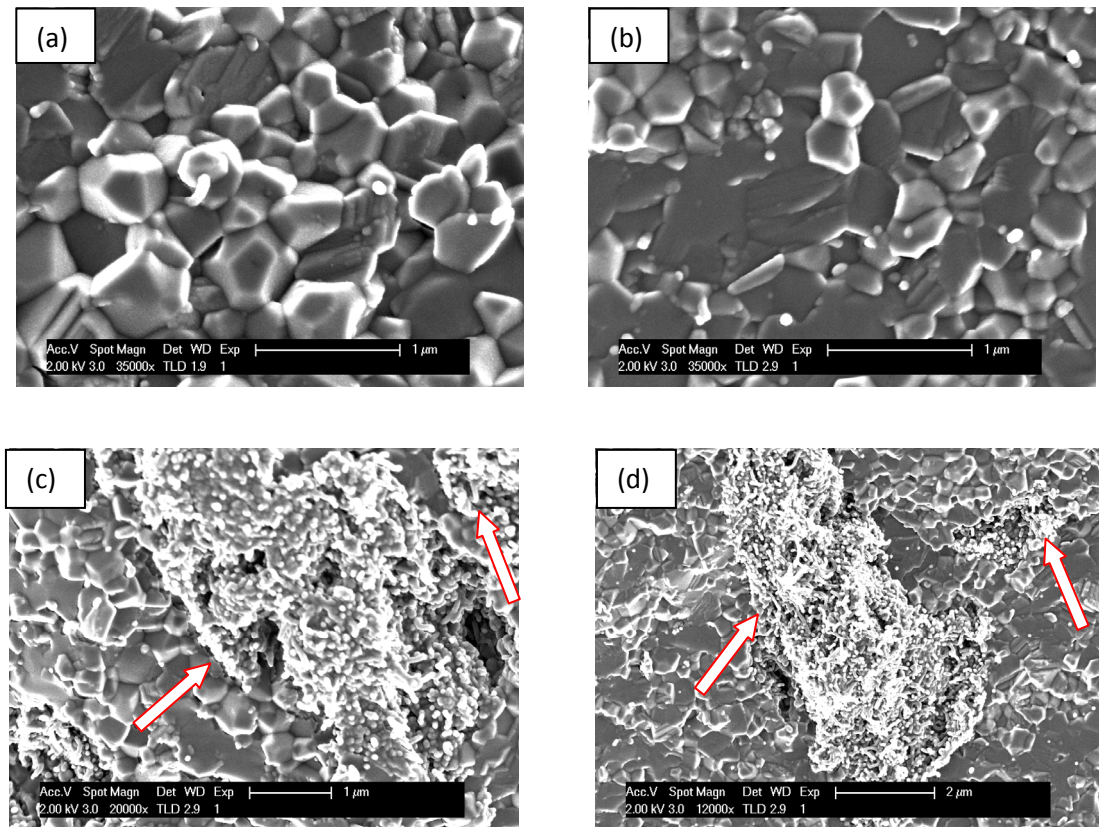


Fig. 6.3. High resolution SEM of fracture surface of alumina composites reinforced with (a) 0.5 wt%, (b) 1.5 wt%, (c) 3 wt% and (d) 5 wt% CNTs. The CNT clusters were indicated by arrows.

As shown in Fig. 6.1, the indentation fracture toughness of the specimens increases with the addition of nanotubes up to 1.5 wt%. The toughening and strengthening mechanisms of composites by CNT additions were presented in chapter 5 and attributed to the uncoiling and stretching of nanotubes, which bridge the gap of the propagating crack. When the crack propagates intergranularly, at first the entangled nanotubes are uncoiled. With further propagation, the uncoiled nanotubes stretch, while their end is anchored within the grains, which produce crack bridging. At the end, with further propagation of crack, the nanotubes separate from ceramic interface or fail. The uncoiling/stretching produces friction work and dissipates energy at the crack tip, which results in higher toughness. The addition of more CNTs may result in CNT agglomeration, rather than dispersion of CNTs between the grains, so that no additional toughening is produced. This could explain why no improvement in toughness is observed, with high CNT contents (i.e. 3 and 5 wt%).

Chapter 6

CNTs addition results in strengthening and hardening, if adequately located between two ceramic grains (CNTs < 1.5 wt%). However, the decrement observed in the specimen hardness with high content of CNTs can be attributed to the presence of porosities between the CNTs in the clusters (Fig. 6.2c and d).

It can be concluded that having a fairly good dispersion of the reinforcing phase through the matrix is not only a must for CNT-ceramics, but also for any other kind of particle or fiber reinforced composite, to obtain ideal properties. The subject has been investigated in different metal or ceramic matrix composites. Such a serious difficulty should be taken into account more precisely in the case of CNT reinforced composites. CNTs are potentially prone to agglomeration resulting from their high surface area as well as from the presence of nano-scale interaction caused by Van der Waals attraction. Consequently, a poor dispersion of CNTs within a ceramic matrix is observed in different specimens with high CNT content. Several reports [3] have shown that such an agglomeration could lead to a noticeable degradation of the mechanical properties in CNT-ceramics.

In the present work, conventional mechanical blending was used to disperse the nanotubes within the ceramic particles. Therefore, the CNT initial condition as well as that of the ceramic particles can have a vital role to get a good dispersion of CNTs within the ceramic powders. Fig. 6.4a-d show the microstructure of the powder composites, alumina TM-DAR powder mixed nanotubes, after mechanical blending. As observed in the sintered composites (Fig. 6.3a-d), the CNTs ropes are not well dispersed within alumina particles in 3 and 5wt% CNTs composites.

Similarly to the zirconia system, where we got relatively good dispersion, we decided to use nano-sized alumina powder, noticing that while the zirconia Tosoh had an average particle size around 70 nm, and the alumina TM-DAR powders have an average size of 150 nm. However, there is no commercially available, sinter-able and pure α -alumina powder. Therefore, two other alumina powders (details are given in 3.2) were used for further investigations pure nano size γ -alumina (γ -Al₂O₃) and less pure nano α -alumina (MK-40).

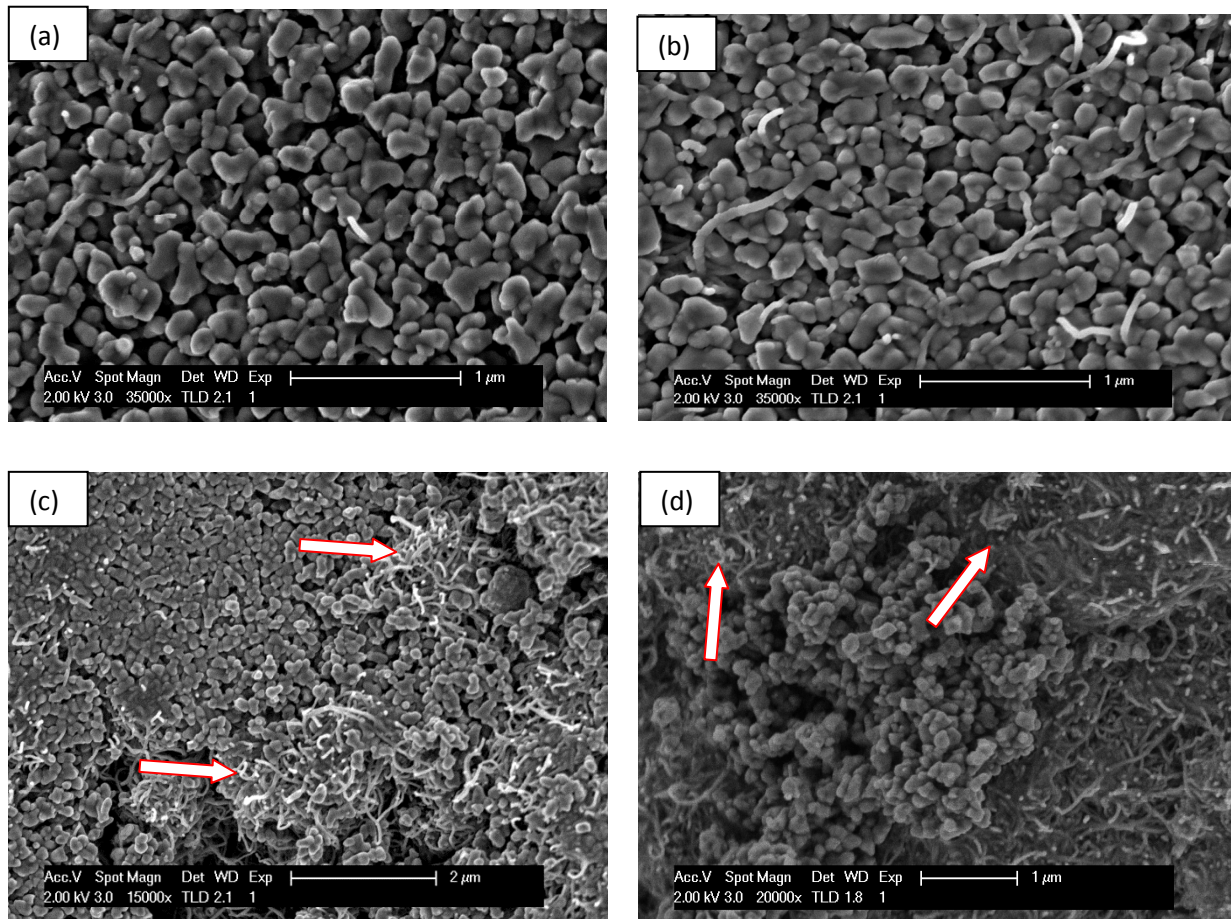


Fig. 6.4. High resolution scanning electron microscopy of blended TM_DAR alumina powder with (a) 0.5 wt%, (b) 1.5 wt%, (c) 3 wt% and (d) 5 wt% carbon nanotubes (arrows indicate CNT clusters).

6.2. Processing and properties obtained in composites produced using nano size γ -alumina powder

Fig. 6.5a and b show the microstructure of the composite powders after mixing the γ -alumina powder with 3 and 5 wt% CNTs, respectively. It can be clearly seen that not only there is no trace of CNTs agglomeration, but also a fair good dispersion within the nanopowder can be observed. The smooth surface that can be seen on the micrographs is probably due to carbon coating to make the samples conductive for electron microscopy.

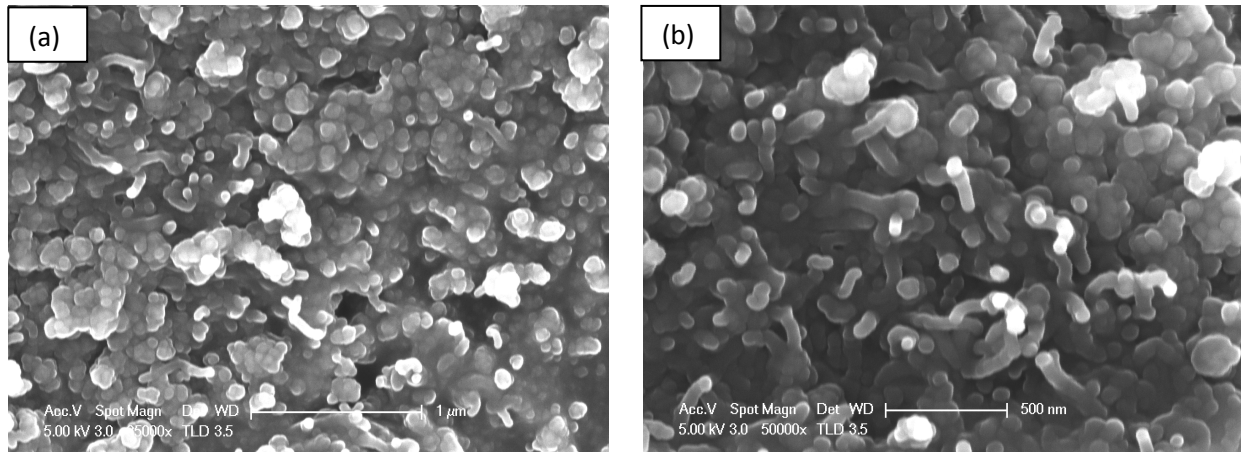


Fig. 6.5. High resolution scanning electron microscopy of blended γ -alumina powder with (a) 3wt%, and (b) 5 wt% carbon nanotubes.

The sintering behavior (shrinkage rate versus temperature) of the 5wt% CNT samples and the sintering program during SPS are presented in Fig. 6.6. The powder was first heated up to 1100 °C and soaked at this temperature for 5 min. Then, the sample was again heated up to 1600 °C with a heating rate of 100 °C min⁻¹. At the final sintering temperature (1600 °C), it was soaked for 2 min. The SPS applied pressure was kept constant (80 MPa) during heating. Fig. 6.6b shows the piston displacement rate during SPS as a function of temperature, which can be considered as the sintering kinetics (shrinkage rate vs. temperature). Two peaks can be distinguished in the sintering kinetics graph, located at 1100 °C and ~ 1350 °C. The first peak (at 1100 °C) is associated with the transition from γ - to α -alumina. It can be seen that the transition is finished with soaking of the sample at 1100 °C, while the deformation rate drops to zero. The second peak is associated with sintering in the α phase.

The typical microstructure of the sintered γ -alumina powder with 5wt% CNTs, at different magnifications, is shown in Fig. 6.7a-c. Fig. 6.7a shows a wide view (low magnification) of the composite fracture surface. It can be seen that there is no trace of CNT bundles as well as porosities. The sample density measurements (Table 6.2) and the microstructural observation confirm that the samples were well densified (~ 98%). However, a bimodal distribution of grains can be observed in Fig. 6.7b (intermediate magnification): large grain size (~2 μ m) and small one (~0.2 μ m).

In Fig. 6.7c (high magnification) one could clearly see that nanotubes are located in the grains, opposite to the general observations in alumina and zirconia composites,

where the CNTs are located at the GBs. This might be attributed to the fast abnormal growth of grains, or fast GB migration, which allows them to swallow the CNTs.

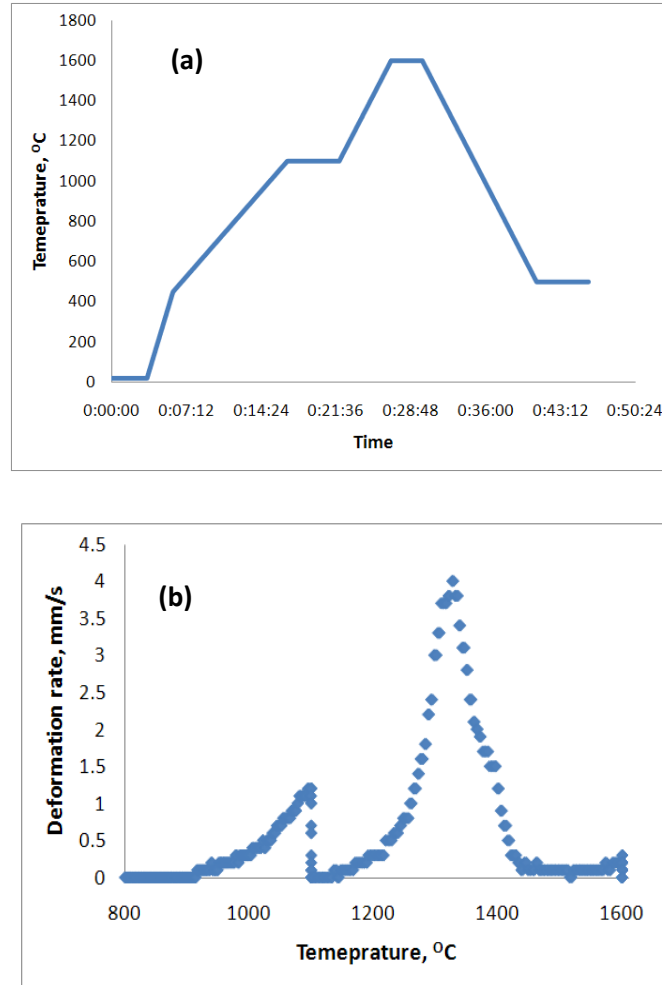


Fig. 6.6. (a) Sintering program (heating profile) during SPS and (b) the sintering kinetic (sintering rate vs. temperature) of γ -alumina powders with 5wt% CNTs.

Table 6.2. Sintering temperature and characteristics of sintered γ -alumina/ 3 and 5 wt% CNTs nanocomposites.

Alumina + X wt% CNT	Sintering Temperature, °C	Relative density, %	Hardness, GPa	Fracture Toughness, MPam ^{1/2}
X= 3	1600	97.8 ± 0.44	18.8 ± 0.41	4.4 ± 0.12
X= 5	1600	98.1 ± 0.31	18.1 ± 0.35	4.6 ± 0.25

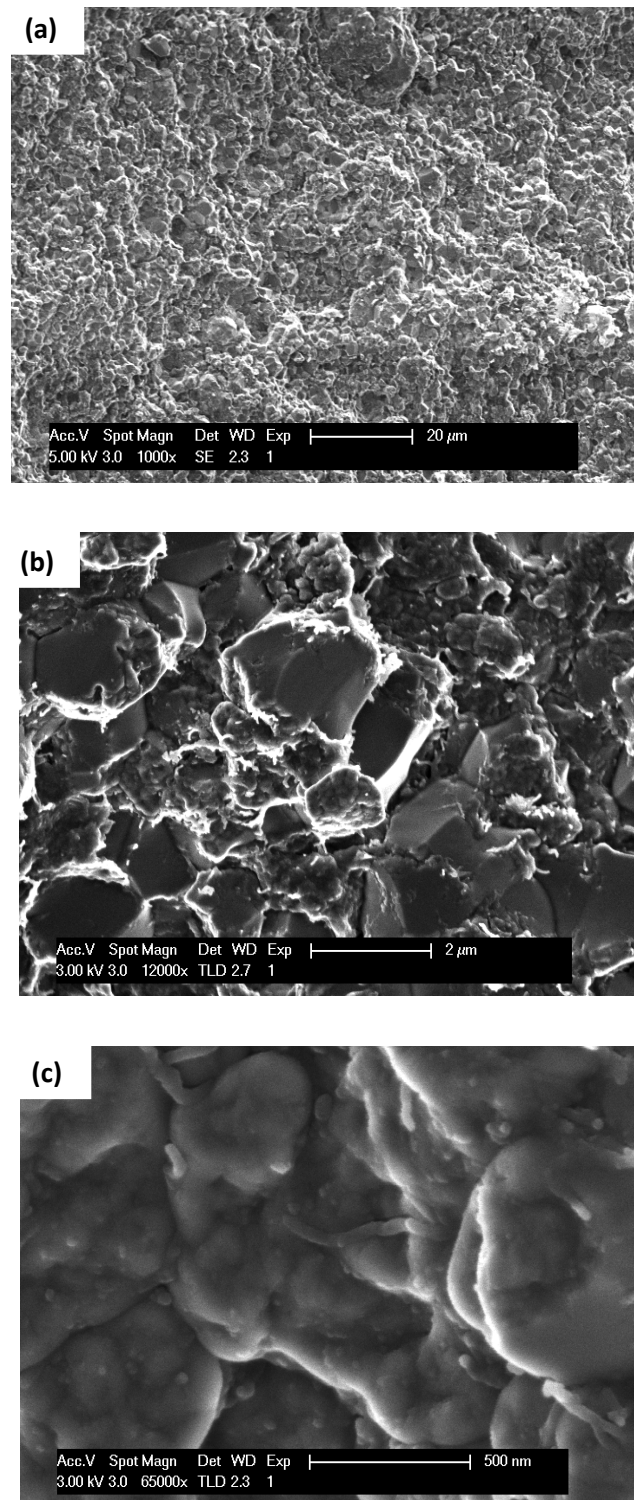


Fig. 6.7. High resolution scanning electron microscopy of sintered γ -alumina powder reinforced with 5 wt% carbon nanotubes. Pictures were taken in different magnifications.

XRD of the sintered γ -alumina with 5wt% CNTs is presented in Fig. 6.8 and compared with the XRD of the raw γ powder and sintered α -alumina. The comparison shows that the γ -phase did not fully transform to α -phase during sintering, while a small peak of the γ phase is seen at $2\theta=67^\circ$.

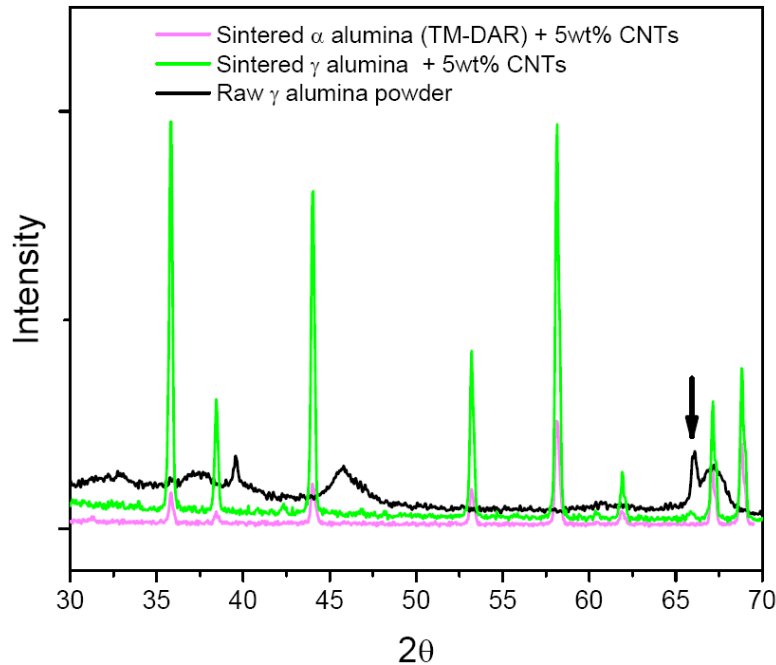


Fig. 6.8. X-ray diffraction pattern of raw γ -alumina powder (black), sintered α -alumina (TM-DAR) composite (red) and sintered γ -alumina composites (green).

In spite of the interesting dispersion of the CNTs, even at high percentage of nanotubes, the mechanical properties (both hardness and toughness), as presented in Table 6.2 have not been improved substantially, in comparison with monolithic alumina specimen (Fig. 6.1). This might be due to (1) the bimodal structure and abnormal growth of alumina grains and (2) the presence of γ phase in the sintered sample, which is non-transformable, even with annealing at very high temperature (1600°C).

Nevertheless, based on the results obtained in the zirconia samples as well as with γ -alumina powder, it can be deduced that the initial size of the particles has a vital role in getting a fair dispersion of CNTs within the ceramic particles. To support this hypothesis, we have used another powder with nano size α -alumina particles (40 nm). However, the purity of the powder is relatively low (95%). The features of the raw powder are presented in chapter 3.2.

6.3. Processing and properties obtained in composites produced using nano-size α -alumina (MK-40)

Table 6.3 summarizes the sintering temperatures and characteristics of sintered nanostructured composites and monolithic MK-40 alumina. Nearly full-dense structures ($\rho > 98\%$ theoretical density) were obtained by SPS processing. Since CNTs hinder densification to some extent, when increasing the CNTs content, higher sintering temperature had to be employed.

Table 6.3. Characteristics of MK-40 alumina/ CNTs nanocomposites.

Alumina + X wt% CNT	Sintering temperature (°C)	Pressure(MPa)/ Heating Rate(°Cmin ⁻¹)/ Soak time(min)	Relative density
X= 0	1300	50 / 100/ 2	97.7
X= 1.5	1350	50 / 100/ 2	98.8
X= 3	1350	50 / 100/ 4	98.0
X=5	1400	50 / 100/ 4	98.2

High resolution SEM (fracture surface) images of MK-40 alumina reinforced with 3 and 5 wt% CNTs are presented in Fig. 6.9a and b. There is no sign of CNTs agglomeration, as it was observed in TM-DAR samples. So, again, this result proves that nanoparticles have the ability to disperse the CNTs. The second feature that can be seen in the SEM images is related to the CNT appearance. It is obvious that the CNTs did not keep their tube shape anymore, while they seem like a continuous phase located at the boundaries (like a glassy phase between the grains). However, the more accurate analysis of this phase needs of high resolution TEM analysis.

Figure 6.10 represents room temperature mechanical properties; i.e. indentation hardness and fracture toughness obtained in MK-40 alumina composites. The mechanical properties of the composites made with MK-40 powders show a significant improvement of the toughness over the whole range of CNT reinforcement (differ from the behavior observed in TM-DAR, Fig. 6.1). A decrease of the hardness is found however when the CNT content is increased as in the case of TM-DAR powders.

Fig. 6.11a and b show the variation of the mechanical loss $\tan(\phi)$ and relative shear modulus as a function of temperature for MK-40 composites with different amounts of CNT in comparison with monolithic MK-40 alumina sample. Clearly, with addition

of nanotubes the mechanical loss background decreases, in the whole range of the measurements, up to 5% CNT reinforcement. Another interesting point to notice in Fig. 6.11b is the higher shear modulus of MK-40/CNTs nanocomposite in comparison with monolithic alumina in the whole range of testing temperature.

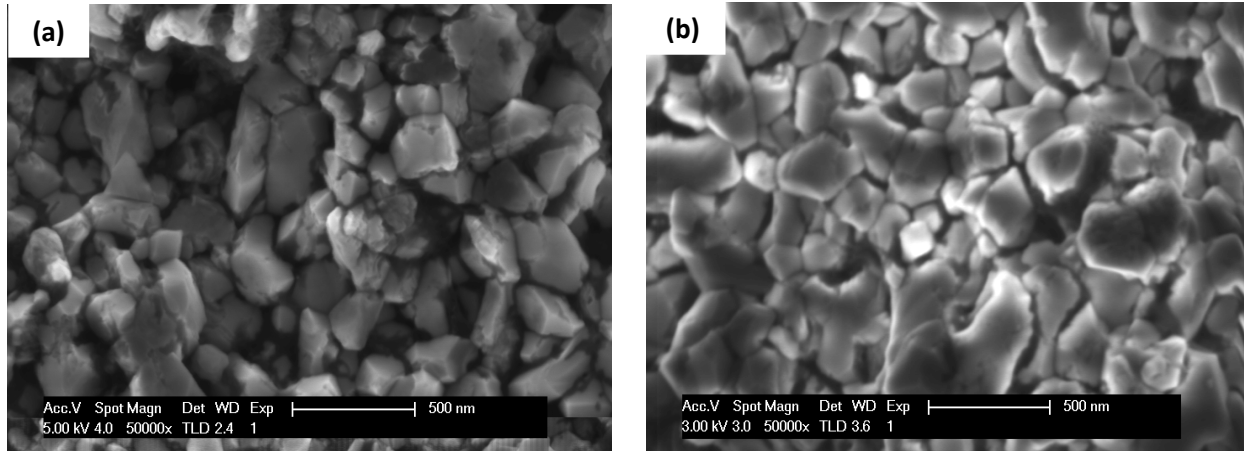


Fig. 6.9. High resolution scanning electron microscopy of sintered MK-40 α -alumina powder reinforced with (a) 3 and (b) 5 wt% carbon nanotubes.

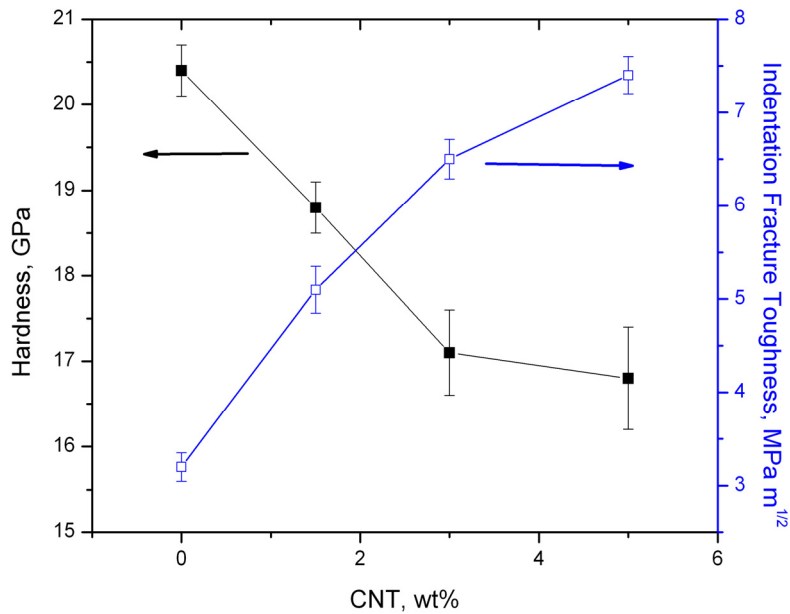


Fig. 6.10. Indentation fracture toughness and Vickers hardness of MK-40 alumina composites as a function of CNTs wt.%.

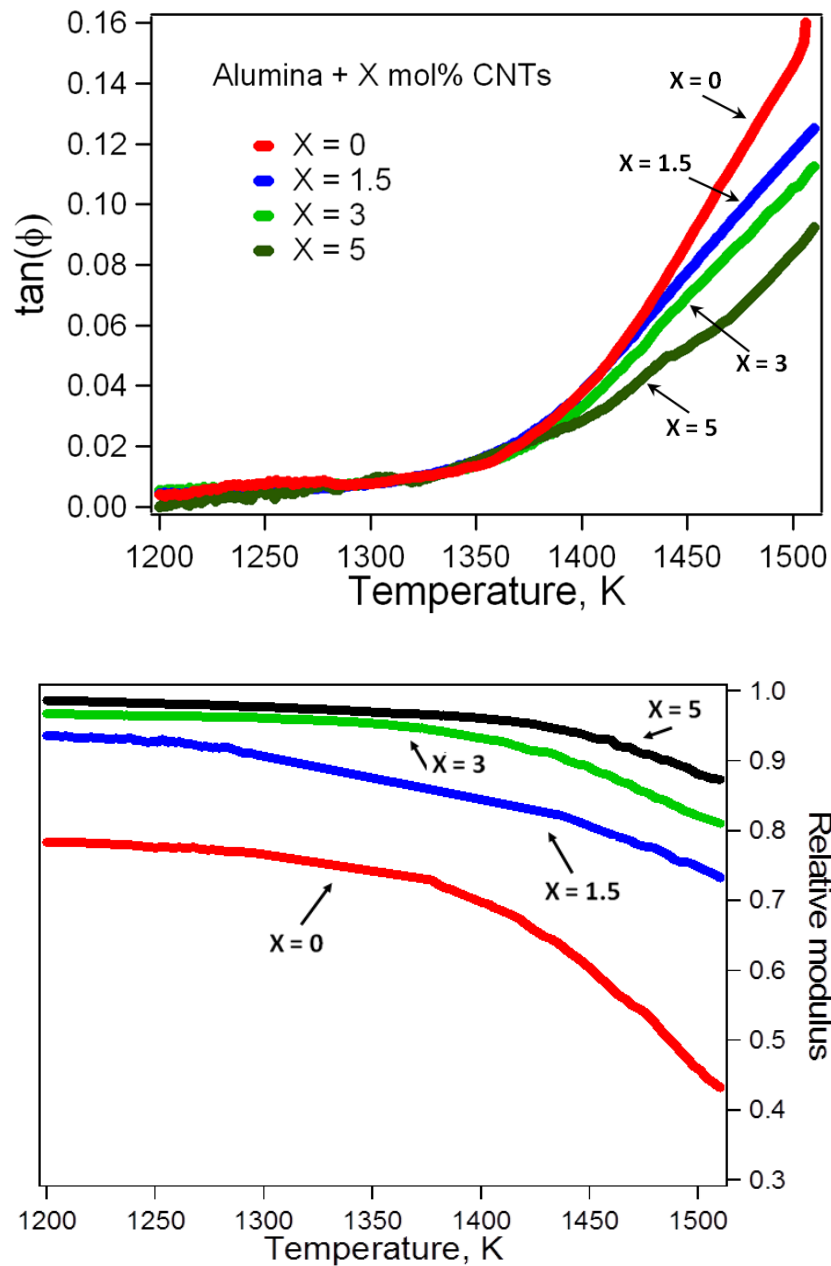


Fig. 6. 11. Mechanical loss ($\tan(\phi)$) and relative shear modulus as a function of temperature for MK-40 alumina/ CNTs nanocomposites in comparison with monolithic alumina. The measurement frequency was 1 Hz.

The comparison between submicron (TM-DAR) and nano (MK-40) alumina composites, show that nano-size alumina represent a promising alternative. In fact as shown in Fig. 6.11 all the amplitudes of the high temperature background show a

decrease at fixed temperature with respect to monolithic alumina and this up to 5% CNT. Same trend for room temperature properties are also observed (Fig. 6.10).

6.4. Conclusion

It can be concluded that a good dispersion of the CNTs is essential in order to obtain composites with improved mechanical properties. Once this condition is obtained, both the room temperature fracture toughness and the high temperature resistance to deformation, increase proportionally to the CNT content.

References

- [1] A. Lakki, Mechanical spectroscopy of fine-grained zirconia, alumina and silicon nitride, in, Vol. Ph.D. Thesis No. 1266, École Polytechnique Fédérale de Lausanne, Lausanne, Switzerland, 1994.
- [2] A. Lakki, R. Schaller, C. Carry, W. Benoit, High temperature anelastic and viscoplastic deformation of fine-grained MgO-doped Al₂O₃, *Acta Materialia* 46 (2) (1998) 689-700.
- [3] E. Zapata-Solvas, D. Gómez-García, A. Domínguez-Rodríguez, Towards physical properties tailoring of carbon nanotubes-reinforced ceramic matrix composites, *Journal of the European Ceramic Society* 32 (12) (2012) 3001-3020.

Chapter 7

General discussion

The aim of this chapter is to present a general analysis and discussion on the original results obtained in the different nanostructured ceramics and composites; from Sialon ceramic to Alumina, Zirconia and their composites. It is shown that how this research questioned the existing GB sliding model by considering different parameters such as the grain shape, the grain size, the grain-boundary glassy phase amount and nature of it. The parameters qualifying the ceramic reinforcement by CNTs (content and dispersion) are then analyzed, according to the possibilities of improving the mechanical properties.

7.1. Effective parameters on grain boundary sliding

The results analysis in previous chapters as well as earlier investigations [1-11] have shown that the high temperature behavior of ceramics (involving alumina, zirconia and silicon nitride) can be associated with GB sliding. On the microstructural level, the grains slide in viscous manner, i.e. velocity dependent. Therefore, 2 parameters should be considered for analyzing the mechanism of GB sliding: the viscosity η of the intergranular glassy phase of thickness δ located between two grains and the resistance of the triple junctions against the sliding. This resistance is called “restoring force, K ”, defined by different parameters (details can be found in (Chapter 2, 2.4.1.2.2)). This force appears in Lakki’s model related to hexagonal grains separated by an intergranular viscous layer.

$$\sigma = \frac{\eta}{\delta} \dot{x} + Kx \quad (2.28)$$

the mechanical loss can be calculated:

$$\tan(\varphi) = \frac{G}{d} \frac{\omega \frac{\eta}{\delta}}{\left(\frac{KG}{d} + K^2\right) + \left(\omega \frac{\eta}{\delta}\right)^2} \quad (2.30)$$

Thus, (1) the magnitude of K , and (2) the amorphous layer viscosity, η , control the gain sliding. For instance, the exponential increase in the mechanical loss results from the weak resistance of triple points ($K \rightarrow 0$), to extensive sliding, while the glassy phase viscosity drops. The glassy phase located in the grain-boundaries, is found to act as the shortcut for transport matter along the boundaries, which accommodate the GB sliding process. Therefore, the quantity/ viscosity of the viscous intergranular phase must influence the GB sliding kinetics.

7.2. Effect of the quantity/ composition of glassy phase

From the model explained in 7.1, one may expect that the higher amount / lower viscosity of the glassy phase at high temperature, the easier the grain sliding and easier plastic deformation at high temperature.

The study of the silicon nitride based samples (Chapter 4) shows that for a ceramic containing a large amount of amorphous phase, a mechanical loss peak is observed.

Based on prior investigations [12, 13], this peak is due to the relaxation associated with the glass transition of these regions, so called “ α -relaxation”.

The advantage of the mechanical spectroscopy is to provide new information about the amount / composition of the glassy phase (crucial parameters to control the high temperature plastic deformation of samples), which cannot be obtained by other techniques such as TEM and XRD. For instance, as it is shown in Fig. 4.3., with different compositions of glassy phase in oxygen and nitrogen, the α -relaxation peak position changes. Moreover, samples with no glassy phase, or samples after re-crystallization at high temperature show no relaxation peak. It has been frequently reported in the literature that with re-crystallization of the glass phase in silicon nitride based ceramics, the high temperature creep resistance strongly improves [10, 14-16].

A high content of glassy phase results in a higher α -relaxation peak intensity. Which was observed in Ca-Sialon samples called Ca2N, Ca4 and Ca8N in chapter 4 (Fig. 7.1). More interestingly, the sensitivity of these spectrum components to microstructure and measurement parameters appears to be in good agreement with compressive deformation results obtained in an SPS apparatus as a function of temperature. The results show that the peak position is a function of glass viscosity and that the intensity of the peak is mainly affected by the glassy phase quantity [17]. Nevertheless, the amount of the glassy phase is not the only parameter that affects the peak intensity, but also it depends on the restoring force due to grain elasticity. Thus, a specimen consisting of elongated grains (Ca16N) shows a lower peak height in comparison with a sample of lower glassy phase content (Ca8N). The presence of elongated grains, which enhance the so called mechanism of “interlocking microstructure”, could improve the fracture toughness at room temperature and the restoring force against grain sliding at high temperature (Fig. 7.1).

It is known that toughening through in-situ formation of elongated grains, very similar to addition of whiskers/ fibers, or even more powerful because of a coherent bonding between the two phases, has the potential to improve the silicon nitride fracture toughness. However, it is the first time that we present the effect of elongated grains on the restoring force strength, which improves the high temperature creep resistance.

By analogy with these results, an improvement in the restoring force in oxide ceramics like zirconia and alumina, might be obtained by adding nano-fibers. And an

improvement of the high temperature creep resistance of these types of composites may be expected.

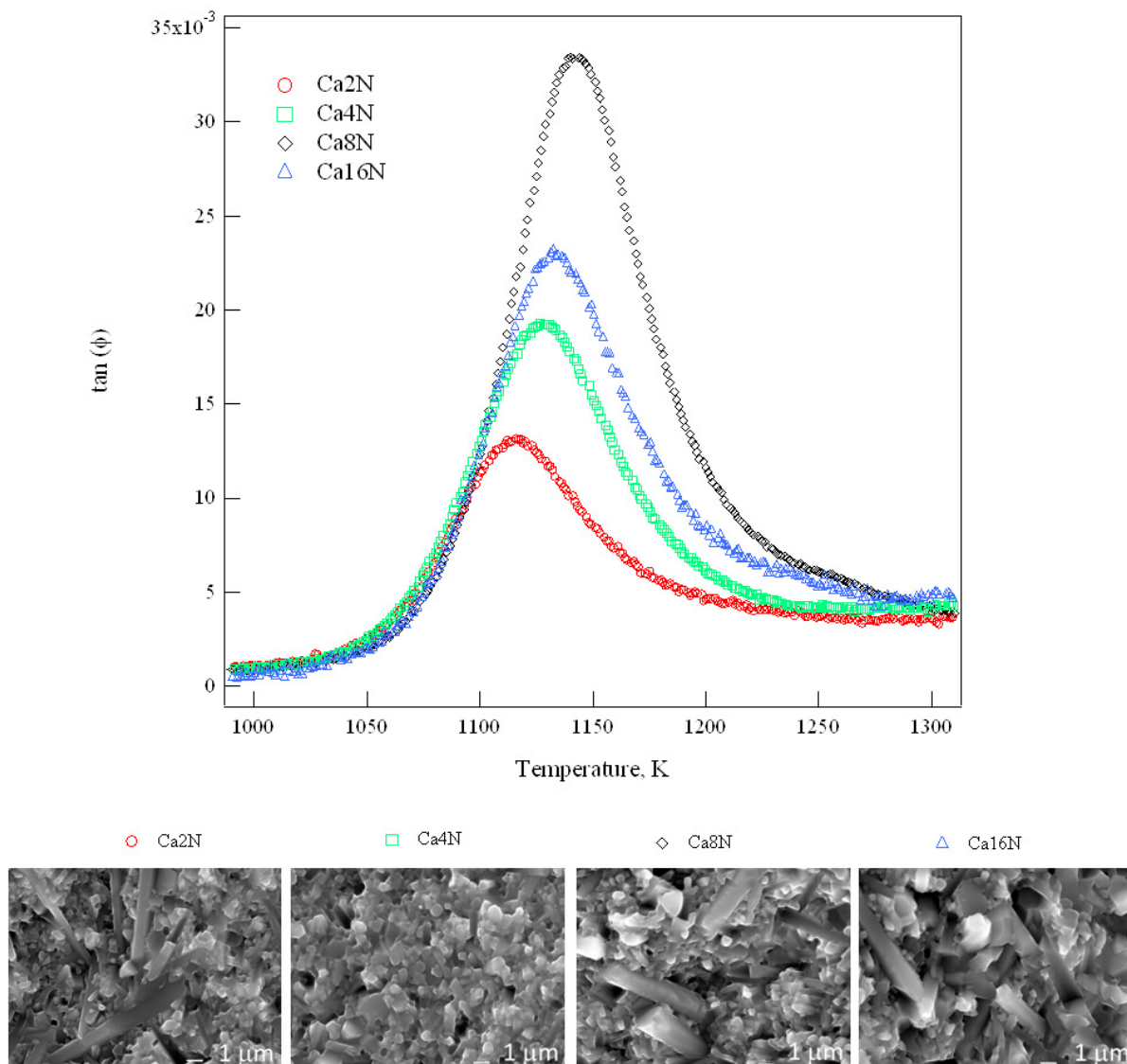


Fig. 7.1. General spectrum of Ca-Sialon specimens with different composites and microstructure. The sample microstructures were embedded in the graph.

7.3. Effect of the pinning agents

Interestingly, it was shown in the past that CNTs could also provide toughening in brittle oxide ceramics for applications at room temperature. However, several attempts in the past [5, 18, 19] were not so successful in improving the high temperature mechanical properties of the ceramics. In fact (1) the pinning efficiency of the nano-powders was not sufficient, since a short circuit for material transport could be possibly taken through grains (instead of grain-boundaries). (2) High temperature sintering of CNT-ceramics using conventional techniques results in amorphous carbon at the grain boundaries.

Addition of CNTs to oxide ceramics, like zirconia (Fig. 7.2), results in two main differences between the mechanical spectra, observed in pure and reinforced 3Y-TZP. First, the addition of CNTs leads to a better resolved mechanical loss peak. Second, the mechanical loss in CNT containing specimens is lower. Both should be due to the pinning effect of CNTs located at grain boundaries, which can hinder GB sliding.

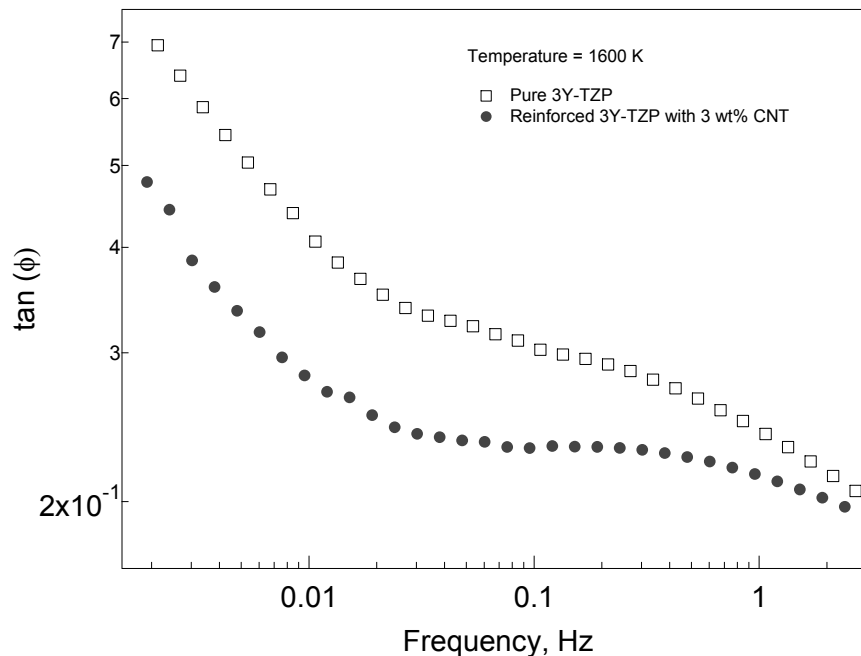


Fig. 7.2. Isothermal mechanical loss of unreinforced 3Y-TZP and 3Y-TZP reinforced with 3wt%CNTs as a function of frequency.

Since CNTs are nano-particles with high aspect ratio, they could occupy the intergranular spaces, as well as the triple junction spaces, and consequently may provide an additional restoring force (Fig. 7.3). In other words, reinforcing the triple junctions with nanosize objects such as the CNTs increases the restoring force coefficient, which gives rise to a decrease of the high temperature mechanical loss.

In monolithic zirconia, the peak is not well-resolved, because of the strong decrement in the restoring force at low frequencies, resulting in exponential increase in the mechanical loss. However, in the CNT reinforced materials, the relaxation could be attributed to GB sliding controlled (i.e. the slowest mechanism) by the nanotube ropes with consequent hardening of triple points.

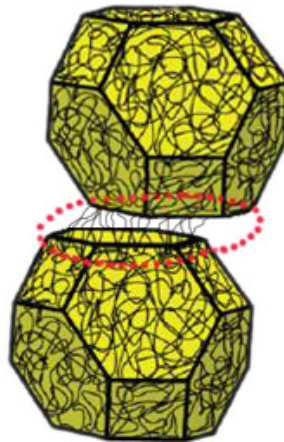


Fig. 7.3. Modified schematic model of two hexagonal grains reinforced with nanotubes separated by an intergranular layer of viscosity.

7.4. Efficiency of the pinning agents: amount and dispersion

According to the model explained in 7.2, it can be drawn that the microstructural features of pinning agents, e.g. the CNT content, CNT dispersion, CNT properties, could strongly affect their efficiency to control the GB sliding mechanism. Naturally, the presence of more nanotubes, if they are well dispersed, has a positive impact on the mechanical properties as it has been confirmed by mechanical-loss measurements (Fig. 4.15).

It seems logic that the effect of CNTs on blocking the GB sliding is directly related to their distribution in the grain boundaries (Fig. 7.4). Moreover the efficiency of CNTs in improving the room temperature toughness increases too with good dispersion of the CNTs. In the present study, the CNT dispersion parameter has been investigated by analyzing two different microstructures (details can be found in Chapter 5), one with homogeneous and the other one with heterogeneous dispersion of the CNTs in the boundaries of alumina composites (in particular in high amount of CNTs). It has been shown that a heterogeneous dispersion of CNTs in the boundaries results in a less effective hindering of GB sliding, while the pinning probability has decreased.

A comparison between the results, which were obtained in different ceramics (alumina and zirconia) with different particles sizes, shows that the use of powders with the initial particle size below 100 nm is essential to obtain a good dispersion of CNTs. It might be due to the fact that CNT bundles form a network (similar to a sieve) with a spacing size less than 100 nm. Therefore, nano-size particles could go through the sieve and consequently are well dispersed among the CNTs, which is not the case for large size particles. I believe that more analysis, e.g. application of more particles with different sizes, is required to prove this hypothesis.

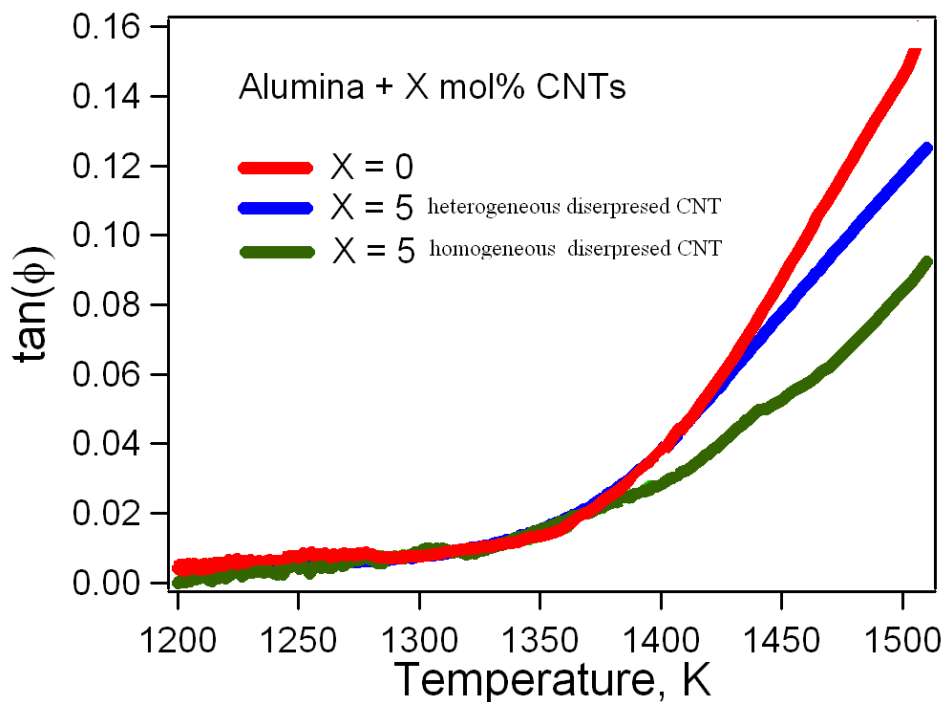


Fig. 7.4. Mechanical loss of monolithic alumina and alumina reinforced with homogeneous and heterogeneous dispersed 5wt%CNTs as a function of frequency.

7.5. Ideas for further research

The most attractive studies, which could be recommended for further investigations are listed as following:

- (1) *Pure analysis of the CNT-Ceramic interfaces:* While CNT-containing ceramics have demonstrated superior mechanical properties both at room and high temperatures; such as distinguished fracture toughness as well as better creep resistance compared to the monolithic ceramic bodies, the mechanisms for such strengthening and reinforcing effects have not been thoroughly investigated. On the other hand, the interfacial area between CNTs and ceramic matrix can play a key role in the determination of the final properties of the ceramic composites reinforced with carbon nanotubes. Moreover, the interfacial region entails grain boundaries of the material in which the most critical microstructural phenomena of the ceramics occur. It is needless to say that developing a solid knowledge of these effects as well as exploration of bonding characteristics and prospect intermediate phases in the ceramic-CNTs systems would lead to a better understanding of the strengthening mechanisms in the light of CNTs addition. This idea should initially focus on high resolution TEM analysis.
- (2) *Effect of CNTs on Sialon ceramics:* In a way similar to what was done in zirconia, CNTs could be added to silicon nitride ceramics. In the present work, an improvement in the toughness of bimodal Si_3N_4 structure was observed. However, there is no report in the literature explaining the CNT effect on high temperature properties of Sialon ceramics. Therefore, this idea could be interesting for continuation of this project.
- (3) *An investigation of the toughening mechanism* using in-situ monitoring of crack propagation (in-situ nanomechanical monitoring test in an electron microscope) can be considered to develop a visual understanding over the mechanical effects of CNTs in the microstructure of the composites.
- (4) *Well-dispersed of CNTs* within ceramic particle are required to improve the composite properties. A further analysis to understand the main parameters to obtain well-dispersed CNTs in the ceramic composites would be useful. For instance, effect of initial particles sizes on CNTs dispersion can be considered.
- (5) In the present study, the *grain size of the samples* was in the range of nano- or submicro- meter. However, the CNT addition in microsized grain can be interesting, since two interesting advantages can be predicted (1) higher length of pull-out in fracture and (2) stronger pinning effect in creep resistance, since the length of CNTs would be in the same range as the ceramic grain sizes.

References

- [1] M. Jimenez-Melendo, A. Dominguez-Rodriguez, High Temperature Mechanical Characteristics of Superplastic Yttria-Stabilized Zirconia. An Examination of the Flow Process, *Acta Materialia* 48 (12) (2000) 3201-3210.
- [2] M. Jiménez-Melendo, A. Domínguez-Rodríguez, A. Bravo-León, Superplastic flow of fine-grained Y₂O₃-stabilized ZrO₂ polycrystals: constitutive equation and deformation mechanisms, *Journal of the American Ceramic Society* 81 (11) (1998) 2761-2776.
- [3] R. Schaller, A. Lakki, Grain boundary relaxations in ceramics, *Materials Science Forum* 366-368 (2001) 315-337.
- [4] M. Daraktchiev, R. Schaller, High-temperature mechanical loss behaviour of 3 mol% yttria-stabilized tetragonal zirconia polycrystals (3Y-TZP), *Physica Status Solidi (A) Applied Research* 195 (2) (2003) 293-304.
- [5] C. Ionascu, R. Schaller, Influence of carbon nanotubes and silicon carbide whiskers on the mechanical loss due to grain boundary sliding in 3-mol% yttria-stabilized tetragonal zirconia polycrystals, *Materials Science and Engineering A* 442 (1-2 SPEC. ISS.) (2006) 175-178.
- [6] A. Lakki, R. Schaller, C. Carry, W. Benoit, High temperature anelastic and viscoplastic deformation of fine-grained MgO-doped Al₂O₃, *Acta Materialia* 46 (2) (1998) 689-700.
- [7] R. Schaller, C. Ionascu, High-temperature mechanical loss and creep behavior of fine-grained zirconia-containing nano-sized reinforcements, *Materials Science and Engineering A* 521-522 (2009) 217-220.
- [8] G. Bernard-Granger, A. Addad, C. Guizard, Superplasticity of a Fine-Grained TZ3Y Material Involving Dynamic Grain Growth and Dislocation Motion, *Journal of the American Ceramic Society* 93 (3) (2010) 848-856.
- [9] T.G. Nieh, D.L. Yaney, J. Wadsworth, Analysis of grain boundaries in a fine-grained, superplastic, Yttria-containing, tetragonal zirconia, *scripta Metallurgica* 23 (2) (1989) 2007-2011.
- [10] S. Testu, R. Schaller, Internal friction peak in silicon nitride sintered without additives, *Diffusion and Defect Data. Pt A Defect and Diffusion Forum* 206-207 (2002) 167-170.
- [11] S.Y. Yoon, H. Kashimura, T. Akatsu, Y. Tanabe, S. Yamada, E. Yasuda, Grain size dependency on the creep rate in hot-pressed silicon nitride, *Nippon Seramikkusu Kyokai Gakujutsu Ronbunshi/Journal of the Ceramic Society of Japan* 104 (10) (1996) 939-944.
- [12] L. Donzel, A. Lakki, R. Schaller, Glass transition and relaxation in Y-Si-Al-O-N glasses and in Si₃N₄ ceramics studied by mechanical spectroscopy, *Philosophical Magazine A: Physics of Condensed Matter, Structure, Defects and Mechanical Properties* 76 (5) (1997) 933-944.
- [13] L. Donzel, R. Schaller, Mechanical spectroscopy of a YSiAlON glass, *Journal De Physique. IV : JP 6* (8) (1997) C8-663-C668-666.
- [14] F.F. Lange, Relation between strength, fracture energy, and microstructure of hot-pressed Si₃N₄, *Journal of the American Ceramic Society* 56 (10) (1973) 518-522.
- [15] F.F. Lange, Fabrication and properties of dense polyphase silicon nitride, *American Ceramic Society Bulletin* 62 (12) (1983) 1369-1374.
- [16] S. Testu, R. Schaller, J.L. Besson, T. Rouxel, G. Bernard-Granger, Mechanical spectroscopy connected to creep and stress relaxation in a high resistant silicon nitride, *Journal of the European Ceramic Society* 22 (14-15) (2002) 2511-2516.

Chapter 7

- [17] M. Mazaheri, Z.R. Hesabi, F. Golestani-Fard, S. Mollazadeh, S. Jafari, S.K. Sadrnezhad, The Effect of Conformation Method and Sintering Technique on the Densification and Grain Growth of Nanocrystalline 8 mol% Ytria-Stabilized Zirconia, *Journal of the American Ceramic Society* 92 (5) (2009) 990-995.
- [18] M. Daraktchiev, B.V.d. Moortèle, R. Schaller, E. Couteau, L. Forró, Effects of Carbon Nanotubes on Grain Boundary Sliding in Zirconia Polycrystals, *Advanced Materials* 17 (1) (2005) 88-91.
- [19] C. Ionascu, R. Schaller, High temperature mechanical loss spectrum of 3Y-TZP zirconia reinforced with carbon nanotubes or silicon carbide whiskers, in: *Diffusion and Defect Data Pt.B: Solid State Phenomena*, Vol. 137, 2008, pp. 29-34.

Conclusions

In this work, the mechanical properties of nano-structured ceramics such as silicon nitride base (Sialons), zirconia and alumina based composites, have been studied in a wide range of temperature. Sialons were taken as a model of two-phase material: (1) polycrystalline ceramics separated by an intergranular viscous layer and (2) pure glass, located in the GB triple points. Zirconia and alumina composites were chosen as model materials for ultra-fine grain structure reinforced with nano-objects (CNTs), with homogeneous and heterogeneous dispersion. From the mechanical loss spectra of each material and their comparison the following conclusions can be drawn:

- (1) In polycrystalline ceramics, the amorphous phase resulting from impurities or sintering aids can be found as a thin layer between grains or concentrated in large pockets in the triple points. In ceramics, with a high amount of glassy phase (Si_3N_4 bases ceramics), the amorphous pockets undergo the glass transition upon heating, which results in a mechanical loss peak, interpreted as the α -relaxation in the glassy phase. Analysis of the results shows that the peak position is mainly a function of glass viscosity, which depends on the chemistry and composition of the glass. The amplitude of the peak is not only affected by the glassy phase quantity but also depends on the restoring force due to the surrounding grains. Therefore, despite a higher amount of glassy phase, specimens containing elongated grains may show a lower peak. A rheological model accounting for the relaxation in a two phase (polycrystalline + glass) material was developed, which shows a good agreement with experimental results.
- (2) The amplitude of the internal friction peak corresponding to the α -relaxation can be used to predict the creep response of silicon nitride based ceramics. While, the sensitivity of these spectra components to the microstructure and measurement parameters appears to be in good agreement with compressive deformation results.
- (3) In ceramics without glass pockets (Alumina or Zirconia based composites), the mechanical loss spectra are mainly composed of a relaxation peak, which is not well-resolved, turning to an exponential background at lower frequency or higher temperature. This background is interpreted as extensive relative sliding of grains without obstacles, while the grain junctions lose their strength and macroscopic creep occurs. The experimental results as well as a theoretical model, show that the addition of nano-particles (e.g. CNTs), could

Conclusions

hinder GB sliding with providing additional obstacles against GB sliding. Therefore, the mechanical loss decreases and a better resolved peak was observed. Consequently, creep rate drastically decreases with CNT additions.

- (4) The processing has a vital role on the efficiency of nano-objects in improving the performance of a composite. For instance, it was shown that the heterogeneous dispersion of CNTs in alumina samples could not produce any improvement (or very limited improvement) in either room fracture toughness or high temperature creep resistance. On the other hand, carefully added CNT to zirconia composites, i.e. well-dispersed and undamaged CNTs in powder and sintered bodies, results in a significant improvement in room temperature fracture toughness and shear modulus as well as an enhanced creep performance at high temperature. The responsible mechanisms for toughening and strengthening were proposed.

MEHDI MAZAHERI

@
www

mmazaheri@gmail.com
<http://people.epfl.ch/mehdi.mazaheri>
Male / Single, Born in Tehran, Iran @ 15.09. 1983

EDUCATIONS

- Oct 2008 – July 2012 **PhD in Materials Physics**
EPFL: École Polytechnique Fédérale de Lausanne, Switzerland
High temperature properties of nanostructured ceramics;
- Sep 2005 – Dec 2007 **MSc in Materials Selection & Characterization**
Sharif University of Technology, Tehran, Iran; GPA: 17.61 / 20.00 (1st rank of the faculty);
Processing and properties of 3 mol% yttria stabilized zirconia nanoparticles;

AWARDS & HONORS

- June 2012 *Graduate Student Fellowship, from Gordon Research Conference in Ceramics*
- Mar 2012 *American Ceramic Society Award; Travel grant to attend the 4th International Congress on Ceramics (ICC4) in Chicago, Illinois, made available through support from Wiley.*
- Nov 2009 *Nano Award 2009, Distinguished researcher in Nanotechnology, Ranked as Top (1st) young researcher, by the Iranian Nanotechnology Initiative Council; Awarded by Vice President in Science & Technology.*

Work / TEACHING EXPERIENCES

- Oct 2008 – Present **Research Assistant**
Laboratory of Physics of Complex Matter (<http://lpmc.epfl.ch>), EPFL, Switzerland
- Sep 2009 – Present **Academic Advisor**
Refractory Research Group (<http://rrg.iust.ac.ir>), Iran University of Science and Technology, Tehran, Iran.
Co-supervising three master theses, in collaboration with Prof. Golestanifard:
- Sep 2005 – Aug 2007 **Research Assistant**
Research Center of Nano Metric and Advanced Materials (<http://cnam.ir>), Sharif University of Technology, Tehran, Iran.
My MSc thesis was carried out in a laboratory, which was mainly about processing and sintering mechanism of nano size zirconia (3Y-TZP) particles. ([Details 1](#), [Details 2](#))
- Sep 2008 – Present **Teaching Assistant**
Physics department, EPFL, Lausanne, Switzerland.
-

RESEARCH SUMMMARY

- 34 Peer reviewed journal papers
- 349 citations (**H-index: 13**);
- 2 Featured articles
- 21 Conference presentations
- 3 Awarded presentations/posters

Full text of all publications are available online at my EPFL personal webpage
"http://people.epfl.ch/mehdi.mazaheri"

and citation details can be found at Scopus.com (author ID: 23134862400):
"http://www.scopus.com/authid/detail.url?authorId=23134862400"

MAIN AWARDED PUBLICATIONS

- **Mehdi Mazaheri**, A. M. Zahedi, S. K. Sadrnezhad, *Two Step Sintering of Nanocrystalline ZnO Compacts: Effect of Temperature on Densification and Grain Growth*, **Journal of the American Ceramic Society**, 91 [1] 56-63 (2008).
Award: Featured as Hot Paper, TOP CITED ARTILCE in 2008; 3rd rank, and selected for free-access
No. of Citations: 36
- **Mehdi Mazaheri**, D. Mari, R. Schaller, *High temperature mechanical spectroscopy of yttria stabilized zirconia reinforced with carbon nanotubes*, **Physica Status Solidi**, 207A [11] 2456-60 (2010). [FULL TEXT]
Award: Featured as Front Cover Page.
- **Mehdi Mazaheri**, D. Mari, R. Schaller, G. Fantozzi, *Mechanical properties of carbon nanotube/ alumina nanocomposites: From room to high temperatures*, **4th International Congress on Ceramics (ICC4) in Chicago, Jul 2012**.
Award: Awarded the travel grant to attend the conference through support from Wiley.

REFEREED JOURNAL PAPERS EXTRACTED FROM MY PHD THESIS

- M. Mazaheri, D. Mari, Z.R. Hesabi, R. Schaller, G. Fantozzi, Multi-walled carbon nanotube/nanostructured zirconia composites: Outstanding mechanical properties in a wide range of temperature, **Composites Science and Technology** 71 (7) 939-945.
- M. Mazaheri, D. Mari, R. Schaller, High temperature mechanical spectroscopy of yttria stabilized zirconia reinforced with carbon nanotubes, **Physica Status Solidi (A) Applications and Materials Science** 207 (11) 2456-2460. (Cover Page)
- M. Mazaheri, D. Mari, R. Schaller, G. Bonnefont, G. Fantozzi, Processing of yttria stabilized zirconia reinforced with multi-walled carbon nanotubes with attractive mechanical properties, **Journal of the European Ceramic Society** 31 (14) 2691-2698
- M. Mazaheri, D. Mari, R. Schaller, Y. Cai, S. Esmailzadeh, Z. Shen, High-temperature mechanical spectroscopy of nitrogen-rich Ca-SiAlON ceramics, **Journal of the American Ceramic Society** 94 (5) 1536-1545.
- M. Mazaheri, D. Mari, R. Schaller, G. Fantozzi, High temperature mechanical spectroscopy study of 3 mol% yttria stabilized tetragonal zirconia reinforced with carbon nanotubes, in: Diffusion and Defect Data Pt.B: **Solid State Phenomena**, Vol. 184, pp. 265-270.
- M. Mazaheri, D. Mari, R. Schaller, Z. Shen, High temperature mechanical loss of nanostructured yttria stabilized zirconia (3Y-TZP) reinforced with carbon nanotubes, in: **Ceramic Engineering and Science Proceedings**, Vol. 31, pp. 79-85.
- D. Mari, R. Schaller, M. Mazaheri, Mechanical spectroscopy of nanostructured composite materials, **Journal of Physics: Conference Series** 304 (1).

